Reduction of crystalline defects in III-V thin buffer layers grown on Si(100) and Ge(100) substrates by MOCVD for solar fuels

Dissertation

zur Erlangung des akademischen Grades
doctor rerum naturalium (Dr. rer. nat.)

eingereicht in der Fakultät für Mathematik und Naturwissenschaften
Technische Universität Ilmenau

von M. Sc. Manali Nandy

Gutachter:
1. Univ.-Prof. Dr. rer. nat. habil. Thomas Hannappel
2. Univ.- Prof. Dr. rer. nat. habil. Stefan Krischok
3. Dr. Frank Dimroth

Tag der Einreichung: 21.07.2022
Tag der wissenschaftlichen Aussprache: 25.01.2023

DOI: 10.22032/dbt.55641
URN: urn:nbn:de:gbv:ilm1-2023000017

Zusammenfassung

Die Heteroepitaxie von III-V auf Si und Ge Substraten eignet sich für kostengünstige, qualitativ hochwertige Epitaxieschichten, die eine geeignete Bandlücke für Mehrfachsolarzellen aufweisen. Jedoch ist die III-V-Heteroepitaxie auf diesen Substraten aufgrund von Antiphasengrenzen, die durch polares III-V Wachstum auf den unpolaren Substraten entstehen, eine Herausforderung. Außerdem müssen Kristalldefekte, die sich an der Heterogrenzfläche III-V/Substrate bilden können und dann in den III-V-Schichten die solare Konversionseffizienz erheblich beeinträchtigen, unbedingt vermieden werden. Dazu sind eine genau kontrollierte Heterogrenzfläche sowie optimierte III-V-Wachstums-bedingungen notwendig. Die vorliegende Arbeit untersucht die Präparation von Si- und Ge-Oberflächen mit wohldefinierten Heterogrenzflächen sowie das nachfolgende Wachstum von GaP- und III-P- Schichten mit geringen Defektdichten mittels metallorganischer chemischer Gasphasenabscheidung, die präzise kontrollierte, auf industriellen Maßstab skalierbare Epitaxie von III-V-Halbleitern mit hoher Reinheit ermöglicht. Für das Wachstum von GaP auf Si wurde die Ausbildung von Doppelstufen auf der Arsen-terminierten Si(100)-Oberfläche und die dazugehörige Dimer Orientierung durch Variation der Prozessparameter (Temperatur, Druck, Arsenquelle) genau kontrolliert. Um die Kristallqualität der GaP-Pufferschicht zu verbessern, wurde die Pulsabfolge der Ga- und P-Präkursoren für die Nukleation modifiziert, indem die ersten fünf TEGa-Pulse durch TMAl ersetzt wurden. Die kristallinen Defekte wurden mittels "Electron channeling contrast imaging" (ECCI) untersucht. Die quantitative Analyse der Defekte zeigte, dass bei GaP, das auf einer GaP/AlP Nukleationsschicht gewachsen wurde, im Durchschnitt die Dichte von Durchstoß-versetzungen (engl. threading dislocations, TDs) und Stapelfehlern (engl. stacking faults, SFs) um eine bzw. zwei Größenordnungen reduziert werden konnte, verglichen mit Pufferschichten, die auf einer binären GaP Nukleationsschicht gewachsen wurden. Darüber hinaus war die Oberflächenmorphologie in der Anfangsphase des Wachstums dieser Schichten im Vergleich zu Schichten, die auf einer reinen GaP-Nukleationsschicht gewachsen sind, deutlich glatter. Bei der Heteroepitaxie von III-P/Ge(100) ist ein erster Prozessschritt vor dem eigentlichen Wachstum entscheidend, bei dem die Ge(100):As-Oberfläche dem TBP-Precursor ausgesetzt wird, um die As-Atome durch P-Atome zu ersetzen. Unterschiedliche molare Flüsse des TBP-Precursors während dieses Prozessschritts beeinflussen die chemische Zusammensetzung sowie die Oberflächenrekonstruktion der Ge(100):As-Oberflächen; außerdem wirken sich die molaren Flüsse des TBP-Angebots auf die Bildung von Defekten in der III-P-Schicht aus. Ein

optimierter Zwischenschritt vor der Keimbildung wurde verwendet, um eine defektfreie III-P-Schicht auf einem Ge(100)-Substrat zu erzeugen. Diese Arbeit hat somit gezeigt, dass beim Wachstum von III-V-Verbindungshalbleitern auf Si und Ge eine genau kontrollierte Heterogrenzfläche erforderlich ist, um die hohe Kristallqualität der III-V-Schichten zu erreichen.

Abstract

Epitaxial growth of III-V compound semiconductors on Si(100) or Ge(100) substrates is highly desired for both microelectronics, photovoltaic and photoelectrochemical applications. The integration of III-V materials with main-group IV (Si or Ge) substrates have the potential to achieve high solar conversion efficiency in multi-junction photo devices. The main challenge during the growth of the III-V materials on Si(100) or Ge(100)substrates is to avoid anti-phase domains (APDs) which originate at the substrate. In addition, lattice mismatch between the epitaxially grown layer and the substrate generally introduces crystalline defects in the bulk. The presence of defects in a III-V buffer layer significantly limits the theoretical maximum solar conversion efficiency. Thus, in order to avoid APDs as well as other defects in the III-V layer, a precise preparation of atomically well-ordered substrate surface and the control of the III-V/substrate heterointerface is required. Double-layer atomic steps at the Si(100) or the Ge(100) surface are a crucial prerequisite to avoid APDs in the III-V epilayers. In addition, optimized III-V growth conditions are required to achieve low defect densities in the bulk. The present work focuses on the surface preparation of Si(100) and Ge(100) surfaces as well as the involved heterointerfaces for low-defect GaP/Si(100) and III-P/Ge(100) epilayers. The entire surface preparation and the growth of III-V layers were carried out in a metalorganic chemical vapor deposition reactor. Prior to the III-V growth, we are able to control over the dimers on both the Si and Ge surfaces. Moreover, a low temperature, rapid process route, in particular for the Si surfaces in III-V ambient was established. In order to improve the crystal quality of the GaP layer grown on Si(100):As substrates, a modified nucleation layer introducing Al was developed. For III-P/Ge, we have studied pre-growth step on Ge(100):As surfaces prior to III-P(100) buffer growth in which different molar flows of TBP precursor during the pre-growth steps were varied. The crystal defects in both the GaP(100) and the III-P(100) buffer layers were investigated by electron channeling contrast imaging (ECCI). ECCI scans showed that GaP epilayers grown on the Al-containing nucleation layers exhibit drastically reduced densities of threading dislocations and stacking faults, by 1 and 2 orders of magnitude, respectively, compared to the epilayers grown on binary GaP nucleation layers. For the III-P growth on the Ge(100) surface, we observed that the III-P layer exhibits no defects while grown on Ge(100):As substrates annealed under high TBP molar flow for a certain time, while a high defect density results in the case of III-P epilayers grown on Ge(100):As substrates annealed under low TBP molar flow. This suggests that a controlled pre-growth step is mandatory to prevent defects in the III-P layers. In both cases, either for GaP/Si(100) or for III-P/Ge(100) surfaces, preparation of the heterointerface is a crucial process step which determines the crystal quality of the subsequent III-V epilayers.

List of publications

Peer-reviewed journal articles:

1. M. Nandy, A. Paszuk, M. Feifel, C. Koppka, P. Kleinschmidt, F. Dimroth, T. Hannappel, *A route to obtaining low-defect III-V epilayers on Si(100) utilizing MOCVD*, ACS Crystal Growth & Design 21 (2021) 5603. https://doi.org/10.1021/acs.cgd.1c00410.

2. M. Nandy**,** A. Paszuk, P. Kleinschmidt, T. Hannappel, *Optical In Situ Studies of Ge(100) Interfacial Exchange Reactions in GaAs-Rich MOVPE Reactors for Low-Defect III-P Growth*, ACS Applied Electronic Materials xx (2023) xxxx. https://doi.org/10.1021/acsaelm.2c01775.

3. T. E. Saenz*, M. Nandy*, A. Paszuk, D. Ostheimer, J. Koch, William E. McMahon, J. D. Zimmerman, T. Hannappel, E. L. Warren, *MOCVD Surface Preparation of V-Groove Si for III-V Growth*, Journal of Crystal growth 597 (2022) 126843 (*equal contribution). https://doi.org/10.1016/j.jcrysgro.2022.126843.

4. A. Paszuk, O. Supplie, M. Nandy, S. Brückner, A. Dobrich, P. Kleinschmidt, B. Kim, Y. Nakano, M. Sugiyama, and T. Hannappel, *Double-layer Stepped Si(100) Surfaces Prepared in As-rich CVD ambience,* Applied Surface Science 462 (2018) 1002. https://doi.org/10.1016/j.apsusc.2018.07.181.

5. O. Supplie, A. Heinisch, A. Paszuk, M. Nandy, A. Tummalieh, P. Kleinschmidt, M. Sugiyama, T. Hannappel, *Quantification of the As/P content in GaAsP during MOVPE growth*, Applied Physics Letters 117 (2020) 061601. https://doi.org/10.1063/5.0012948.

6. B. Borkenhagen, A. Paszuk, F. N. Knoop, O. Supplie, M. Nandy, G. Lilienkamp, P. Kleinschmidt, T. Hannappel, W. Daum, *Structure and origin of antiphase domains and related defects in thin GaP epilayers on As-modified Si(100)*, ACS Crystal Growth and Design 22(12) (2022) 7040. https://doi.org/10.1021/acs.cgd.2c00697.

7. O. Romanyuk, A. Paszuk, I. Bartoš, R.G. Wilks, M. Nandy, J. Bombsch, C. Hartmann, R. Félix, S. Ueda, I. Gordeev, J. Houdkova, P. Kleinschmidt, P. Machek, M. Bär, P. Jiříček, T. Hannappel, *Band Bending at Heterovalent Interfaces: Hard X-ray*

Photoelectron Spectroscopy of GaP/Si(001) Heterostructures, Applied Surface Science 565 (2021) 150514. https://doi.org/https://doi.org/10.1016/j.apsusc.2021.150514.

8. O. Romanyuk, A. Paszuk, I. Gordeev, R.G. Wilks, S. Ueda, C. Hartmann, R. Félix, M. Bär, C. Schlueter, A. Gloskovskii, I. Bartoš1, M. Nandy, J. Houdková, P. Jiříček, W. Jaegermann, J.P. Hofmann, T. Hannappel, *Combining advanced photoelectron spectroscopy approaches to analyse deeply buried GaP(As)/Si(100) interfaces: Interfacial chemical states and complete band energy diagrams*, Applied Surface Science 605 (2022) 154630. https://doi.org/10.1016/j.apsusc.2022.154630.

9. A. Paszuk, O. Supplie, B. Kim, S. Brückner, M. Nandy, A. Heinisch, P. Kleinschmidt, Y. Nakano, M. Sugiyama, T. Hannappel, *GaAsP/Si tandem solar cells: In-situ study on GaP/Si:As virtual substrate preparation,* Solar Energy Materials and Solar Cells 180 (2018) 343. https://doi.org/10.1016/j.solmat.2017.07.032.

10. A. Paszuk, O. Supplie, S. Brückner, E. Barrigón, M.M. May, M. Nandy, A. Gieß, A. Dobrich, P. Kleinschmidt, I. Rey-Stolle, T. Hannappel, *Atomic surface control of Ge(100) in MOCVD reactors coated with (Ga)As residual*, Applied Surface Science 565 (2021) 150513. https://doi.org/10.1016/j.apsusc.2021.150513.

Contributions to international conferences:

(a) Conference proceeding articles:

1. M. Nandy, A. Paszuk, M. Feifel, C. Koppka, P. Kleinschmidt, F. Dimroth, T. Hannappel, *Reduction of defects in GaP layers grown on Si (100) by MOCVD*, 2021 IEEE 48th Photovoltaic Specialists Conference (PVSC), 1344-1347.

2. A. Paszuk, M. Nandy, P. Kleinschmidt, T. Hannappel, *In-situ monitoring of As-P exchange on Ge (100) surfaces in GaAs-rich CVD reactors for low-defect III-V multijunction solar cells,* 2021 IEEE 48th Photovoltaic Specialists Conference (PVSC), 0339-0341.

3. A. Paszuk, O. Supplie, M. Nandy, S. Brückner, A. Dobrich, P. Kleinschmidt, B. Kim, Y. Nakano, M. Sugiyama, T. Hannappel, *As-modified Si (100) Surfaces for III-V-on-Si Tandem Solar Cell*s, 2018 IEEE 7th World Conference on Photovoltaic Energy

Conversion (WCPEC) (A Joint Conference of 45th IEEE PVSC, 28th PVSEC & 34th EU PVSEC), 0233-0236.

(b) Selected presentations:

1. M. Nandy, A. Paszuk, P. Kleinschmidt, T. Hannappel, *''In situ monitoring of As-P exchange on Ge(100) surfaces in GaAs-rich CVD reactors for low defect III-V multijunction solar cells,''* **poster**, tandemPV 2022 International Workshop, Freiburg, May, 2022.

2. M. Nandy, A. Paszuk, M. Feifel, C. Koppka, P. Kleinschmidt, F. Dimroth, T. Hannappel, *''Reduction of defects in GaP layers grown on Si (100) by MOCVD,''* **talk**, IEEE 48th Photovoltaic Specialists Conference (PVSC) virtual conference, June, 2021.

3. M. Nandy, A. Paszuk, M. Feifel, C. Koppka, P. Kleinschmidt, F. Dimroth, T. Hannappel, *''Reduction of defects in GaP layers grown on Si (100) by MOVPE,''* **talk**, Compound Semiconductor Week (CSW) virtual conference, Stockholm, May, 2021.

4. M. Nandy, A. Paszuk, M. Feifel, C. Koppka, P. Kleinschmidt, F. Dimroth, T. Hannappel, *''Reduction of defects in GaP layers grown on Si (100) by MOCVD,''* **poster**, 84th Annual meeting of DPG and DPG-Tagung of the Condensed Matter Section (SKM), virtual conference, September, 2021.

5. M. Nandy, C. Koppka, A. Paszuk, M. Feifel, P. Kleinschmidt, F. Dimroth, T. Hannappel, *''Impact of Al on defect density reduction in GaP buffer layers on Si(100) substrates studied by electron channeling contrast imaging,''* **talk**, 18th conference on Defects-Recognition, Imaging and Physics in semiconductors (DRIP), Berlin, September, 2019.

6. M. Nandy, C. Koppka, A. Paszuk, M. Feifel, P. Kleinschmidt, F. Dimroth, T. Hannappel, *''Impact of Al on defect formation in GaP buffers grown on Si(100) substrates,''* **poster**, The 18th European Workshop on Metal-Organic Vapour Phase Epitaxy (EW-MOVPE 18th), Vilnius, Lithuania, June, 2019.

7. M. Nandy, C. Koppka, A. Paszuk, M. Feifel, P. Kleinschmidt, F. Dimroth, T. Hannappel, *''Impact of Al on defects introduced during GaP nucleation on Si(100)2° substrates by MOCVD,''* **talk**, 83rd Annual meeting of DPG spring meeting, Regensburg, April, 2019.

8. M. Nandy, A. Paszuk, C. Koppka, M. Feifel, P. Kleinschmidt, F. Dimroth, T. Hannappel, *''Impact of Al on defect density in GaP buffer layers on Si(100) substrates studied by electron channeling contrast imaging,''* **talk**, DGKK workshop on Epitaxy of III-V Compounds, Dresden, December, 2019.

9. M. Nandy, A. Paszuk, A. Dobrich, O. Supplie, P. Kleinschmidt, T. Hannappel, *''AlP/GaP(100) surfaces studied in situ during MOVPE preparation for III-V/Si multijunction solar cells,''* **poster**, 17th European Workshop on Metalorganic Vapor Phase Epitaxy, Grenoble, France, 2017.

Table of content

Zusammenfassung .... **I**

Abstract III

List of publications .... **V**

1 Introduction **1**

2 Theoretical and experimental background **5**

2.1 Multi-junction solar cell 5

2.2 III-V-on-IV(100) heteroepitaxy 8

2.3 Crystalline defects 10

2.4 Si(100) and Ge(100) surfaces 15

2.4.1 Interaction of hydrogen with Si(100) and Ge(100) surface and atomic step formation 17

2.5 Experimental background 19

2.5.1 Metalorganic chemical vapor deposition 19

2.5.3 Reflection anisotropy spectroscopy 23

2.5.4 X-ray photoelectron spectroscopy 27

2.5.5 Low energy electron diffraction 30

2.5.6 Electron Channeling Contrast Imaging 32

2.5.7 Scanning tunneling microscopy 36

2.5.8 Atomic force microscopy 38

2.5.9 X-ray diffraction 38

3 State of the art **41**

3.1 Anomalous double layer stepped formation on Si(100) surface in clean H_2 CVD ambience: Energetics vs Kinetics 41

3.2 Si(100) surface preparation in As-rich CVD ambience 43

3.3 GaP(100) surface grown on both Si(100):H and Si(100):As surfaces 45

3.3.1 *In situ* monitoring during GaP nucleation on Si(100):H surfaces 47

3.3.2 Characterization of defects in GaP/Si(100) buffer layers by ECCI 49

3.4 Ge(100) surface preparation in group V-rich CVD ambience 50

3.5 GaInP(100) nucleation on Ge(100) surface 52

4 Sample preparation **55**

4.1 Chemical pre-treatment of Si(100) substrates by Wet Chemical Etching 55

4.2 Si(100) surface preparation in As-ambient 55

4.3 GaP and GaP/AlP nucleation and subsequent growth of GaP buffer layers 56
4.4 Ge(100) 6° surface preparation and subsequent GaInP growth 56
5 *In situ* control of dimer orientation and atomic structure of As-modified Si(100) surfaces..59
5.1 Preparation of double-layer stepped As-modified Si(100) surfaces in As-rich CVD ambience. 59
5.2 Low temperature preparation of As-modified Si(100) 2° in III-V reactor 69
5.3 Summary of this chapter 74
6 Crystalline defects in GaP buffer layers grown on Si(100) substrate.....................................75
6.1 Crystalline defects in GaP buffer layers grown on H-terminated Si(100) surfaces 75
6.2 Crystalline defects in GaP buffer layers grown on As-modified Si(100) surfaces 80
6.3 GaP/AlP nucleation on Si(100):As 82
6.3.1 *In situ* control of AlP(100) buffer layer grown on GaP(100) substrate 82
6.3.2 Al-modified GaP nucleation on Si(100) 86
6.3.3 Evolution of GaP/AlP nucleation layers on Si(100) heterointerface 89
6.4 Crystal defects in the GaP buffer layers grown on GaP/AlP nucleation on Si(100):As 2° surface 93
6.5 Stress - strain in the GaP(100) buffer layers 101
6.6 Influence of the Al on the GaP(100) surface morphology 103
6.7 Crystalline defects in GaPN 105
6.8 Summary of this chapter 108
7 III-V growth on Ge(100):As in coated GaAs MOCVD reactors...111
7.1 Ge(100):As in phosphorus-rich MOCVD ambience.. 111
7.2 Defects in the III-P(100) buffer layers in dependence on the pre-growth procedure applied on the Ge(100) surfaces 119
7.3 Summary of this chapter 124
8 Conclusion 125
References...129
Acknowledgement 141
Declaration.. 143
List of samples 144

1 Introduction

Currently, the world's energy consumption in large part comes from burning fossil fuels. With increasing population, high demand for energy source is equally rising, which leads to a high emission of carbon dioxide (CO_2) into the atmosphere. CO_2 and other greenhouse gases trap solar radiation in the atmosphere and the CO_2 concentration today has never been higher. This causes the Earth's temperature to rise which further results in climate change disrupting the weather patterns and the usual balance of the nature. Reduction of CO_2 is therefore a necessary measure to save our environment. In 2019, Council of the European Union (EU) agreed to achieve a climate-neutral environment by 2050, which refers to an economy with 'net-zero' greenhouse gas emission. To achieve that, most of electricity generation must come from renewable sources.

The alternative renewable energy source can be solar energy which converts sun light into electricity by using a solar device based on semiconductors, such as Si or III-V materials, organic solar cell, or perovskite solar cell etc. The cost of solar photovoltaics (PV) has been decreasing over years now. According to Swanson's Law, the price of solar PV modules tends to drop 20 % for every doubling of the production capacity of the solar industry [1]. Prices for Si solar cells decreased from $76.67 per watt (W) in 1977 to $0.16-0.20 per W in 2022. Improving the efficiency of these solar PV is highly relevant for reducing the cost of electricity. Another challenge is the storage of the produced energy. One option is to store this energy in form of hydrogen (H_2) produced from water by conversion of sunlight via a photoelectrochemical (PEC) cell. H_2 has a high energy density and can be stored in a bottle in a gas form. However, its high production costs ($8.43/kg as of 2020) have to be overcome to compete with other alternative carbon-free energy sources [2]. For direct solar water splitting in an 'artificial leaf', a photovoltage above 1.7 V must be generated by the PEC cell. In order to increase the efficiency of the solar cells as well as to overcome the photovoltage of 1.7 V PEC devices tandem photo absorbers need to be produced. Tandem structure is a combination of multiple p-n junctions of different semiconducting materials which absorb different part of the solar spectrum and are transparent for each sub cells, and thus the absorption losses of the device are minimized. The record solar-to-electricity and solar-to-hydrogen (STH) conversion efficiencies are achieved by devices based on multi-junction III-V compound semiconductor photo absorbers [3–7]. These optoelectronic devices were grown on expensive substrates, mostly Ge or GaAs. Significant price reduction per kilogram H_2 and the tandem PV devices can be achieved by substituting the expensive substrates with well-established and cheap silicon (Si) substrates. Applying metalorganic

chemical vapor deposition (MOCVD) ensures upscaling at industrially relevant scale and high-quality III-V semiconductor growth. A Si bottom cell in combination with a III-V top absorber with a bandgap in the range of 1.6 to 1.8 eV is predicted to yield tandem PV and the STH efficiencies close to optimum [8,9]. A good material for the top absorber is $GaAs_{1-x}P_x$, due to its direct and tunable bandgap [10], which can be controlled by the ratio of arsenic (As) to phosphorus (P). To overcome the big lattice mismatch between Si and GaAsP, step graded GaAsP buffers, starting with pseudomorphic GaP and an increasing As content up to about 75%, have been established [11] and recently very low densities of mismatch-related defects have been achieved [12]. However, the different crystal structures of GaP and Si require precise control of the interface formation in order to avoid formation of defects which can cause poor optical properties and decrease PV or STH efficiency of the device. Besides, the III-V-on-Si heterostructures, low-defect III-P epilayers on Ge(100) substrates are also advantageous to achieve high solar conversion efficiency.

This work focuses on the Si(100) and Ge(100) surface preparation and subsequent growth of low-defect GaP(100) and III-P(100) buffer layers, respectively, by MOCVD. The MOCVD is a highly complex process due to the presence of a process gas, which strongly interacts with the surface, complex metalorganic sources and their chemical reactions. Defect formation in III-V buffer layers strongly depends on the surface preparation as well as the nucleation parameters. Therefore, the formation of the buried interface between the substrate and the III-V layer needs to be better understood and low-defect nucleation processes need to be developed. Antiphase domains (APDs) are defects which originate from the growth of the polar III-V compounds on nonpolar substrates [13]. To avoid these defects, the Si(100) and the Ge(100) surfaces must be prepared with steps of even numbered atomic height (‘single-domain’). The Si(100) surface preparation in hydrogen-based MOCVD systems is well-established for both nominal and vicinal Si(100) surfaces terminated with either hydrogen or arsenic [14,15]. Similar to the Si(100) substrates, vicinal Ge(100) substrates with double-atomic steps are established in H_2-only [16], As-rich [17] and in more realistic, GaAs-rich CVD-ambience [18]. Here, we focus on the double atomic stepped Si(100) and Ge(100) surface preparation under the arsenic precursor in ‘industrially relevant’ III-V reactor conditions, which is challenging since the III-V residuals from previous processes could hinder the surface preparation. In addition, a specific process route to reduce the temperature and the time of the Si(100) surface preparation is developed. A surface sensitive optical probe, *in situ* reflection anisotropy spectroscopy (RAS) allows to continuously monitor these surfaces studied here by providing characteristic RA spectra which contain rich information about the probed surfaces. Electron-based ultrahigh vacuum (UHV) techniques, such as X-ray photoelectron spectroscopy, low energy electron diffraction and scanning tunneling microscope enable to study chemical compositions, surface symmetry and atomic structure of these surfaces in detail, and to benchmark the

complex RAS signals with their specific surface chemical composition and reconstruction. Here, a contamination-free MOCVD-to-UHV transfer system is applied to transfer the MOCVD as-prepared samples into all the UHV surface sensitive techniques. Beside APDs, the formation of other defects in the III-V buffer layers, such as threading dislocations (TDs) and nucleation related defects, stacking faults (SFs) [19] and stacking fault pyramids (SFPs) [20] can be minimized by precisely controlled nucleation process route. In this work a standard GaP(100) nucleation procedure was modified to significantly reduce density of these defects. For the III-P/Ge(100), different pre-growth steps were studied and applied on As-terminated Ge(100) substrates in phosphorus-rich ambient to achieve a low-defect III-P(100) epilayer. *In situ* RAS and other surface sensitive methods cannot provide information about defects and therefore, defects in both, GaP(100) and III-P(100) epilayers were investigated and quantified *ex situ* by electron channeling contrast imaging (ECCI). The ECCI has been established in Ilmenau during this work and proved as a fast, non-destructive mothed for defect quantification on a large scale. We have developed controlled preparation routes for both of the GaP(100) and III-P(100) epilayers. In particular, we show here that in cooperation of Al during the initial GaP nucleation stage remarkably reduces the densities of TDs, SFs and SFPs in subsequently grown GaP(100) buffer layers. Moreover, application of Al facilitates a two-dimensional growth at the initial growth stage. In addition, a defect-free III-P(100) buffer layers with a smooth surface morphology can be grown by applying an optimized pre-growth step on the Ge(100):As surface. In both of the III-Vs procedures, we observe that the heterointerface between the layer and the substrate is the key to understand which determines the surface quality of the subsequently grown III-V layers. The combination of the *in situ*, *in vacuo* with the complementary *ex situ* methods allows to investigate, understand and to fine-tune in atomic scale the preparation of the critical surfaces, Si(100):As and Ge(100):As, and the subsequent nucleation step for low-defect III-V buffer layers: Our studies show process routes for a significant reduction of defect density in GaP(100) and III-P(100) buffer layers grown on Si(100):As and Ge(100):As substrates, respectively.

2 Theoretical and experimental background

In this section, the challenges of the integration of III-V materials with Si(100) and Ge(100) substrates for highly-efficient multi-junction solar cells will be discussed. The theoretical background of multi-junction solar cells and basics regarding III-V-on-IV heteroepitaxy, the involved crystal structures, and surfaces will be summarized. Further, the main experimental techniques applied in this work are introduced with focus on their principles and operation during the characterization.

2.1 Multi-junction solar cell

Solar cells are electrical device which enable conversion of light energy to electricity by the photovoltaic effect. A solar cell consists of a semiconducting material with a specific bandgap E_g and a p-n junction. In a single junction cell, in particular in a p-n junction, the photons which has energy $h\nu$ larger than the bandgap E_g can be absorbed. Absorbed photons have the potential to transfer their energy, $h\nu$, to an electron generating an electron-hole pair or an exciton. The electron-hole pairs are separated by both the diffusion and drift of charge carriers due to concentration gradient along the p-n junction which accelerates both electrons and holes towards their respective n-doped and p-doped region. The resulting current Ig is called the generated photocurrent. The photons which has energy less than the cell bandgap are not absorbed and considered as transmission losses. Photons with energy equal to the bandgap are ideally converted and the photons with energy higher than the bandgap are lost as a thermalization losses in which carrier kinetic energy is converted to heat by phonon emission. Therefore, the conversion efficiency of the solar cell principally depends on the band gap of the solar cell material. An average energy of an electron after thermalization can be given by $Eg+3k_BT/2$, where k_B is the Boltzmann's constant and T is the temperature. In addition, there are extraction losses related to the balance between collecting carriers at a high electrical potential and collecting those carriers before they recombine. For a single junction cell, Shockley and Queisser calculated the theoretical conversion efficiency η of the incoming radiation into electrical energy to be limited at about 30 % [21].

Multi-junction solar cells (MJSC) are combined solar cells of multiple p-n junctions which are made of different semiconducting materials. A MJSC can be at least three junctions of solar cells in electrical series connection. Each of the p-n junctions produces electric current in response to different wavelengths of incident light. For a MJSC the sub-cells must be selected in a order of decreasing bandgaps from top cell to bottom cell so that the top cell

allows maximum absorption of light and further transmit completely into the last sub-cells. In addition, the use of multiple semiconducting materials allows the absorbance of a broader range of wavelengths and improves maximum conversion efficiency. Moreover, these combined cells reduce thermalization and transmission losses which enables conversion efficiencies beyond the Shockley-Queisser limit. Figure 2.1 shows a solar spectrum AM 1.5 divided in four regions defined by materials with a different bandgap: GaInP, GaAs, GaInNAs, Ge. The graph indicates different part of wavelengths of a solar spectrum can be absorbed by the material depending on their bandgap. The gaps in the spectrum at around 900 nm, 1100 nm, 1400 nm, 1900 nm, etc. are due to the absorption in the atmosphere mainly by CO_2 and H_2O.

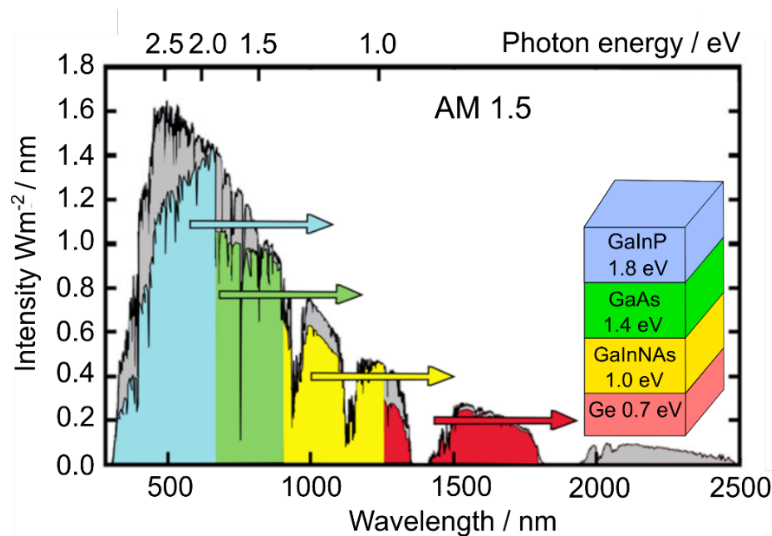

Figure 2.1: AM 1.5 solar spectrum, divided in four different absorption regions - an expample of a multijunction solar cell: semiconductors with different bandgaps convert different ranges of the solar spectrum, thereby thermalization and spectral losses are reduced. The graph shows the evolution of multijunction solar cell structures from the existing GaInP/GaAs 2-junction device to 3- and 4-junction devices by incorporation of an III-V material with 1 eV bandgap energy, as future generation solar cells. Theoretical efficiencies are idealized (practical efficiencies can be expected to be decreased to ~80 %) and given for the AM0 (for space application) and AM1.5 500 suns (based on [22]).

Theoretically, an ideal 2-junction (tandem) solar cell can reach 42 % efficiency, a 3-junction cell - 49 % and an infinity-layer cell - 68 % and 86 % under concentrated sunlight [23,24]. Under one sun AM1.5 spectrum, even higher conversion efficiencies of 46 %, 52 %, 56 % for 2- 3- and 4- junction solar cell, respectively, can be achieved according to Bremner et al. [25]. A good candidate for a substrate in MJSCs is a binary compound GaAs. Its bandgap 1.42 eV provides the maximum theoretical efficiency limit for the AM 1.5 solar spectrum

[21]. Tandem solar cell of InGaP as a top absorber cell (20 % efficiency as a single junction solar cell [26]) with GaAs as a bottom cell, with a lattice constant 5.64 Å and the bandgap energy of 1.86 eV and 1.42 eV, respectively, exhibits a theoretical conversion efficiency of 34 %, under one sun AM1.5 [27]. This solar cell structure already exceeded 30 % efficiency under one sun AM1.5 [28].

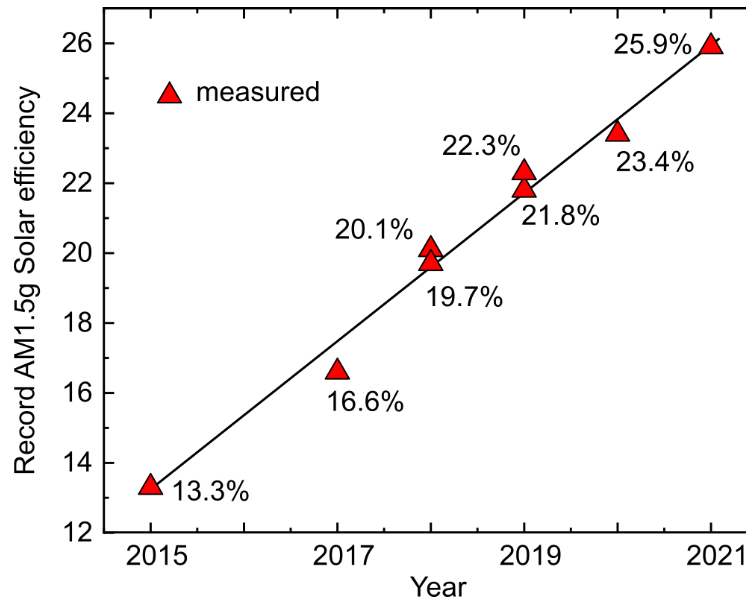

Figure 2.2: Year wise development of record solar conversion efficiency of Si-based solar cells under the AM1.5g condition. A gradually increment of solar efficiency has been observed from the year 2015 (13.3%) to 2021 (25.9%). The efficiency chart showing in the graph is based on the measured value from the cells without a concentrator used.

Recent advances of MJSC show solar conversion efficiency of 47.1% (measured) from a GaAs based 6- junction cells [4]. GaAs based substrate with 4- junction wafer bonded tandem cell under the concentrated light achieved a solar conversion efficiency of 44.7% [5]. King et al., have showed a practical achievable conversion efficiency of 40% (AM1.5D at 240 suns) is possible from a 3- junction metamorphic GaInP/GaInAs/Ge cells [29]. Although advanced PV technology provides high solar conversion efficiency, the cost of these III-V solar cells limits their use in terrestrial applications. However, Ge wins over GaAs as a substrate material since it is cheaper, but Si is way more cheap, abundant and mechanically stable for solar cell applications. In contrast to GaAs or Ge based solar cells, Si based PV technology provides significant price reduction of MJSC. In addition, the bandgap of Si (1.12 eV) is close to the theoretical maximum efficiency for a single-junction solar cell, based on the Shockley-Queisser limit [21], and its bandgap is a perfect candidate for a high efficient tandem device. So far, the world record efficiency of 25.9% has been

achieved from a 3-junction GaInP/GaAs/Si cell under AM1.5 [7]. In 2020, an epitaxial GaAsP/Si dual-junction solar cell with a verified AM1.5g conversion efficiency of 23.4% has been presented by Lepkowski et al. [30]. A similar GaAsP/Si design with an in-house measured (uncertified) efficiency of 25.0% was presented by Fan et al. [6]. Some previous works of Feifel et al. showed 22.3 % and 19.7 % conversion efficiencies from 3- junction Si cells [31,32]. A year wise development of solar conversion efficiency under AM1.5g is shown in Fig. 2.2.

So far, MJSCs were mainly established to power satellites in space due to their high efficiency and production costs. However, current progress on converting the sunlight to electrical energy is ongoing by concentrator photovoltaic (CPV) technology which allows to reduce the area of the solar cell (material reduction) and to increase its conversion efficiency by increasing the solar concentration factor. Here, lenses or mirrors focus the sunlight on a smaller solar cell area, and a tracking system follows the course of the sun. Typically, concentrations are in the range of 500 to 1000 suns. However, high material and production costs of III-V MJSC limit their use in CPV application. Calculated current values for CPV power plants are from 0.08 / kWh to 0.15 / kWh € [33].

In addition to achieving solar efficiency, controlling low defect densities in the epitaxially grown films as well as ideal band gap combinations are crucial for high performance solar cell devices. Here we focus on the binary GaP growth on Si substrate since GaP represents a popular III-V material having a lattice constant (5.45 Å) close to Si lattice constant (5.43 Å). Alternatively, GaP could serve as a window layer in Si solar cell [34], a collector in combination with Si absorber [35,36] or as a buffer layer for other III-V compounds, e.g. GaAsP solar cell [12,37–39]. Similar to the GaP/Si(100) heteroepitaxy, the work also focuses on a defect free III-P buffer layer on Ge(100) substrate.

2.2 III-V-on-IV(100) heteroepitaxy

The monolithic integration of high-efficient III-V compound solar cell materials and devices with Si substrates has been a main driving force in fundamental photovoltaics research for decades. As a substrate, Si has a number of physical properties that are particularly advantageous for photovoltaics usage versus other conventional substrates (e.g. Ge, GaAs, InP), including low mass density, high fracture toughness, and high thermal conductivity, in addition to the substantial cost benefits of working on the low-cost, large-area, scalable Si platform. Besides working as a substrate, Si can be utilized as a high-performance active sub-cell, enabling the production of high-efficiency, spectrum-optimized III-V/Si MJSC. However, growth of III-Vs on Si is indeed challenging because of lattice mismatch between

the III-V layers and Si substrates which commonly introduces tensile or compressive lattice strain [40]. Different thermal expansion coefficient of both substrate and layer materials result in unequal strain after cooling down from the growth temperature. This further leads to form crystal defects in the III-V layers [41]. Other challenge is polar-on-nonpolar heteroepitaxy [13], which introduces anti-phase domains in the III-V layers. These are the defects originate at the III-V/Si heterointerface and propagate through the material towards the growth direction. In addition, inter-diffusion of materials between the layer and substrates is sometimes uncontrollable unless appropriate growth condition addressed and could form cross doping either in the substrate or in the grown layers [42,43].

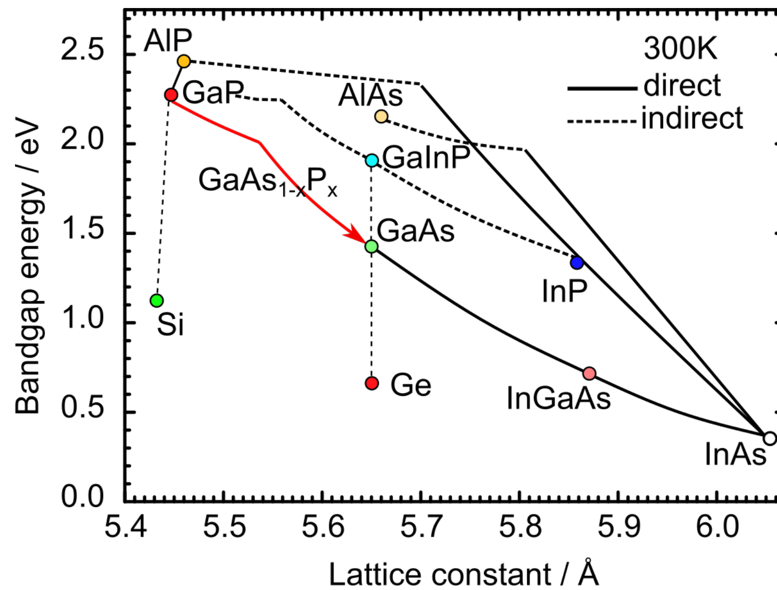

Figure 2.3: Relation between bandgap and lattice constant of binary, ternary, quaternary III-V compounds, and Si and Ge. Direct and indirect bandgaps are indicated by the style of the line and symbol. The diagram is based on data from Vurgaftman et al. [44].

III-V semiconductors exhibit ideal properties for application of MJSC. A ternary or quaternary III-V compounds have tunable bandgap and lattice matching over a wide range of substrates which is relevant for MJSC. Fig. 2.3 displays a plot of bandgap of III-V semiconductors over their lattice constants which clearly indicates the potentials of III-Vs and challenges of the heteroepitaxy on group IV substrates.

Binary GaP deposition on a Si(100) substrate is a very common and well-known heterostructure because GaP (a_{GaP} = 5.45 Å) exhibits a small lattice mismatch to Si (a_{Si} = 5.43 Å) of only 0.37 % at room temperature. The pseudomorphic GaP films can be grown on Si(100) substrates until the critical thickness of the film (approximately ≤ 50 nm) [45]. Therefore, GaP/Si can be used as a template for further III-V integration. A successive

change in lattice constant by changing the composition of ternary GaAsP buffer layer (graded layers) on GaP/Si template results in an attractive heterostructure on Si in which the grading layers enables to release the lattice strain in the top GaAsP layer and therefore, prevent formation of defects like threading dislocations [12,46,47]. Moreover, the bandgap of GaAsP is tunable which open opportunities for a broad range of photovoltaic applications. On the other hand the novel material system of dilute nitrides (GaIn)(NAsPSb), which features incorporation of small amounts of N (<5%), enables lattice matched growth on Si(100) and a direct bandgap [48,49]. Beside GaP, lattice matched GaInP can be grown either on Ge(100) or GaAs(100) substrates which is a common heteroepitaxy relevant for photovoltaic applications [50]. Although small lattice mismatch between layer and substrate is suitable for epitaxial growth, but formation of defects in III-V films, in particular for thicker films is unavoidable and therefore, an appropriate growth environment must be employed. In the next section, the crystal defects formed mostly in the III-V layers will be discussed.

2.3 Crystalline defects

Since the III-V compound semiconductors have excellent optoelectronic properties, their monolithic hetero-integration on Si substrates enable a multiple application of solar devices. However, due to the lattice mismatch between most III-V semiconductors and Si substrates, monolithic growth inevitably leads to the formation of strain releasing defects which degrade the final device performance and reliability. From a general perspective, a crystal defect is any kind of deviation from a perfect periodic arrangement of the semiconductor crystal atoms. Hence, it is a break in the crystal symmetry. Depending on structural formation, defects can be classified as zero-, one-, two- and three- dimensional. Zero-dimensional point defects in III/V semiconductors are interstitials, vacancies, anti-sites and impurity atoms. Misfit dislocations (MDs) and threading dislocations (TDs) are one-dimensional line defects. Stacking faults (SFs), stacking fault pyramids (SFPs) and antiphase domains (APDs) between crystal regions of different polarities expand two-dimensionally and can be considered as planar defects. Twinned regions, grains and precipitates are defined as three-dimensional volume defects. In order to avoid these defects, improved growth techniques, the increase in purity of precursor sources, optimized device design as well as the availability of substrates with very low defect density are the key parameters.

Antiphase domains

The main challenge during the growth of III-V/Si(100) epitaxy, is polar-on-nonpolar growth which commonly introduces APDs in the subsequent layers [13]. Diamond structure of Si holds two interpenetrating 'fcc sublattices' and thus, each atom is connected to its four surrounding neighbors by four tetrahedral bonds which differ in spatial orientation for the two sublattices (Fig. 2.4). Both sublattices are occupied by the same atom. In contrast, III-V semiconductors exhibit zincblende crystal structure where the two sublattices are occupied by different atomic species and correspondingly the symmetry in the zincblende structure is reduced compared to the diamond structure. In a single-domain crystal, only one sublattice orientation exists.

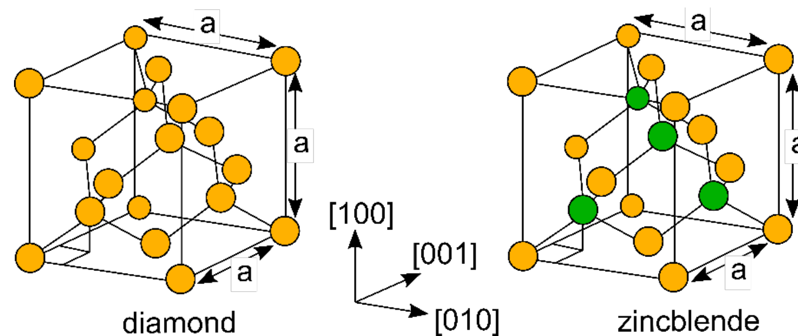

Figure 2.4: Three-dimensional sketch of diamond and zincblende lattice structures.

During the III-V growth, III-V compound semiconductors have polar bonds and a lattice base which consists of two different atoms while Si is a nonpolar semiconductor. Any real Si(100) or Ge(100) substrates exhibit atomic steps. In case of single atomic step on Si(100) or Ge(100) substrate, during the III-V growth, unwanted group III-III or group V-V homopolar bond originate from the heterointerface (Fig. 2.5). These bonds form electrically charged defects at the interface which are called APDs and propagate along the (111) plane through the crystal. When two APDs propagating along the two opposite (111) planes meet with each other, they annihilate after a certain thickness of the III-V layers. In order to avoid these defects, a double atomic step or even number of atomic steps on the substrate is a mandatory step prior to any III-V integration. The detail of surface preparation will be discussed in following chapters.

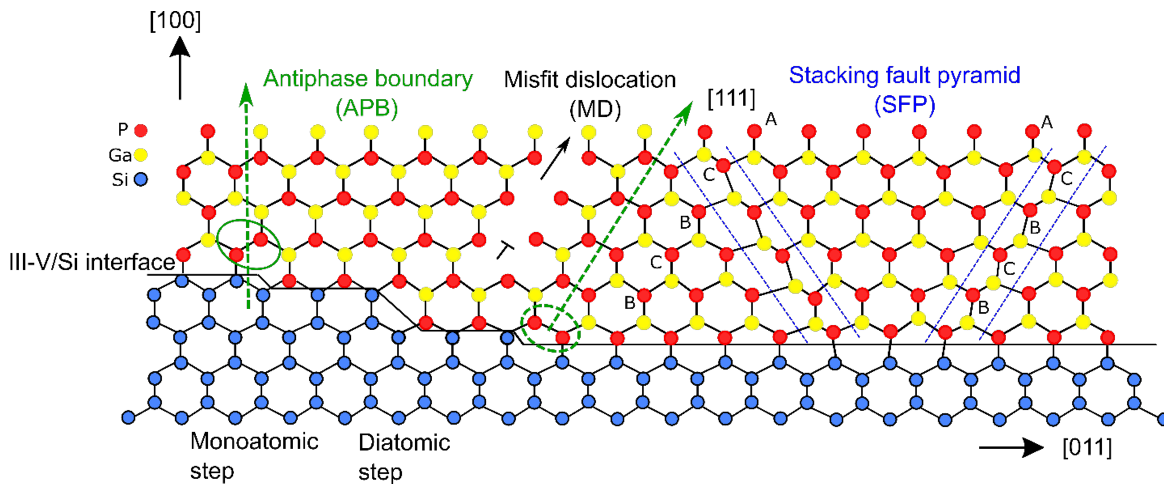

Figure 2.5: Sketch of formation of antiphase boundary due to presence of monoatomic steps on Si(100) surface, misfit dislocation gliding through the (111) slip plane and stacking fault pyramid that originates from the interface and propagate through set of (111) planes.

Misfit and threading dislocations

MDs and TDs are the line defects in a crystal. The epitaxial deposition of a lattice mismatched III-V material on Si(100) substrates leads to the build-up of strain energy which is absorbed by elastic strain relaxation up to a certain critical layer thickness. If the epitaxial layer exceeds the critical layer thickness, it becomes energetically more favorable to introduce dislocations to reduce the strain energy. This marks the beginning of plastic relaxation via defect formation. All relevant III-V devices integrated on Si require a III-V layer thickness mostly larger than the critical thickness and therefore, the formation of MDs and TDs are inevitable to accommodate the strain due to the lattice mismatch.

Fig. 2.6 depicts a sketch of formation of MDs in a crystal from the substrate-layer heterointerface and dislocation half-loop propagating from surface towards heterointerface. A pre-existing MD/TD from the substrate could glide on the layer. However, the gliding of pre-existing TD will not play an important role as a relaxation mechanism in III/V on Si since Si substrates contain nowadays a very low density of defects [51]. In a zincblende crystal, the MDs originating from the heterointerface glide along the slip planes and extends through the crystal in order to release elastic strain of the layer [12]. The TD segment present at the end of the MD. Dislocation half-loops can nucleate homogeneously or heterogeneously at the growth surface and glide down towards the heterointerface while laterally expanding. When the half-loop reaches the interface, misfit segments are formed again to release the strain. The two associated TD ‘arms’ penetrate the whole layer and end at the crystal surface with little contribution to the strain release. A dislocation is classified by the angle between the Burgers vector and the dislocation line. The MDs can be 90° (edge),

0° (screw) and 60°-unit dislocations. In addition, partial dislocations, which are separated by a stripe of SFs, also play an important role in plastic relaxation. The core atoms along the defect line have incomplete, broken or dangling bonds.

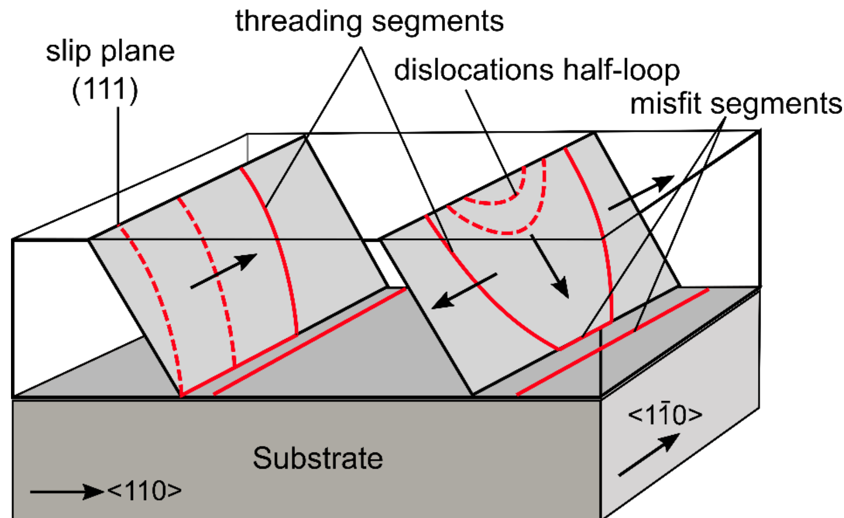

Figure 2.6: Schematic of formation of misfit and threading dislocations glide along the slip planes. In particular for zincblende crystals, misfit dislocations originate from the III-V/Si heterointerface and glide through the slip planes which are 60° type dislocations. Other misfit dislocations whether 90° (edge) or 0° (screw) do not glide into the slip planes. In addition, dislocation half-loops which nucleate at the surface and subsequently propagate gliding down towards the heterointerface. Figure is taken from *Ref.* [51] and redrawn.

MDs and TDs introduce electronic states in the band gap of the III/V material system caused by the atoms distorted in the crystal. The energy states correlated with the dislocation cores are mostly deep level traps in the band gap, whereas the local strain fields due to the distorted atoms induce shallow energy states. These energy states introduced by dislocations have a strong electrical and optical impact on III-V based device performance. They can act as non-radiative recombination centers reducing the photon emission efficiency and/or the minority carrier life time. States in the band gap can also initiate carrier generation and increase the leakage current in devices. Electronic traps can be charged and behave as donors or acceptors with a strong influence on the carrier density. Therefore, it is evident that MDs and TDs in the active volume of a device have a clear detrimental effect on the device performance and reliability. Dislocation defects outside the active layer stack might not have a direct impact on the device characteristics but can induce an indirect or delayed degradation.

Stacking faults and stacking faults pyramids

These types of defects are the two-dimensional planar defects. Single SFs are alternation of atoms in the {111} plane in a zincblende crystal formed by insertion or removal of additional atoms. Processes like condensation of excess vacancies or interstitial atoms can lead to such an alternation in the stacking sequence along the {111} planes [51]. The interruption in stacking sequence carry a certain stacking fault energy. They are bounded by partial dislocations. Two partial dislocations dissociated from a unit dislocation are separated by a stripe of SFs. The width of the SFs depends on the repulsive force between the two partial dislocations while dissociating into two dislocations.

The nucleation layer during the initial deposition on the substrate must be precisely controlled since island growth, which is common at the III-V/Si heterointerface, facilitate the formation of these SFs in the subsequent III-V layers. They can be originated upon coalescence of these islands formed at an early stage during the epitaxial growth on substrates and propagate along one of the {111} planes [52,53]. Any kind of surface damage, precipitates, impurities such as residual oxide on the substrate surface could cause the nucleation of these defects. Therefore, the cleaning and pre-treatment of the substrate before the III-V growth is a very crucial process step to avoid formation of defects. Furthermore, the choice of very low growth temperatures, as typically used for the III-V nucleation layer on Si(100) substrate, requires appropriate adjustment of the growth rate, V-III ratio and switching sequence [52–54] to avoid the formation of these defects.

SFPs are composed of four intersecting SFs, which occupy four {111} planes such as $(\bar{1}\bar{1}\bar{1})$, $(\bar{1}\bar{1}1)$, $(\bar{1}11)$ and $(\bar{1}1\bar{1})$ planes if the surface normal is considered as (100). The pyramid normally forms at the III-V/Si(100) heterointerface and propagate through all four sets of {111} planes towards the (100) surface and intercept with the (100) plane at an angle of 54.74° [55]. Thus, a smooth, abrupt and two dimensional heterointerface during the III-V growth on Si(100), which is free of three-dimensional islands, appears highly beneficial.

Fig. 2.7 (a) shows a schematic of a SFP which is considered to be originated from the heterointerface and propagate through the all four {111} planes. The lateral dimension can be directly related to the thickness of the film if the SFP originates from the heterointerface [56]. The lateral dimension can be calculated by the trigonometric function $\tan\Theta = 2h/a$, where 'Θ' denotes the angle between (100) and (111) planes, 'a' is the length of one side of SFP in (100) plane and 'h' is the lateral dimension correlated to the film thickness. If the length of the SFP in (100) plane (a or a/2) is known, then the lateral dimension 'h' can be determined by the trigonometric function as shown below (Fig. 2.7 (b)).

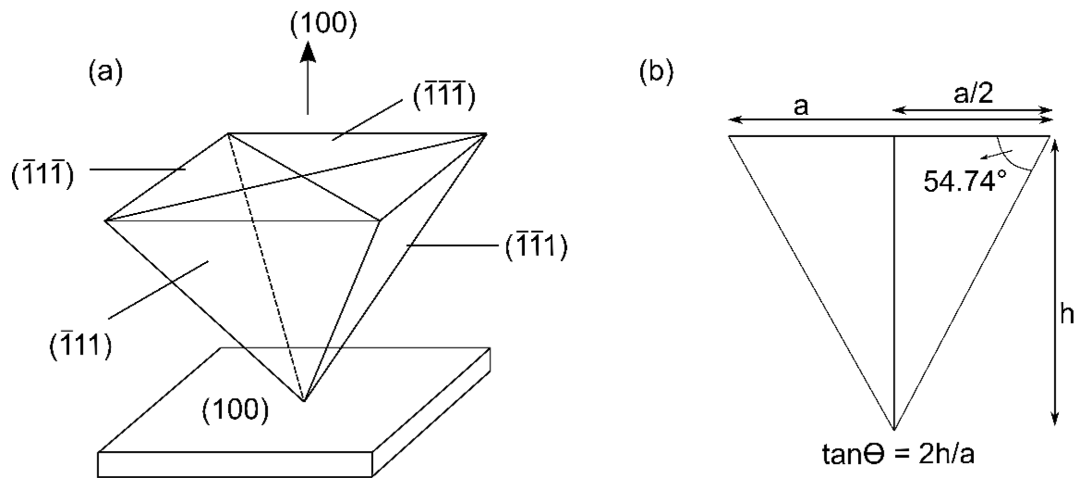

Figure 2.7: (a) Schematic of a stacking fault pyramid originating from (100) surface and propagating thorough four ($\bar{1}\bar{1}\bar{1}$), ($\bar{1}\bar{1}1$), ($\bar{1}11$) and ($\bar{1}1\bar{1}$) planes. (b) One side of a set of {111} planes through which an SFP propagates and intercepts the (100) plane at an angle of 54.74°. The length 'a' of the edges in (100) plane of a SFP can be used to determine the depth of the SFP 'h'.

SFs and SFPs are the defects which are unavoidable from the bulk layer. If they originate, they continue to propagate through the layer up to the surface. The size of these defects depends on the thickness of the grown film which means the size of the SFP increases with the thickness of the layer.

2.4 Si(100) and Ge(100) surfaces

Both Si(100) and Ge(100) surfaces are group IV elements and crystallize in diamond crystal structure. Each Si or Ge atom is bonded with four other Si or Ge atom; two below and two above. However, the Si or Ge atoms on the surface exhibits two available bond sites. Therefore, the broken bond on the surface at the outermost layer could not fulfil the traditional diamond structure. In order to reduce the number of broken bonds as well as to minimize the surface energy, the Si or Ge atoms rearrange and create bond with the neighboring atoms. When the silicon atoms bond with each other, they are pulled towards each other and out of their diamond lattice positions. A rows of silicon atom pairs form on the surface which are commonly known as dimer rows.

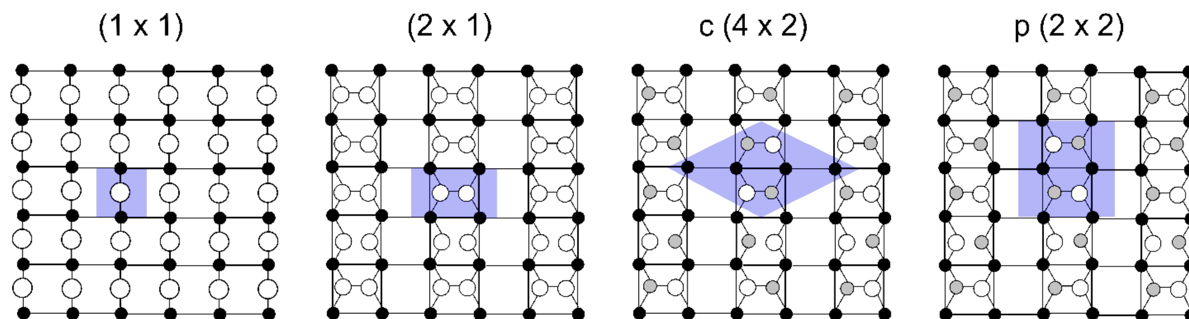

Figure 2.8: Ball and stick model of the Si(100) and Ge(100) surface: (1×1) ideal unreconstructed surface, (2×1) reconstruction with symmetric dimers, c(4×2) and p(2×2) reconstruction due to dimer buckling. Blue shaded areas represent the unit cell of the surface reconstruction.

Earlier studies on Si(100) surfaces based on surface sensitive LEED measurement revealed that the Si(100) surfaces exhibited (2×1) surface reconstruction when the surface was prepared under UHV ambient [57]. In this surface reconstruction, vertical separation between the Si atoms located up and the down atom within the dimer is about 0.72 ± 0.05 Å and the dimer bond length of 2.24 ± 0.08 Å has been found which is slightly smaller than the Si-Si distance in bulk (2.35 Å) [58]. On Si(100) surface, the dimers are buckled by 19°. The formation of Si dimers induces significant distortions in the substrate, which employ surface compressive stress along the dimer rows and tensile stress building up perpendicular to the dimer rows. The overall distortions extend down to fifth layer of the Si surface [58]. The Si surface exhibits both symmetric and asymmetric dimers. Fig. 2.8 shows a sketch of (1×1) ideal unreconstructed surface, (2×1) reconstruction with symmetric dimers, and asymmetric c(4×2) and p(2×2) reconstruction due to dimer buckling on the surface. Grey areas represent the unit cell of the surface reconstruction. In case of symmetric dimers, the atoms in pair have equal height above the surface. In contrast, for the asymmetric buckled dimers the atoms in pair have different height above the surface plane. Mechanical stress could be generated on the surface when exhibits buckled dimers, in which the stress could be released by the dimers if they are buckled in alternating form. This further reduces the surface energy as well. For Si, asymmetric c(4×2) periodicity has the lowest surface energy. In the Ge(100) surface, dimer buckling is present at ambient temperature, in which dimers rows of (2×1), c(4×2) and p(2×2) surface reconstructions coincide on very clean surfaces [59]. Both Si and Ge surfaces exhibit monoatomic steps where the dimers are separated by the atomic steps and they have a balanced distribution of (2×1) and (1×2) dimers on the surface [60].

2.4.1 Interaction of hydrogen with Si(100) and Ge(100) surface and atomic step formation

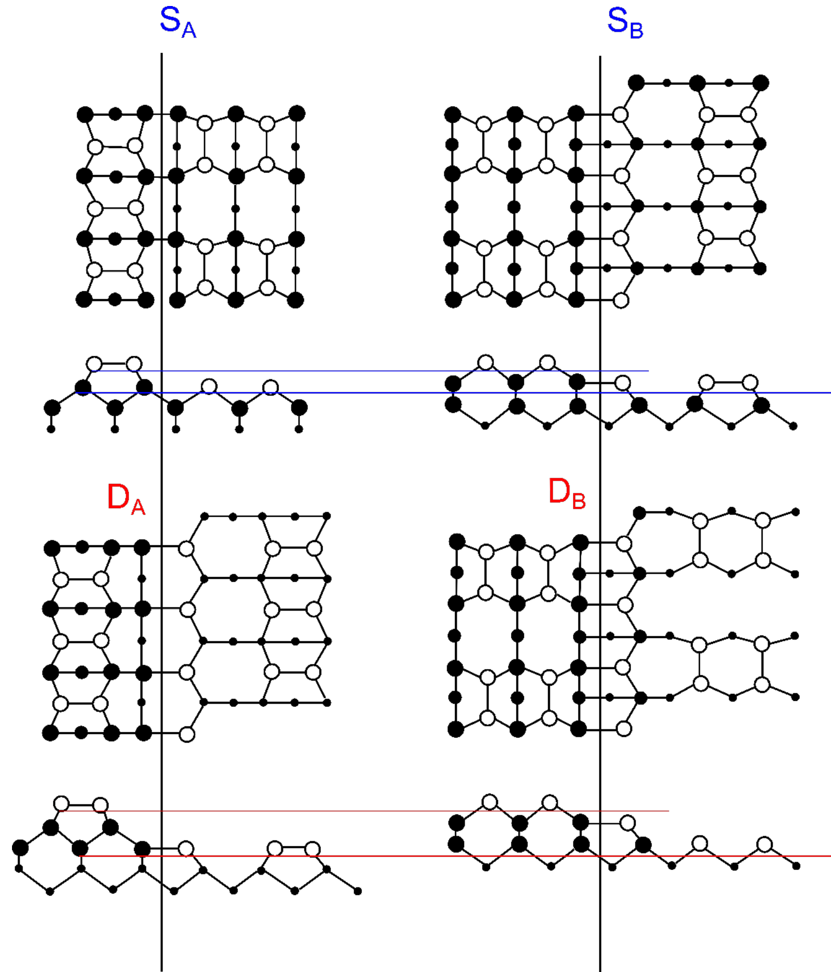

Figure 2.9: Ball and stick model of S_A-, S_B-, D_A-, and D_B-type steps of the Si(100) surface according to Chadi [61].

After the removal of native oxide from the Si(100) surface at high temperature (~1000°C), interaction of process gas hydrogen with Si(100) surface leads to H-passivation on the Si surface [62]. The H-passivated Si(100) surface can exist in three different surface reconstructions [63]: monohydride phase (2×1), dihydride phase (1×1) and a mixed phase (both monohydride and dihydride phase included) (3×1) surface reconstruction. Depending on the temperature and chemical potential of hydrogen, these three surfaces can be formed.

During the monohydride terminated Si(100) surface preparation, the hydrogen atoms equally saturate the remaining dangling bonds of the Si dimers at the surface and suppress the interaction between the dimers. The hydrogen coverage on the Si surface strongly depends

on the hydrogen flux and the substrate temperature. Exposing the Si surface to a moderate amount of atomic hydrogen at elevated temperature results in 1 monolayer (ML) coverage of hydrogen on the surface and form monohydride termination on the Si surface. Monohydrides phase of the Si surface is stable in the temperature range between 450°C - 530°C [64]. By varying the temperature and the hydrogen flux, higher H-coverage can be achieved from the dihydride (1×1) (2 ML) or mixed (3×1) (1.5 ML) Si surfaces. Beside the passivation of the Si surface, interaction of hydrogen with the Si surface changes the atomic structure of the steps which can impact the Si(100) surface atomic step and domain formation [65]. Chadi et al. [61] represented a model which showed four possible Si surfaces depending on atomic height and Si dimer orientation on the surface: either single (S) or double (D) layer step according to their atomic height and the dimer orientation of either perpendicular (A-type) or parallel (B-type) to the step edge.

Fig. 2.9 depicts the four possible surface arrangements based on the model [61], single atomic step with A-type (S_A, top left) and B-type domain (S_B, top right) and double atomic step with A-type (D_A, bottom left) and B-type domain (D_B, bottom right). In order to understand the atomic step formation on the Si surface, energetics as well as kinetics on the surface have to be regarded. According to total energy calculations of Chadi et al., [61], formation of double-layer steps (D_B) are considered to be energetically favorable over the combination of S_A and S_B single-layer steps, while D_A double-layer steps are considered least energetically favorable and mainly kinetically driven process. The atomic structures of S_B, D_A, and D_B steps exhibits rebonded edge atoms which means that the second-layer edge atoms are bonded with the lower terrace atoms (Fig. 2.9). The A-type domains on the S_A and D_A terraces form perpendicular to the [011] atomic step direction and correspond to a (1×2) surface reconstruction. In opposite, B-type domains on both S_B and D_B terraces correspond to (2×1) surface reconstruction. Comparing the A- and B-type domains on the single-layer steps (S_A or S_B) the dimer orientation is rotated by 90° in each of the lower terraces. Si surface containing both S_A and S_B induces a two-domain or mixed surface. In case of double-layer steps the dimers retain their orientation on each step resulting in a single-domain surface. The S_B-type step edge exhibits two possible configurations, a rebonded and a non-rebonded S_B step. Since the rebonded S_B step consists a smaller number of dangling bonds, it is more energetically favorable compared to the non-rebonded S_B step. The single-layer step S_A does not lead to large strains or to extra dangling bonds and therefore has lowest formation energy. According to Chadi et al., [61] the D_A step for Si(001) with 5.4° offcut requires the most energy to form after the S_B and the D_B, while the S_A step has the lowest formation energy. Single-layer steps are more commonly seen on 0° offcut Si(001) substrates, while double-layer steps are more favorable on tilted surfaces [61]. Griffith et al., [66] further confirmed this model on Si(001) substrates with a 2° or 4° offcut in $[1\bar{1}0]$ direction after sputtering by argon (Ar) and annealing at ~900 °C in UHV. The alternating

A-type and B-type single steps with many kinks on the 2° surface were confirmed by STM. In addition, they have showed straight and evenly spaced D_B steps on the 4° substrate. Other reports on STM scans of Si(100) prepared in UHV, proposed a model in which, for substrates with an offcut lower than 7.3° towards [011] direction, S_A and S_B steps are more probable over D_B steps [65].

Atomic step formation and hydrogen termination on Si(100) substrates with 0.1°, 2°, 4° and 6° offcut in [011] direction was intensively studied by our group [15,62,67,68]. Si surface annealing for 30 min in H_2 ambient ensures a surface free of oxide and other contamination [69]. FTIR analysis from the Si(100) surface prepared H_2 ambient revealed monohydride termination of the surface [70]. Depending on process conditions, in particular cooling procedure, a Si surface of either D_A or D_B steps with two different dimer orientation can be prepared [14]. Depending on the adsorption and desorption of hydrogen on the Si surface, kinetically driven D_A steps are formed while the mechanisms for the D_B step formation is energetically favorable. The surface analytic of Si(100) 4° and 0.1° surface prepared in MOCVD ambient will be discussed in more detail in **chapter 5**.

Similar to the Si(100) surface, Ge(100) surface interacts with hydrogen and forms monohydride phase, (2×1) surface reconstruction. Double atomic step with A-type domain formation on the Ge surface is driven by kinetically and the atomic step with B-type domain is more energetically favorable. The Ge substrate with small offcut mainly exhibit single-layer atomic steps while substrates with higher offcut show double layer steps (usually offcut angle > 5°). In analogy to Si(100), the interaction between the hydrogen and the Ge(100) surface annealing at elevated temperature under the purified hydrogen results in a monohydride terminated Ge(100) surface [16] and the Ge(100) surface exhibits either a D_A steps with (1×2) surface or D_B step with (2×1) surface reconstruction [18].

2.5 Experimental background

2.5.1 Metalorganic chemical vapor deposition

Metalorganic chemical vapor deposition (MOCVD) is an enhanced variant of chemical vapor deposition used for producing epitaxial high purity crystalline semiconducting thin films and nanostructures. MOCVD deals with a larger variety of ultra-pure group III and group V elements which act as precursors for crystalline layer growth. In principle, selective precursors in their gaseous form are transported by a purified carrier gas into the reactor at a certain temperature required for decomposition of that particular precursors. The precursors are thermally decomposed and undergo a pyrolysis reaction in gas phase into the

reactor. As a result, the subspecies absorb onto the heated substrate surface and then diffuse at the surface preferential sites. The reactive species react in heterogeneous phase to give rise to the formation of films. The byproduct of the reaction leaves the reactor through the outlet. The advantages of MOCVD is the ability to grow crystalline samples with large precision fine-tuning of precursor flows and controllable growth parameters to give good uniformity of the growth rate and doping levels, and sharp layer interfaces.

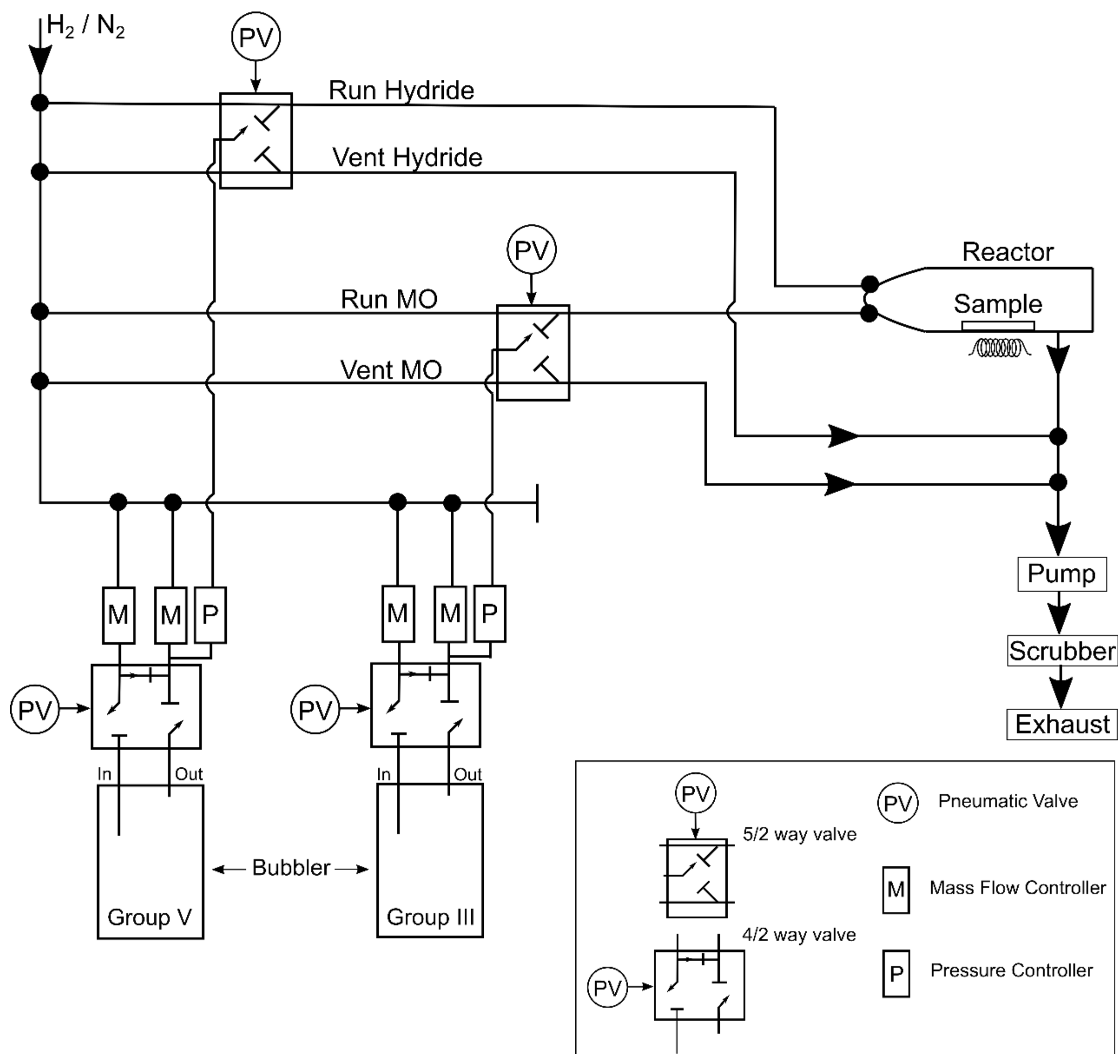

Figure 2.10: Schematic drawing of the MOCVD setup. The precursor source is stored in a temperature-controlled bubbler and transported) by a carrier gas to the reactor. The precursors have separate lines for group-III and group-V precursors.

The principle of MOCVD was first shown by Manasevit and Simpson [71,72] for the growth of GaAs. For the growth of thin films, a typical process pressure of 10-1000 mbar is used. In order to grow thin films, the process temperature is usually in the range of 300°C-600°C. Due to the high reproducibility of III-V compound semiconductor epitaxy and high throughput, MOCVD quickly became a well-established industrial technique for the growth of III-V semiconductor devices. MOCVD turns to superior over UHV-based techniques such as molecular beam epitaxy (MBE) due to its high scalability. The applied pressures during MOCVD preparation enable easier sample handling compared to UHV-based MBE growth. However, growth processes in MOCVD environment are less understood, since the growth reactions are much more complex. Here, reactions in the vapor phase, reactions on the substrate surface, as well as reaction with reactor residues from earlier deposited material have to be considered. Additionally, the presence of a process gas complicates analysis of the surface by standard UHV-based surface science tools.

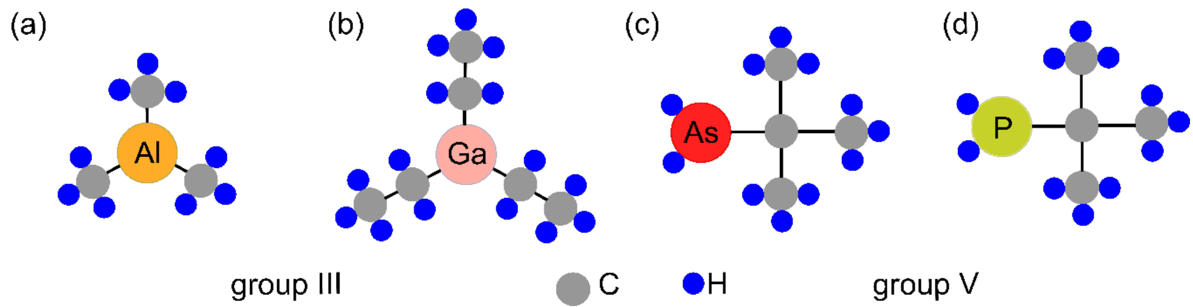

Figure 2.11: Schematic diagrams of precursor molecules used in this work: (a) TMAl, (b) TEGa, (c) TBAs, (d) TBP. The small blue and medium size grey circles represent hydrogen and carbon atoms, respectively.

In this work, an AIXTRON AIX-200 MOCVD reactor was used for the entire growth process of the samples. The reactor is a horizontal designed low-pressure reactor equipped with an optical in-situ spectroscopy system which is especially applicable to examine the sample surface during MOCVD sample preparation. After the sample preparation, a MOCVD-to-UHV transfer system enables contamination free transfer of samples to UHV based surface sensitive tools. Since the MOCVD process is itself a complex method, it is indeed important to correlate the *in situ* spectroscopy results probed during the sample preparation with the surface science tools. Here, the samples are mounted on molybdenum carriers which are placed into the carrier. The sample carriers are compatible to the UHV transfer shuttle and therefore can easily be transferred to UHV environment. Fig. 2.10 shows a schematic drawing of the MOCVD reactor. In this study, the group III precursors of trimethylaluminum (TMAl), triethylgallium (TEGa), trimethylindium (TMIn) and the group V sources of tertiarybutylarsine (TBAs), tertiarybutylphosphine (TBP) are used (Fig. 2.11).

The precursors are stored in form of liquid organometallic compounds in a bottle called 'bubblers'.

The bubblers are maintained at a certain temperature and pressure to restrict from crystallization. The purified carrier gas H_2 or N_2 are transported through the respective inlet into the bubblers and carriers the organometallic precursors into the reactor as shown in the left part of the Fig. 2.10. The molar flow of each of the precursors are adjusted by mass flow controller. In order to avoid any pre-reaction as well as contamination, the group III and group V precursors are conducted in two separate pipe-lines and they mix to each other only after transported into the reactor chamber. These separate pipe-lines are designated as RunMO and RunHyD, respectively. During a process run, RunMO is commonly assigned for the group III and RunHyD is for the group V precursors. The total flow of hydride introduced into the carrier is controlled by these two pipe-lines. The samples mounted on molybdenum carriers are placed in a graphite susceptor which is heated by six IR lamps. The process temperature is readable by the thermocouples placed inside the susceptor block. The maximum process temperature of 1010°C can be achieved in our study. The reactor is a strain free glass tube containing a horizontal glass liner inside. The beam path of RAS enters into the reactor through an optical view port and directs onto the sample surface. The byproduct gases removed from the reactor through an outlet and are first filtered by a scrubber controlled by the process pump as shown in the right side of the Fig. 2.10.

2.5.2 MOCVD to UHV transfer

In order to study the MOCVD prepared samples with UHV based surface science tools, our MOCVD reactor is equipped with a prestigious contamination free UHV transfer shuttle which can serve a low pressure in the order of 10^{-10} mbar. It consists of an interim chamber, which is connected to the main reactor, a main UHV chamber, a transfer rod for sample handling and a mobile UHV shuttle which is accessible to the other surface analysis tools. Each of the chambers are connected through many valves (see Fig. 2.12) which only open while needed. The shuttle is usually baked at 120°C for a minimum of 8 hours (usually overnight). In addition, the main UHV chamber is pumped down by a turbo molecular pump leading to a pressure of 10^{-10} mbar. At the end of sample preparation, the reactor is evacuated pressures < 1 mbar. Before opening the gate valve between the reactor and the interim chamber, the turbo molecular pump is temporarily turned off and the valve between the interim chamber and the mobile UHV shuttle remain closed. After the transfer of the sample from reactor to interim chamber, the gate valve is closed and the pump is immediately turned on to resume the UHV pressure. The pressure in the interim chamber is now slowly decreased to 10^{-9} mbar and with the help of LN_2 in another 5 min, the UHV pressure can

reach again to 10^{-10} mbar. The sample located in the interim chamber is finally transferred to the mobile UHV shuttle by a transfer rod and ready to transfer to the various instruments. A battery powered ion getter pump maintains the UHV pressure of 10^{-10} mbar in the mobile shuttle.

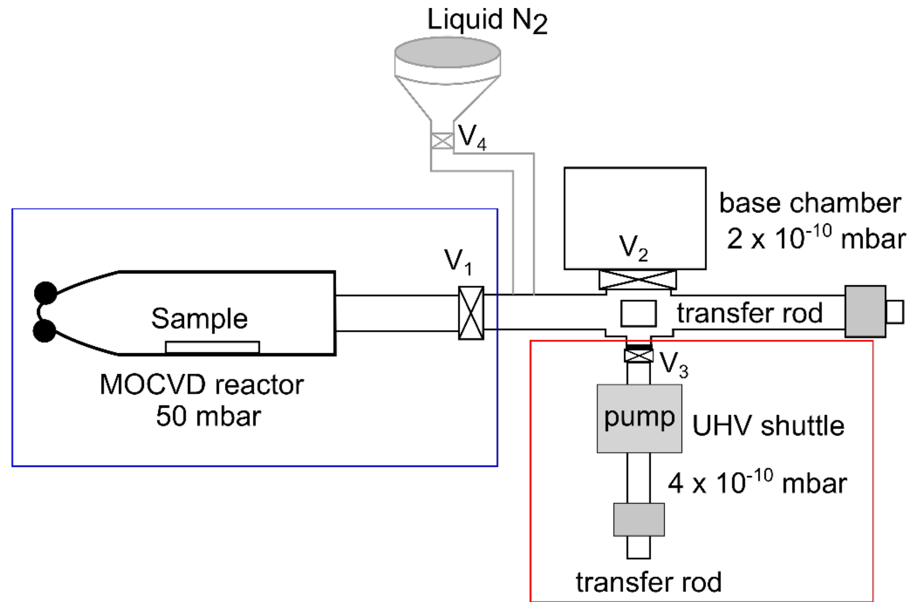

Figure 2.12: Simplified schematic sketch (top view) of the MOCVD to UHV transfer system. Red rectangular indicates mobile part of the UHV shuttle and V_1 –V_4 indicate valves.

2.5.3 Reflection anisotropy spectroscopy

Reflection anisotropy spectroscopy (RAS), also known as reflection difference spectroscopy (RDS) is a non-destructive, surface sensitive, *in situ*, optical spectroscopy equipped with MOCVD reactor. RAS measures normalized difference in reflection between two mutually perpendicular crystallographic directions in a (100) surface plane (x, y). For (100) semiconducting surface, the two perpendicular directions are chosen as x = $[0\bar{1}1]$ and y = [011]. The RAS signal measured in these directions can be defined as:

$$Re\left(\frac{\Delta r}{r}\right) = 2Re\left(\frac{r_{[0\bar{1}1]} - r_{[011]}}{r_{[0\bar{1}1]} + r_{[011]}}\right)$$

and it contains a real (*Re*) and an imaginary part (*Im*):

$$\frac{\Delta r}{r} = Re\left(\frac{\Delta r}{r}\right) + iIm\left(\frac{\Delta r}{r}\right)$$

The origin of surface optical anisotropy can be correlated with the dielectric function of the material since the anisotropy originates from the dielectric function of the semiconductor bulk. If the thickness of a film surface 'd' is smaller than the wavelength of light 'λ', the RAS signal can be expressed as:

$$\frac{\Delta r}{r} = -\frac{4\pi i}{\lambda}\frac{d\Delta\hat{\epsilon}_s}{(\Delta\hat{\epsilon}_b - 1)}$$

where, $\Delta\hat{\epsilon}_s$ is the anisotropy of the complex surface dielectric function ($\Delta\hat{\epsilon}_s$=$\epsilon[x]$−$\epsilon[y]$) and $\Delta\hat{\epsilon}_b$ is the bulk dielectric function. The phrase d · $\Delta\hat{\epsilon}_s$ defines the surface dielectric anisotropy (SDA) and enables to correlate the RAS signal to dielectric function of the surface layer. Moreover, this SDA occurs due to the surface dipoles originating from the local dimer orientation on the sample surface. Therefore, for a crystalline sample, optical anisotropies occur due to the modification of the surface structure such as surface reconstruction, atomic steps, adsorbates or due to high degree of doping. In addition, changes in the RAS signals, particularly in the intensity of the RAS signals, originate from the imbalance of majority to minority domain ratio or due to defects like anti-phase boundaries present on the sample surface. In contrast, ideal cubic crystals are isotropic and induce no RAS signal.

The interband transitions of a semiconductor which determines optical properties of that semiconductor (such as refractive index n or extinction coefficient k) is correlated with the dielectric function of that material. The real part of the dielectric function is related to polarization and anomalous dispersion, while the imaginary part is associated with absorption properties of the medium [73]. The main contributions in the imaginary part of the dielectric function is correlated with interband critical points. The real and imaginary part of dielectric function for Si and their correlation with the interband critical points have been shown in *Ref.* [74]. The similar dielectric behavior can be found in Ge and other common III-V semiconductors.

In this work, RAS has been used to determine the semiconductor surfaces while interacts with precursors and to understand resulting surfaces after processed through various process parameters in a MOCVD reactor. Since the MOCVD process is itself a complex process and the obtained RAS signals contain individual contributions based on the processed surfaces, we correlate the RAS signal with UHV-based other surface sensitive tools (XPS, LEED, STM) in order to identify all the contributions or features in the RAS signals. The RA spectra presented in this work mainly reflect the dimer arrangement on the surface and electronic transitions from the valence band states to the states in the conduction band caused by photon absorption in case of (100) semiconductor surfaces. Here, we have employed a RAS

spectrometer from the manufacturer Laytec (EpiRAS 200) based on the development by Aspens *et al*. [75] and illustrated schematically in Fig. 2.13.

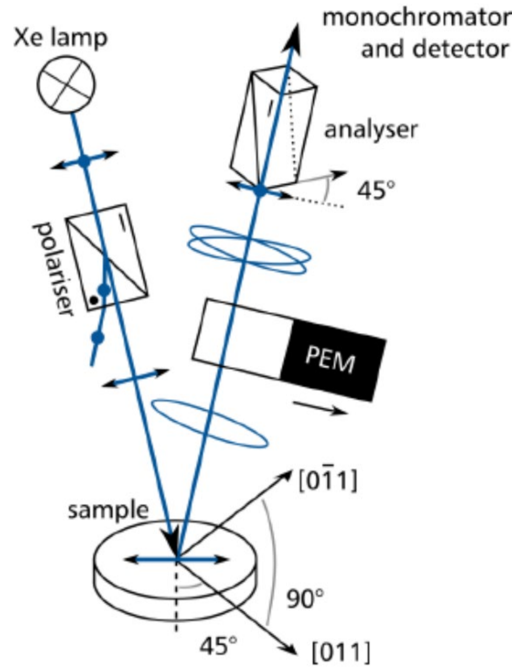

Figure 2.13: Principle of the RAS setup according to Aspens et al. [75]. The schematic shows the path of incident and reflected light beam. Figure is taken from *Ref*. [75].

The RAS setup is mounted on the roof of the MOCVD reactor so that an incoming light beam passes through additional optics to direct the light beam through a lens on the sample. This optical window is an additional optical element in the light path and might introduce an additional phase shifts due to windows strain. The light of a Xenon-arc-lamp (spectral range: 1.5 to 5.3 eV (~225 nm - ~837 nm)) is linearly polarized by a polarizing Rochon prism, and focused on the sample. In our set up, the sample is adjusted so that the polarization of the incident beam is in the sample plane and the RAS signal measured in this work is defined as:

$$Re\left(\frac{\Delta r}{r}\right) = 2Re\left(\frac{r_{[0\bar{1}1]} - r_{[011]}}{r_{[0\bar{1}1]} + r_{[011]}}\right)$$

An anti-wobble mirror (AWM) compensates tilt and directs the reflected light on the reversed path as the incoming light (see Fig. 2.14, optical path of RAS). Here, the beam is reflected twice on the sample. The optics are protected by a metal shield and constantly cooled by a fan. In addition, the heating system, the IR lamps mounted below the susceptor

are shielded. The optical viewport at the reactor tube is strain-free and purged. The resulted reflected beam is elliptically polarized and passes through a photo elastic modulator (PEM), where it is phase modulated.

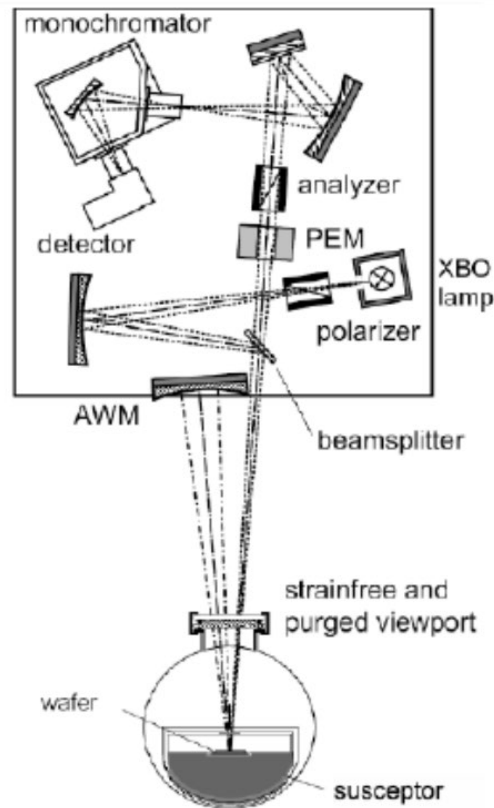

Figure 2.14: Optical path of RAS (EpiRAS-200) applied in this work (note that intermediate optic is not shown here). Figure is taken from *Ref.* [76].

The RAS signal is determined by normalizing the alternating current (AC) components ($I_{1\omega}$ and $I_{2\omega}$) of the detector output to the respective direct current (DC) I_0 [75]. The phase modulation of the light signal in an analyzing prism, is converted in an intensity modulation. In the set-up there is a Si photo-diode in combination with a grating-monochromator where the light is detected. As a result, the measured modulated signal is processed in the connected electronics, which includes a lock-in amplifier for analysis of the small RAS signals in the range of $\pm\ 5\cdot10^{-3}$. The resulted signal mainly consists of two components: a large DC component I representing the isotropic reflectance *r* and a very small AC component ΔI representing the surface anisotropy.

RAS can be operated in three different modes:

(i) the spectroscopic mode, where the change of dr/r or surface anisotropy is measured between the range of photon energy of 1.5 eV – 5.0 eV at a fixed temperature. A single RA spectrum is useful here to identify the processed surface after benchmarking the surface with other surface sensitive tools.
(ii) the colorplot mode, where RA spectra are measured continuously over time between the energy range of 1.5 eV – 5.0 eV. This mode enables to understand a continuous change on the sample surface during application of process parameters at different stages of a process
(iii) the time resolved (transient) mode, where the change of dr/r is measured at a fixed photon energy in dependence of process time. This mode helps to observe the changes of the surfaces during a process similar to the colorplot mode.

Since, the light passes through the optical window, lenses, and then through the MOCVD liner parts, there might be additional contribution from the RAS set-up in the resulted RAS signal, which needs to be avoided. The easiest way to eliminate this contribution is to mount an additional isotropic oxidized Si(100) or Si(111) (preferably low offcut) and take a RAS signal from these surfaces and then simply subtract it from the measured RAS signal. All the RAS signals shown in this work are baseline corrected based on the oxidized Si surface measured before starting the process.

2.5.4 X-ray photoelectron spectroscopy

X-ray photoelectron spectroscopy (XPS) is a powerful surface sensitive technique to determine the elemental chemical composition of surfaces. XPS is applied to a wide range of materials, in order to obtain a variety of analytical information. The technique deals with photoelectric effect first observed by H. Hertz [77] and later described by A. Einstein [78]. Although the development of XPS into a sophisticated analytical method is a result of the meticulous work of Swedish Nobel Laureate Kai Siegbahn and his colleagues, the first well documented reports of the production of photo-electron spectra are due to Robinson, who, using Cu Kα radiation, produced XPS spectra from several metals. The historical development of XPS has been emerged later by Jenkin et al. over the period of 1900-1960 [79].

In principle, the X-ray photon interacts with an electron in the core level and causes emission of photoelectron from a sample. The binding energy of the photoelectron E_B, the parameter that defines both the element and atomic level from which it emanated, is measured as the distance from the core levels to the Fermi level as shown in the Fig. 2.15. The work function separates the vacuum level and the Fermi level which is at the top of the valence band in case of a metal. In order to excite a core electron into vacuum level, an energy $h\nu$ should be

larger than the sum of binding energy E_B and work function Φs. If the photoelectrons escape into the vacuum, their kinetic energy E_{kin} and momentum can be detected by an electron-energy analyzer. Usually the analyzer work function Φa is smaller than the sample work function Φs. Consequently, the kinetic energy of all electrons increases by Φs – Φa. The kinetic energy E_{kin} of the ejected electrons is related to the electron binding energy E_B. If the X-ray photon energy and the work function Φ are known, the kinetic energy can be determined in the following manner:

$$E_{kin} = h\nu - \Phi\text{a} - E_B$$

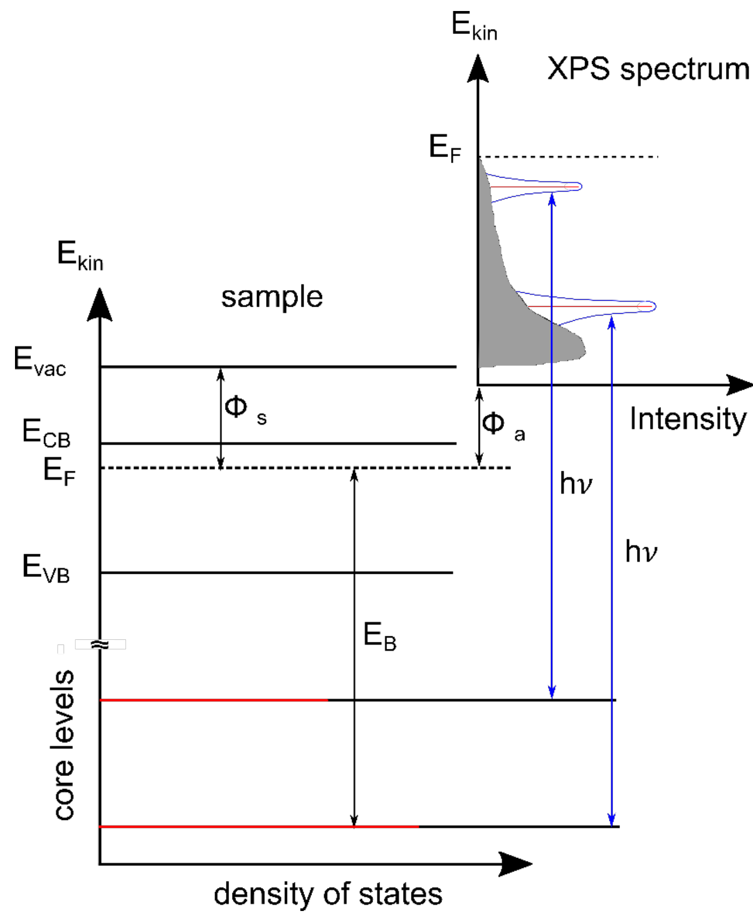

Figure 2.15: Schematic of the photoemission process. Electrons with binding energy *EB* can be excited above the vacuum level *Evac* by photons with energy $h\nu > E_B + \Phi_S$. The photoelectron distribution (intensity) can be measured by an electron energy analyzer and in approximation is equal to N(*EB*), the occupied density of electronic states (DOS) in the sample.

The XPS spectrum from an element is a function of either kinetic energy or binding energy measured from photoelectrons which are emitted from the core levels. The binding energy of the photoelectrons is an intrinsic material property and do not change with the X-ray source photon energy, but it could show slight variations for a particular element and energy level depending on the exact chemical environment of the atom. The binding energy of a particular atom can be varied in dependence on different chemical bonding of the same atom which is referred as chemical shift. The shift towards the lower or higher binding energy literally determines the bonding state and the type of element bonded with that particular atom.

XPS holds a very high surface sensitivity due to the inelastic mean free path λ_e of the electrons in the solid. The photoelectrons are subjected to energy losses by different scattering processes. The specific losses lead to a dependence of λ_e on E_{kin} which is depicted in Fig. 2.16 [80]. The curve exhibits a minimum of λ_e for photoelectrons with E_{kin} 20 – 70 eV. For higher kinetic energies, which correspond to excitation of photoelectrons by X-rays, λ_e increases to values in the range of 20 – 30 Å, while for low energies, λ_e increases quickly about several hundred Å and the surface sensitivity is reduced.

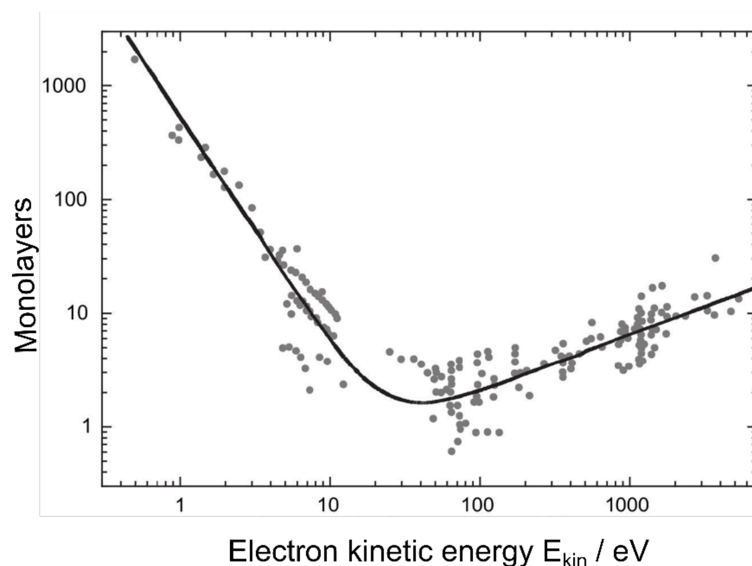

Figure 2.16: Inelastic mean free path for electrons depending on their kinetic energy E_{kin} in different solids (grey dots) and the empirically derived “universal“ curve [80].

In this work, monochromatic Al Kα and Ag Lα were used as X-ray sources (Specs Focus 500). The kinetic energies were filtered with a hemispherical analyzer (radius 100mm) and detected with channeltrons (Specs Phoibos 100).

2.5.5 Low energy electron diffraction

Low energy electron diffraction (LEED) is a UHV based, surface sensitive electron diffraction technique in reciprocal space. The tool enables to determine the periodic symmetry of crystalline materials. An electron gun is used from which monochromatic electrons are emitted by a cathode filament with respect to the sample. The electrons are accelerated and focused into a beam by a series of electron lenses on the sample surface in normal incidence (Fig. 2.17 (a)). The elastically diffracted electrons are collected on a fluorescent screen where the image is resembled to the periodicity of the sample surface, called diffraction pattern. According to the low energy of the electrons (energy range E ≈ 10 – 1000 eV), their De Broglie wavelength ($\lambda_{DB} = h/p$) is in the order of the lattice constant of the crystals and the inelastic mean free path of the electrons is only a few Angstroms [80]. A high pass filter is used which blocks other electrons except the elastically scattered electrons and therefore only the top atomic layer of a sample contributes to the diffraction pattern. In order to keep the studied sample free from contamination, LEED are performed in an UHV environment (~10^{-10} mbar). In this work, a commercial LEED setup (Specs ErLEED 100-A) with reverse view LEED optics was used. The diffraction patterns were recorded by a digital video camera.

The diffraction pattern is a combination of constructive and destructive interference of the elastically scattered electrons, which represents the reciprocal space of the surface unit cell including the surface reconstruction. Constructive interference of scattered electrons is given by the Laue condition:

$$\overrightarrow{K_f} - \overrightarrow{K_0} = \vec{G}$$

where $\overrightarrow{K_0}$ is the wave vector of the incident electrons and $\overrightarrow{K_f}$ the vector of the diffracted electrons with $\left|\overrightarrow{K_f}\right| = \left|\overrightarrow{K_0}\right| = \frac{2\mu}{\lambda}$ for elastically scattered electrons, and $\vec{G}$ is a reciprocal lattice vector.

The Ewald's sphere construction represents a visualization of the Laue condition of the reciprocal lattice of a (100) surface (see Fig. 2.17 (b)). Therefore, the wave vector of the incident electron $\overrightarrow{K_f}$ is drawn ending on a reciprocal lattice point. The Ewald's sphere is centered on the origin of the incident wave vector with the radius $\overrightarrow{K_0}$. In case of a surface, the Laue conditions is undefined perpendicular to the surface, since $\vec{K}_\perp$ can exhibit any value. Accordingly, the reciprocal lattice of a surface is equivalent to a 2D lattice with rods which propagate perpendicular to the sample surface. Accordingly, the lattice points can be replaced by lattice rods perpendicular to the surface in the Ewald's construction. The spots

in the diffraction image correspond to the intersection of the reciprocal lattice rods with the Ewald's sphere.

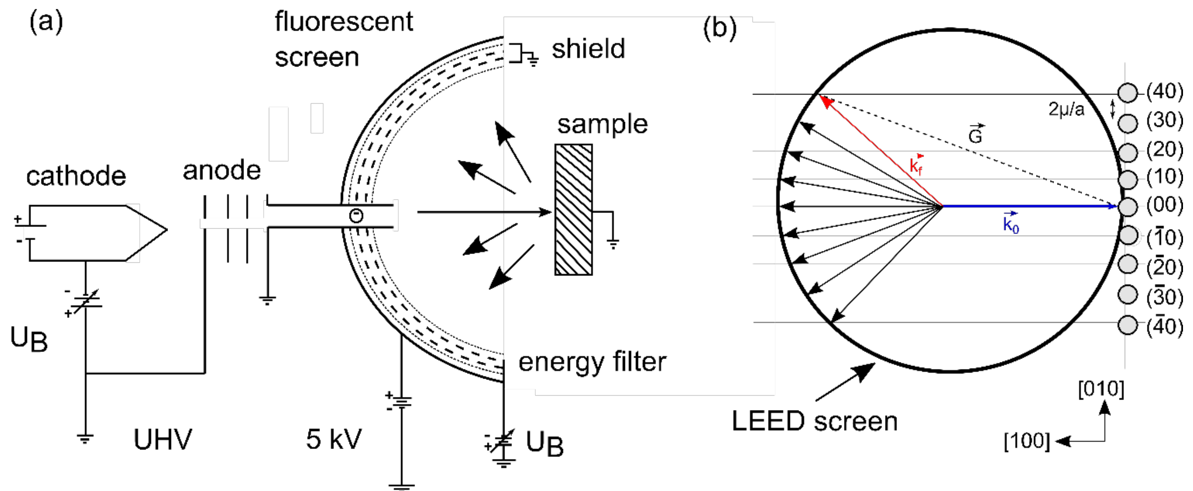

Figure 2.17: (a) Schematic drawing of the LEED setup and (b) visualization of the Laue condition by the Ewald's sphere construction. The spots (rods) are numbered by their hkl value. Points where the rods cross the sphere coincide with the Laue condition.

During the LEED experiment, the elastically scattered electrons are visible on a spherical fluorescent screen (Fig. 2.17). Hence, the diffraction pattern observed on the fluorescent screen is equivalent to the reciprocal lattice of the surface. Since the radius of the Ewald's sphere is proportional to the electron energy, the LEED pattern gets smaller and spots of higher order become visible on the screen with increasing electron energy. LEED enables determination of the size, orientation and symmetry of the primitive cell of a surface. Fig. 2.18 shows a comparison between an ideal (1×1) symmetry and (1×2) surface reconstruction from a surface which leads to an additional half-order spots in the LEED pattern. A single-domain (2×1) surface exhibits half-order spots only in one main crystal direction, while a two-domain (2×1)/(1×2) surface shows half-order spots in both directions. Accordingly, LEED enables analysis of the domain distribution on the sample surface.

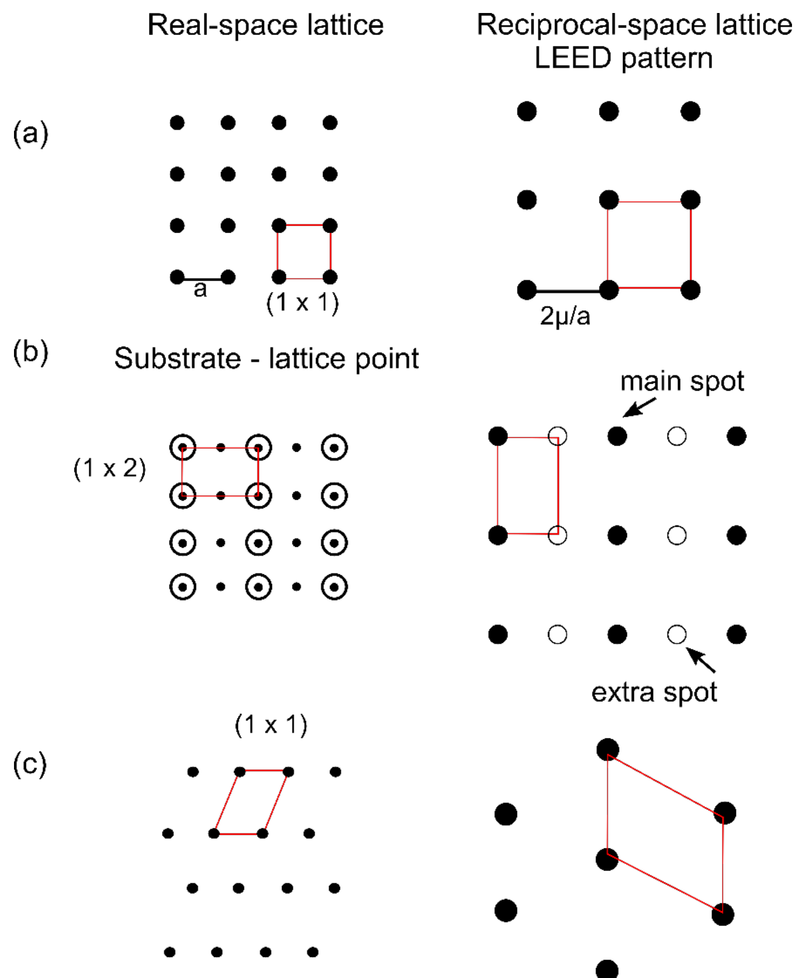

Figure 2.18: (a), (b), and (c) are examples of real space lattice and their reciprocal lattices. In the real space, the superlattice points are shown by open circles. In the LEED patterns, the main spots are shown by black circles and the extra-spots (coming from the superlattice) are shown by small white points. The (a) (b) corresponds to (1×1) and (1×2) surface reconstruction of Si(100), respectively. The (c) corresponds to (1×1) surface reconstruction of Si(111).

2.5.6 Electron Channeling Contrast Imaging

'Kikuchi-like' bands were first observed by D. G. Coates in 1967 for imaging single-crystals using a conventional scanning electron microscope (SEM) [81]. It has been showed that the crystallographic orientation-dependent diffraction patterns formed by backscattered electrons superimpose on the normal topographical image obtained in SEM. The mechanism for originating these Kikuchi bands in the SEM was defined as 'electron channeling'. In addition, a stage-rocking configuration was introduced where the crystallographic sample

was tilted with respect to a fixed incoming electron beam to obtain electron channeling pattern (ECP) from bulk crystals. Booker et. al. [82] confirmed Coates' observation and provided a theoretical interpretation of the phenomenon. They also suggested a possibility to observe individual crystalline defects from a bulk sample at high magnification of the ECP pattern using electron channeling contrast imaging (ECCI).

In ECCI, the 'channeling contrast' principally occurs due to the electron-electron scattering processes inside the lattice [83]. Fig. 2.19 (a), (b) and (c) represent configuration of crystal lattice relative to incoming electron beam during a channeling process. In the first case, the incoming electron beam trajectory is not parallel and therefore a relatively more 'closed channel' occurs in which the electron beam could not travel through the crystal. In contrast, the 'open channel' condition occurs in Fig. (b) where the electron beam channels completely through the crystal. Here, the crystal lattice works as channels or paths for the incoming electron beam which preferably penetrate to a higher depth before scattering as shown in Fig. (a). In Fig. (c), the electron beam could not channel through the crystal due to presence of a local crystal defect such as half of a plane (dislocations) by which the electron beam is blocked and backscattered immediately at the point of defect. In this condition, the presence of a dislocation can locally convert an 'open channel' to 'closed channel' condition in the crystal.

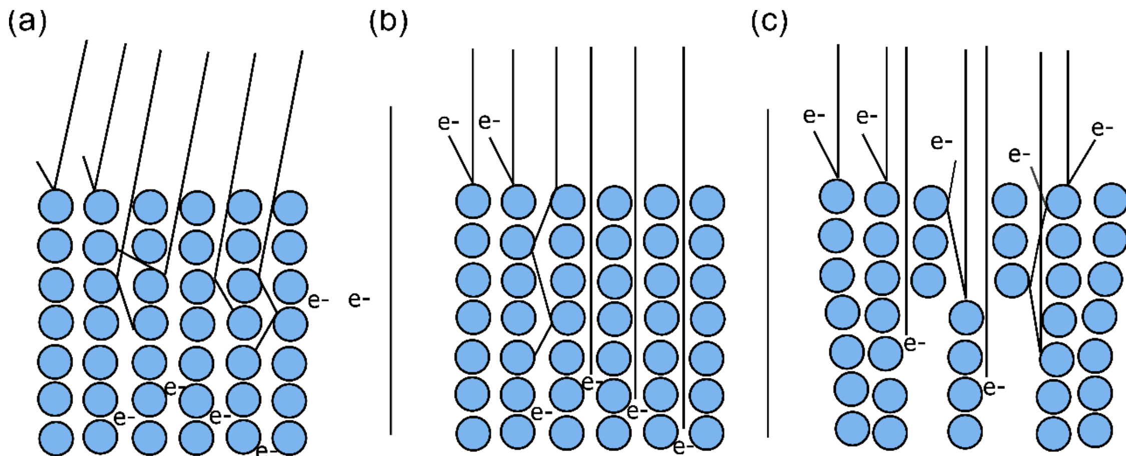

Figure 2.19: Illustration of an atomic lattice relative to incoming electron trajectories so that a relatively more (a) "closed channel" or (b) "open channel" condition is obtained. The presence of dislocation (c) can locally convert an "open channel" to a "closed channel" condition. Figures are taken from *Ref.* [83] and redrawn.

The contrast of the diffraction pattern or the ECP pattern from a cubic GaP/Si(100) is shown in Fig. 2.22 which was taken at low magnification (39x). At low magnifications the scanning motion of the electron beam ensures that many channels are accessed over a wide angular

range, leading to the wide variations in backscattered electrons and the formation of an ECP in the resulting image. At high magnification a single 'channel' corresponding to a specific orientation can be isolated. Hence the image for a perfect crystal at high magnifications should show no contrast or rather a constant signal. But the presence of a local crystal defect like a dislocation or a stacking fault may block the channel and will preferentially scatter more electrons back towards the detector (Fig. 2.19 (c)). As a result, the defect will be visible as a bright feature on a dark background or vice-versa on the sample surface. In this case, the effect gives rise to dislocation contrast via electron channeling.

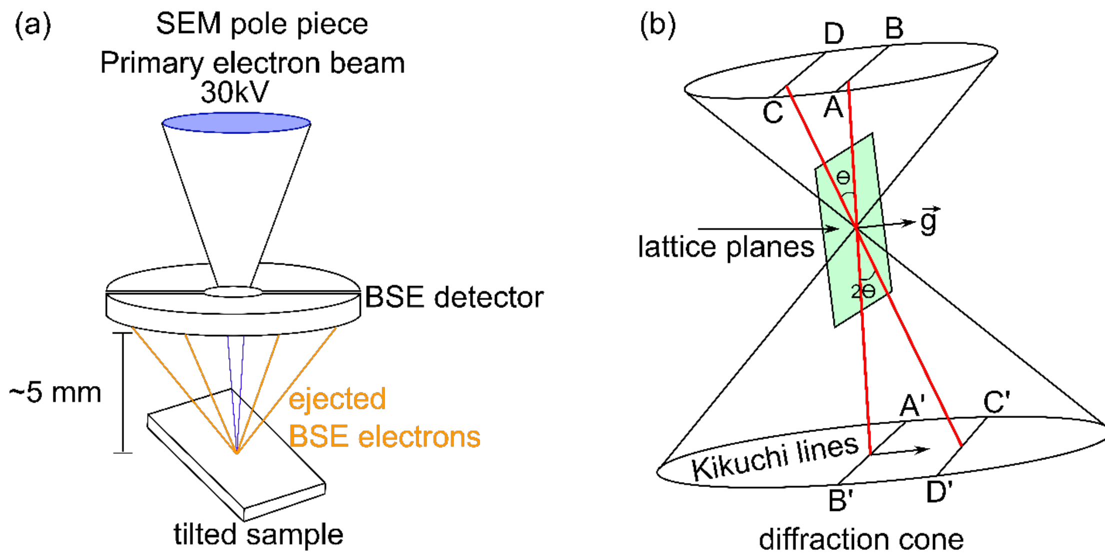

Figure 2.20: (a) Schematic of ECCI set up (left image) where electron beam incidents on a tilted crystallographic sample and the ejected backscattered electrons are collected by the backscattered electron detector. (b) Formation of diffraction cones and Kikuchi lines in the phosphor screen due to the backscattered electrons diffracted back from the sample (right image).

Fig. 2.20 (a) shows a schematic of the geometry of ECCI performed in SEM. A parallel beam of electrons with a high operating voltage of 30 kV and high electron beam current of 2.8 nA is incident on a crystalline sample. A sample surface should be tilted as shown in Fig. 2.20 (a) in such a way so that the electron beam could satisfy crystallographic Bragg's diffraction. As a result, during the channeling the electron beam is diffracted back at a point of defects and ejects inelastically scattered backscattered electrons from the samples. The channeling contrast or intensity of backscattered electrons depends on the relative orientation of planes in a crystal since tilt of the sample allows more electrons to be scattered which increases backscattered electron yield and reduces multiple scattering and energy loss processes, thus leading to enhanced channeling contrast [84]. Therefore, its necessary to tilt the sample in order to change crystallographic orientation. A back scattered electron detector

(BSD) placed at a gap of 5 mm above the sample is employed to collect the inelastically scattered backscattered electrons. These backscattered electrons therefore carry the information about the defects present in the samples. Fig. 2.20 (b) shows a schematic of how these backscattered electrons form diffraction cone and Kikuchi lines in a phosphor screen of the BSD detector. When the electron beam hits the sample's surface at an angle (since the sample in tilted), the diffracted electrons form a pair of diffraction cones (Kossel cones) for each reflecting plane which satisfies Bragg's condition. The projection of these diffraction cones on the phosphor screen produces pairs of Kikuchi lines A'-B' and C'-D' (Fig. 2.20 (b)). These diffraction cones are centered at a point on the diffracting planes and they reflect the crystal symmetry of the electron interaction point which enables the spatially resolved crystallographic identification of a sample. The position of the Kikuchi lines in the phosphor screen also reveals the crystallographic orientation of the analyzed sample. The diffraction vector 'g' originates from the center of the diffraction cone and is indicated as a reference direction in Fig. 2.20 (b).

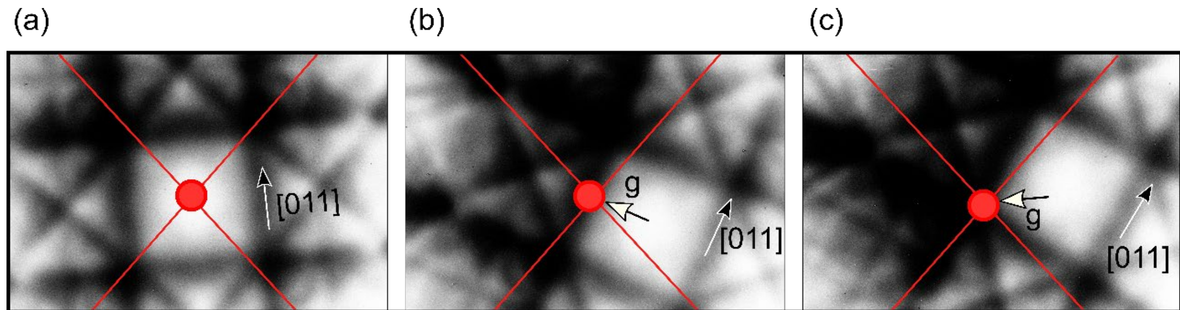

Fig 2.21: Three distinct positions on the ECP pattern where the electron beam targets on (a) center of the ECP, (b) a single Kikuchi line and (c) a position where two Kikuchi lines intercept. Depending on the position electron beam focused, individual defects can be resolved from crystalline samples. For the position (a) defects lying close to the sample surface and for (b) and (c) defects originating from the heterointerface could be observed.

The ECP pattern consisting of Kikuchi line is shown in Fig. 2.21. Each of the Kikuchi lines represent diffraction from a single set of lattice planes in a diffracting crystal volume. The diffracting planes are indicated in Fig. 2.22. The Kikuchi line is described with the corresponding diffraction vector 'g' (white solid and dash-dotted lines in Fig. 2.22). The direction of the vector 'g' is from the center towards a particular Kikuchi line, at which the electron beam is targeted (Fig. 2.21 (b) and (c)). Similar to conventional transmission electron microscopy, the imaging contrast in ECCI is determined by the invisibility criteria $\vec{g} \cdot \vec{b} = 0$ and $\vec{g} \cdot \vec{b} \times \vec{u} = 0$, where $\vec{g}$ is diffraction or channeling condition, $\vec{u}$ is the dislocation's line direction and $\vec{b}$ is the dislocation's Burgers vector.

There can be a minimum of three distinct positions on the ECP where the electron beam should be targeted in order to resolve extended defects from a crystalline sample. Focusing of the electron beam on different positions of ECP can be varied by a combination of rotation and tilt of the sample. The first focus position can be $\vec{g}$ = (100) at the center of the ECP shown in Fig. 2.21 (a), where the electron beam channels near the surface and, therefore, in this channeling condition defects close to the surface can be resolved. The other channeling conditions can be either on a single line of one of the Kikuchi line, or on the corner of the ECP where two non-parallel planes intercept as indicated in Fig. 2.21. In order to resolve MDs, TDs, SFs the electron beam must be focused under $\vec{g}$ = $(0\bar{2}\bar{2})$ or (022), $\vec{g}$ = $(0\bar{2}2)$ or $(02\bar{2})$, $\vec{g}$ = $(00\bar{4})$ or (004), $\vec{g}$ = $(0\bar{4}0)$ or (040). The channeling conditions of $(00\bar{4})$ or (040) (here indicates by while circles), $(0\bar{4}0)$ or (004) are capable of showing orthogonal sets of MDs, SFs and SFPs. Moreover, the channeling of $\vec{g}$ = $(0\bar{4}0)$ and (040) are exactly two adjacent channeling conditions on the opposite sides in the ECP shown in Fig. 2.22, in which the same defects can be observed: MDs propagate along both orthogonal [011] and $[01\bar{1}]$ directions, but their contrast differs depending on the different Burgers vectors. In these channeling conditions, the electron beam is able to travel deep into the crystal and therefore, crystal defects originating at the heterointerface are visible.

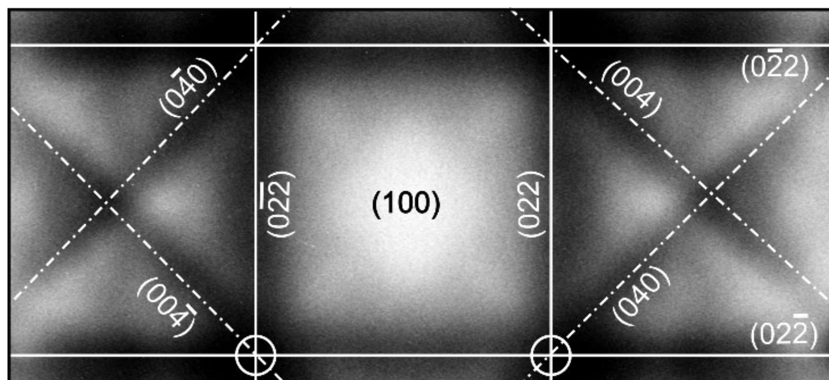

Figure 2.22: ECP with indexed representation of diffraction vectors from a 60 nm thick GaP/Si(100) sample. The white circles indicate the interception of the diffraction vector $\vec{g}$ = $(00\bar{4})$ with nonparallel crystal planes $(0\bar{2}\bar{2})$ and $(02\bar{2})$, or (040) with (022) and $(02\bar{2})$.

2.5.7 Scanning tunneling microscopy

Scanning tunneling microscope (STM) enables analysis of the microscopic structure of solid surfaces at atomic level. STM scans the surface by using an extremely sharp conducting tip that can distinguish features smaller than 0.1 nm with a 0.01 nm (10 pm) depth resolution

and records a direct real space image of the surface. Simultaneously, STM records the electron tunnel current as a function of position scanning at that time. STM is based on the concept of quantum/electron tunneling. Electron tunneling is a quantum mechanical effect in which electrons travel from one conductor through a potential barrier into a second conductor. Tunneling occurs when the wave functions of the two conductors reach into the potential barrier and overlap within the classically forbidden regions. In the STM, electrons tunnel from the tip through a vacuum gap into the sample surface (or vice versa) only when there is significant overlap, which corresponds to atomic-scale distances. Fowler and Nordheim expressed an approximation for the tunneling current I_t which depends exponentially on the distance d between tip and surface [85]:

$$I_t \propto \frac{U}{d} exp(-Kd\sqrt{\phi})$$

where U is the applied voltage between tip and sample, ϕ the average work function, and K a constant with a value of about 1.025 $Å^{-1} \cdot (eV)^{-1/2}$ for a vacuum gap. For distances of several tens of Angstroms, a tunnel current I_t is measurable [86]. Lateral resolution of atoms on the surface requires controlled movement of the tip within 1 – 2 Å. Tip or sample movement requires coarse and fine. Piezoelectric plates enable fine positioning of the tip or sample. A suspension or damping system is essential to avoid mechanical vibrations from the environment which disturb the measurements.

During scanning of the sample surface, changes in the surface height and density of states affect the tunnel current I_t. There are two main operation modes for STM: Constant current and constant height mode. In constant current mode It is kept constant during scanning of the sample surface. As a consequence, the tip images surfaces of constant local density of states at the position of the tip [86]. In constant height mode voltage and height are kept constant and variations in I_t are measured during scanning. Here, the resulting images are related to the charge density of the surface. STM can also be used in spectroscopic mode (scanning tunneling spectroscopy – STS) which gives local information on the electronic structure of the sample surface. Here, the current is measured in dependence of the voltage at specific positions on the sample.

In this work, we employed a commercial SPECS 150 Aarhus STM in a separate UHV chamber which has been accessed by our UHV shuttle. We used tungsten tips, prepared by electrochemical polishing in potassium hydroxide solution with direct current. Ar ion sputtering enabled cleaning and conditioning of the tip at the STM in the UHV chamber.

2.5.8 Atomic force microscopy

The surface morphology of a samples can be measured by atomic force microscopy (AFM). The AFM consists of a cantilever with a sharp tip (probe) at its end which is used to scan the sample surface. The cantilever is typically from silicon or silicon nitride with a tip radius in the order of nanometers (the radius of the tip used in this work is ~ 8 nm). In this work the measurements were done in a tapping mode. In principle, in AFM, the sharp tip is brought to close contact to a sample, in a constant oscillation at high amplitude. The difference in height in the surface morphology results in changes in the distance between the surface and the tip, meaning a change in the van-der-Waals forces between the tip and the sample, which leads to a change in the tip oscillation amplitude. The height is adjusted to maintain constant cantilever oscillation amplitude. The deflection is measured using a laser spot reflected from the top surface of the cantilever into an array of photodiodes. The deviation of the tip allows to determine the impact of forces between the tip and the surface. The surface morphology is related to the forces between the tip and the sample surface. The movement of the tip is controlled by a piezoelectric element, due to which the tip can be moved very precisely in x, y and z directions. In this work, the AFM scans were done using a Bruker Dimension V system, both with a damping stage. The AFM data were evaluated by the software WSxM 5.0 Develop 6.5 [87]. The surface roughness of the samples is given by a statistical measure, root mean square (RMS) [88].

2.5.9 X-ray diffraction

High-resolution X-ray diffraction (HRXRD) is used for the non-destructive structure analysis of epitaxial III-V semiconductor crystals, details are sufficiently described in the literature. This method is widely used for the ex-situ analysis of binary, ternary and quaternary compound semiconductors and provides information about the composition, the crystalline quality, the tension or lattice relaxation of the layers and the layer thickness. Since the wavelength of the X-rays used $Cu\ K_{\alpha 1}$ (λ = 0.15405 nm) is in the order of magnitude of the spacing between the lattice planes of the III-V semiconductors, diffraction occurs at the crystal lattice. The incident beam is elastically bent at the crystal lattice, creating constructive interference. The diffraction condition is given by the Bragg equation, it describes the relationship between the wavelength (λ) of the X-ray radiation, interplanar distance (d) and the angle of incidence (θ) at which constructive interference can be observed. The diffraction order is given by n.

$$n\lambda = 2d_{(hkl)} Sin\Theta$$

If the lattice constant of the epitaxially grown layer differs slightly from that of the substrate ($a \neq a_0$), the layer initially grows tense with the lattice constant of the substrate ($a_\parallel = a_0$), while the lattice constant extends in the direction of growth ($a_\perp$) distorted. This works up to a certain so-called "critical layer thickness". If this is exceeded, the tension in the layer is so strong that it relaxes and the grid takes on its cubic shape again. The stresses are relieved by structural defects such as dislocations. The greater the tension, the smaller the critical layer thickness of the system. In order to grow as defect-free, unstressed layers as possible and sufficiently thick layers, the lattice constant of the III-V mixed crystal layer must be matched as precisely as possible to that of the substrate via the composition. In the present work, a high resolution XRD instrument (XRD, D8 HR Bruker) was used for determination of lattice relaxation in heteroepitaxial GaP/Si(100), when growth exceeded the critical layer thickness.

3 State of the art

This chapter summarizes previous work of our group regarding the Si(100) and Ge(100) double atomic stepped surface preparation in both, H_2-rich and As-rich CVD reactor ambience. Previous work regarding characterization of these defects in the III-V buffer layers grown on Si(100) substrates and, the knowledge about the GaInP nucleation on Ge(100) substrates from other groups is also discussed.

3.1 Anomalous double layer stepped formation on Si(100) surface in clean H_2 CVD ambience: Energetics vs Kinetics

The formation of double layer stepped Si(100) surface due to an interaction of the surface with H_2 carrier gas in MOCVD reactor was studied in great detail [14,89,90]. The hydrogen termination of the Si(100) surface depends strongly on H_2 pressure and the temperature of the substrate and both parameters determine its adsorption and desorption on the Si surface [89,91]. It was shown that the Si(100) surface exhibits a complete hydrogen coverage below 630°C, about 95% coverage at 800°C and about 25% at 1000°C for nearly atmospheric pressure of hydrogen [90]. During annealing at elevated temperatures of Si(100) surfaces, the process gas H_2 induces Si removal (etching), this in turn leads to diffusion of Si vacancies or adatoms, annihilation at the step edges of vacancies or attachment of adatoms at the step edge. This kinetics can be controlled by temperature and pressure of the process. DFT calculations showed that the A-type majority domain (dimers are perpendicular to step edges) on a substrate lower than 2° substrate offcut and the B-type majority domain (dimers are parallel to the step edges) on a substrate higher than 0.5° offcut are energetically favorable [92]. The energetically driven formation of the majority domain is possible by reducing the H_2 pressure at high temperatures (at 1000°C) which further minimize the H_2 coverage on the Si(100) surface [14,93]. At high H_2 pressure, 950 mbar and between 700°C and 850°C, the domain formation is driven by the kinetic processes, and the domain ratio varies continuously, depending mostly on Si vacancy generation, diffusion, and annihilation. By controlling the process parameters the energetically unfavorable majority domain on the Si(100) surface can be prepared. Such, kinetically driven surface formation was shown and explained for Si(100) surface with 2° and 0.1° offcut [14,93]. The Si vacancy generation at the terrace was observed due to etched Si from the surface by formation of SiH_x species. On large terraced substrates with low substrate offcut (0.1°), vacancy diffusion leads to the formation of elongated vacancy islands. When these islands reach a certain size, continuous

Si layer-by-layer removal occurs [93]. On substrates with 2° offcut in [011] direction, the diffusion length of these vacancies is large compared to the terrace width and the vacancy annihilates preferentially at the B-type step edges causing a retreat of this step edge and hence the formation of an A-type majority domain with double-layer steps [14] in the surface.

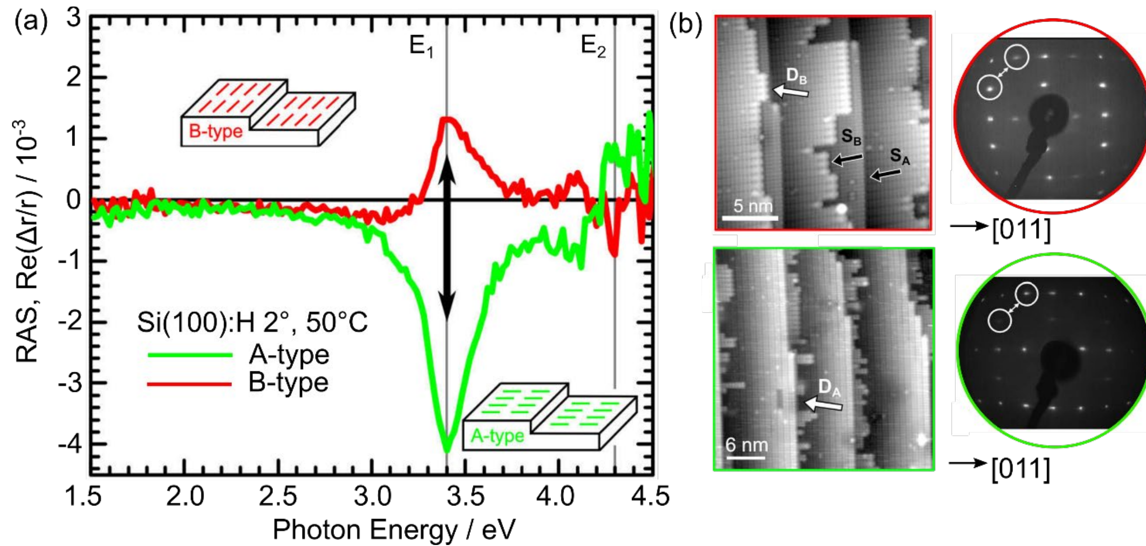

Figure 3.1: (a) *In situ* RAS of Si(100) 2° surfaces with prevalence of A-type (green spectrum) and B-type majority domain (red spectrum) on the surfaces along with corresponding LEED patterns and the STM scans shown in (b) and (c), respectively. The LEED pattern from A-type Si(100) surface (bottom right) displays a clear (1×2) symmetry whereas the B-type Si(100) surface (above right) exhibits a mixed (1×2)/(2×1) surface reconstruction. Accordingly, the STM scans of these surfaces confirm a majority of the A-type domain (green) with residues of the B-type domain adjacent to the step edges of the terraces, while the B-type Si(100) surface contains mainly single atomic steps and only few double atomic steps [14]. Figures are taken from *Ref.* [14] and redrawn.

This removal process, can be observed by RAS due to surface-related anisotropy of the Si dimers and characteristic RA spectra [14,94]. As example, in Fig. 3.1 (a), characteristics RAS signals, sensitive to the dimers formed on the double atomic stepped, monohydride terminated Si surfaces [93] of both of the Si(100):H 2° A-type (green spectrum) and B-type surfaces (red spectrum) [14] are shown. The opposite sign of the RA spectra indicates a rotation of dimers by 90° on the surface (prevalence of either A-type or B-type domain). According to previous research, the first step in the surface preparation is to deoxidize the Si surface in which the oxide layer from the Si(100) surface is removed at 1000°C and 950 mbar H_2 pressure [95]. Subsequent cooling of the Si(100) surface up to 730°C and annealing at this temperature for around 15 min leads to the formation of double atomic steps with A-

type majority domain on the surface [14], kinetically driven surface formation. The Si(100) surface with majority B-type domain, can be prepared after the deoxidation, by a fast cooling step (heater off) at 50 mbar H_2 pressure [14]. During B-type preparation at 50 mbar, the interaction of Si(100) and H_2 (kinetics) is minimalized, and thus the energetically favorable surface formation is prevalent. During cooling the diffusion of Si atoms still occurs leading to minority of A-type domain [91].

The RAS signals exhibit a characteristic peak with opposite sign at 3.4 eV which corresponds to the E_1 interband transition of Si, a lower intensity peak close to the E_2 interband transition and a shoulder in between. Comparison of the RAS peak amplitude at 3.4 eV to *Ref.* [96] indicates an A:B domain ratio of 37:63 for the energetically favorable process (B-type) and an A:B domain ratio of 85:15 for the kinetically driven process (A-type), respectively. The LEED pattern from the A-type Si(100) surface displays a clear (1×2) symmetry where the B-type Si(100) surface rather exhibits a mixed (1×2)/(2×1) surface reconstruction (Fig. 3.1 (b) and (c) at the right side, respectively) [14]. In addition, STM scans of these surfaces confirm a majority of A-type domain (green) with residues of the B-type domain on the edge of steps terraces while the B-type Si(100) surface contains mainly single atomic steps and only few double atomic steps [14].

3.2 Si(100) surface preparation in As-rich CVD ambience

The double-layer stepped Si(100) surfaces preparation was also studied in CVD reactors in the presence of group-V precursors, in particular arsenic [15,67,97]. Arsenic is required for subsequent III-V buffer growth for active photovoltaic and water splitting devices and thus present in the CVD reactors anyway. Lattice mismatched to Si absorber layers bridged by a graded buffer layers in which As content in $GaP_{1-x}As_x$, buffer layers is increased stepwise. [47,98]. Moreover, a lattice matched structure by application of small amounts of N into GaP(As) can be prepared for GaPNAs-on-Si tandem solar cell [99,100].

The double layer stepped, dimerized Si(100) surfaces can be prepared by annealing the surface under TBAs or AsH_3 and by exposure to background As_4 desorbing from inner walls of the reactor and susceptor at elevated temperatures [68] in As-rich (Ga-free) CVD reactor ambience [67,97,101]. It was shown that at high temperature (~1000°C), presence of background As_4 leads to substituting Si atoms after deoxidation of the surface and an energetically favorable Si(100) B-type surface is formed after a quick cooling of the Si(100) sample down to 420°C in the presence of background As_4 [37]. In contrast, the surface preparation by application of TBAs at temperature around 850°C and high reactor pressure (950 mbar) for 1 min and subsequent annealing of the surface in H_2 and background As_4 at

this stage is found to be kinetically driven. For high offcut substrates (~ 6°), the process route for a B-type Si(100) surface was found to be energetically favorable whereas the A-type surface was kinetically driven [37] [68]. To maintain a supply of background As_4 from the reactor walls TBAs precursor was turned on at 670°C while the Si(100) surface was still deoxidized, in order to coat the reactor walls and susceptor [67,68]. Both of the surface preparations depend on the adsorption of H_2 in the Si(100) surface at different temperatures which should be considered.

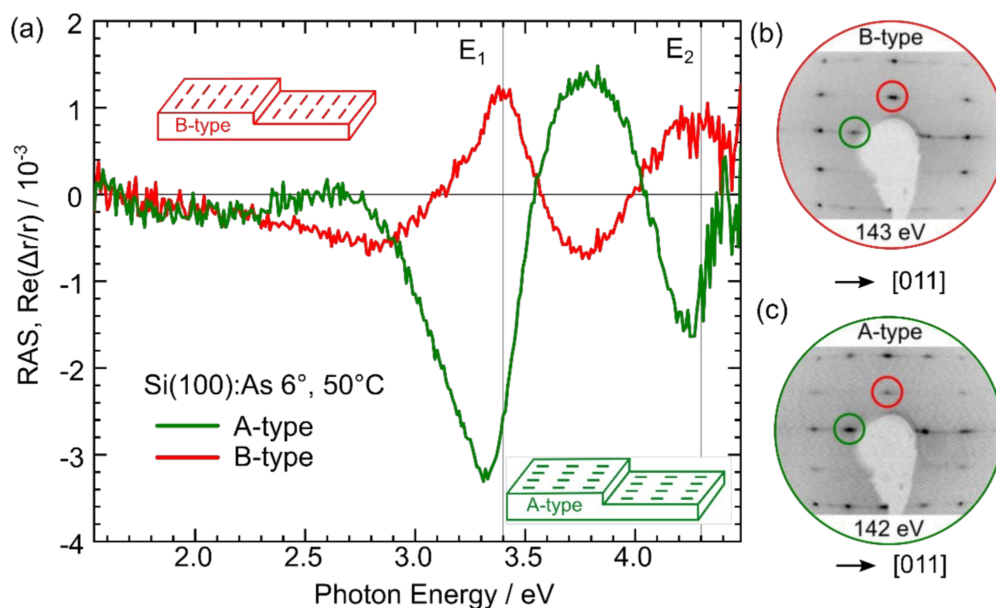

Figure 3.2: (a) Left side: RAS of Si(100):As 6° with predominant (2×1) (red) and (1×2) (green) surface reconstruction - dimers are oriented parallel (B-type domain) or perpendicular (A-type domain) to the step edges, respectively. Gray vertical lines indicate the E_1 and E_2 interband transitions of Si [135]. (b) and (c) Right side: LEED patterns of measured RA spectra, green (A-type) and red circles (B-type) indicate half order spots from (1×2) and (2×1) surface reconstruction, respectively. The figures are reproduced after *Ref.* [68].

Fig. 3.2 (a) show characteristic RA spectra taken at 50 °C of both the A-type (green spectrum) and B-type (red spectrum) Si(100):As 6° surfaces [68]. Similar to the H-terminated Si(100) surface (shown in Fig. 3.1 (a), section 3.1) the RA spectra are flipped with respect to each other depending on the orientation of dimers (either A-type or B-type) on the surface. For Si(100):As A-type (B-type), both of the RA spectra exhibit a broad maximum (minimum) between 2.2 eV and 2.7 eV, a high intensity minimum (maximum) at around 3.4 eV (near the E_1 critical point energy of Si), a maximum (minimum) at ~3.7 eV and a minimum (maximum) at ~ 4.3 eV. Both RA spectra exhibit similar line shape, however, the intensity of B-type surface is lower, which indicates lower ratio of majority to

minority domain on the surface, compared to the A-type. Compared to the H-terminated Si(100) surface, same surface reconstruction was found of these surfaces by the LEED measurement: The LEED pattern (shown in right side of Fig. 3.2 (b) and (c)) from Si(100):As 6° A-type surface exhibits a prevalence of (1×2) type surface reconstruction whereas the B-type surface contains a predominant (2×1) type surface reconstruction. In addition, both of these surfaces exhibit small minority domains on the surface. Moreover, the RAS line shape of the Si(100):As 6° surface (green solid line) is found very similar to the previously established RAS signal of the Si(100):As A-type surfaces with 2° offcut [15] which confirms that the RA spectrum originates mostly from the terraces of the Si(100) surface. We also see that the RAS line-shape of the As-terminated surfaces is different of the H-terminated surfaces. The atomic structure of As-modified surfaces in MOCVD ambience was not studied in detail, yet. Previous study on the As-modified Si(100) 2° surface showed that the Si(100) surface exhibits a majority of the A-type domain on the surface and the step height found on the surface was equal to double-layer steps. In addition, no step bunching was observed [15]. However, due to lack of atomic resolution, the atomic structure of the surface was not resolved. The atomic structure of these surfaces will be discussed in **chapter 5**. Moreover, in *Ref.* [15], the STM scan shown refers to a Si(100):As 2° surface which was initially prepared with H-termination and subsequently annealed in arsenic ambient to prepare the As-modified Si(100) 2° surface. For industrial application, a reduction of the comparatively long process time for double-layer step formation is highly desired. A fast route for the preparation of As-modified Si(100) surfaces will be discussed in **chapter 5**.

3.3 GaP(100) surface grown on both Si(100):H and Si(100):As surfaces

Commonly, GaP is grown on Si(100) substrates because of a close lattice matching. The growth kinetics of GaP and its surface reconstructions have been studied well [15,45,102–104]. GaP(100) can be terminated either by phosphorus, so called ‘P-rich’ surface or by mixed P-Ga mixed dimers, so called ‘Ga-rich’ surface. In MOCVD, the Ga-rich GaP(100) surface exhibits a (2×4) surface reconstruction whereas the P-rich GaP surface exhibits a (2×2)/c(4×2) reconstructed surface with buckled P-dimers terminated by one hydrogen atom [105,106]. As explained by Hahn et al. [107], each of the dimers is stabilized by a single hydrogen atom, saturating one of the dangling bonds of the dimer (see Fig. 3.3, (a)) [105,108]. The buckled dimers are aligned in zig-zag chains along the [011] direction. This leads to rows of buckled phosphorus dimers, where adjacent rows can be arranged in-phase or out of phase. The in-phase arrangement results in a (2×2) unit cell, while the out-of-phase arrangement corresponds to a c(4×2) unit cell. In the LEED pattern, the P-dimers shows

spots at half order along the dimer axis, [101,107] and therefore, the pattern is referred to as a (2×1) like surface reconstruction.

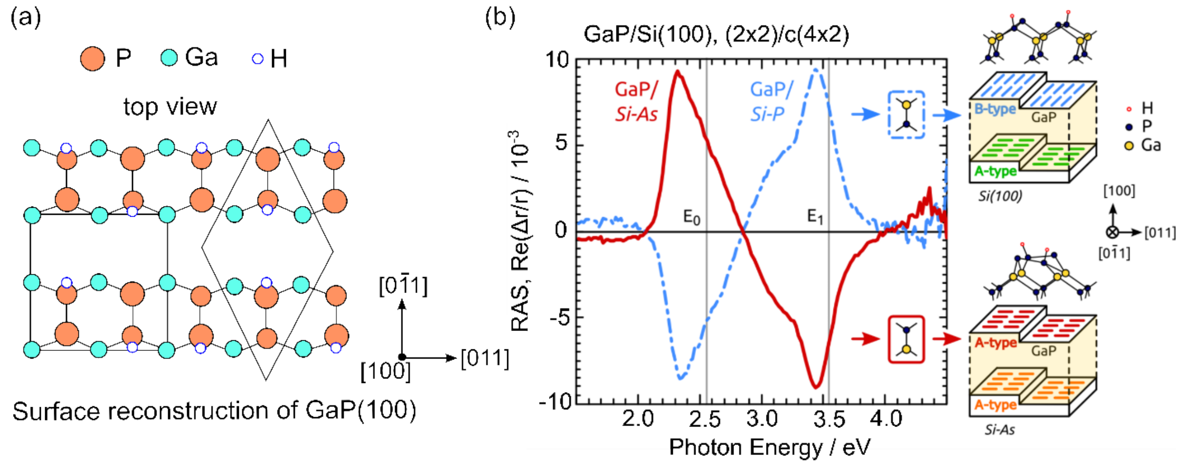

Figure 3.3: (a) P-rich GaP(100) - (2×2)/c(4×2) surface reconstruction (in H_2 ambient) – top view, the black rectangular and rhombus indicate the unit cells. (b) Comparison of RA spectra of GaP(100) P-rich surface grown on Si(100):H (in which the interface considered as Si:P) and Si(100):As surfaces. In both of the cases, the Si(100) surfaces were prepared with majority of the A-type domain on the surface. The GaP/Si heterointerface determines the GaP sublattice orientation and can be distinguished by the flip of the RA spectra indicating a 90° rotation of the sublattice. Figure (b) is taken from *Ref.* [15].

The P-rich and Ga-rich GaP(100) buffer layers grown on the Si(100):H surfaces show two distinguishable RAS signals with distinct characteristic features [109]. In the previous study from our group, the RA signals of the heteroepitaxial P-rich GaP layers grown on Si(100):H 2° A-type surfaces [109] were found very identical compared to that of P-rich GaP(100) surface shown in *Ref.* [105,110]. Both the line shapes, in particular, the sign of RA signals are very similar. For a zincblende crystal, it is known that every subjacent monolayer, the (100) projected bond orientation changes by 90° due to the tetrahedral coordination within the lattice. An inversion of the GaP sublattice corresponds to a rotation of the P dimers by 90° and therefore reflects on the sign of the RA signal of GaP/Si(100). When a P-rich GaP(100) layer grown on H-terminated Si(100) A-type (B-type) surface, its lattice is rotated by 90° and therefore the layer results in a B-type (A-type) GaP(100) surface [109]. In contrast, the P-rich GaP(100) buffer layer grown on the As-modified Si(100) A-type (B-type) surface results in a A-type (B-type) surface. Therefore, the RA spectrum of the GaP(100) layer grown on Si(100) A-type surface was found very comparable and identical to the one grown on the Si(100):H A-type surface, but the sign of the corresponding RA signal is flipped [15]. Fig. 3.3 (b) illustrates a comparison between characteristic RA signals

from P-rich GaP buffer layers grown on H-terminated (blue dashed line) and As-modified (red solid line) Si(100) 2° A-type surfaces [15]. The RA signal from GaP grown on H-terminate (As-modified) surface, shows negative peak (positive peak) at about 2.35 eV and a positive peak (negative peak) at about 3.4 eV, which is a characteristic spectrum for a B-type (A-type) P-rich GaP/Si(100) surface as known for GaP(100) [105,107,109]. The initial Si(100) surface preparation (either A-type or B-type) and the formation of the heterointerface makes a rotation of the P dimers by 90°, and thus impacts on the orientation of the P dimers at the $(2 \times 2)/c(4 \times 2)$ reconstructed GaP/Si(100) surface [102].

3.3.1 *In situ* monitoring during GaP nucleation on Si(100):H surfaces

An optimized GaP nucleation as well as growth condition are necessary to insure a well-ordered heterointerface as a prerequisite to avoid defects in the bulk layer. A two-step growth process, consisting of a pulsed nucleation at 420°C and a subsequent buffer growth at 595°C was previously established for low defect GaP nucleation on Si(100) surface [52,104,111]. The established GaP pulsed nucleation consisted of 10 alternating pulse pair (PP) of TBP and TEGa offered 1 second each on a well-ordered, double-layer stepped Si(100) surfaces, as shown in Fig. 3.4 (a). In *Ref.* [104], it was shown that RAS is a surface sensitive tool to observe the formation of GaP nucleation surfaces even at low GaP coverages and in addition, the evolution of this GaP nucleation surface was demonstrated. In Ref. [] the pulsed nucleation was monitored by a continuous time-resolved RAS measurements (at a photon energy 3.25 eV) during the nucleation of GaP on Si(100):H (see Fig.3.4). The anisotropy signal from the Si(100):H surface disappeared immediately with the first pulse of TBP and an isotropy of opposite sign appeared during the GaP nucleation as observed from the continuous measurement. This already indicates the presence of phosphorus atoms adsorbed on the surface. A gradual decrease of the anisotropy was observed while more than 10 PP of precursor pulses were applied which referred to either disordering of the surface or related to a spectral shift due to surface reaction layer as mentioned in *Ref.* [112]. Therefore, the number of pulses for GaP nucleation was optimized to 10 PP.

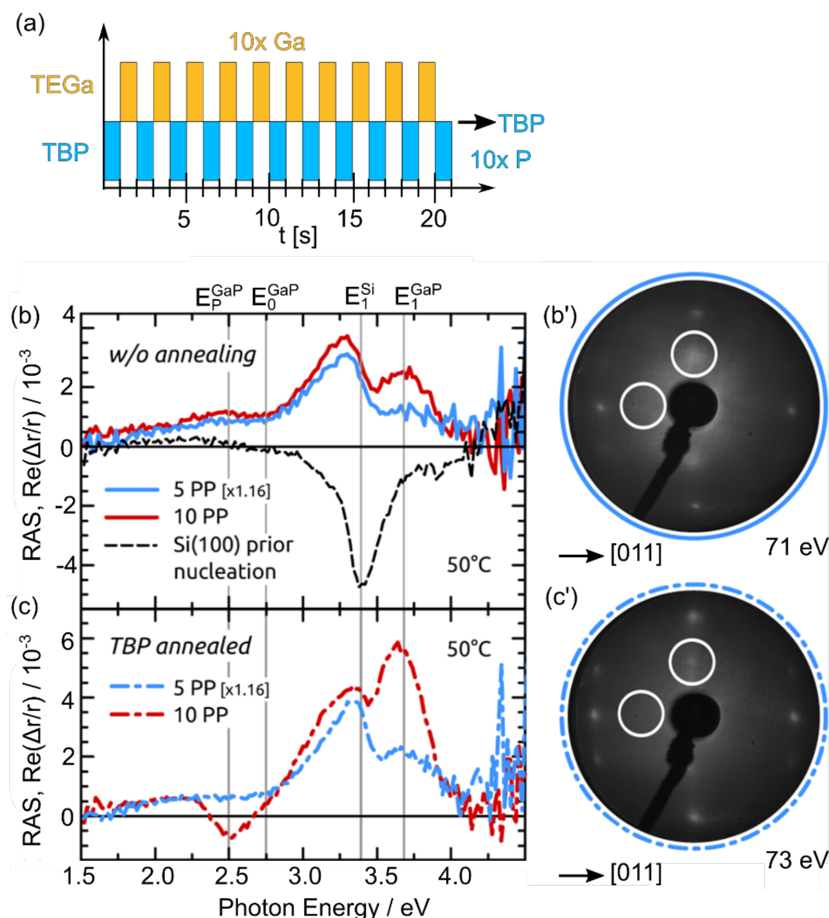

Figure 3.4: (a) Previously established GaP pulsed nucleation in which alternating TBP and TEGa pulses were offered for 1 second each at 420°C. (b-c) RA spectra measured at 50°C: (b) After 5 (blue) resp. 10 (red) PP, scaled so that the Si(100) spectra (black dashed line) prior to pulsing match. (c) Identical samples as in (a) where subsequently heated to 595°C with TBP supply. LEED patterns corresponding to the RA spectra: (b') after 5 PP before annealing and (c') after 5 PP plus annealing in TBP. Figures are taken from *Ref.* [104].

Fig. 3.4 (b) and (c) show the corresponding anisotropy signals (take at 50°C) from the GaP nucleation surfaces prepared with both 5 PP (blue solid line) and 10 PP (red solid line) before and after the annealing under TBP. It has been showed that the anisotropy signal of the GaP nucleation already develops a characteristic peak at around 3.3 eV and a shoulder at the E_1 interband transition of GaP in case of 5 PP. After 10 PP (Fig. 3.4 (b)), the intensity of the anisotropy slightly increased. In contrast, the line shapes for both of the RAS signals become pronounced after annealing at 595°C under the TBP (Fig. 3.4 (c)). Here, an increase of the contribution at E_1 of GaP was observed in particular for the 10 PP sample, while that at 3.3 eV almost remains unchanged and in addition, the contribution at 2.5 eV (E_P^{GaP}) was more pronounced for the 10 PP GaP sample. The increased anisotropy at E_1 corresponding to

surface-modified bulk transition E_1^{GaP} develops faster than the anisotropy at E_P^{GaP} (2.5 eV) corresponding to the surface-state related transition. Since, the anisotropy at 3.3 eV is already established after 5 PP, while the GaP/Si(100) surface is not yet well-ordered, this indicates that the interface forms already during the first pulses at low temperature and not during annealing at higher temperatures, which supports the possibility of a kinetically limited interface formation [104]. After the 5 PP without annealing under the TBP, the surface was not so well ordered, while after the TBP annealing, the surface is well ordered and as a result, bright contrast of the diffraction spots was observed in the LEED pattern as confirmed by LEED shown in Fig. (b') and (c'), respectively.

3.3.2 Characterization of defects in GaP/Si(100) buffer layers by ECCI

GaP(100) is the material of choice for direct epitaxial growth on Si(100) substrates. However, the small lattice mismatch still results in formation of MDs and TDs in the bulk GaP layer. The growth conditions of GaP/Si(100) were minutely controlled to develop a method for suppressing defects in the GaP bulk, but the density of these defects need to be still reduced [52,54] to achieve highly efficient devices. Defects, in particular, MDs were first imaged by ECCI in the heteroepitaxial GaP/Si(100) surfaces by Grassman et. al. [113]. This study demonstrates that formation of MDs depends on the thickness of the GaP epilayers: A thin GaP layer (~30 nm) does not exhibit MDs in the layer, while they start to form when the layer thickness exceeds the critical thickness of ~50 nm [113]. In addition, the quantity and the length of MDs are temperature dependent. The total MD length per unit area for a 50 nm thick GaP sample annealed at a high temperature was measured as more than 10 times larger than the length measured in the GaP layer of same thickness without annealing [113]. The high temperature procedures certainly increase the strain in the GaP layer due to different thermal coefficients of expansion between the layer and the substrate, which results in an increase in lattice mismatch and thus impacts on the formation of MDs in the annealed GaP layer.

The pyramidal shaped defects observed in ECCI from a 120 nm thick GaP epilayers was identified as SFs and SFPs originating from the GaP/Si(100) heterointerface by Feifel et. al. [56]. In ECCI, the observed feature of a single triangle was identified as a SF and a pair of two inverted triangles connected to the same origin, forming a square, was attributed to SFP. However, the shape of the SFP depends on selected channeling conditions: Under the channeling condition $\vec{g}$ = (100), the shape of a SFP is a complete square which consist of four individual SFs [56]. The density of these defects significantly depends on the number of the precursor pulses applied during the nucleation on the Si(100) surface. It has been shown that the SFP density decreases from 6.2×10^7 cm^{-2} (20 pulses of Ga and P) by more

than two orders of magnitude to 4.3 × 10^5 cm^{-2} (5 pulses of Ga and P) [56]. In addition, these defects form approximately 5 nm height of hills in the layer during the GaP growth which increase the overall surface roughness. Moreover, the blocking behavior commonly observed in FCC metals was also observed in the GaP crystal in which some MDs were found to be blocked by the SFPs. Since, the size of the SFPs depends on the layer thickness, the effect of dislocation blocking might be increased with higher layer thickness [56].

The use of ECCI for imaging defects in the GaP/Si(100) was further demonstrated in *Ref.* [114]. In order to compare the defects in different positions of a sample surface, a small part along the radius of a full wafer (sample grown on a 4 inch wafer) was cut and imaged at multiple points along the radius of the wafer under the ECCI [114]. A high number of MDs was visible near the center of the wafer compared to the edge of the wafer, which showed nonuniformity of MDs. This observation is important to understand inhomogeneity of the epilayer on larger sized samples. Moreover, the number of MDs and the MD length varied from the center toward the edge of the wafer: The MD length and the number of MDs per area is higher near the center of the wafer compared to the one obtained at the edge [114]. The overall study performed by ECCI to investigate defects in the GaP layer shows that ECCI can play a significant role as a non-destructive technique for a rapid defect characterization on a large scale.

3.4 Ge(100) surface preparation in group V-rich CVD ambience

Vicinal Ge(100) surface is a common substrate for high-efficiency multi junction solar cells since lattice matched III-V subcells on Ge(100) can be grown by MOCVD. The interaction of the Ge(100) substrate with the process gas H_2 [115] or As [30] results in formation of monohydride or As-termination. Like Si(100) surface the Ge(100) surface preparation, prior to the growth of III-V layers, in particular, the formation of double atomic stepped, dimerized surfaces is necessary to prevent APDs in the III-V layer.

H-terminated Ge(100) surfaces can be prepared in a clean H_2 ambient by annealing the surface under pure H_2 at a temperature of 730°C [115]. The surface annealing at this temperature leads to formation of a double atomic stepped, single domain Ge(100):H surface which exhibits a characteristic RA spectrum corresponding to a predominant (2×1) surface reconstruction which further indicates a complete monohydride termination [16]. A surface study at the atomic scale by STM showed a regular step structure with double atomic height and symmetric dimers on the terraces. The step height and the orientation of the dimers observed in the STM scan indicate preferential B-type dimers, i.e dimers parallel to the step edges on adjacent terraces [115].

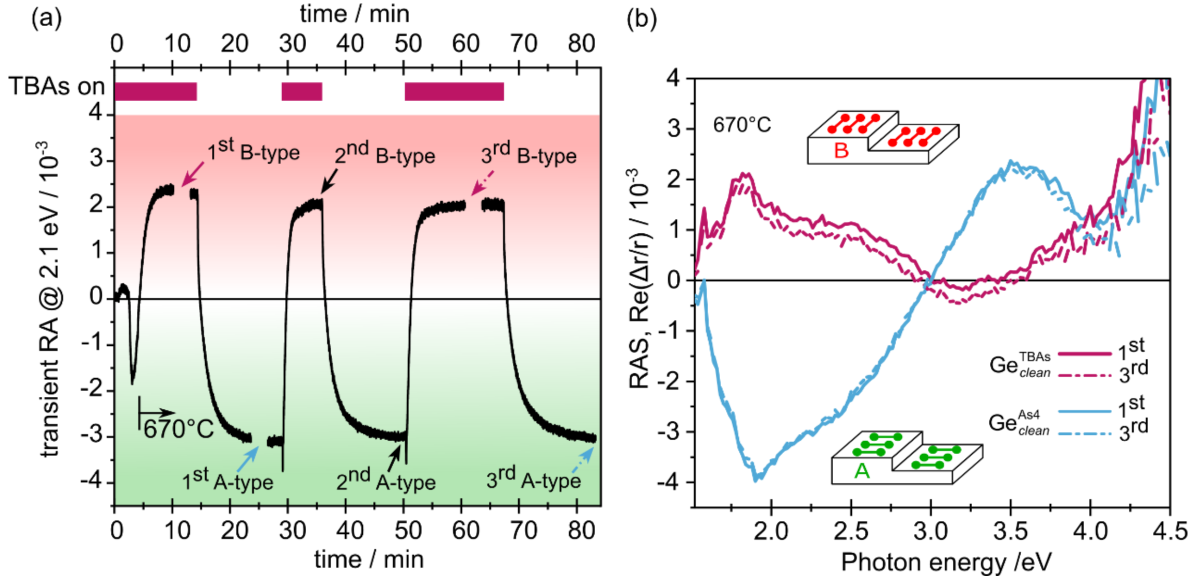

Figure 3.5: (a) continuous in situ RAS measurement at 2.1 eV of Ge(100) surface with switching between predominant A-type and B-type domain during annealing at 670 ◦C in dependence on the TBAs precursor supply (shown as bars on top). The violet and blue arrows indicate a break in the recording of the transients to measure RA spectra which are shown in (b). The insets illustrate the prevalent As dimer orientation on the surface with respect to the step edges. Figures are taken from *Ref.* [18] and redrawn**.**

Beside the surface preparation of Ge(100) under clean H_2 ambient, the Ge(100) surface preparation was also established in As-rich, P-rich and more realistic GaAs-rich reactor conditions [18,116,117]. The presence of only group-V elements (such as As or P, that is in absence of Ga) influences the order at the surface significantly: As dimers oriented perpendicularly to the step edge form A-type, (1×2) reconstructed terraces when background As_4 and AsH_3 are present due to reactor residuals, and a direct supply of TBAs to the Ge(100) surface leads to As dimers oriented parallel to the step edges corresponding to the B-type terraces [18], (2×1) reconstruction. Both of these surfaces show characteristic RA spectra indicating double layer steps and corresponding surface symmetry [18]. The dimer orientation on these Ge(100) surfaces can be controlled by switching on or off of the TBAs precursor at a constant temperature of 670°C as shown in Fig. 3.5 (a) [18]. Fig. 3.5 (a) depicts a continuous RAS measurement (transient at 2.1 eV) while annealing the Ge(100) surface at 670°C in dependence of arsenic source as shown in *Ref.* [18]. After the transient started at 300°C and the sample was heated up to 670°C with the TBAs source, the Ge(100) surface was deoxidized, and within 10 min a stable Ge(100) surface with majority of B-type domain was formed. After switching off the TBAs source at the same temperature, the B-type surface was exposed to background As_4 and immediately the transient signal showed a decrease in

the line shape. A continuous annealing for next 10 min at this stage led to formation of a stable A-type Ge(100) surface. Subsequently, these two steps were repeated twice back and forth to confirm that the flip of the dimer orientation was only due to the two different arsenic sources. Therefore, it has been found that each time, when the TBAs precursor is opened or closed, an immediate change from the A- to B-type or from B- to A-type majority domain on the Ge(100):As surface can be seen. The corresponding RAS signals from these A-type and B-type surfaces are shown in Fig. 3.5 (b) exhibiting similar line shapes from both A-type and B-type Ge(100):As surfaces which correspond to (1×2) and (2×1) reconstruction on the surface [18].

Besides TBAs, the Ge(100) surface can also be prepared after annealing the surface in TBP precursor (when the TBAs is off) resulting in a characteristic RA spectrum [117] which was completely different from the surfaces prepared in clean H_2 [115] or As-rich ambient [18]. The phosphorus coverage on this Ge(100) surface was confirmed by XPS. However, a detailed study of these Ge(100) surfaces has not been performed yet. This Ge(100) surface prepared in P-rich ambient is expected to be advantageous for subsequent III-P buffer layer.

In contrast to the As-rich ambient, in the reactor coated with GaAs, a Ge(100):As surface with prevalence of an A-type majority domain was prepared under the TBAs while heating up the substrate up to 750°C [18]. This indicates that the source of As and the reactor conditions have a significant influence on the dimer formation. The amplitude and line shapes of the characteristic RAS signals observed from these Ge(100):As surfaces correspond to double atomic stepped, dimerized surfaces [18], but the line shape is different than the one prepared in the As-rich ambient [17]. Similar to the As-rich ambient [17], the LEED patterns confirmed (1×2) type surface reconstructions from the A-type Ge(100):As surfaces.

3.5 GaInP(100) nucleation on Ge(100) surface

Deposition of lattice matched $Ga_xIn_{1-x}P$(100) buffer layer on a Ge(100) or GaAs(100) substrate has is of interest because of its wide application in optoelectronics, in particular, for MJSC. Growth of lattice matched GaInP on Ge(100) substrate allows for further deposition of III-V epilayers with desired bandgap for high efficiency devices. To minimize density of defects in the subsequently grown III-V buffers, the GaInP(100) epilayers must be defect-free. Thus, optimized nucleation and growth conditions such as process temperature, pressure, and V/III ratio must be precisely tuned to control the formation of defects (APDs, TDs etc.) in the layer [13,118].

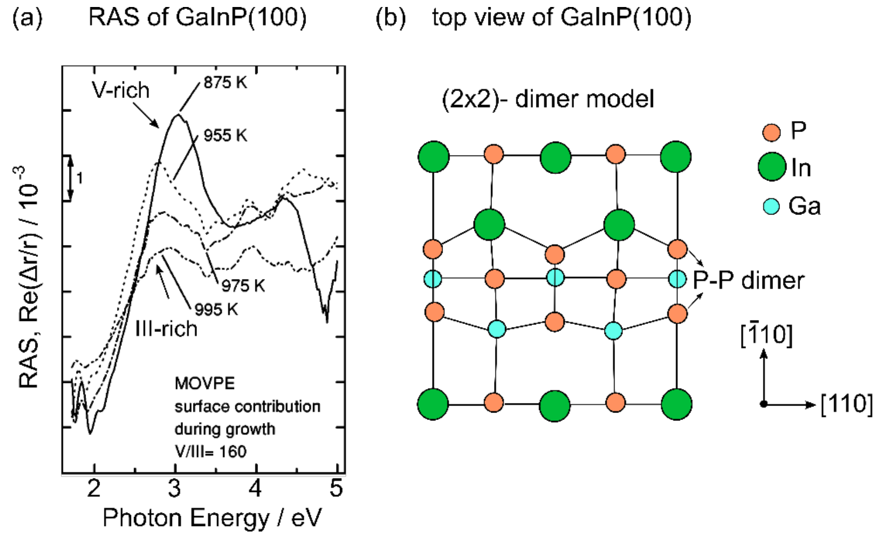

Figure 3.6: (a) RAS of V-rich and III-rich GaInP(100) surfaces. The V-rich surface changes to III-rich surface upon heating from 600°C to 720°C (taken from *Ref.* [119]). (b) P-rich dimer model for GaInP(100)- (2×1). The atomic model ends with the P–P dimer on top of a group III (In/Ga) layer.

Similar to the GaP(100) surfaces, GaInP(100) surface exhibits two different surface reconstructions, either III-rich or V-rich surface. During the growth in MOCVD, atomically ordered GaInP(100) surfaces of both V-rich and III-rich can be prepared [119]. In *Ref.* [119], characteristic RA spectra corresponding to two different GaInP surface reconstructions (V-rich and III-rich) were shown in dependence of the growth temperature. Fig. 3.6 (a) displays the measured RA spectra at different temperatures from these GaInP surfaces [119]. Annealing of the P-rich GaInP surface from 600°C to 720°C with a constant heating rate results in a III-rich GaInP surface, with a change of the surface reconstruction from a (2×1)-(P-rich surface) to a mixed (2×4)-like symmetry (III-rich surface) [119]. The line shape between the V-rich and III-rich surfaces differ mainly in the energy range of 3 eV: a sharp characteristic positive peak around 3 eV of RAS of the V-rich surface, vanishes after heating up the surface to 720°C when the III-rich surface is reached. This change in the RAS line shape is caused by the desorption of phosphorus at high temperature, which leads to a change in the surface reconstruction [119]. A side view of an atomic model from the P-rich (2×1)-like GaInP(100) surface has been shown in Fig. 3.6 (b). The model of GaInP shown here starts from the P atoms bonded with Ge(100) substrate and continues the chains with Ga or In atom each bonded with P atoms. The atomic model ends with the P–P dimer on top of a group III (In/Ga) layer.

The surface roughness and the morphology of GaInP layers grown on the Ge(100) substrate strongly depend on nucleation procedure and the MOCVD reactor ambient [120]: The GaInP layers with low surface roughness can be achieved while preparing the sample in an 'clean' (free of III-Vs material) reactor, or by maintaining a sufficient overpressure of group-V

elements to minimize the desorbed III-V species from the reactor walls when prepared in a III-V coated reactor. Regarding the defects in the GaInP layers, two characteristic crystal defects - so called arrowhead and asymmetric truncated pyramids have been observed in the GaInP layers [121]. It was found that the density of the arrowhead defects increases as the layer gets more Ga-rich. However, the quantity of asymmetric pyramids does not depend on a layer composition and might be prevented by optimizing the growth condition. So far, there is a lack of experimental studies on characterization of structural defects in the GaInP(100) buffer layers grown on Ge(100) substrates by MOCVD.

4 Sample preparation

Here, sample preparation and standard MOCVD processes are described.

4.1 Chemical pre-treatment of Si(100) substrates by Wet Chemical Etching

Before the Si(100) as-received wafers were processed in the MOCVD reactor, a wet-chemical treatment consisting of three steps: – RCA 1 + HF dip + RCA 2 was applied. In the first step (RCA 1), removal of organic contaminations and residual metals was done by boiling the substrate (~ 80°C) for 10 min in a basic etch solution consisting of ammonium hydroxide (NH_4OH, 25%), hydrogen peroxide (H_2O_2, 30%), and deionized (DI) water (H_2O) at the ratio of 1:1:6. In the second step, the etched substrates were dipped into hydrogen fluoride (HF) solution, mixed with DI water in 1:4 ratio for 1 min to remove native oxygen. In the final step (RCA 2), the substrates were treated with a solution consisting of hydrochloric acid (HCl, 32%), hydrogen peroxide (H_2O_2, 30%), and DI water at a ratio of 1:2:6. The substrates were dipped in this solution for 10 min at a constant temperature of 90°C. In this stage, a well-defined thin oxide layer is reformed on the surface. The substrates were rinsed with the DI water for minimum 5 min between each of the stages. The wet-chemical pretreatment ensured similar starting conditions for all samples.

4.2 Si(100) surface preparation in As-ambient

All samples were prepared in AIXTRON (AIX-200) MOCVD reactor (details in sub-chapter 2.7.1). All the Si(100) surfaces were thermally deoxidized at 1000°C and 950 mbar for approximately 30 minutes [69] in As-rich MOCVD reactor. Subsequently, in order to prepare double-layer stepped, A-type surfaces, Si(100) substrates with 2° and 4° offcut were exposed to TBAs precursor at 830°C [122]. The TBAs precursor was applied three times for around 3 minutes with annealing in H_2-ambience (TBAs off) for around 3 minutes in between. The reactor pressure was set to 950 mbar. For the preparation of Si(100) 0.1° A-type, TBAs was turned on at 450°C-670°C for 15 min while the Si surface was still oxidized, to ensure an arsenic ambience in the reactor. After turning off the TBAs, the Si(100) 0.1° surface was deoxidized at 1000°C under the background arsenic (As_4) and a quick cooling to 420°C under low pressure (~50 mbar) was applied [122]. In order to prepare Si(100) 0.1°

with B-type surface, after the deoxidation step, the samples were exposed to TBAs, similar way as for 2° and 4° surfaces but at relatively lower temperature of 770°C [122]. The process route of B-type Si(100) 4° surface preparation was almost identical as the A-type Si(100) 0.1° surface, only the reactor pressure was unchanged during cooling the surface from 1000°C to 420°C.

4.3 GaP and GaP/AlP nucleation and subsequent growth of GaP buffer layers

GaP or GaP/AlP thin buffer layers were grown on double atomic stepped, single domain Si(100):As 2° substrates. Precursors of TEGa, TMAl and TBP, were used for the Ga, Al and P source, respectively. The nucleation of GaP or GaP/AlP nucleation layers (NLs) was conducted at 420 °C and the subsequent GaP buffer layer growth at 595 °C [104]. The GaP nucleation consisted of 10 alternating precursor pulses each of TBP and TEGa (1 sec. each with 1 sec. pause in between). In case of the GaP/AlP nucleation, the first five TEGa pulses were substituted by TMAl [123]. The molar flow of both precursors (TEGa and TMAl) was set to 4×10^{-5} mol/min, and 2.6×10^{-4} mol/min for TPB. Some preliminary experiments were carried out by replacing two, five and ten pulses of TMAl, each pulse followed by a TBP pulse to fine-tune the precursor pulses. Samples with a pure GaP NL were prepared in a reactor, which had never been exposed to TMAl in order to avoid any Al residuals on the Si(100) surface prior to the nucleation step. For comparison, selected GaP buffer layers were grown on GaP NLs in an Al-containing reactor (Al residuals were present). The reactor pressure was kept constant at 50 mbar during the epitaxy. After the growth of 60 nm thick GaP buffer layers, the samples were cooled to 420 °C under TBP supply and annealed for 10 min without the precursor supply in order to desorb excess of phosphorous and precursor residuals from the surface and to form a dimerized, P-terminated GaP(100) (2×2)/c(4×2) reconstructed surface [45,107].

4.4 Ge(100) 6° surface preparation and subsequent III-P growth

The standard procedure of Ge(100):As surface preparation followed by III-P growth starts with deoxidation of the Ge surface in a MOCVD reactor. Prior to each process the reactor parts were “coated” with around 1 µm of GaAs in order to insure ‘industrially relevant’ more realistic processing ambience. We employed vicinal Ge(100) substrates with 6° offcut towards [011] direction. TBAs is used as a precursor for As source. Ge(100) samples were thermally deoxidized and annealed at elevated temperature above 600°C in TBAs in order

to prepare the (1×2) Ge(100) As-terminated surface [18,116]. The reactor pressure was kept constant at 100 mbar during the surface preparation. Prior to the growth of III-P buffer layer, the TBAs precursor flow was closed and the Ge(100):As surfaces were annealed under two different TBP molar flows referred as ‘high TBP’ and ‘low TBP’ at 600°C for around 4 minutes. For comparison, one sample without the additional annealing under the TBP prior to the III-P growth was prepared, referred to as ‘no As/P exchange’. Subsequently, 60 nm thick III-P layers were grown on each of the Ge(100) surfaces with the same V/III ratio. Finally, P-rich III-P layers were prepared after cooling down the surface with the TBP precursor up to 330°C and a subsequent annealing without the TBP at 380°C to desorb excess of P from the surface [45].

5 *In situ* control of dimer orientation and atomic structure of As-modified Si(100) surfaces

This chapter focuses on Si(100) surface preparation in both As-rich and III-V-rich MOCVD reactor ambience. We investigate the Si(100) surfaces in dependence on annealing at elevated temperatures with different source of arsenic and other process parameters such as pressure and temperature of the process. Subsequently, a quick process route to lower the maximum process temperature of the Si(100) surface preparation is determined. Finally, we study these surfaces in atomic scale by STM in order to resolve the surface structure on the Si surfaces. Parts of this subchapter are published in *Refs.* [67,68]. ([69]…..M. Nandy et al., Appl. Surf. Sci., 462 (2018) 1002, [70]…..M. Nandy et al., Sol. Energy Mater. Sol. Cells, 180 (2018) 343.)

5.1 Preparation of double-layer stepped As-modified Si(100) surfaces in As-rich CVD ambience

In order to avoid APDs in GaP(100) buffer layers, Si(100) substrate must be prepared with a single domain, i.e. double atomic stepped surface. In the following, we show *in situ* study on the Si(100) surfaces in dependence on the Si(100) substrate offcut e.g 0.1° and 4° in arsenic ambience. We also discuss the influence of process parameters which impact the dimer orientation on the Si(100) surface.

Fig. 5.1 (a) depicts characteristics RA spectra from both of the As-modified Si(100) 4° (solid lines) and 0.1° (dashed lines) surfaces prepared in As-rich ambient. Depending on the cooling procedure and process parameters, the dimer orientation of prevalent A-type or B-type domain on the Si surface is detected. Two different process routes are followed here which lead to RA spectra of similar shape but opposite of sign. The opposite sign of RA spectra clearly indicates orientation of prevalent dimers rotated by 90°compared to the other. The spectral line shape, consisting mainly of the local extrema at the Si E_1 and E_2 interband transitions and a third local extremum in between, reflects the characteristic fingerprint of the As-terminated Si(100) surface [15,97,101,124]. We first focus on the Si(100) 0.1° surfaces, on which A-type majority dimer formation is prepared by exposure of the Si surface

to background As_4 and a quick cooling at 50 mbar H_2 pressure. In contrast, the B-type majority dimer formation is prepared by an additional annealing at 770°C with direct application of TBAs in a sequence of 'on/off' for 3 times [67], see subsection 4.2. The RA spectrum of the Si(100) 0.1° surface A-type developed already at 1000°C (under the As-rich ambience) after the oxide layer is removed. Suppressed interaction between the Si surface and H_2 at this temperature facilitates adsorption of As to the Si(100) surface from the background As_4 [62]. Thereafter, a quick cooling further limits interaction with H_2 and background arsine (AsH_3) and develops an intense RA spectrum corresponding to a stable Si(100):As surface (Fig. 5.1, red solid line).

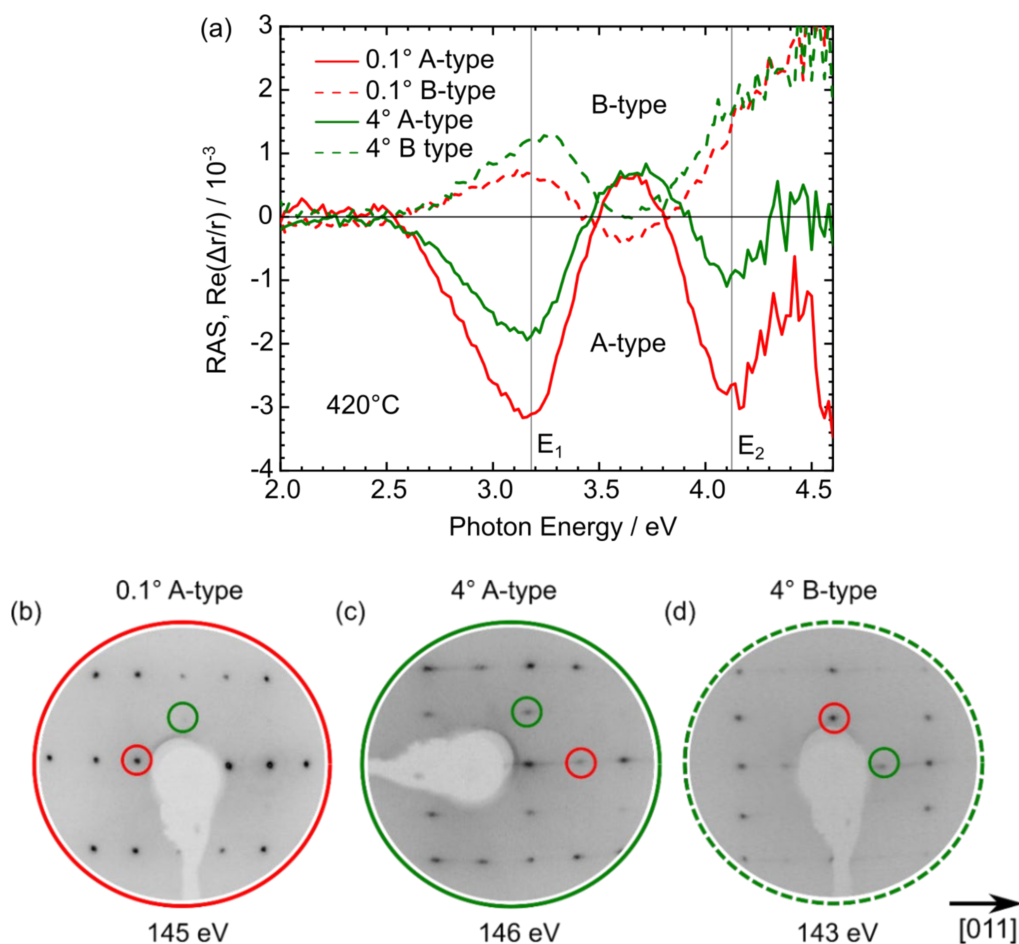

Figure 5.1: (a) RAS of Si(100):As with 0.1° and 4° misorientation exhibiting predominant (2×1) ("B-type", dashed lines) and (1×2) ("A- type", solid lines) surface reconstruction domains, respectively. Gray vertical lines indicate the E_1 and E_2 interband transitions of Si [125]. (b), (c) and (d) represent the corresponding LEED patterns of the Si(100):As 0.1° A-type, 4° A-type and 4° B-type surfaces, respectively.

For nearly exactly oriented Si(100) substrates modified with As, the A-type surface was calculated to be energetically favorable [126]. During the preparation of Si(100) 4°, the process route is opposite for both majority A-type and B-type surfaces compared to Si(100) 0.1° surfaces.[1] The Si surface is exposed to background As_4, while the B-type surface already developed at 1000°C and a quick cooling without lowering the H_2 pressure leads to a stabilized B-type surface. Here the B-type surface preparation is energetically favorable. In order to prepare the A-type surface, the surface was exposed to TBAs at around 830°C for three times. The RA spectrum of both Si(100):As 4° A-type and B-type surfaces (green solid and dashed lines) show the same characteristic features as the 0.1° surfaces (red solid and dashed lines), which confirms that the RA spectrum is terrace related, as it was suggested in *Ref.* [15]. Similar to Si(100):As 0.1° surfaces, the RAS amplitude of the Si(100):As 4° B-type surface is lower compared to the Si(100):As 4° A-type surface. Same as for H-terminated Si(100) surface, the process route for the preparation of the Si(100) surface with double-layer steps strongly depends on the offcut of the Si substrate, pressure, temperature of the process, and in addition, on the source of arsenic.

Fig. 5.1 (b), (c) and (d) show LEED patterns from Si(100):As 0.1° and 4° surfaces. The A-type Si(100):As 0.1° and 4° surfaces ((b) and (c)) exhibit a clear majority of (1×2) surface reconstruction with strong diffraction spots towards $[0\bar{1}1]$ direction and in contrast, the B-type Si(100):As 4° surface shows a majority of (2×1) surface reconstruction towards [011] direction. But the LEED patterns from both the 4° A-type and B-type surfaces show residual amount of minority domain, which appear as weak spots towards the [011] and $[0\bar{1}1]$ directions for A-type and B-type surfaces, respectively. Such a difference of the domain imbalance could explain the different RAS intensities of Si(100):As 4° A- and B-type surfaces.

[1] The Si(100):As 0.1° B-type surface preparation was done by Dr. Agnieszka Paszuk.

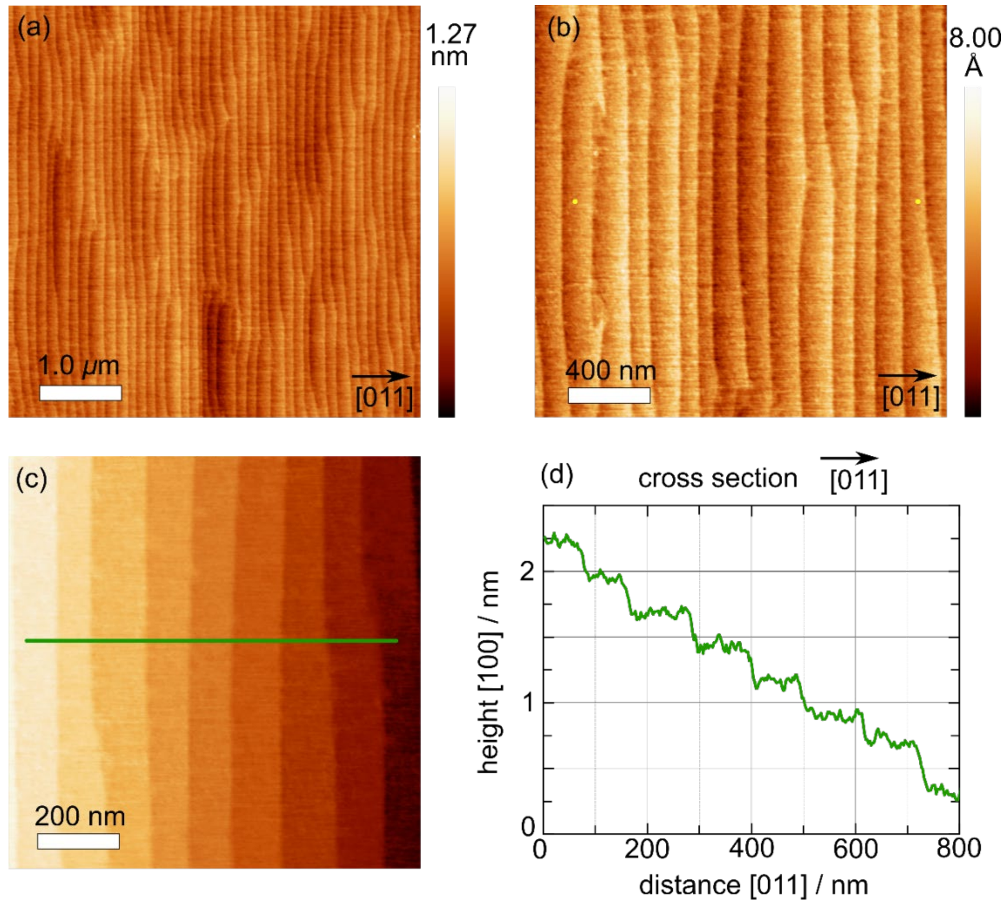

Figure 5.2: AFM scans of Si(100):As 0.1° (A-type): (a) (5×5) μm^2, (b) (2×2) μm^2 image, (c) (1×1) μm^2 image with a local plane flatten and the corresponding line scan which corresponds to even number of atomic steps on the Si surface. [2] The figure is reproduced after *Ref.* [67].

Fig. 5.2 displays two representative AFM images and a line scan of the A-type Si(100):As 0.1° surface showed in Fig. 5.1. The (a) 5×5 μm^2 and (b) 2×2 μm^2 images exhibit an RMS roughness below 1.1 Å and 0.9 Å, respectively. The observed terraces from the AFM scan seem atomically flat. The step edges are regularly ordered running straight along [011] direction. Fig. 5.2 (c) and (d) show the AFM scan (with local plane flatten) of 1×1 μm^2 image and corresponding line profile scan in which both the terrace width and the step height is calculated around 3Å which confirm the presence of double-layer steps. Residuals of the B-type domain are not visible at the step edges. Such a surface is ideally suitable to completely suppress APDs in subsequent III-V epilayers.

[2] The AFM scan of the Si(100):As 0.1° A-type surface was done by Dr. Agnieszka Paszuk.

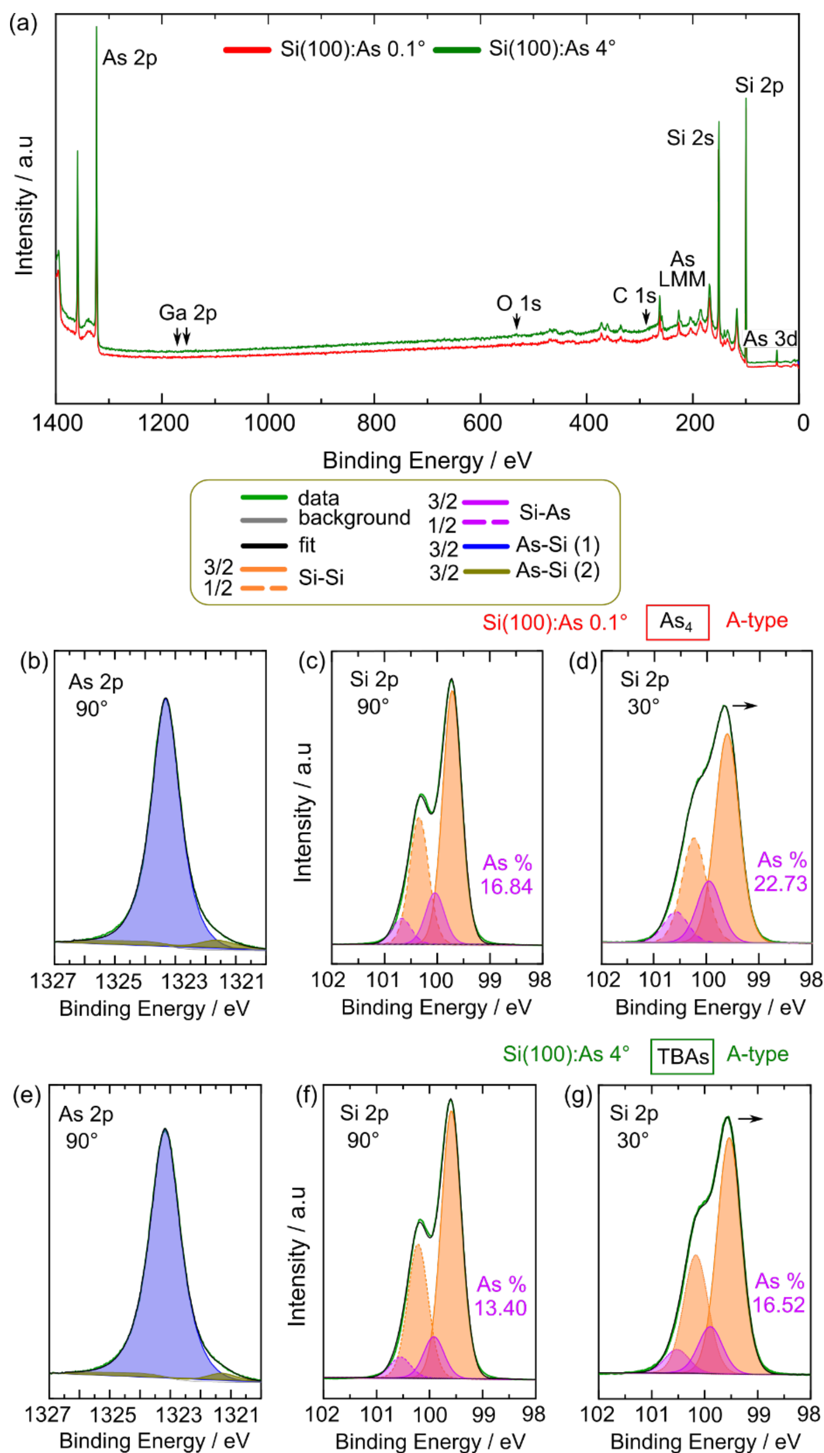

Figure 5.3: (a) XPS overview spectra of the Si(100):As 0.1° (redlines) and 4° (blue line) A-type samples. The Si 2p P.E lines were measured at 90° and 30° along with the As 2p P.E lines at 90° for both of the Si(100):As 0.1° (b), (c), (d) and for 4° (e), (f), (g) surfaces. The fit envelop (black line) and its components: Si-Si (bulk, orange solid and dash lines), Si:As (violet solid and dash lines), As-

Si (1) and As-Si (2) (blue and yellow lines) are indicated. The entire XPS measurement was performed by the monochromatic Al Kα excitation energy and the binding energy was given with respect to the Fermi level.

In the following we compare the XPS analysis of the Si(100)0.1° surface prepared in background As_4, energetically driven surface preparation with the Si(100)4° surface, prepared under TBAs, kinetically driven surface preparation. The as-prepared samples were contamination-free transferred from MOCVD to XPS by using a mobile UHV shuttle [127]. Fig. 5.3 show XPS scans from both samples: an overview scans (a), core levels of As 2p (b)-(e) and Si 2p (c)-(f). In order to increase the surface sensitivity measurement, the photoelectron take-off angle was varied from 90° to 30° against normal emission, and spectra of Si 2p taken at 30° are shown in Fig. 5.3 (d) and (g). The presence of As on both of the Si(100) surfaces is confirmed by As $2p_{3/2}$ photoemission lines (P.E lines). Compared to the elemental As $2p_{3/2}$ P.E lines, As $2p_{3/2}$ P.E lines is shifted to lower binding energy (EB) by 0.68 eV and 0.84 eV for Si(100):As 0.1° and 4° surfaces (Fig. 5.3 (b) and (e)), respectively. From both of the Si(100):As surfaces, the As $2p_{3/2}$ P.E lines consist of one main contribution, which we assign to As-Si (1) and in addition, one small contribution As-Si (2) at lower EB (~1321 eV). These two components have a pronounced chemical shift between each other. Since we do not observe any other contaminants such as oxygen and carbon bonded with Si 2p, we suggest that the chemical shift is due to As-Si bonds on the surfaces. This implies that arsenic atoms are present on the surfaces in two different chemical states with a relative chemical shift of 1.98 eV and 1.83 eV for Si(100):As 4° and 0.1° surfaces, respectively. We propose that the bigger component As-Si (1) is related to the As-Si bonds present at the surface, and the smaller peak As-Si (2) could originate from buried As atoms [15]. The Si 2p P.E lines from both Si(100):As surfaces consist of two spit-orbit splitting of equal full width half maximum (FWHM); intensity ratio of $Si2p_{3/2}$ to $Si2p_{1/2}$ equal to 2:1, and with a spin-orbit splitting of 0.63 eV between each other. In both Si 2p PE lines, measured at 90° (Fig. 5.3 (c) and (f)) and at 30° (Fig. 5.3 (d) and (g)) photoelectron take-off angle, two spin-orbit pairs are fitted and shifted to each other by 0.33 ± 0.2 eV for both of the Si(100):As surfaces. This chemical shift also in line with the presence of Si-As bonds. The area of the smaller peaks shifted to the higher EB increases with surface sensitivity. As observed for Si(100):As 2° surfaces [15], the change of intensity ratio between both components indicates that the components shifted to the higher EB (violet solid and dash line) is closer to the surface and originate from Si-As bonds, while the other component (orange solid and dash line) arises from bulk silicon atoms (Si-Si) [15,128]. These two Si(100):As surfaces were prepared by different form of arsenic source; either by TBAs or by background As_4. We suggest that different form of arsenic sources provides an unequal amount of As incorporation close to the Si surface region and into the bulk. The area ratio of As/Si or Si/As was determined by using CasaXPS software. The As content (violet solid and dash curve)

in Si 2p was calculated 16.84% (90°), 22.73% (30°) and 13.40% (90°), 16.52% (30°) of the Si(100):As 0.1° and 4° surfaces, respectively (see Table I). The As content in Si 2p increases while changing from 90° to surface sensitive 30° measurement and in particular large increase is observed in the Si(100):As 0.1° surface which shows the As content is higher in the Si(100):As 0.1° surface compared to the Si(100):As 4° surface. In addition, we determine the area ratio of $As2p_{3/2}$ to Si2p which shows higher (0.0206, at 30°) for the Si(100):As 0.1° surface compared to that ratio for the Si(100):As 4° surface (0.0190, at 30°). The integrated peak area of Si2p, $As2p_{3/2}$ and As3d was corrected by photoelectron ionization cross section taken from Yeh and Lindau [129] and transmission functions were derived from the spectrometer. Since, $As2p_{3/2}$ P.E line is more surface sensitive, the quantification of the area ratio of $As2p_{3/2}$ to Si2p indeed indicates higher amount of As present on the Si(100):As 0.1° surface. The area ratio of Si2p to As3d though suggests a large As content in the Si(100):As 4° surface, but As3d is less surface sensitive and probes arsenic from the bulk. Moreover, A small shift of both Si 2p and As 2p P.E lines was observed towards lower EB for both of the samples at the surface sensitive 30° measurement compared to 90° measurement, which indicates a Fermi level shift towards upward band bending for both of the samples (arrow indicated in Si 2p P.E lines at 30°, Fig. 5.3 (d) and (g)). Overall, the XPS analysis and quantification of area ratio suggest that the process route and the source of arsenic influence chemical composition of the Si(100) surfaces. A summary of the area ratio calculated from the core levels of As and Si is in a following table.

Table I: Quantification of the Si and As P.E lines measured by XPS.

Sample	A-type Si(100):As 0.1°				A-type Si(100):As 4°			
XPS P.E lines	Si 2p/As 3d	Si 2p/As $2p_{3/2}$	As $2p_{3/2}$/Si 2p	As content in Si 2p %	Si 2p/As 3d	Si 2p/As $2p_{3/2}$	As $2p_{3/2}$/Si 2p	As content in Si 2p %
90°	50.29	61.00	0.016	16.84	42.93	54.23	0.018	13.40
30°	21.12	48.35	0.0206	22.73	18.22	52.51	0.0190	16.52

The surface preparation of As-terminated Si(100) surfaces discussed here were investigated by STM. As already mentioned earlier, these samples were transferred by contamination-free UHV transfer to the STM. All of these Si(100) samples were thermally deoxidized prior to the formation of double atomic stepped on the surfaces and were separately prepared for particular STM study. The aim of this STM measurement was to investigate the Si(100)

surface while prepared in As- ambient, in particular, we were interested in the dimer orientation and symmetry, i.e. whether the dimers on the Si surfaces are symmetric, e.g As-As dimers, or asymmetric, e.g As-Si-H dimers.

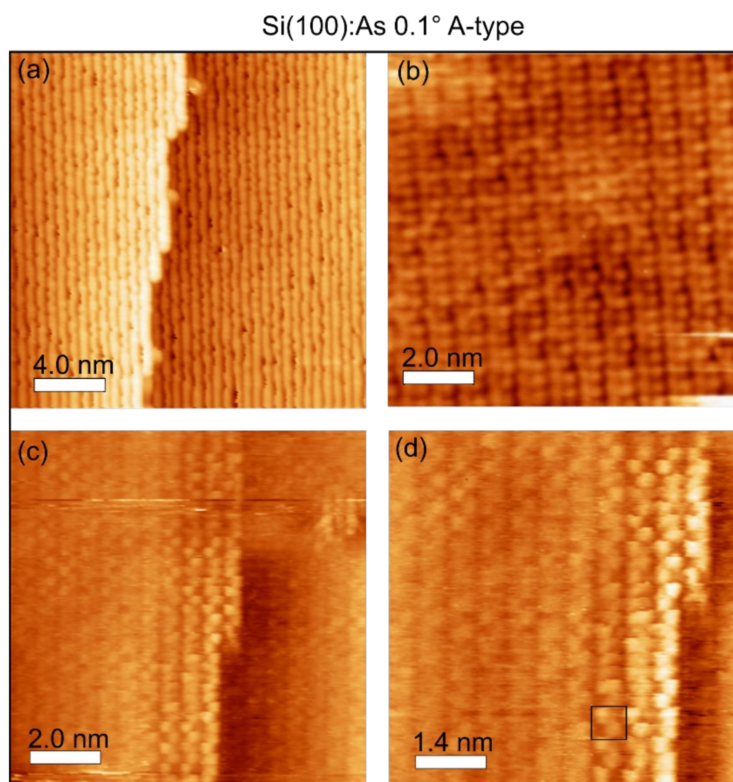

Figure 5.4: Selected STM scans of Si(100):As 0.1° surfaces, dimer row along the atomic step edges (a) and (b). The Si surface shows symmetric dimers and in addition, some dimers alternates indicating asymmetric ones (c) and (d). [3]

Fig. 5.4 depicts selected STM scans from a Si(100):As 0.1° surface. The surface shows clear atomic step edges towards the substrate [011] offcut direction. The surface exhibits dimers with zig-zag structures which are arranged dimer rows (see (a) and (b)) oriented parallel to the step edges. This is equivalent to A-type terraces. There are small kinks observed at the atomic step edges which probably comes from a slight misorientation of the substrate offcut (~0.1°) from the [011] direction.

In order to understand the formation of dimers, some more scans were taken from the same Si(100):As sample as shown in Fig. 5.4 (c) and (d). Here, we observe that the direction of the tilting of the dimers varies along the dimer rows. In many positions on the samples, it

[3] All the STM scans were done by Dr. Peter Kleinschmidt and B.Sc. Aaron Geiß.

alternates over some dimers and therefore, they exhibit a close-range order. In Fig. 5.4 (c) and (d) this kind of alternating dimers was observed which indicated a (2×2) reconstructed surface (as shown by a square in Fig. 5.4 (d)). However, a long-range order does not exist since there are sometimes two asymmetric dimers with the same tilt adjacent along a dimer row. Since the previous study in LEED confirmed a prevalence of (1×2) surface reconstruction from this surface [67], the alternating tilt of dimers does not represent a dominant structure here.

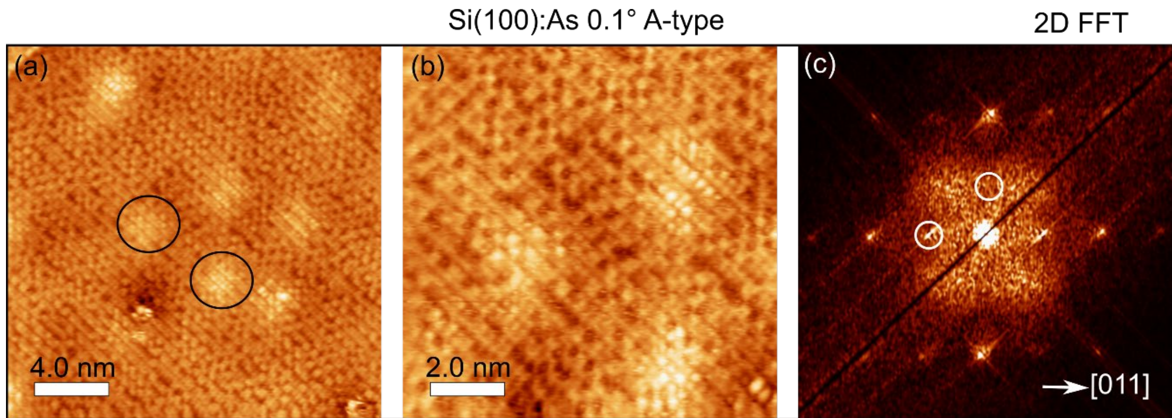

Figure 5.5: (a) - (b) STM scans of the Si(100):As 0.1° surface taken diagonally to the dimer orientation and (c) corresponding 2D Fourier transform (2D FFT) of selected STM image from Si(100):As 0.1° surface. The image was taken diagonally in order to avoid any display errors. The surface clearly shows A-type majority of dimers on the surface. The circled mark indicates elevations on the surface which extend over some dimers.

Fig. 5.5 (a) shows a large area STM image which was taken diagonally to the dimer orientation to prevent possible display errors that could occur along the dimer orientation. From these scans, we observe that the Si surface exhibits random dark and bright areas (marked with circles in Fig. 5.5 (a)). We assign them to a different local electronic structure which may indicate diffusion of As atoms under the surface [15,122]. For the images with near atomic resolution, 2D Fourier transforms were calculated. The 2D Fourier transform of a real image reflects the periodicity (Fig. 5.5 (c)), i.e. the reciprocal lattice of the surface. One can see a clear (1×2) reconstruction. This shows a good agreement with the surface reconstruction found out from LEED measurement. The imaged dimer series often shows a zigzag structure (Fig. 5.4 (a) and (b) and Fig. 5.5 (b)) and therefore this is indicative of asymmetric dimers present on the Si surface. From this selected STM scan, we observe that most of the dimers are asymmetric (tilted) in which one of the atoms in the dimer is shown in higher position than the other (Fig. 5.4 (c) and (d)). On the other hand, symmetric dimers are also observed.

Since depending on the process route, the formation of dimers on the Si(100) surfaces varies, in addition to the Si(100):As 0.1° surface, we have also studied the atomic structure of Si(100):As 4° surface. Fig. 5.6 (a) and (b) show selected STM scans of a Si(100):As 4° surface. In analogy to the Si 0.1° surface, the Si(100) 4° surface also exhibits zig-zag dimers which are formed along dimer rows. We observe a prevalence of terraces with dimer rows perpendicular to the atomic step edges which are equivalent to a majority of the B-type dimers on the surface. As usual the surface also exhibits a small amount of the minority A-type surface. As compared to the Si(100):As 0.1° surface, the observed dimers are symmetric or asymmetric, with alternating dimer tilt in some positions.

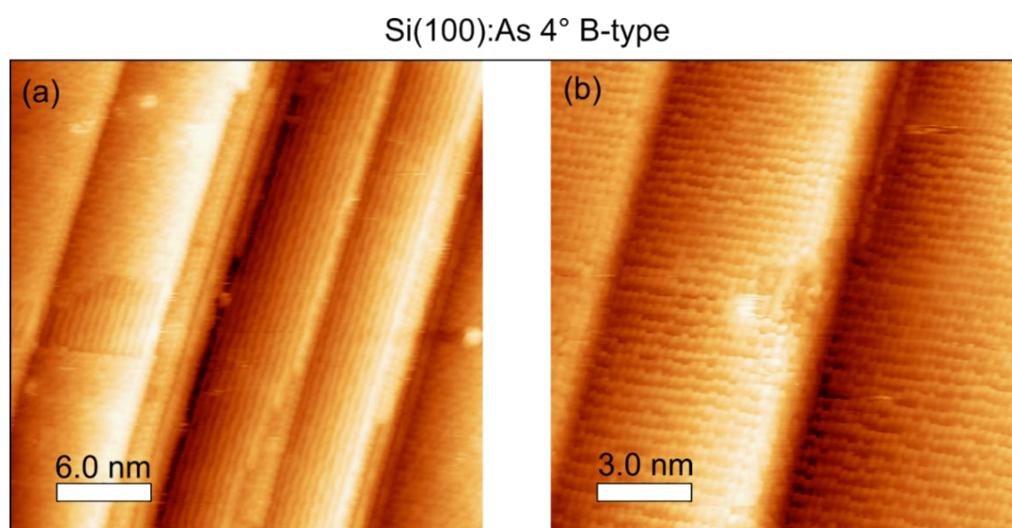

Figure 5.6: Selected STM scans of Si(100):As 4° B-type surfaces, dimer row perpendicular to the step edges (equivalent to majority of parallel B-type surface) (a) and (b). The Si surface shows symmetric dimers and in addition, some dimers alternates indicating asymmetric ones.

In summary, we observed both symmetric and asymmetric dimers on the Si(100):As 0.1° and 4° surfaces. The symmetric dimers could be Si-Si or As-As dimers. However, since the sample was exposed to a large amount of arsenic, and XPS measurements have already shown that the arsenic bonds to the Si, As-As dimers are more probable to be present on the surface. The asymmetric dimers could be either As-Si dimers or As-As dimers with an asymmetric distribution of bonded hydrogen atoms, since it is possible that an arsenic atom could bond to none, one or even two hydrogen atoms [130].

5.2 Low temperature preparation of As-modified Si(100) 2° in III-V reactor

Single domain Si(100) surface preparation with different offcut angles of 0.1°, 2°, 4° and 6° in As-rich ambient has been studied in great detail [15,67]. These studies mostly applied high temperature deoxidation step at 1000°C for around 30 min to remove oxide layer from the Si surface. Due to the high temperature and long time of the annealing, the production cost of a sample becomes high. In addition, high temperature could increase in-diffusion of contaminants from reactor parts into the Si surface, which strongly lowers the minority carrier lifetime. In order to avoid this high temperature deoxidation step, a common approach is to dip the Si sample in HF solution for 1 min prior to loading the sample in the MOCVD reactor. This helps to remove oxide layer by wet chemical pretreatment and thereby allows to run the entire Si surface preparation process at low temperature, around 800°C [97]. Here, we have studied low temperature Si(100) surface preparation in more ‘realistic III-V rich’ reactor condition.

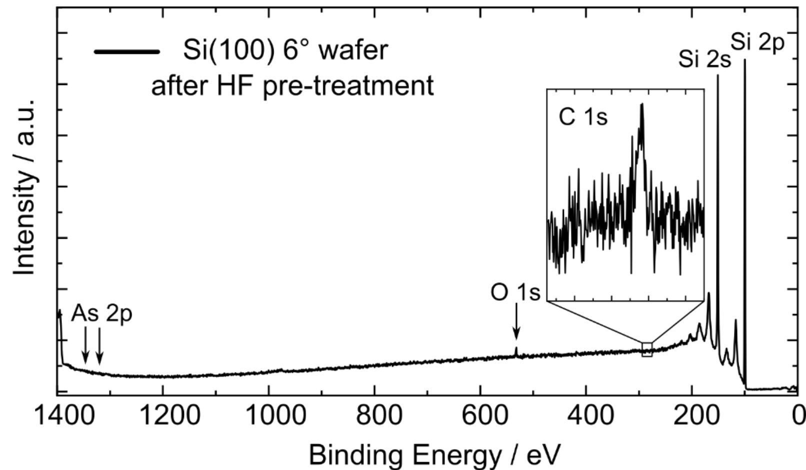

Figure 5.7: XPS survey spectrum of Si(100) 6° wafer after the HF pre-treatment. The wafer was directly loaded into the XPS chamber prior to the processing in MOCVD reactor. The surface clearly shows residuals of carbon (C 1s, shown as large in inset) and oxygen (O 1s) in the surface.

Prior to process the surface preparation in the MOCVD ambient, the wafer after the HF pre-treatment was directly loaded into the XPS chamber in order to observe whether the HF pre-treatment is able to remove the oxygen layer and other contaminants from the surface. Fig. 5.7 shows the XPS survey spectrum of the Si(100) 6° surface after the HF pre-treatment. From the XPS survey spectrum, we observe small traces of oxygen and carbon present in the surface. The results from the XPS clearly confirms that the HF pre-treatment is not

enough to completely remove the native oxide as well as other contaminants from the Si(100) surface and thus additional surface preparation is required in the MOCVD ambient. Warren et al., showed that a Si(100) surface loaded directly in a MOCVD reactor after an HF pre-treatment and in combination with TBAs supply applied at around 740°C-800°C leads to form a double atomic stepped, single domain, (1×2) reconstructed As-modified Si(100) surface [97]. Similar observation was noticed in our study.

Here, a Si(100) 2° wafer after the HF pre-treatment was directly loaded into the MOCVD ambient and the As-modified Si(100) surface was prepared under the TBAs supply. As for a reference, one Si(100) 2° wafer was not processed by the HF pre-treatment and thermally deoxidized at 1000°C. The sample preparation with thermal deoxidation step at 1000°C is considered as high temperature (HT) process and the sample with wet chemical pretreatment in HF, which was annealed at around 810°C is denoted as low temperature (LT) process.

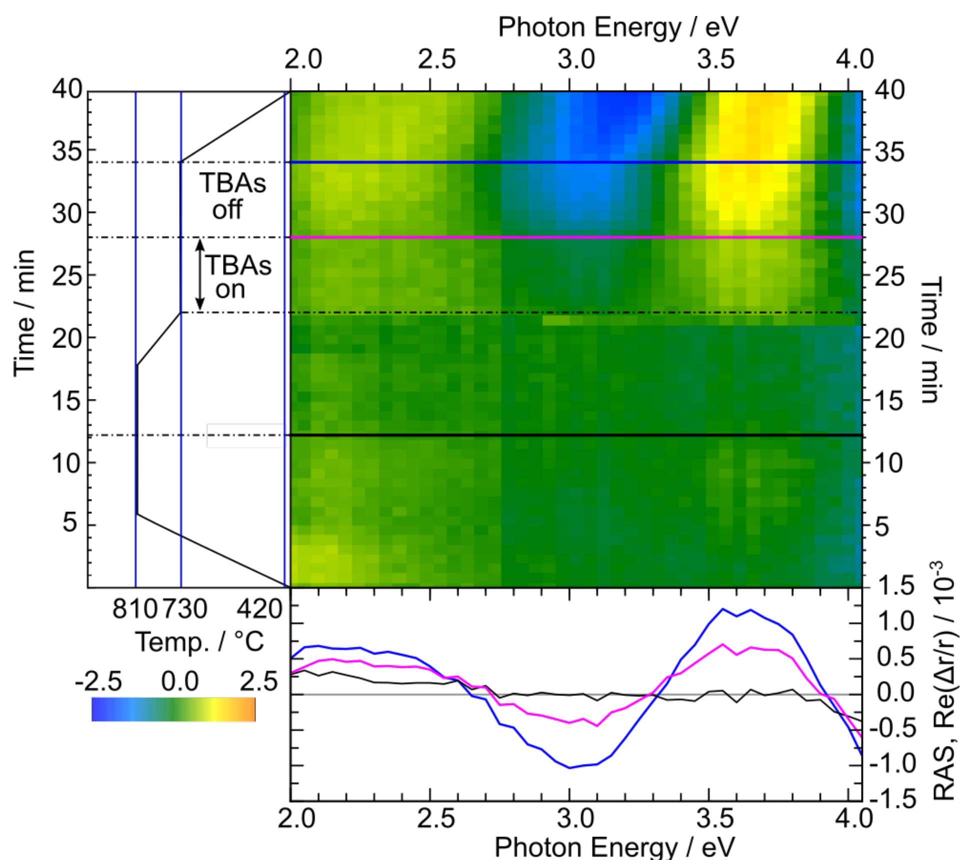

Figure 5.8: Continuous *in situ* RAS measurements in color plot (CP) representation (~45 s per spectrum) during the As-modified Si(100) 2° surface preparation. The graph on the left-hand side indicates the corresponding temperature. The RA spectra below the CP correspond to the colored horizontal lines taken at different steps of the process. The figure is reproduced after *Ref.* [37].

In the LT process, we applied an annealing step without TBAs supply at 810°C for 10 minutes and subsequently the As-modified Si(100) 2° surface was prepared by two-step annealing at 730°C, first with TBAs supply (P_{TBAs} = 1.0 mbar) and then without TBAs supply in H_2 (and unavoidable As_x background pressure from the susceptor and reactor walls). The HF-treated Si(100) 2° surface loaded in the MOCVD reactor does not exhibit any features in the RA spectrum during annealing at around 810°C since the dihydride Si(100) surface has no dimers on the surface. However, the same Si(100) surface exposed under the TBAs supply facilitates formation of dimers and double atomic steps in the surface. Moreover, at the annealing step 810°C, the Si surfaces were etched by the background As_x and H_2 or the arsine (AsH_3) present in the reactor environment which remove possible hydrocarbon residuals from wet chemical etching. In case of the HT-Si(100) 2° sample, the Si surface was deoxidized at 1000°C before the 730°C-TBAs steps and without annealing at 810°C, the surface was directly cooled down to 730°C and prepared with the TBAs supply at this temperature.

Fig. 5.8 shows *in situ* RA measurements in color-coded representation (color plot, CP) during the LT preparation of an As-modified Si(100)2° A-type surface. Temperatures during the preparation are indicated at the left-hand side. Below the CP, selected RA spectra are plotted as indicated by color-coded horizontal lines in the CP. The necessary temperature for the additional annealing was found to be 810°C. At this temperature the Si(100) surface shows no dielectric anisotropy (black line) and in addition, the Si surface (which was H-terminated after HF dipping) is still almost completely covered by hydrogen (95%) [62]. High hydrogen coverage on the Si surface most likely suppresses As adsorption (indirectly supplied from the susceptor and reactor walls). From the CP, we observe that the As-modified Si(100) A-type surface starts forming directly upon TBAs exposure at 730°C. During this step, we observe that the most pronounced change in the RAS amplitude is in the region of the second maximum between 3.4 and 3.9 eV, in comparison to other peaks, as was also observed in *Ref* [15]. The TBAs source was closed when the RAS amplitude was constant (see pink horizontal line in the CP and pink RA spectrum). The reduced intensity of the RA spectrum indicates a certain degree of disorder at the surface. From literature, it is known that exposure of Si(100) to TBAs or to AsH_3 and its sub-hydrides may induce roughening of the surface, which recovers during additional annealing in H_2 (and unavoidable As_x indirectly supplied from the susceptor and reactor walls) [101]. Indeed, the intensity of the TBAs annealed RA spectrum increased almost immediately after switching off the TBAs precursor. The RAS intensity becomes twice as large after annealing without TBAs supply in H_2 and As_x (see the blue horizontal line in the CP and blue RA spectrum) indicating a more ordered atomic surface structure. Furthermore, we did not observe the A-type step formation, either with or without TBAs supply below 700°C or above 800°C. This specific preparation of the As-modified Si(100)2° surface allows to shorten the total process

time by more than a half, and reduce the maximum process temperature from 1000°C to 810°C in comparison to *Ref.* [15].

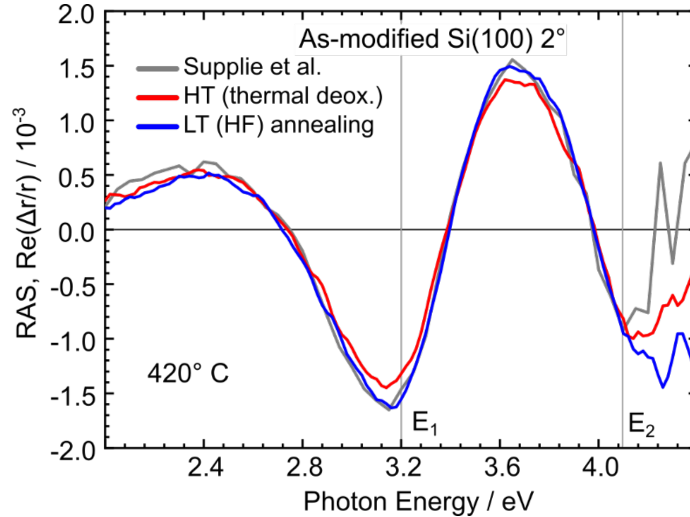

Figure 5.9: RAS of As-modified Si(100) 2° surfaces without (red) and with HF pre-treatment (green) and, as a reference, of As-modified Si(100) 2° surface (grey) taken from *Ref.* [15]. On all surfaces, the predominant dimer orientation is (1 × 2) (see inset for a simplified sketch). Grey vertical lines indicate the interband transition energies of Si at 420 °C [125]. The figure is reproduced after *Ref.* [37].

Fig. 5.9 depicts the characteristic RA spectra from the As-modified Si(100)2° surfaces prepared at HT and LT process conditions. In addition, a reference RA spectrum from the Si(100):As 2° surface is added here, in which the Si(100) surface was first prepared with H-passivation and then exposed to TBAs. We observe that all three RA spectra exhibit a comparable amplitude and identical line shapes. In particular, we observe a broad maximum between 2.0 eV and 2.8 eV, a high intensity minimum at ~3.2 eV (near the E_1 critical point energy of Si), a maximum at ~3.7 eV and a minimum at ~ 4.2 eV. These characteristic peaks were previously benchmarked to As-modified, A-type, (1×2) reconstructed Si(100) with dimers aligned in rows in parallel to the step edges [15,97,124] and therefore we conclude that the surfaces are predominantly (1×2) reconstructed. Moreover, processing can be strongly simplified and shortened by applying the LT process without significant differences in the anisotropic response of the surface: The identical line shape indicates that the microscopic, atomic order at the terraces of both the HT and LT processing is comparable to that on the reference surface from *Ref.* [15].

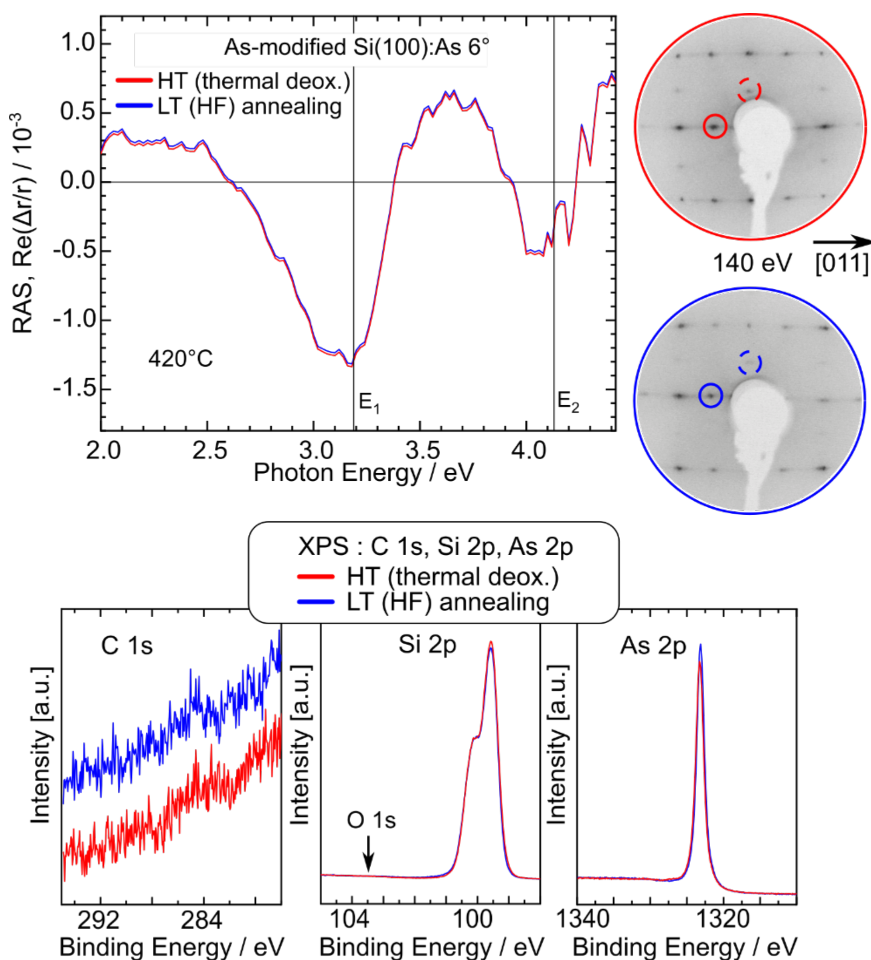

Figure 5.10: *In situ* characteristic RAS of As-modified Si(100) 6° surfaces with and without HF pre-treatment and corresponding LEED patterns. The line shape of both of the RA spectra are very identical and both of the surfaces exhibit a prevalence of (1×2) surface reconstruction. XPS shows no traces of carbon and oxygen in both of the surfaces.

Similar to the Si(100) 2° surface, the HF pre-treatment was also studied on the Si(100) 6° offcut surfaces. The surface preparation by the LT procedure was nearly identical as 2°, however, the maximum process temperature was 830°C. We observe that the line shape as well as the amplitude of the RA spectra of both of the Si(100) 6° surfaces is identical prepared by HT and LT processes (see Fig. 5.10). Moreover, the line shape is very comparable to the one observed from the As-modified Si(100) 2° surface (see Fig. 5.9) which further confirms double stepped, A-type majority domain in these surfaces. The LEED patterns of these Si(100) surfaces shown in Fig. 5.10 show a prevalence of (1×2) surface reconstruction. In addition, the XPS measurement shows no traces of oxygen and carbon in both of these surfaces prepared by both HT and LT processes (see Fig. 5.10). The P.E line of Si 2p bonded with oxygen should show an additional contribution at around 103.5 eV

which is not observed here (see the arrow in Si 2p XPS peak). The XPS measurement also shows that the Si surface after HF pre-treatment exhibits residual oxygen (Fig. 5.7) but after an additional TBAs treatment in MOCVD, the same Si surface does not exhibit oxygen in the surface. From the overall study, we observe no significant difference in RAS, LEED and XPS measurement of the Si(100) samples prepared by HT and LT processes which indeed indicates that the LT process can be applied to prepare the double layer stepped Si(100) surface involving As in the surface. Moreover, the low thermal budget and short process time advances the feasibility of direct growth of III-Vs on Si for industrial applications.

5.3 Summary of this chapter

In summary, we have studied the Si(100) surfaces of different substrate offcut in As-rich MOCVD reactor ambience *in situ* by RAS. In dependence on the type of As source either TBAs or background As_4 and on process route, we are able to control the dimer orientation of either majority A-type or B-type domain on the Si surfaces. We have showed that the prevalence of the majority domain is strongly dependent on the substrate offcut and requires a different, fine-tuned process route. We have seen that for low offcut Si(100) surface (~0.1°), the surface prepared in background As_4 and cooling in low H_2 pressure (50 mbar) leads to an energetically driven, majority of A-type, (1×2) reconstructed surface. In contrast, for the surface with high offcut (~4°), the well-ordered, kinetically driven, A-type, (1×2) reconstructed surfaces can be prepared in a controlled manner at around 830°C while TBAs is applied directly from the precursor. The majority of B-type domain on the Si(100):As 4° surface can be prepared with background As_4 and cooling with high H_2 pressure (950 mbar) whereas exposure of the Si(100):As 0.1° surface to TBAs at 770°C results in majority of B-type surface. The B-type surface leads to prevalence of (2×1) surface reconstruction as confirmed by LEED. The analysis by XPS and the quantified component ratio between the bulk and the close to the surface region confirm that the As is present on the Si(100) surfaces. From the STM scans, we confirm that the As-modified Si(100) surfaces do not entirely consist of symmetric dimers but exhibit as well as zig-zag dimers. We suggest that the symmetric dimers could be Si-Si or As-As dimers and the asymmetric dimers could be As-Si dimers or As-As dimers with an asymmetric distribution of bonded hydrogen atoms. Furthermore, we show a process route in which the time and the maximum temperature of the preparation of Si(100) surfaces with double-layer steps is significantly reduced. The preparation consists of a HF pre-treatment coupled with annealing in TBAs. These surfaces also exhibit double atomic steps, similar to the surfaces prepared after thermal deoxidation at a high temperature and are suitable for the subsequent III-V growth.

6 Crystalline defects in GaP buffer layers grown on Si(100) substrate

In this subchapter we investigate the crystal defects in GaP(100) buffer layers grown on Si(100):As 2° surfaces. Initially, we study the influence of the precursor pulses in the nucleation step in dependence of their injection time and the Si(100) substrate offcut on a formation of crystalline defects in the GaP buffer layers. Further, we study impact of Al introduced during the GaP nucleation on the density of crystal defects in subsequently grown GaP(100) buffer layer and its impact on GaP(100) surface morphology. The *in-system* analysis of the chemical composition of the nucleation layers is performed by XPS, the crystal defects are investigated by ECCI and the surface morphology of the GaP layers is measured by AFM. We will show that precisely fine-tuned nucleation procedure can significantly lower the density of defects in the GaP(100) buffer layers. Parts of this results were published in *Ref.* [131] (M. Nandy et al., ACS Cryst. Growth Des. 21 (2021) 5603).

6.1 Crystalline defects in GaP buffer layers grown on H-terminated Si(100) surfaces

The formation of crystal defects in a III-V layer depends on various parameters during an epitaxial growth. In III/V-Si heteroepitaxy, first challenge is to prepare a well-ordered, double atomic stepped Si(100) surface in order to avoid APDs, as already discussed in chapter 5. Most of III/V semiconductors have a different lattice parameter than Si, and thus, hetero-epitaxial growth leads to a plastic deformation via generation of MD and TD. The difference in bond polarity and thermal expansion coefficient of both hetero-materials also cause defect formation in the epitaxial buffer layer. Therefore, a successful monolithic III/V device integration on Si is only possible if the active device has a sufficiently low defect density. The main challenge in the heteroepitaxy of III/V materials on Si is to control the nucleation layer on Si(100) surfaces to achieve a two-dimensional growth. Island formation at an early stage during epitaxial growth on Si substrates leads to the formation of defects like SFs [52,53]. Thus, a smooth GaP/Si heterointerface, which is free of three-dimensional islands, appears highly beneficial. Prior to the application of Al in the nucleation layer (NL), established GaP pulse nucleation (10 alternating pulse pairs of Ga and P) followed by a GaP buffer layer was grown on H-terminated surface [52,104,111]. In this section, we focus on the formation of defects in the GaP(100) buffer layers grown on the H-terminated Si(100)

surfaces. In addition, quantitative analysis of structural defects and the morphology of the GaP(100) buffer layers have been studied.

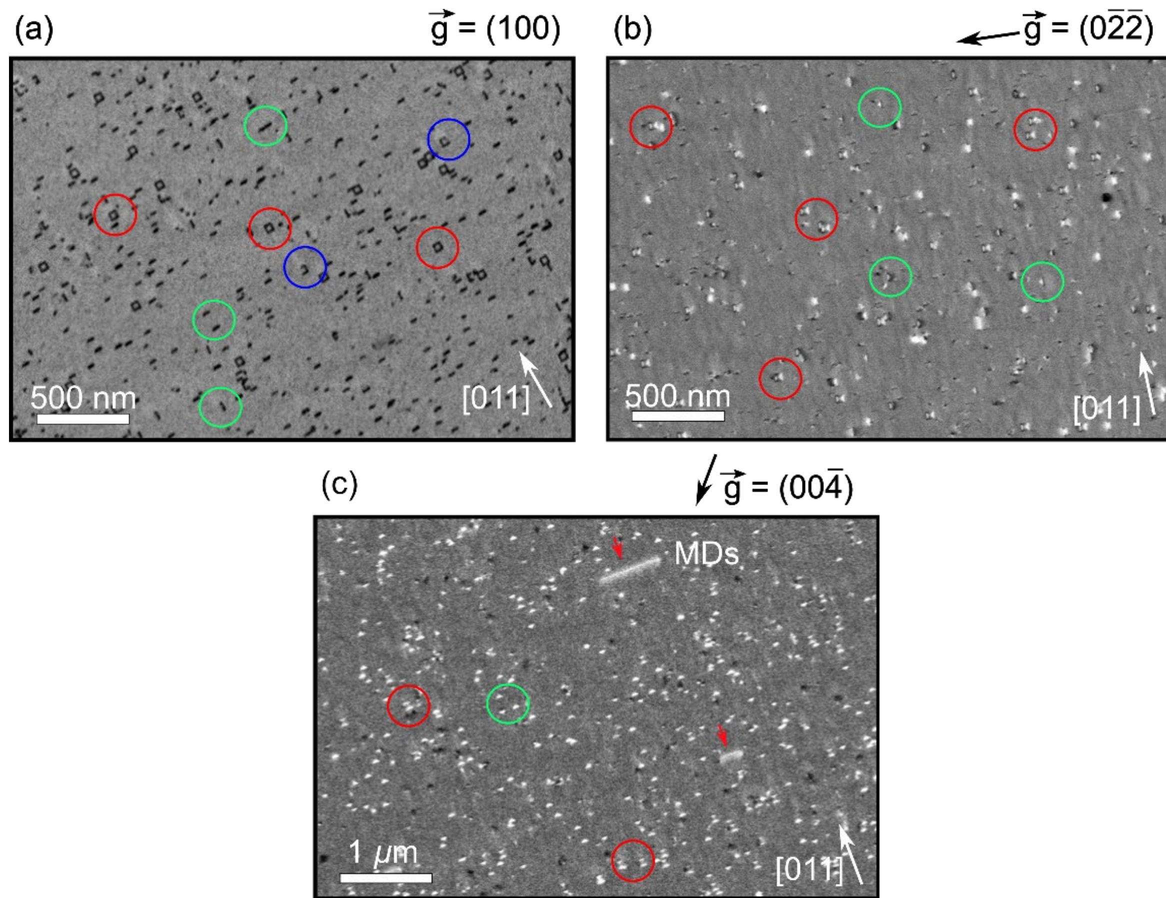

Figure 6.1: ECCI micrographs of 60 nm thick GaP/Si(100):H 2° grown on GaP NL (without pause between precursor pulse pairs) under different channeling condition (a) $\vec{g}$ = (100), (b) $\vec{g}$ = (0$\bar{2}\bar{2}$) and (c) $\vec{g}$ = (00$\bar{4}$) (the direction of the g vector is marked with the black arrow on top). The arrow at the right bottom indicates the offcut direction [011] of the Si(100) substrate. SFPs, SFs and incomplete SFs are indicated by red, green and blue circles, respectively. Red arrow in (c) indicates MDs present in the buffer layer. [4]

60 nm thick GaP(100) buffer layer was grown with the established GaP NL as identical shown in *Ref.* [104]. Fig. 6.1 (a), (b) and (c) depicts ECCI scans of the GaP(100) buffer layer grown on a Si(100)2° H-terminated surface, in an As-free reactor measured at three different channeling conditions. In the first scan (a), the channeling condition was selected as $\vec{g}$ =

[4] ECCI measurement has been developed during this work and all the ECCI scans are performed in TU Ilmenau.

(100) and therefore, the defects such as SFs, SFPs and TDs can be resolved. Here, we observe SFPs visible as squares (four closed boundaries, indicated by red circles). In addition, the GaP buffer layer exhibits SFPs with a missing edge, partially formed in the layer (indicated by blue circle). These type of defects were identified as incomplete SFPs [55,132]. In addition, we observe a high density of dark short lines which correspond to SFs (indicated by green circles). By rotating and tilting the sample, the channeling condition $\vec{g}$ = $(0\overline{2}\overline{2})$ was selected and the corresponding ECCI scan was taken as shown in Fig. 6.1 (b). In this ECCI scan, the SFs appear as a single triangle and the SFPs appear as a pair of triangles forming a 'bow tie'-like shape. This is because the visibility of the defect features only depends on the invisibility criteria of the diffraction condition. Under this channeling condition $\vec{g}$ = $(0\overline{2}\overline{2})$, only one pair of the SFPs fulfils the invisibility criteria and therefore they are visible. Another pair of the SFP remains invisible, which in particular does not fulfill the rule of invisibility criteria. The invisible part of the pairs can be observed under the channeling $\vec{g}$ = $(00\overline{4})$, as shown in Fig. 6.1 (c), in which the visible side of the pairs observed in Fig. 1 (b) is now invisible. All of the SFs and the SFPs observed in this channeling condition are lying along the substrate offcut [011] direction. This might indicate their formation from the heterointerface could be related to the terraces on the Si(100) substrate. From the quantitative analysis, the densities of SFs and SFPs are calculated to 2×10^{11} cm^{-2}. The SFPs originate from the (100) heterointerface and propagate through {111} plane intercepting the (100) plane at an angle of 54.74°, therefore, their lateral dimension or the depth can be correlated with the layer thickness [56]. In order to calculate the depth of the SFP, we measured the length of the side of SFPs in the (100) surface plane and then calculated the lateral dimension of the pyramid in order to compare the thickness of the buffer. The calculation was made only on the SFPs which are distinct and fully formed on the surface. An incomplete SFP usually provides relatively smaller length in the (100) surface and therefore the calculated lateral dimension cannot be correlated with the thickness of the buffer layer. The depth of the SFP was calculated to around 53 nm considering the SFPs observed under the channeling condition $\vec{g}$ = (100). This confirms that the SFPs originate from very close to the heterointerface. In order to compare the depth of the SFP from other channeling conditions, the depth was calculated from ECCI sans taken under $\vec{g}$ = $(0\overline{2}\overline{2})$ and $\vec{g}$ = $(00\overline{4})$, in which the calculated depth is 54.65 nm and 52.38 nm respectively. The estimated depth of SFPs in this GaP(100) buffer layer, calculated from three different channeling conditions is in average 53.34 nm. For this estimation, three different scan areas from each channeling condition were considered. In addition to SFs and SFPs, MDs are present but compared to the density of SFs and SFPs, their density is significantly lower.

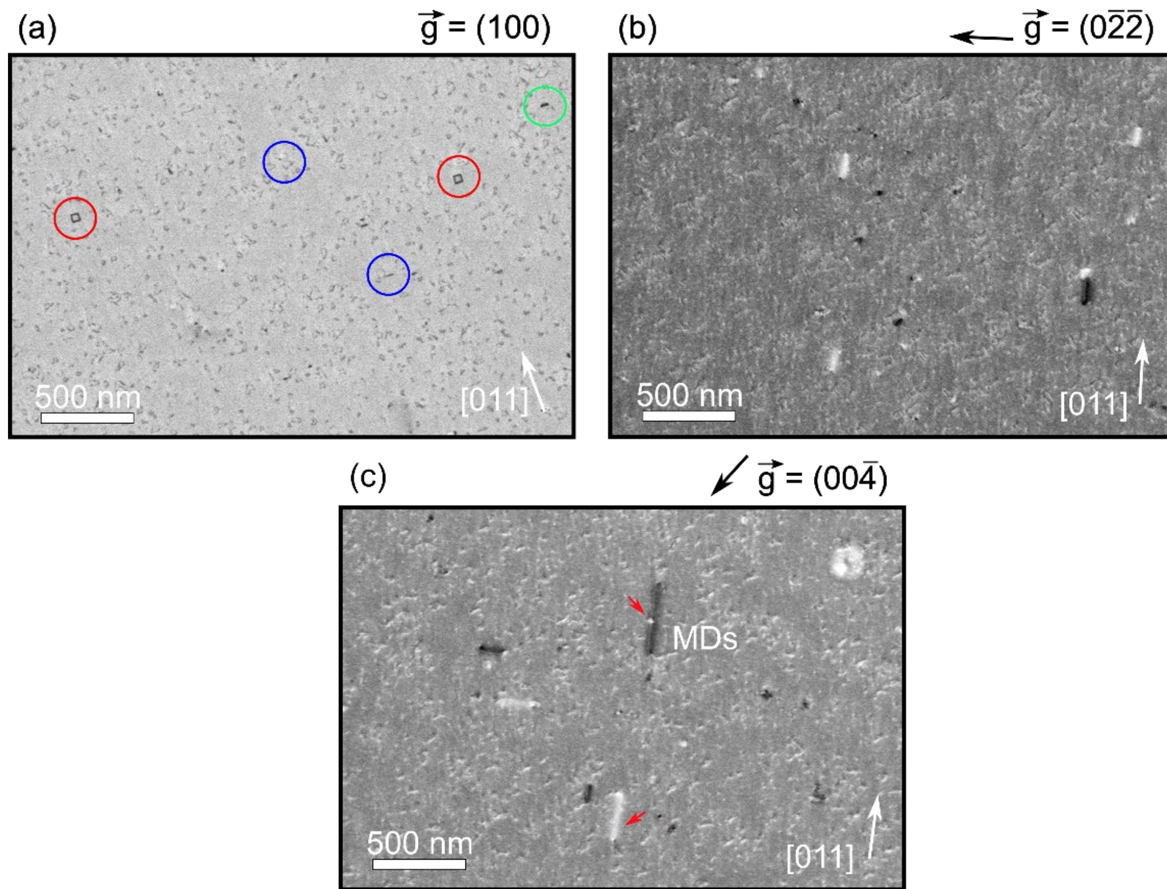

Figure 6.2: ECCI micrographs of 60 nm thick GaP/Si(100) 2° grown on GaP NL (with pause between pulse pairs) under different channeling condition (a) $\vec{g}$ = (100), (b) $\vec{g}$ = (0$\overline{2}\overline{2}$) and (c) $\vec{g}$ = (00$\overline{4}$) (the direction of the g vector is marked with the black arrow on top).

In order to understand the influence of precursor pulses (1 sec. for each of the pulses) on the formation of defects in the GaP layers, the GaP layer was separately nucleated including 1 sec. pause between the TBP and TEGa pulses. The number of pulse pair (PP) was kept constant same as the GaP layers shown in Fig. 6.1. Fig. 6.2 (a), (b) and (c) illustrate selected ECCI micrographs of crystal defects in 60 nm thick GaP buffer layers prepared on the Si(100):H 2° surface. These ECCI images were taken under the same channeling conditions as shown in Fig. 6.1. Under the channeling condition $\vec{g}$ = (100) in Fig. 6.2 (a), the GaP buffer layer exhibits SFPs which appear as squares (red circles), as observed in the GaP layer grown on the nucleation layer (NL) without 1 sec. pause between the pulses (Fig. 6.1 (a)). In addition, SFs are visible on the surface under this channeling, but they are not visible in the selected scan shown here. Moreover, we observe incomplete SFPs (same as in Fig. 6.1 (a)) on the surface. The layer exhibits some features which have irregular shape and distributed randomly on the surface. These features can be the incomplete SFs or SFPs, present in the GaP(100) buffer layer. Compared to the SFs or SFPs observed in the layer, these features

seem to be smaller and visible only under the channeling condition $\vec{g}$ = (100). Moreover, they were not observed in the GaP(100) buffer layer grown on the GaP NL without 1 sec. pause between pulses as shown in Fig 6.1. Under the channeling conditions $\vec{g}$ = $(0\overline{2}\overline{2})$ and $\vec{g}$ = $(00\overline{4})$, we observe very different defect features compared to the GaP(100) buffer layer, shown in Fig. 6.1. Here, we observe very short MDs, which appear as bright or/and dark lines in the image. The contrast of the MDs depends on both the Burgers vectors and the crystallographic line direction of the misfit segment. The MDs observed under the channeling $\vec{g}$ = $(0\overline{2}\overline{2})$, are oriented towards [011] direction. In contrast, the MDs observed under the $\vec{g}$ = $(00\overline{4})$ are visible in both [011] and $[01\overline{1}]$ directions, parallel and perpendicular to the Si(100) step edges, and exhibit both dark and bright contrast. This is because the invisibility criteria yield non-zero values for all possible Burgers vectors and line directions of the MDs under this channeling condition. At the ends of each MD, TDs are observed, which appear as dark or bright points (not clearly visible here). The calculated density of SFs and SFPs in this buffer layer is 2×10^8 cm^{-2} which is three unit of magnitude lower than the buffer layer grown on the GaP NL without 1 sec. pause between the pulses (shown in Fig. 6.1). The depth of SFPs is estimated to around 55.14 nm, 56.56 nm and 56.02 nm for three different channeling conditions, in average, 55.90 nm, which confirms that they form very close to the GaP/Si(100) heterointerface. The calculated depth of SFPs is comparable to the depth of the SFPs calculated for the GaP buffer layer grown on GaP NL without pause between the pulses. The application of the precursor pulses with and without 1 sec. pause between the pulses thus has an impact on the density of the defects, in particular the formation of SFs and SFPs in the GaP(100) buffer layer.

The surface morphology of the GaP(100) buffer layers described above (shown in Fig. 6.1 and 6.2) was also studied by AFM and selected, representative scans are shown in Fig. 6.3. Both of the GaP surfaces show pits on the surface: The GaP layer nucleated with the pulse pairs without 1 sec. pause exhibits comparatively high density of pits on the surface (Fig. 6.3 (a), (10×10) μm^2 area scan) compared to the GaP surface nucleated with the pulses with 1 sec. pause between them (Fig. 6.3 (c), (10×10) μm^2 area scan). In addition, selected scans of (2×2) μm^2 (see Fig. 6.3 (b)) of the GaP layer shows large pits of around 10 nm height. These types of large pits are not observed in the (2×2) μm^2 scan of the GaP layer shown in Fig. 6.3 (d). However, the RMS surface roughness of the GaP buffer layer grown on the GaP NL with and without 1s pause in between the precursor pulses is almost comparable as 0.60 nm and 0.68 nm, respectively.

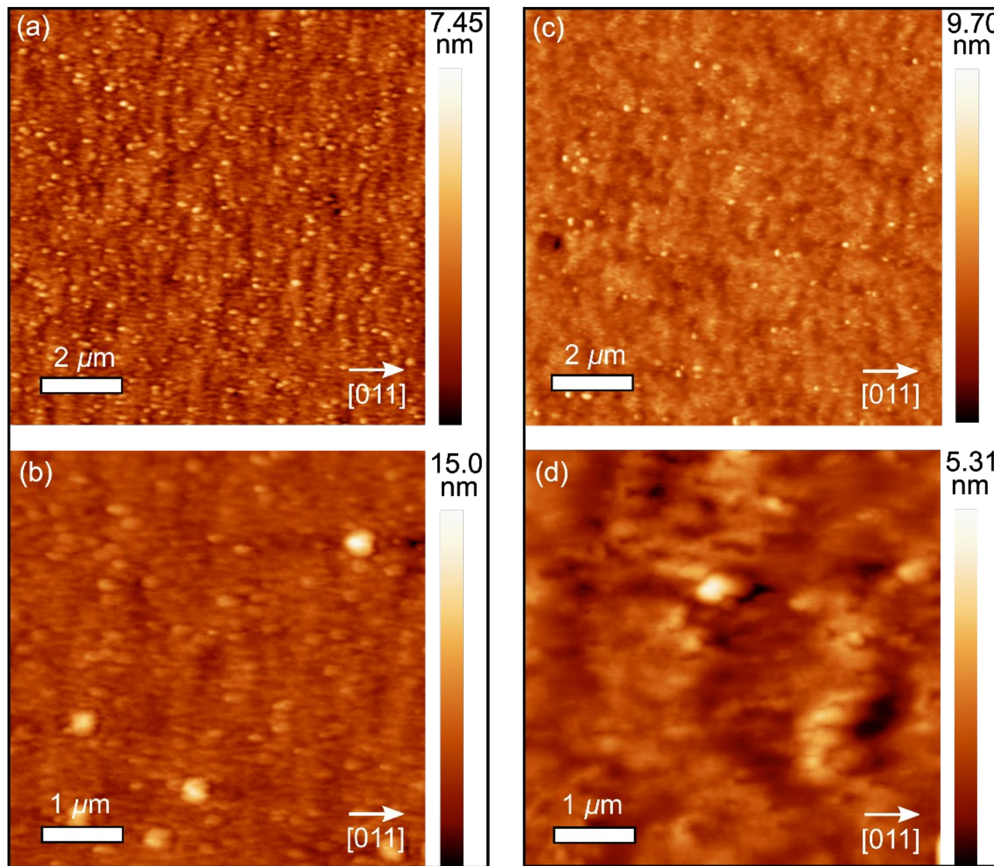

Figure 6.3: Selected AFM scans of (10×10) μm^2 and (2×2) μm^2 area of the 60 nm thick GaP buffer layers grown on GaP NLs (a) and (b) without 1 sec. pause; and (c) and (d) with 1 sec. pause between TBP and TEGa precursor pulses, respectively.

6.2 Crystalline defects in GaP buffer layers grown on As-modified Si(100) surfaces

In the previous section, we focused on the influence of precursor pulses with and without 1 sec. pause between the pulses on the formation of defects in the GaP buffer layers grown on H-terminated Si(100) substrates. Here, we investigate crystal defects in subsequently grown GaP(100) buffer layers grown on As-modified Si(100) surfaces in dependence on the Si substrate offcut angle. The detailed study on the Si(100)2° surface will be discussed in **subsection 6.4** in comparison with the Al induced GaP nucleation on Si(100):As 2° surface. Here we focus on the 0.1° and 4° offcut of the Si surfaces.

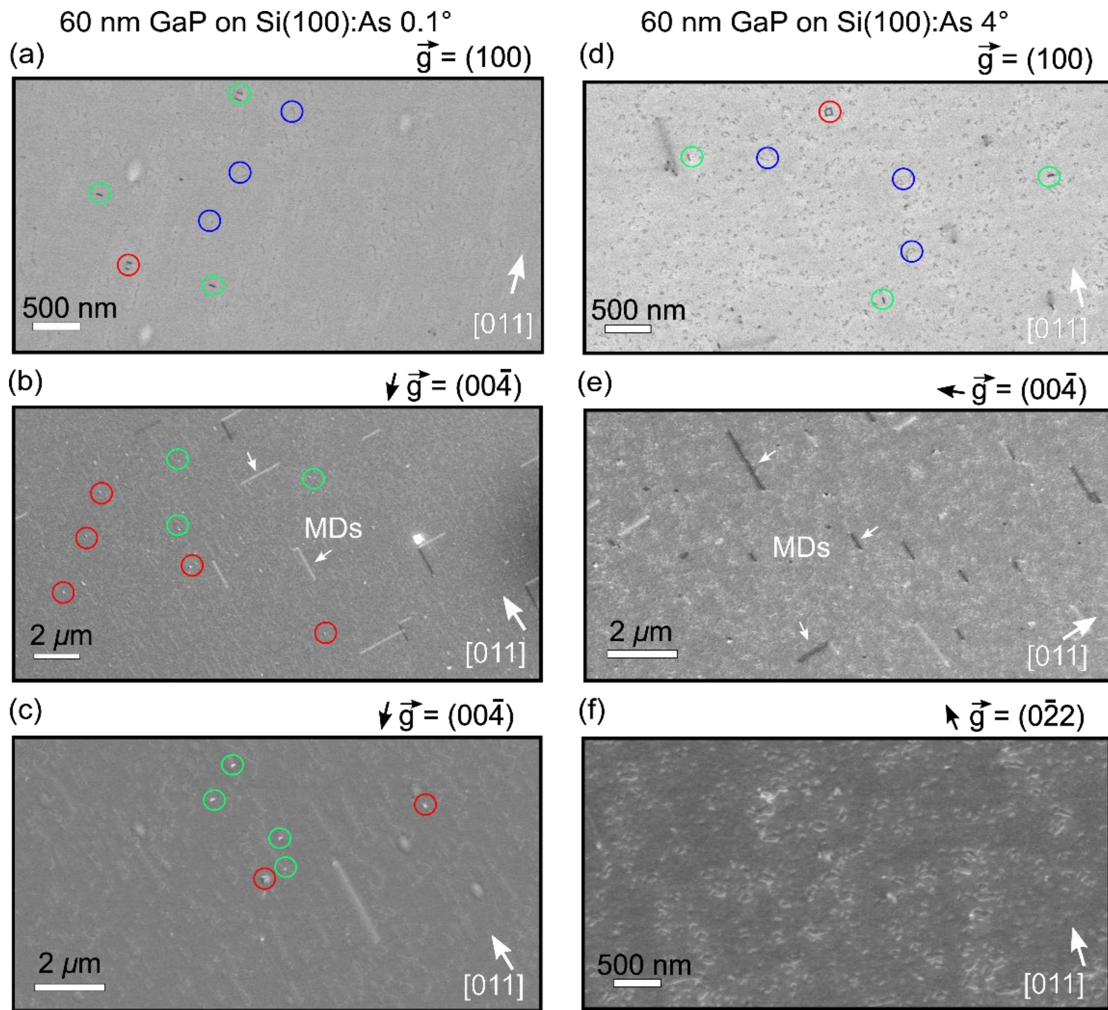

Figure 6.4: ECCI micrographs of 60 nm thick GaP buffer layers grown on (a-c) Si(100) 0.1° and (d-f) Si(100) 4° substrates. (c) and (f) correspond to the scans which were taken at high magnification. The channeling condition and the substrate offcut direction are marked in each of the images.

Fig. 6.4 shows selected ECCI micrographs from 60 nm thick GaP buffer layers grown on Si(100):As substrates with 0.1° ((a), (b), (c)) and 4° ((d), (e), (f)) offcut, under the channeling condition of $\vec{g}$ = (100), $\vec{g}$ = (00$\bar{4}$), and $\vec{g}$ = (0$\bar{2}$2). Under the $\vec{g}$ = (100), we observe both, SFs (green circles) and SFPs (red circles) in both GaP(100) layers ((a) and (d)). In the GaP(100) buffer layer (Fig. 6.4 (d)) grown on the Si(100):As 4° surface, in addition to the SFs and SFPs, the buffer layer exhibits some randomly distributed features (see blue circles) which appear with weak contrast. These types of features were already observed in the GaP layer grown on H-terminated Si surface (Fig. 6.2 (a)) and identified as incomplete SFs or SFPs. The GaP buffer layer grown on the Si(100):As 0.1° surface shown in Fig. 6.4 (a) does not exhibit these features. The ECCI scans of the GaP buffer layers on both Si(100) 0.1° and 4°

surfaces shown in Fig. 6.4 (b) and (e) display MDs propagating along both [011] and [01$\overline{1}$] directions. The GaP buffer layer grown on the Si(100):As 0.1° surface (b) exhibits very short MDs with both, dark and bright contrast. In addition, the buffer shows many white spots. These white spots observed in the GaP layer grown on the Si(100):As 0.1° substrate shown in (b) are the SFs and SFPs shown in magnified ECCI scan in (c). In the GaP buffer layer grown on the Si(100):As 4° surface, the length of the MDs propagating along the [01$\overline{1}$] direction is shorter compared to the length of MDs propagating along the [011] directions. Moreover, from the magnified ECCI scan (f) such features of incomplete SFs or SFPs, similar as in (d), was observed larger. Quantitative estimation shows that the average length of each MD is 1.26 µm and 0.6 µm in the GaP(100) buffer layers grown on the Si(100):As 0.1° and 4° substrate, respectively. However, the GaP buffer layer grown on Si substrate with 4° offcut exhibits higher number of MDs (1.5×10^3 cm^{-1}) compared to the Si substrate with 0.1° offcut (6.3×10^2 cm^{-1}). Thus, the density of TDs is higher, 5×10^7 cm^{-2}, compared to the Si substrate with 0.1° offcut, 1.2×10^7 cm^{-2}. The quantifications were done using an 'ImageJ' software. Quantitative analysis indicates a small reduction of the density of TDs in the GaP buffer layer grown on the Si(100):As 0.1° substrate. In addition, on this substrate we observe a small reduction of the density of SFs and SFPs (2×10^7 cm^{-2}) compared to the density of SFs and SFPs (3×10^7 cm^{-2}) in the GaP(100) buffer layer grown on the Si(100):As 4° substrate. Here, we understood that the substrate offcut angles highly influence the formation of defects in subsequently grown GaP buffer layers though we do not observe a significant difference in the density of overall defects estimated here between these two GaP layers grown on both Si(100):As 0.1° and 4° substrates. In a currently ongoing project, we have collaboration with Philipps university Marburg (PUM) to resolve the defects in atomic scale by TEM and to understand the different origin of these defects.

6.3 GaP/AlP nucleation on Si(100):As

6.3.1 *In situ* control of AlP(100) buffer layer grown on GaP(100) substrate

AlP is a transparent compound semiconductor over a wide part of the visible wavelength having an indirect bandgap of about 2.5 eV. The material has a very small lattice mismatch to GaP of about 0.3% and exhibits same crystal structure of GaP [133]. The AlP/GaP stack layer therefore is almost lattice matched to Si substrate. Thus, AlP can be a good candidate for several optoelectronic device application, in particular for Al based lasers and light emitting diodes. The optical properties and the electronic structure of thin AlP layers (several of atomic layers) in GaP/AlP multiple quantum wells and superlattice have been

theoretically and experimentally investigated [134,135]. Although the GaP/AlP heterostructure is almost lattice matched, its growth and, especially, achieving high quality interfaces are not straightforward. In particular, high crystalline quality of AlP(100) is difficult to prepare and to measure due to its high chemical reactivity with oxygen [44].

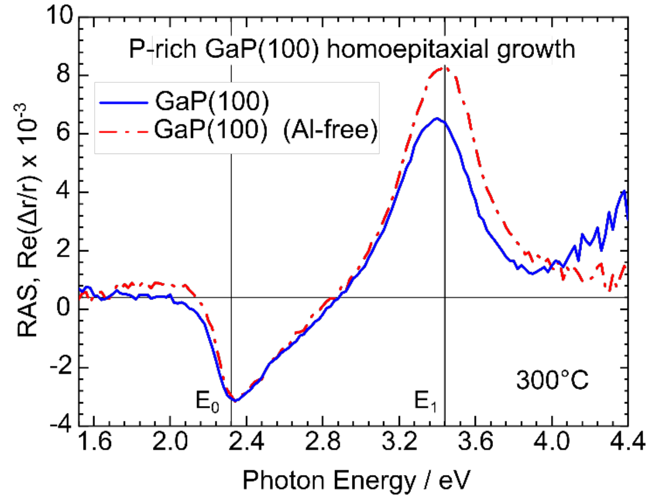

Figure 6.5: Characteristic RA spectrum (blue line) of homoepitaxially grown GaP(100) layers (P-rich) grown on GaP(100) substrate in an Al-containing reactor prior to the growth of AlP(100) buffer layers. The line shape of the RA spectrum (blue line) is identical compared to the RA spectrum from a reference GaP layer (red dotted line) which was grown in Al-free MOCVD reactor.

In our study, we try to understand the AlP(100) surfaces in regard to its anisotropy such as interband transition energy or temperature dependent shift of energetic peak position *in situ* by RAS. RAS enables us to study these surfaces by reflectivity signals during the growth of each of the grown layers. Prior to the growth of AlP layer, a homoepitaxial growth of GaP surface on the GaP(100) substrate under the background of Al in the reactor plays an important role in order to compare the GaP(100) homoepitaxial buffer layer deposited in a reactor without containing Al. Fig. 6.5 shows *in situ* RA spectrum (blue curve) taken at 300°C from the homoepitaxially grown GaP(100) surfaces in Al-containing reactor. The spectrum (blue curve) shows almost similar trajectory in line shape as well as in peak position as compared to the reference GaP RA spectrum (red dashed curve) which was deposited in Al-free reactor. The GaP spectrum here consists of a sharp minimum and a maximum at about 2.32 eV and 3.38 eV respectively. In the *Ref.* [105] it is previously determined that the minimum at 2.32 eV is related to the surface related interband transition which arises due to the surface terminated by oppositely buckled phosphorus dimers on top of GaP surface. The maximum at around 3.38 eV is corresponding to the surface modified bulk transition. The standard procedure to stabilize the GaP surface by cooling down under

TBP precursor at 420°C and an additional annealing at this temperature without the TBP supply led to the formation of P-rich GaP (2×2)/c(4×2) surface. Similar to the reference GaP RA spectrum (red dashed curve), as the nature of the RA spectrum of GaP surface resembles with the reference GaP spectrum, so it would be definitely corresponding to phosphorus rich (P-rich) surface. If the TBP supply is omitted during annealing at above 490°C, a transition to the well-known (2×4) reconstructed Ga-rich configuration of the surface occurred [45].

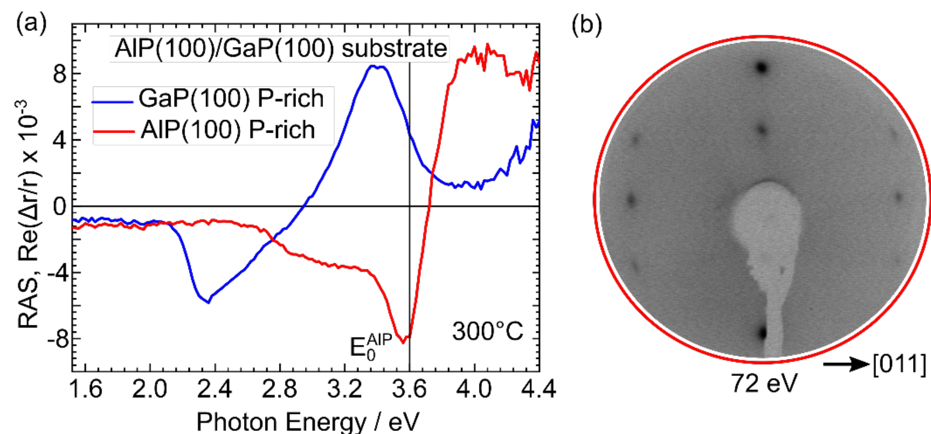

Figure 6.6: (a) Characteristic RA spectrum of AlP(100) P-rich surface shows very intense distinguishable peak at 3.26 eV at 300°C as compared to GaP(100) P -rich surface at the same temperature and (b) LEED patterns of AlP(100) P-rich surfaces at 72eV, which exhibit a single domain, (2×1) reconstructed surface towards [0$\bar{1}$1] direction. The diffraction pattern observed from the AlP surface is very similar to the diffraction pattern from a P-rich GaP surface.

After the growth GaP(100) homoepitaxial buffer layer and cooling down to 300°C, the temperature was ramped up to 600°C for subsequent growth of AlP layers. Fig. 6.6 shows *in situ* RA spectrum taken at 300°C from AlP(100) surface after the standard P-rich preparation same as in the case of GaP(100) surfaces. This surfaces shows a distinguishable RA spectrum (red line), with a different line shape from GaP(100) (blue line), which corresponds to P-rich AlP(100) surface. The RA spectrum from the AlP layer (see Fig. 6.6, red spectrum) consists of a broad minimum in the range between 2.4 eV and 3.4 eV, a pronounced negative peak at slightly below 3.60 eV and a positive peak at around 4.0 eV. The negative peak of the RA spectrum is close to the E_0 interband transition of AlP measured at 300K [136]. The characteristic of the RA spectrum can be due to the phosphorus dimers on the surface as it was cooled down under TBP supply up to 400°C (the temperature below P desorption temperature). In order to benchmark the RA spectrum as well as to conduct a detailed assessment of the observed *in situ* RA spectrum from the P-rich AlP surface, the AlP(100) surface was transferred by contamination free UHV shuttle to the LEED chamber where the surface reconstruction in atomic scale is further analyzed. Fig. 6.6 (b) shows

LEED pattern from the AlP surface corresponding to the sample shown in Fig. 6.6 (red curve). LEED shows strong contrast between the background and the diffraction spots and the P-rich AlP surface exhibits a single domain, (2×1)-like surface reconstruction. The P-rich AlP(100) surface exactly follows the similar surface reconstruction as the GaP(100) substrate [106].

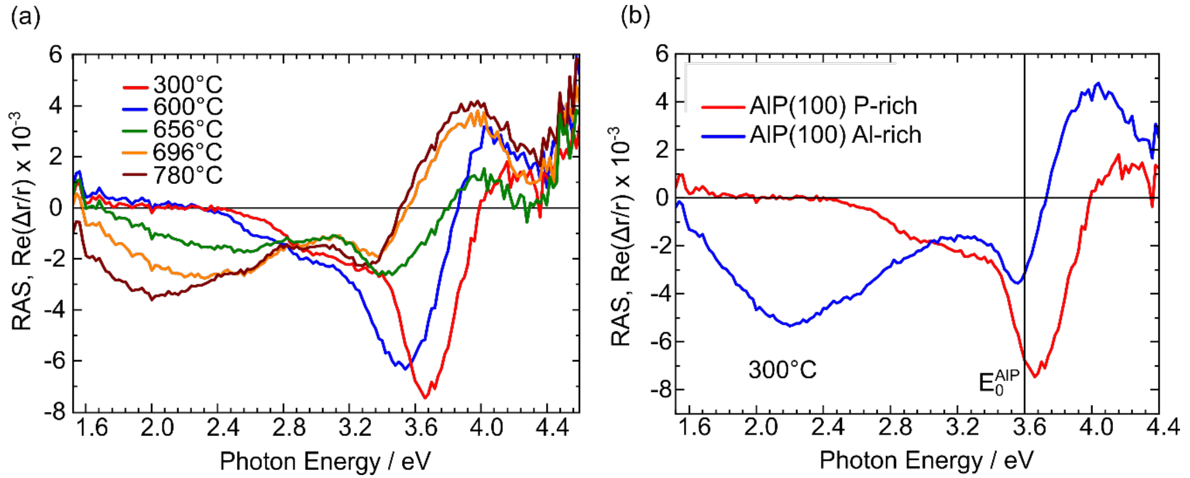

Figure 6.7: (a) Characteristic RA spectra of AlP(100) surface in dependence of temperature in which the temperature start to rise from 300°C up to 800°C, (b) The RA spectra of AlP(100) P-rich surface differs compared to AlP(100) Al-rich surface at 300°C.

In order to observe changes on the surface in dependence on the temperature, the prepared P-rich AlP(100) surface was gradually heated up to 800°C with a rate 2.08°C/min, without TBP precursor supply. During the slow heat up process, *in situ* RA spectra were measured continuously. Fig. 6.7 (a) shows five selected RA spectra at different temperatures with different line shapes. Very slow increase in the temperature during the experiment leads to quasi-equilibrium conditions, while each of the single spectrum was recorded. From Fig. 6.7 (a) we observe an uninterrupted red shift of the minimum with increasing temperature up to 600°C which is most probably related only to the thermal shift of the RA spectra [45]. In addition, a simultaneous broadening of the negative peak at 3.62 eV (which was for P rich AlP surface) is observed which is indeed due to increasing lattice vibrations and electron-phonon interactions, as was already observed and described for GaP(100) and InP(100) [45,137]. Above 636°C (green line) we observe a significant change in the RAS line shape which is due to the phosphorus desorption from the surface at high temperature. At 760°C, this change becomes pronounced and the line shape of this RA spectrum differs from the one taken at 300°C. This RA spectrum could correspond to “Al-rich” surface. An abrupt transition from a “P-rich” to “Al-rich” AlP(100) has been observed at above 620°C. The AlP(100) surface was annealed at 800°C until no further change in the RA signal was

observed and subsequently the sample was cooled down to 300°C to take a reference spectrum. Selected RA spectra prepared as "P-rich" and "Al-rich" AlP(100) surfaces are shown in Fig. 6.7 (b). The line shape of these two spectra differs significantly and serve as a benchmark of two different surface reconstructions.

6.3.2 Al-modified GaP nucleation on Si(100)

The defect free nucleation of III/V epilayer structure on Si(100) substrate is the key for future integration of III/V device structure. It has been showed that a low temperature nucleation of GaP and the application a GaP pulse nucleation consisting of 10 alternating pulses of P and Ga provide an island-free two dimensional growth [52,111]. However, few reports show that excess of Ga on Si surface during the GaP nucleation leads to the formation of metallic Ga clusters or droplets [138,139] on the Si substrate and upon diffusion leads to the formation of cross sectional triangular pits with a SF at the Si-Ga heterointerface. In order to suppress the formation of Ga droplets and a possible GaP islands during nucleation, an alternative route to the commonly applied GaP nucleation process could be supplemented with an additional application of Al. Additions of Al to GaP were found in other heteroepitaxial structures to induce planar growth as a result of the stronger bonding between Al and Si compared to Ga and Si [140,141]. In molecular beam epitaxy (MBE), Maruyama et al. showed a nearly two-dimensional growth mode of AlP on Si(100) growth [142]. Similarly, Santana et al. also observed island suppression upon addition of Al to GaP [143]. A more abrupt and smoother interface between AlGaP and Si was observed by Lin et al., which was explained by the lower surface mobility and diffusion length of Al compared to Ga, which should support a homogeneous surface coverage [144]. In MOCVD, island formation during nucleation on Si(100) was largely suppressed for $Al_xGa_{1-x}P$ with Al contents above 0.2, resulting in planar heteroepitaxial layers [145]. The stronger bonding between Al-Si compared to Ga-Si [140,141] could compensate the tendency of the Ga atoms to form clusters or droplets. Therefore, we try to establish an optimized nucleation route by application of Al in the GaP nucleation on Si(100) surface.

Fig. 6.8 depicts schematically four different precursors sequences over the time: For the standard GaP nucleation (Fig. 6.8 (a)), the nucleation starts with TBP and subsequently 10 alternating PP of TBP and TEGa was offered for 1 sec. each of the sources and 1s break between these pulses. In order to optimize the PP for the GaP/AlP nucleation, preliminary experiments were carried out to tune the number of TMAl pulses. We have applied 2× TMAl & 8× TEGa, 5× TMAl & 5× TEGa, and 10× TMAl pulses, each pulse followed by a TBP pulse (10 TPB pulses in total) prior to the growth of 30 nm thick GaP buffer layers (see Fig. 6.8 (b), (c) and (d)).

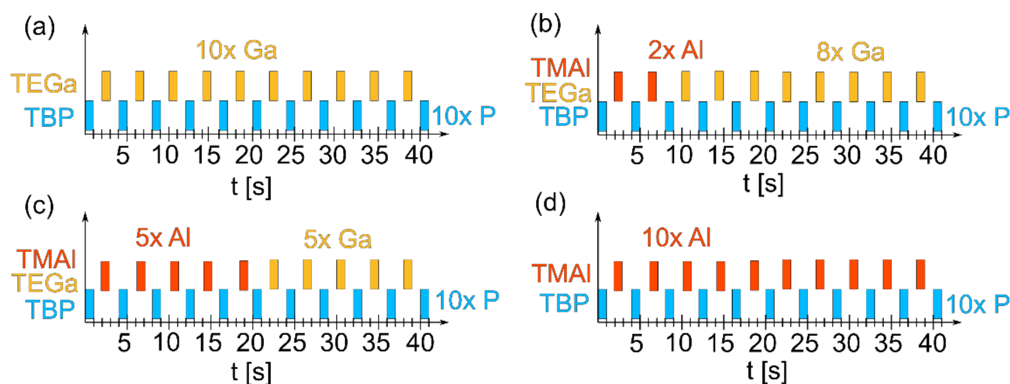

Figure 6.8: Standard GaP nucleation with ten pulse pairs of Ga-P, (b) GaP/AlP nucleation with two pulse pairs of Al-P, (c) GaP/AlP nucleation with five pulse pairs of Al-P, and (d) AlP nucleation prior to the GaP growth on Si substrates.

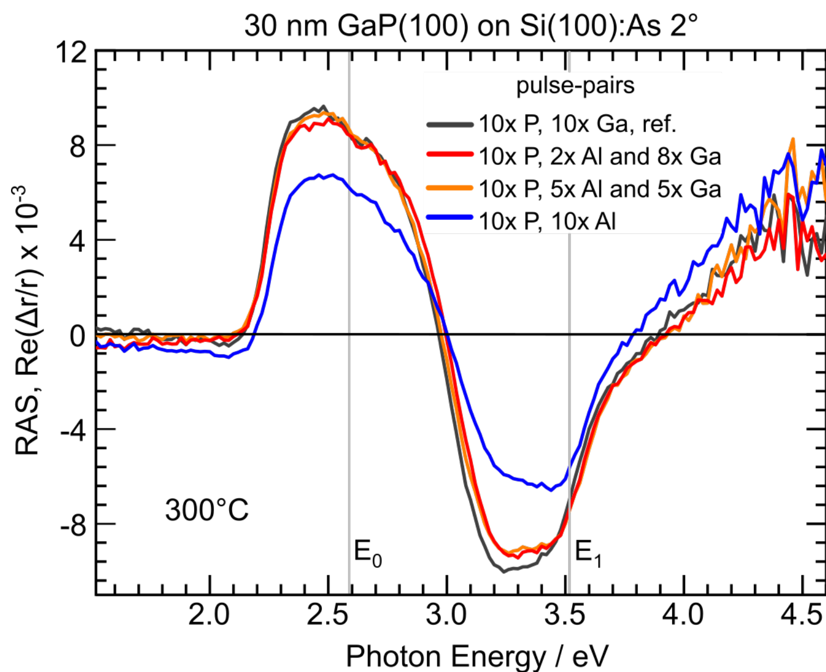

Figure 6.9: Characteristic RA spectra of GaP buffers grown on GaP and GaP/AlP nucleation with variation of precursor pulses during the pulse nucleation.

Fig. 6.9 shows the *in situ* RA spectra measured at 300°C of 30 nm thick GaP buffers grown on Si(100) 2° As modified surface by varying the nucleation sequences. Here, all the GaP buffers are prepared in a Al-containing reactor to observe the influence of nucleation layer in the *in situ* spectrum. The dark grey spectrum is corresponding to the GaP buffer grown on standard GaP nucleation on Si. In contrast, the red and the orange in-situ RA spectra are

from the GaP buffers grown on GaP/AlP nucleation consisting of two pulse pairs and five pulse pairs of Al-P respectively. The change in nucleation layer with additional few Al pulses did not influence the *in situ* RA spectra. These two RA spectra (red and orange) are comparable to the reference GaP spectrum with identical line shape and almost equal amplitude. The blue RA spectrum corresponding to the GaP buffer grown on AlP nucleation exhibits in lower intensity compared to the other GaP buffers, which indicates intense influence of nucleation layer in the in-situ spectrum. The low intensity of RA spectrum for this buffer layer indicates atomic disordering on the surface and a different majority to minority domain ratio on the surface. The surface morphology of these GaP surfaces is further studied by AFM.

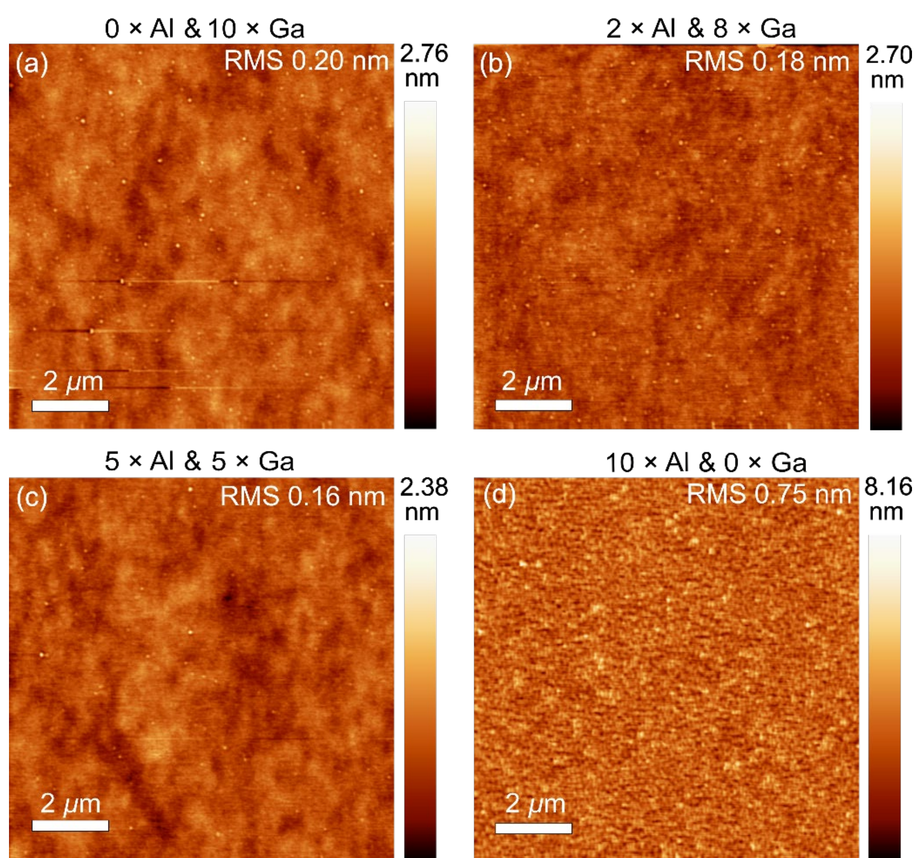

Figure 6.10: AFM scans of GaP buffers on (a) standard GaP nucleation with 10 pulse pairs of Ga-P, (b) GaP/AlP nucleation with 2 pulse pairs of Al-P, (c) GaP/AlP nucleation with 5 pulse pairs of Al-P, and (d) a complete 10 pulses of Al-P (AlP nucleation) on Si substrates, respectively.

Fig. 6.10 depicts the corresponding AFM scans of GaP buffer layers with (a) standard GaP nucleation, and GaP nucleation modified by (b) 2, (c) 5 and (d) 10 PP of Al-P. The GaP

buffers grown either on standard GaP nucleation or on GaP/AlP nucleation exhibit in very similar surface morphology with comparable RMS roughness. However, the GaP buffer grown on AlP nucleation shows very high surface roughness and indicates three-dimensional growth on the surface. This can be correlated by *in situ* RA spectra where the spectrum of GaP buffer grown on AlP nucleation appeared in low intensity (described in Fig. 6.9, blue spectrum). Since, the precursor sequences of 2× TMAl & 8× TEGa and 5× TMAl & 5× TEGa show very comparable surface morphologies of the GaP buffer layer, 5× TMAl & 5× TEGa has been selected as a precursor sequence to continue further investigation in the GaP layer (explained in next section).

6.3.3 Evolution of GaP/AlP nucleation layers on Si(100) heterointerface

The following experiment was carried out to understand the evolution of both GaP and GaP/AlP NLs on the Si(100):As 2° surface. Since, the RA signal provides characteristic, anisotropy signal from a dimerized surface, changes on the Si surface structure during the application of III-V precursor pulses will reflect in the RA signal. The spectral change in the characteristic RA signal upon application of III-V precursors can therefore be used to distinguish rich information between the Si surface and the NLs as well as between these two NLs.

Fig. 6.11 (a) and (b) shows RA spectra taken at 50°C of pure GaP (blue curve) and GaP/AlP (red curve) NLs (10 PP each) before and after heating the samples up to the GaP growth temperature (595 °C) with continuous TBP precursor supply (after annealing), respectively. For GaP/AlP NLs, selected precursor sequence, 5 PP of Al and 5 PP of Ga followed by P for each of the pulses was applied. As a reference, the spectrum of the As-modified Si(100)2° surface prepared prior to the GaP nucleation is shown (light grey dashed line). The spectral line shape, sign and intensity of the Si(100):As RA spectrum confirms a prevalence of the (1×2) domain [15,67,97]. Supplie et al. have discussed that a characteristic RA spectrum of the GaP NL grown on a H-terminated Si(100) surface with the same misorientation (2°) already develops during the very first precursor pulses of TEGa and TBP [104]. We observe that the line shape of both of the RA spectra from the NLs (blue and red curves) are clearly different from each other and clearly different from the Si(100):As 2° surface. In both of the cases (Fig. 6.11 (a) and (b)) the RA spectra of the pure GaP NL is very similar to that one of the GaP nucleation on H-terminated Si(100) surface discussed in *Ref.* [104]. The RA spectra from both the GaP and GaP/AlP NLs before and after annealing

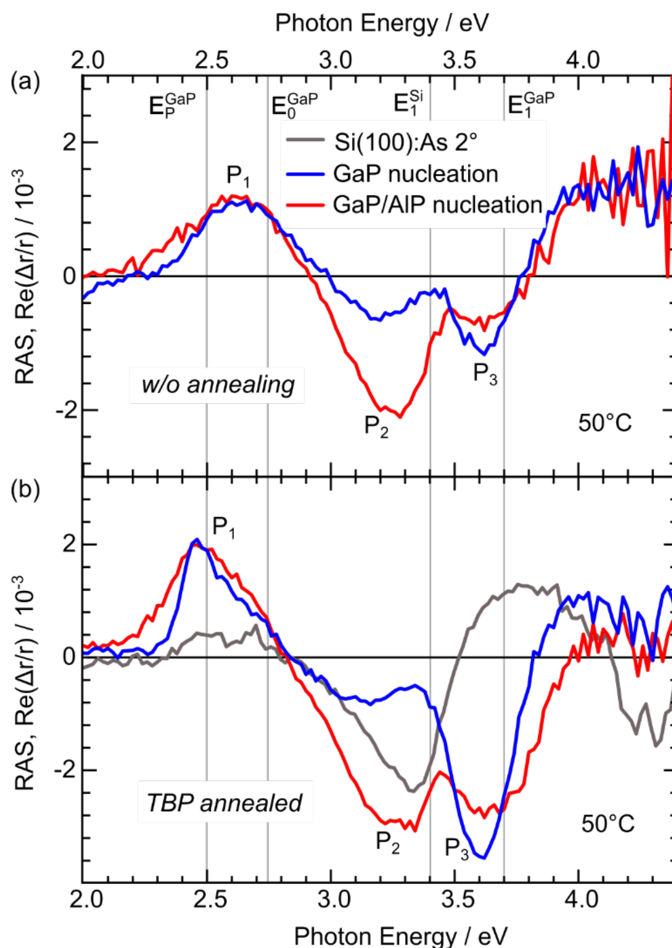

Figure 6.11: RA spectra (taken at 50 °C) of the Si(100)2°:As surface (dashed light grey line) along with pure GaP, and GaP/AlP nucleation surfaces (a) before and (b) after annealing with TBP supply (see experimental, blue and red solid line).

under TBP exhibit a significant difference in intensity at P_2 and P_3 energy position. However, the peak at P_1 before the annealing under TBP exhibits same intensity for both of the NLs. In Fig. 6.11 (b), after the annealing under TBP, the anisotropy of the peaks at P_1, P_2 and P_3 increases and the peak at P_1 is shifted to 2.5 eV for both of the NLs. The increment of the anisotropy after the annealing indicates a well-ordered GaP and GaP/AlP nucleation surfaces. The RA spectra of the GaP/AlP NL agrees better with the RA spectrum of pure GaP nucleated with only five pulse pairs (PP) in *Ref.* [104]. Here, both of the RA spectra in Fig. 6.11 (a) and (b) are flipped in sign, compared to *Ref.* [104], as the GaP sublattice is inverted due to the As reconstruction on the Si surface [15]. The RA spectra from the NLs exhibit maxima at E_P^{GaP}(2.5 eV, P_1), which originate from electronic transitions between surface states related to the P-dimerized, H-passivated GaP(100) surface [104,146] and the conduction band minimum. Indeed, the characteristic LEED pattern discussed in the following part, indicates the presence of P-dimers on the surface. After the annealing, the

RA spectra (Fig. 6.11 (b)) from both nucleation surfaces consist of pronounced shoulder at around 3.2 eV (P_2) and one intense peak in the energetic range of the interband transition of GaP E_1^{GaP} (3.6 eV, P_3 (in both Fig. 6.11 (a) and (b)). The amplitude of those two peaks in the RA spectrum from the GaP/AlP nucleation surface is almost the same, whereas in the spectrum of the pure GaP NL the amplitude of the P_2 peak is significant lower and the amplitude of the P_3 peak is higher. Since the contribution at E_1^{GaP} (P_3) is related to the surface-modified bulk E_1^{GaP} transition [104], and the peak at around 3.2 eV (P_2) is related to the GaP/Si and GaP/AlP/Si heterointerfaces, respectively, the higher intensity of P_3 compared to P_2 of the GaP sample (blue curve) might indicate that the thickness of the GaP NL is higher than the one of GaP/AlP. The more pronounced RAS contribution P_2 originating from the GaP/AlP/Si:As (100) interface (red curve) may also suggest a more defined interface formation of the GaP/AlP nucleation sequence compared to a pure GaP one. Here, it is important to state that the two nucleation procedures reflect the well-known RA spectra and the electronic transitions of the GaP NL as well as of the interface, and that they evidently display differences.

Fig. 6.12 (a) and (b) displays the corresponding LEED pattern of the GaP and GaP/AlP nucleation surface which were prepared after annealing under TBP precursors. Both of the surfaces exhibit a clear (1×2) symmetry with streaks along $[0\bar{1}1]$ direction related to the H-passivated P dimers [104,109] on top of GaP(100). In order to confirm if Al is present in the GaP/AlP NL or on the GaP NLs prepared in an Al-containing reactor, the samples were measured by XPS. Fig. 6.12 (c) and (d) show that both samples are free of any traces of carbon or oxygen (note that the small peak at 532 eV in Fig. (c) corresponds to the satellite contribution from the Ga Auger photoemission (Ga LMM)).

Fig. 6.12 (e) shows a section of the XPS survey spectrum with P 2p, Ga 3p, Si 2p, As 3d, and Al 2p (see the inset) core level peaks of these two samples. XPS measurements on the GaP/AlP NL confirm that only five pulses from the TMAl precursor are sufficient to deposit a significant amount of Al on the Si(100) surface. The integrated peak area of Al 2p and As 3d were corrected by photoelectron ionization cross sections taken from Yeh and Lindau [129] (0.0072 and 0.025, respectively) and transmission functions were derived from the spectrometer. The ratio of As to Al is 1.44 to 1. We exclude that an excess of As is present on the GaP/AlP surface based on the characteristic RA spectrum and the LEED pattern correlated to P-dimers on the GaP/AlP surface. The As content at the heterointerface is rather beyond a single monolayer [147,148] and As residuals can diffuse into the surrounding heterointerfacial environment as there might be a significant background partial pressure of As residuals in the MOCVD reactor ambience originating from the Si:As preparation procedure before the nucleation [148]. Considering that, the small difference in the peak

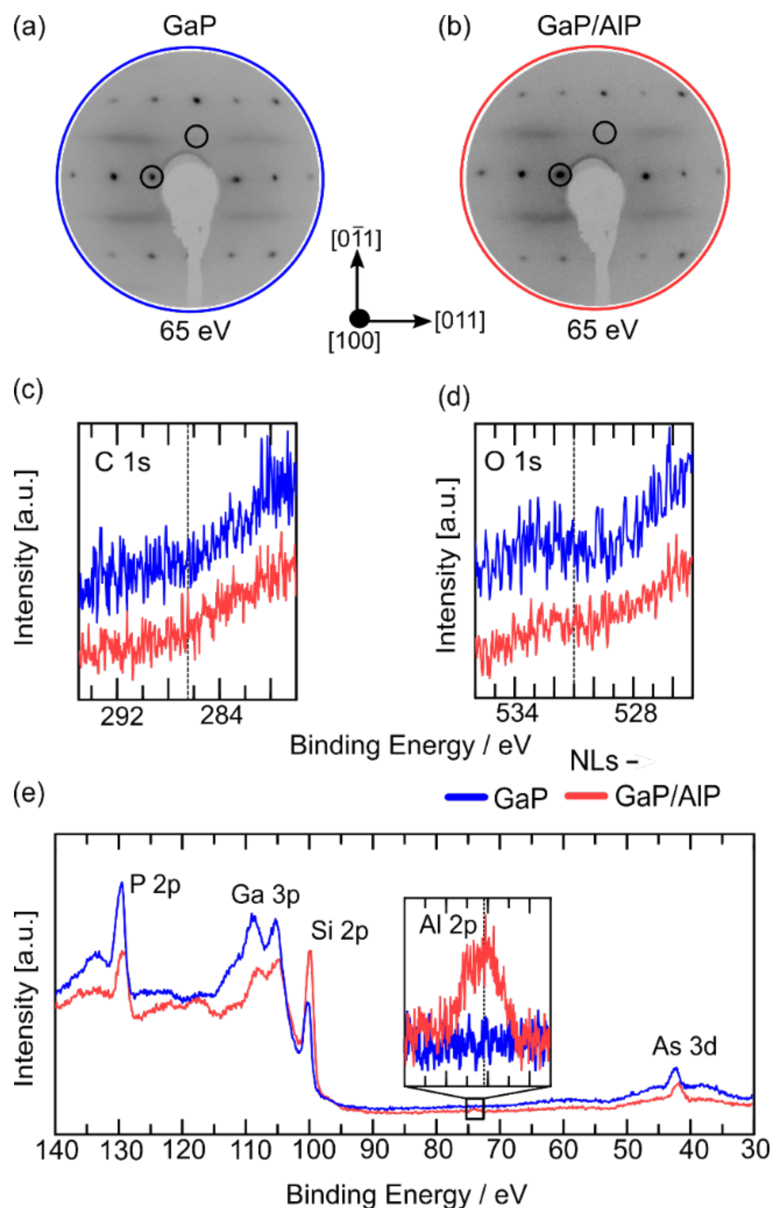

Figure 6.12: (a) and (b) LEED pattern of the GaP and GaP/AlP NL grown on the Si(100):As 2° surface and XPS spectra from the GaP buffer layers grown on GaP (green spectrum) and on GaP/AlP NLs (black spectrum) in the range of (c) C 1s, (d) O 1s and (e) P 2p, Ga 3p, Si 2p, Al 2p, and As 3d photoemission lines. The figures are redrawn after *Ref.* [123].

areas between the As 3d and Al 2p core level peaks indicates that the amount of Al in the NL is close to the amount of As. We did not observe any traces of Al on the pure GaP NL (within the detection limit of XPS). However, the photoionization cross-section needs to be considered, as the Al 2p core level exhibits a 3.5 times weaker contribution to the photoemission spectra compared to As 3d, which makes its identification more challenging. For the GaP/AlP NL, the area ratio of P 2p and Ga 3p to Si 2p core levels (1.0 in each ratio)

is smaller than the ratio of the same peaks from the pure GaP nucleation (3.0 and 2.2 respectively), and the ratio of As 3d to Si 2p is higher compared to the ratio of As to Si from the pure GaP nucleation, which in summary suggests that the GaP/AlP NL is thinner than the pure GaP NL. Nevertheless, both RAS and LEED of the GaP/AlP NL indicate that the Si substrate is completely covered, and XPS confirms the presence of Al.

6.4 Crystal defects in the GaP buffer layers grown on GaP/AlP nucleation on Si(100):As 2° surface

Fig. 6.13 depicts selected ECCI micrographs of 60 nm thick GaP buffer layers grown on (a) the pure GaP NL in an Al-free reactor ambience, (b) the pure GaP NL in an MOCVD reactor containing Al residuals, and (c) the GaP/AlP NL under the channeling condition of $\vec{g}$ = (100). All of the GaP buffer layers were grown on Si(100):As 2° surfaces. Under this channeling condition $\vec{g}$ = (100), crystal defects such as TDs, SFs and SFPs are commonly resolved. In Fig. 6.13 (a) and (b), the GaP buffer layer grown on the GaP NL in an Al-free and Al-containing reactor exhibit SFs (green circles) and SFPs (red circles) on the surface. The SFs bear strong contrast, while the SFPs appear with weak/faint contrast. Under this particular channeling condition, in addition to the SFs and SFPs, there are some features which are irregularly distributed on the surface in the buffer layer shown in Fig. 6.13 (a). These features hold a very weak contrast and already identified as the incomplete SFs or SFPs. Similar features were observed in the GaP buffer layers while grown particularly on Si(100):H 2° (Fig. 6.2) and on Si(100):As 4° surfaces (Fig. 6.4 (a)), explained in the previous section. In contrast, in Fig. 6.13 (c), in the GaP buffer layer grown on the GaP/AlP NL, we observe SFs and SFPs, however, the density of these defects is much reduced. In addition, we do not observe that particular type of incomplete SFs/SFPs in this GaP buffer layers. In order to resolve extended defects in the GaP layers, additional ECCI scans were taken under other channeling conditions.

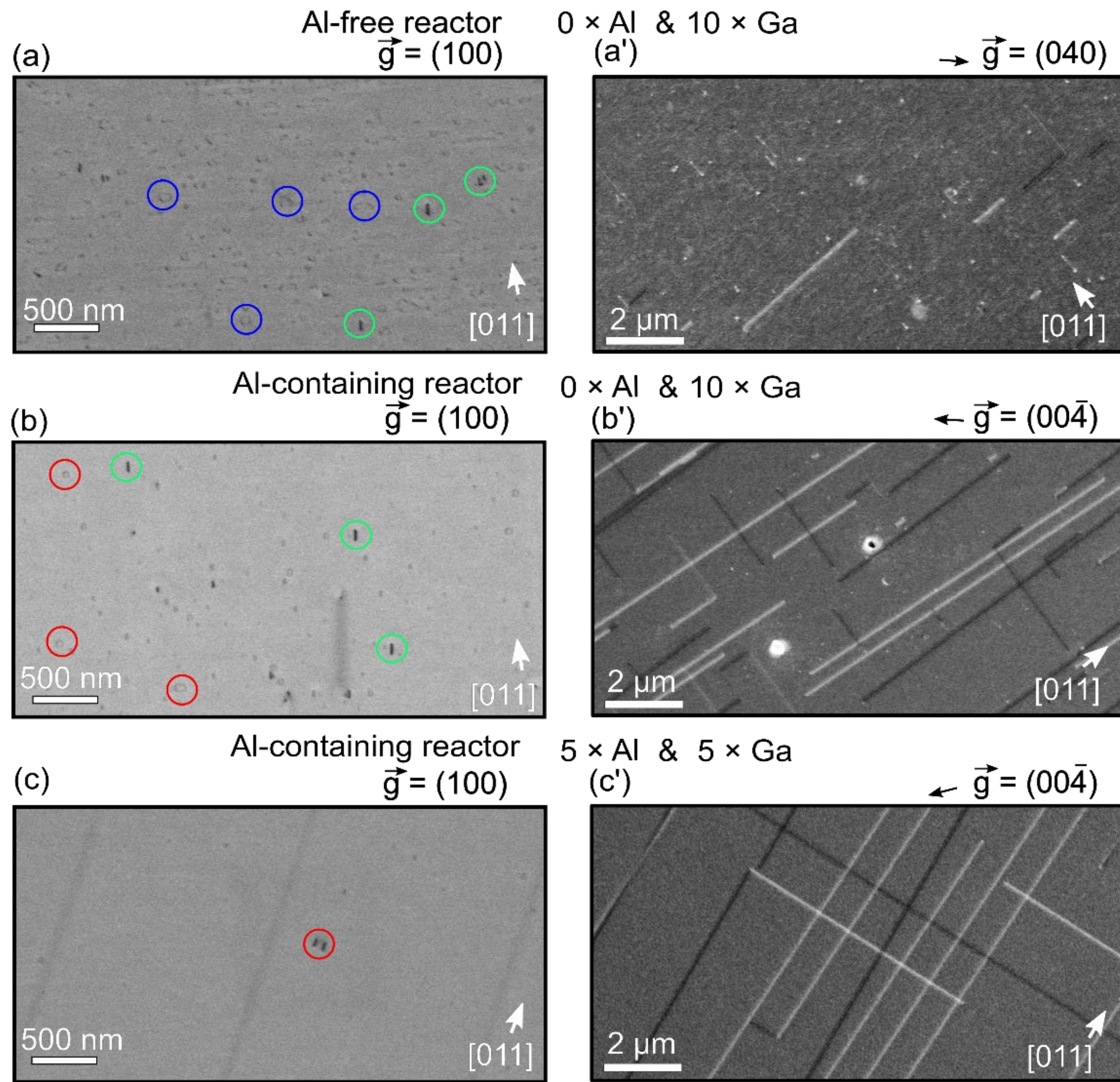

Figure 6.13: ECCI micrographs of 60 nm thick GaP/Si(100) 2° grown on different NLs: (a), (a') pure GaP prepared in an Al-free MOCVD reactor with $\vec{g}$ = (100), $\vec{g}$ = (040), (b), (b') pure GaP prepared in a reactor containing Al-precursor residuals with $\vec{g}$ = (100), $\vec{g}$ = (00$\bar{4}$), (c), (c') GaP/AlP with $\vec{g}$ = (100), $\vec{g}$ = (00$\bar{4}$) (the direction of the $\vec{g}$ vector is marked with the white arrow on top). The arrow at the right bottom indicates the offcut direction [011] of the Si(100) substrate. The figures are redrawn after *Ref.* [123].

Fig. 6.13 (a'), (b') and (c') are the ECCI scans of the same GaP samples shown in Fig. 6.13 (a), (b) and (c) obtained with the following channeling conditions: $\vec{g}$ = (040) in Fig. 6.13 (a') and $\vec{g}$ = (00$\bar{4}$) in Fig. 6.13 (b') and (c'); the $\vec{g}$ vectors are indicated by white arrows, respectively. The invisibility criteria for these two channeling conditions lead to non-zero values for all possible Burgers vectors $\vec{b}$ and line directions $\vec{u}$. Therefore, in all ECCI images

in (a'), (b') and (c'), we observe MDs, which appear as bright and dark lines in both orthogonal [011] and [01$\bar{1}$] directions. The contrast of these MDs depends on the corresponding Burgers vectors. At the ends of each MD, dark or/and bright points are visible, which are the TDs. For quantification, an ECCI scan area of 3.2 × 10^{-6} cm^2 (magnification of 5000x) was taken for the GaP sample grown on a GaP NL in an Al-free reactor. For the two GaP samples grown on the GaP and GaP/AlP NL in an Al-containing reactor, the scan area of 2 × 10^{-5} cm^2 (low magnification of 1000x) was taken to resolve the long MDs. Both, the total number and the average length of MDs in both orthogonal [011] and [01$\bar{1}$] directions were measured using the 'ImageJ' software [149,150]. In order to calculate the line density of MDs, the average length of the MDs from both orthogonal [011] and [01$\bar{1}$] directions were summed up and divided by area. The calculation was done from at least five different scans from three different positions on each sample and averaged. Each sample was prepared (grown) three times to insure the repeatability of the quantification.

The GaP buffer layers grown on the pure GaP NL (Fig. 6.13 (a')) exhibits very short MDs with an average length of each MD of 0.8 µm. In contrast, in the GaP buffer layer prepared in the MOCVD reactor containing Al-precursor residuals (Fig. 6.13 (b')), the observed MDs are longer, and the average length of each MD is around 6 µm. Therefore, the total (added) length of the MDs per unit area (line density of MDs) is higher (9.3×10^3 cm^{-1}) in the GaP buffer layer shown in Fig. 6.13 (b') compared to the GaP buffer layer (line density of MDs = 1.2×10^3 cm^{-1}) shown in Fig. 6.13 (a'), whereas the density of TDs is very similar. The TDs density is quantified as 3×10^7 cm^{-2} in the buffer layer in Fig. 6.13 (a'), comparable to the one of 2.6×10^7 cm^{-2} in the buffer layer in Fig. 6.13 (b').

In the GaP buffer layer grown on the GaP/AlP NL (Fig. 6.13 (c')), the MDs are significantly longer and the average length of each MD is assessed to 11.6 µm. The total length of the MDs per unit area (line density of MDs) for this buffer layer is measured as 4.1×10^3 cm^{-1}. In all these GaP samples, the number of MDs in the [011] direction is significantly higher than in the orthogonal [01$\bar{1}$] direction: 30 to 15, 170 to 88 and 47 to 24 for the samples (a), (b) and (c), respectively. Approximately, this ratio is equal to about 2:1 for all the samples. Since the total number of expanding MDs in the GaP buffer layer grown on GaP/AlP NLs is significantly lower compared to both of the buffer layers in the Al-free and Al-containing reactor, the density of the TDs decreases from 3×10^7 cm^{-2} (GaP nucleation in an Al-free reactor) by almost one order of magnitude to 6.5×10^6 cm^{-2} (GaP/AlP nucleation). A summary of the quantitative defects extracted from ECCI is added in Table II. The low density of TDs is especially important for the device performance, as the TDs are known to act as non-radiative recombination centers [51]. The difference in MD length between the two GaP samples prepared in Al-free and Al-containing reactor ambiences can be due to the impact of Al residuals in the reactor. It is important to note that prior to each growth run, the

MOCVD reactor parts were annealed at 1010°C for 30 min in order to remove III-V residuals from previous processes. However, a complete removal of residuals can hardly be realized and therefore, we expect small amounts of Al residuals in the reactor ambience after the preparation of Al-containing NLs. We observed a comparable density of TDs in both of the buffer layers with the pure GaP nucleation independently of the reactor ambience. This further indicates that a decrease of the TD density in the buffer layer with a GaP/AlP nucleation is due to the interfacial Al induced during nucleation.

Table II: Quantitative comparison of the density of defects in 60 nm thick GaP buffer layers; the green background indicates samples prepared with Al in the nucleation layer.

Quantitative data extracted from ECCI	Al-free reactor		Al-containing reactor		
	0 × Al 10 × Ga	0 × Al 5 × Ga	0 × Al 10 × Ga	5 × Al 5 × Ga	5 × Al 10 × Ga
Average length of each MDs (µm)	0.8	1.3	6.0	11.6	13.2
Line density of MDs (cm^{-1})	1.2×10^3	8.0×10^3	9.3×10^3	4.1×10^3	3.4×10^3
Density of TDs (cm^{-2})	3.0×10^7	2.0×10^7	2.6×10^7	6.5×10^6	5.8×10^6
Density of SFs and SFPs (cm^{-2})	1.5×10^9	2.2×10^9	8.0×10^8	2.0×10^7	2.8×10^7

In addition to MDs and TDs in Fig. 6.13 (a'), we observe a very high density of defects, which appear as white dots. Fig. 6.14 shows ECCI scans taken under higher magnification with the same channeling conditions as shown in Fig. 6.13. We see that the visible white points in Fig. 6.13 correspond to either SFs or SFPs indicated with green triangles, red circles, respectively (Fig. 6.14 (a, b, and c)). The white squares indicate TDs at the ends of MDs. A quantitative estimation shows that the density of SFs and SFPs (2×10^7 cm^{-2}) in the GaP buffer layers grown on the GaP/AlP NL is lower by almost two orders of magnitude, compared to 1.5×10^9 cm^{-2}, the density, when GaP is grown on the GaP NL in an Al-free reactor. In the buffer layer grown on the pure GaP NL prepared in a reactor containing Al-residuals, the density of SFs and SFPs was quantified to 8×10^8 cm^{-2} (see Table I). Considering all the channeling conditions shown in Fig. 6.13, the quantification of SFs and SFPs was done from different positions on the samples. The magnified images of the SFPs

from the three different GaP buffer layers are shown on the right-hand side in Fig. 6.14 (a'), (b') and (c') respectively. In Fig. 6.14 (a') we observed clear and sharp edges of the SFPs, which appear as two triangles (two individual SFs) pointing at each other and resembling a bow-tie, similar to Fig. 6.14 (b'). Two opposite triangles are visible with strong contrast in this particular channeling condition, otherwise the SFP appear as a square, where four individual SFs are involved and joined together, as shown in Fig. 6.13 (b) (red circles).

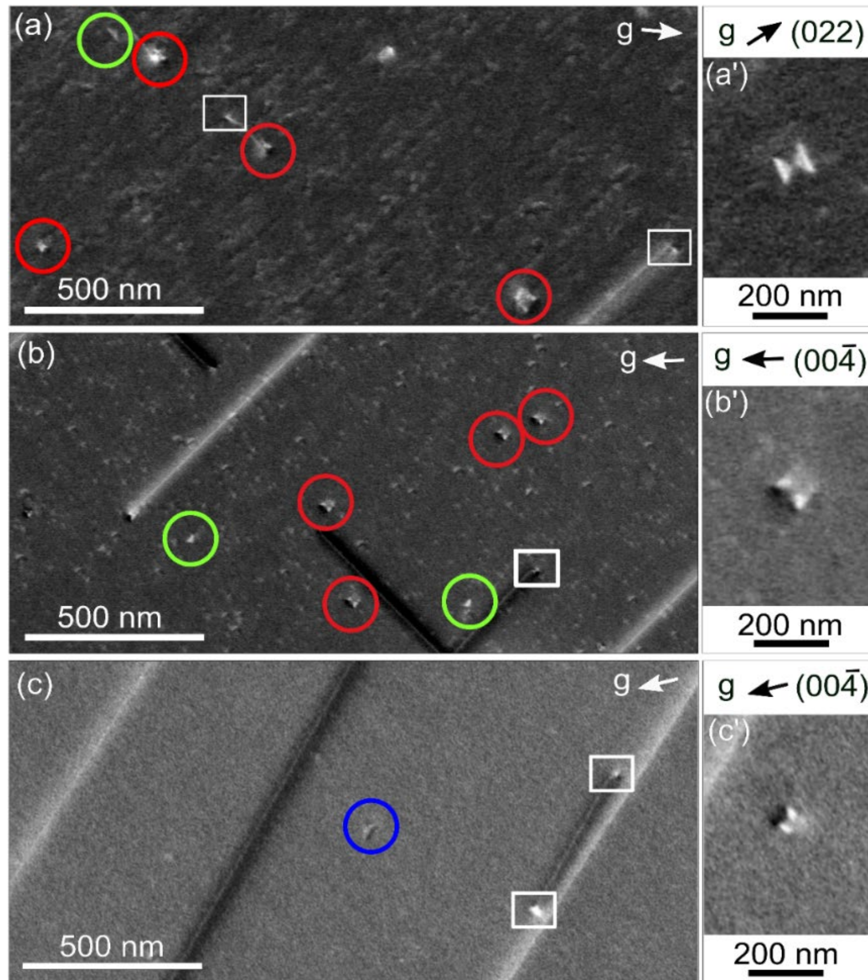

Figure 6.14: Left-hand side: magnified ECCI scans of GaP buffer layers grown on different NLs: (a) pure GaP in Al-free ambience, (b) GaP prepared in a reactor containing Al-residuals, and (c) GaP/AlP. Right-hand side: Corresponding magnified images of SFPs. Red and green circles indicate SFPs and SFs, respectively and in addition blue circle in (c) indicate a possible incomplete SF. The figure is redrawn after *Ref.* [123].

In the GaP buffer layer grown on the pure GaP nucleation, we observed that a few MDs start/end with SFPs (see the red solid circles in Fig. 6.14 (a) and (b)). From several ECCI

scans of GaP films grown on pure GaP NLs in Al-free reactor ambiences, taken from three different positions, we observe that 12 out of 31 (39%) MDs have been blocked by SFPs. In contrast, in the GaP buffer layers grown on GaP NLs in an Al-containing MOCVD reactor, only a very small number of SFPs show the blocking behavior (5 out of 40) corresponding to a percentage of 12.5%, significant less compared to an Al-free ambience. In the GaP buffer layers grown on GaP/AlP NLs (Fig. 6.14 (c)), we did not observe any MD blocked by an SFP. Thus, with an increasing density of SFPs the probability that the MDs will be blocked gets higher, as shown by Feifel et al. [56]. Since the stress due to lattice-mismatch in the grown buffer layer must be released through the glide of MDs, hindering the propagation of MDs leads to many, but short MDs, and thus, a high number of TDs (see Fig. 6.13 (a')) [56]. Therefore, it is crucial to grow materials with low densities of SFPs, in which the gliding of the MDs is not blocked. This is especially important in thicker films, in which the SFPs are larger in diameter and the density of MDs is higher. The lower density of SFs and SFPs in the buffer layer with GaP/AlP nucleation (shown in Fig. 6.13 (c')) can further explain the longer MDs. In addition, there are small variations of the lattice-mismatch between the GaP/AlP and GaP NLs. Thus, MDs in the GaP buffer layers grown on GaP/AlP NLs could start to form earlier in the epilayer and expand longer in order to accommodate the larger built-in strain, due to a slightly higher lattice constant of AlP compared to GaP, as another indication that the modification of the nucleation sequence by Al can influence the density of these defects, which is indeed important for device performance.

The SFP originating from the (100) surface propagates through the four sets of {111} planes at an angle of 54.74° intercepting the (100) plane as shown in the Fig. 6.15 and the length of the edges of the SFP visible in the surface plane can be considered to determine the depth of these defects in the GaP film. Since on all three preparation routes we found different sizes of SFPs (see the red circles in Fig. 6.14 (a) and (b)), we estimated the depth of the largest and the smallest SFP we have observed in two different scan areas under the same magnification. The estimation of the depth of SFPs are done on the SFPs, which are distinct and fully visible on the surface (for example, as Fig. 6.14 (a')). There might also arise incomplete, partially formed SFPs, which would either appear as squares with a missing edge or partly visible triangles on the surface [55,132]. For the smaller SFPs in the 60 nm film, we can hardly distinguish between a complete (fully formed) and incomplete (partially formed) SFP, even under maximum magnification. An incomplete SFP causes a smaller length of one side of the SFP on the (100) plane compared to a complete, fully formed one. Since the majority of the SFPs in the GaP layer grown on the GaP/AlP NL is significantly smaller, we can either state a smaller penetration depth of them as estimated below or a significant larger number of incomplete SFPs. For these estimations, we consider three GaP buffer layers grown either on (i) pure GaP (nucleation in an Al-free reactor), (ii) pure GaP (nucleation in an Al-containing reactor) and on (iii) GaP/AlP NLs. In the GaP buffer layer

grown on the GaP NL (Al free reactor) (Fig. 6.14 (a)), the longest side of the largest SFPs in the (100) plane is equal to 85 nm, which corresponds to a thickness of the GaP film of 59.71 nm. This agrees very well to the expected thickness of 60 nm and therefore, confirms that the largest SFPs nucleate at the GaP/Si heterointerface [56]. The thickness of 60 nm of all three GaP buffer layers was confirmed by white light interferometry. The lateral dimension of the smallest SFPs corresponds to a GaP thickness of 46.80 nm, which indicates that they nucleate during GaP layer growth. In contrast, in the GaP buffer layer grown on the GaP NL in the Al- containing reactor (Fig. 6.14 (c)), the longest side of the largest SFP in the (100) plane is equal to 72 nm, which corresponds to a penetration depth of the SFP into the GaP film of 50.90 nm. For the smallest SFP, a thickness of the GaP film of 38.17 nm is suggested. In case of GaP buffer layers grown on GaP/AlP NLs (SFP shown separately in Fig. 6.14 (c')), in average, the size of the SFPs is smaller compared to the other two GaP layers. The lateral length of the largest SFP in (100) orientation is 71 nm corresponding to a thickness of the GaP film of 50.32 nm and for the smallest SFP, its calculated depth results in 23.40 nm. The respective depth of the largest and smallest observed SFP is summarized in Fig. 6.15.

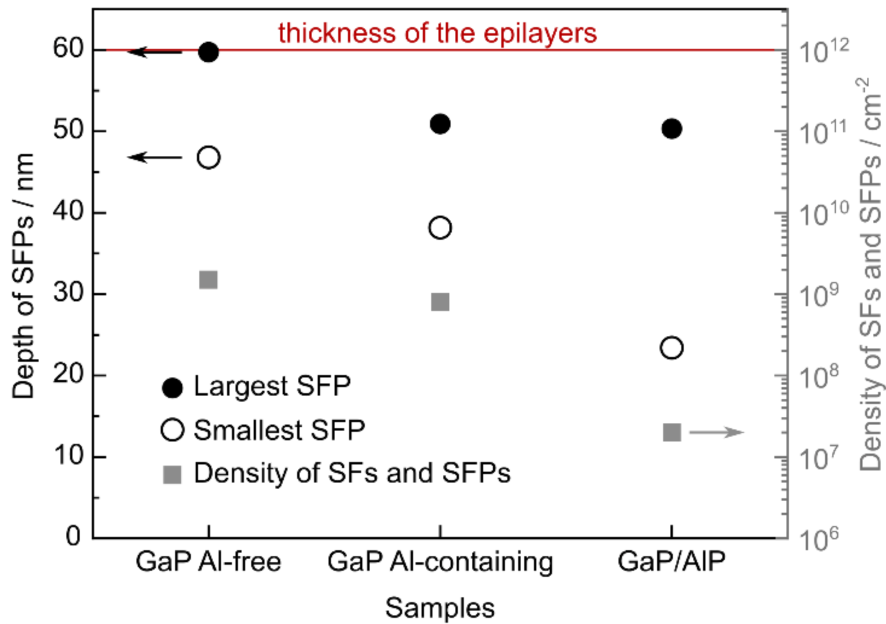

Figure 6.15: Depth profiles of the respective largest and smallest SFPs observed (left y-axis) and the density of SFs and SFPs (right y-axis) in GaP buffer layers grown on pure GaP NL in Al-free ambience, on pure GaP NL prepared in a reactor containing Al-residuals, and on GaP/AlP NLs. The figure is redrawn after *Ref.* [123].

In the GaP buffer layers grown on GaP NLs prepared in Al-free and Al-containing reactors the amount of large SFPs prevails over the small ones. Since the thickness of these two buffer

layers is 60 nm, most of the SFPs must start to form already at the heterointerface (during the GaP nucleation and/or right after). We observed that only the large SFPs block the propagation of MDs (shown in Fig. 6.14 (a) and (b)). In contrast, the majority of the SFPs in the buffer layers grown on the GaP/AlP NLs are significantly smaller. This indicates that the SFPs start to form in these layers during the GaP growth, but not at the heterointerface (considering complete, fully formed SFPs). Since their density is also significantly lower, it confirms that the presence of Al at the heterointerface has a high impact on the formation of SFPs. In general, this could be a result of different surface reconstructions and morphologies of the NLs; depending on the surface formation, the SFPs start to form later in the GaP buffer layer with GaP NL in an Al-containing reactor and with GaP/AlP NLs, possibly after the coalescence of islands. Therefore, in order to observe the GaP surface morphology shortly after the two different nucleation procedures, AFM measurements were carried out, and are discussed in the following.

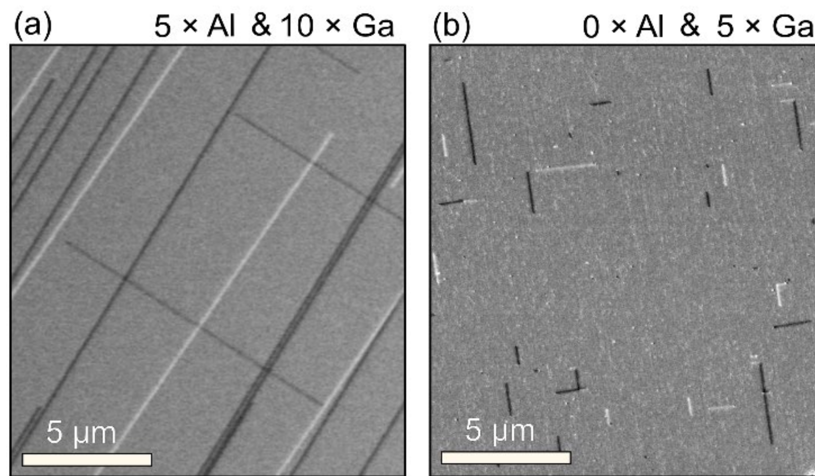

Figure 6.16: ECCI micrographs of 60 nm thick GaP/Si(100)2° grown on (a) 5 PP of Al and 10 PP of Ga, and (b) 5 PP of Ga followed by P for each Al and Ga pulses. The figure is redrawn after *Ref.* [123].

So far, it has been discovered that the number of GaP(/AlP) pulses applied during the pulsed nucleation has a strong impact on the density of SFPs [56]. Decreasing the number of Ga pulses from 10 to 5 (each followed by a P pulse) leads to a lower density of SFPs. Since both RAS and XPS indicate that the thickness of the GaP/AlP NL is thinner than the pure GaP one, in the following, we want to assure that the reduced density of defects is indeed due to the presence of Al and not only due to the lower amount of Ga (pulses). Thus, we prepared two 60 nm thick GaP samples on (i) a GaP/AlP NL, which consisted of 5 PP of Al and P, followed by 10 Ga and P PP, so that the number of Ga pulses remained equal, compared to the pure GaP NL displayed in Figs. 6.14 (a),(a') and 6.15 (a); and (ii) a GaP NL, which

consisted only of 5 Ga and P PP, prepared in the Al-free reactor, so that the number of Ga pulses is equal to the sample shown in Figs. 6.14 (c), (c') and 6.15 (c).

The ECCI scans of those two samples are shown in Fig. 6.16. In the first sample (Fig. 6.16 (a)), we observe very long MDs and a very low density of SFPs, similar to the case of GaP buffer layers grown on GaP/AlP NLs with 5 Ga pulses. Also, the line density of MDs (3.4×10^{3} cm^{-1}) as well as the density of TDs (5.8×10^{6} cm^{-2}), SFs, and SFPs (2.8×10^{7} cm^{-2}) is within the same order of magnitude as represented in Fig. 6.13 (c), (c'). The second sample prepared on a pure GaP NL with only 5 PP (Fig. 6.16 (b)) exhibits very similar short MDs as reflected in Fig. 6.16 (b) prepared with 10 PP. The defect density is on the same order of magnitude as in the GaP sample (10 PP) shown in Fig. 14 (a), (a') (see Table I). Nevertheless, these two additional experiments confirm that the density of SFs and SFPs as well as the length of the MDs (and thus, the density of the TDs) is indeed due to the presence of Al in the NL and not due to a modified amount of Ga pulses.

6.5 Stress - strain in the GaP(100) buffer layers

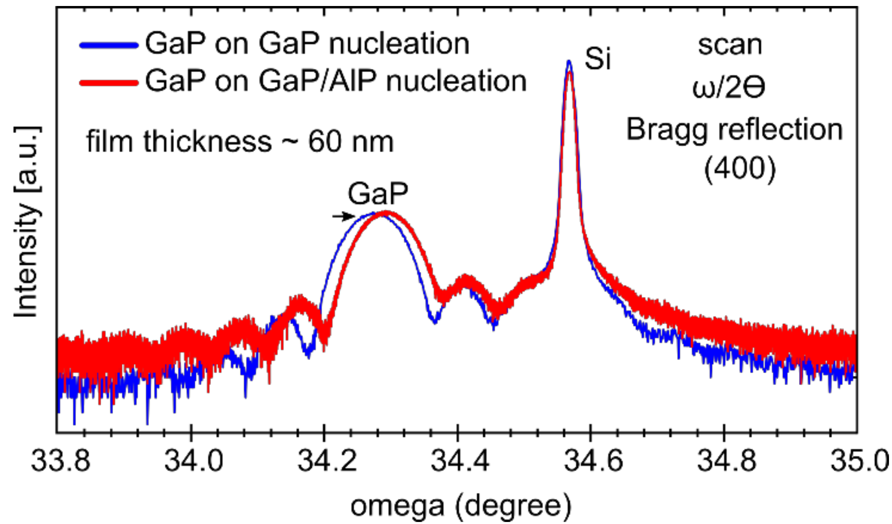

Figure 6.17: HR-XRD ω/2Θ scan of the 60 nm thick GaP layers grown on pure GaP (blue line) and GaP/AlP (red line) NLs on Si(100):As 2°. The figure is redrawn after *Ref.* [123].

Since we observe a significant difference in the density of MDs, which affects the strain relaxation in the buffer layer, XRD profiles of symmetrical (004) diffraction were carried out on both GaP buffer layers. The XRD measurements were performed parallel to the atomic step edges in order to avoid any contribution from the Nagai tilt. Therefore, the ω/2Θ scans in this measurement only involves stress/strain or compositional behavior of the samples. Fig. 6.17 shows the respective ω/2Θ scans from 60 nm thick GaP layers grown on

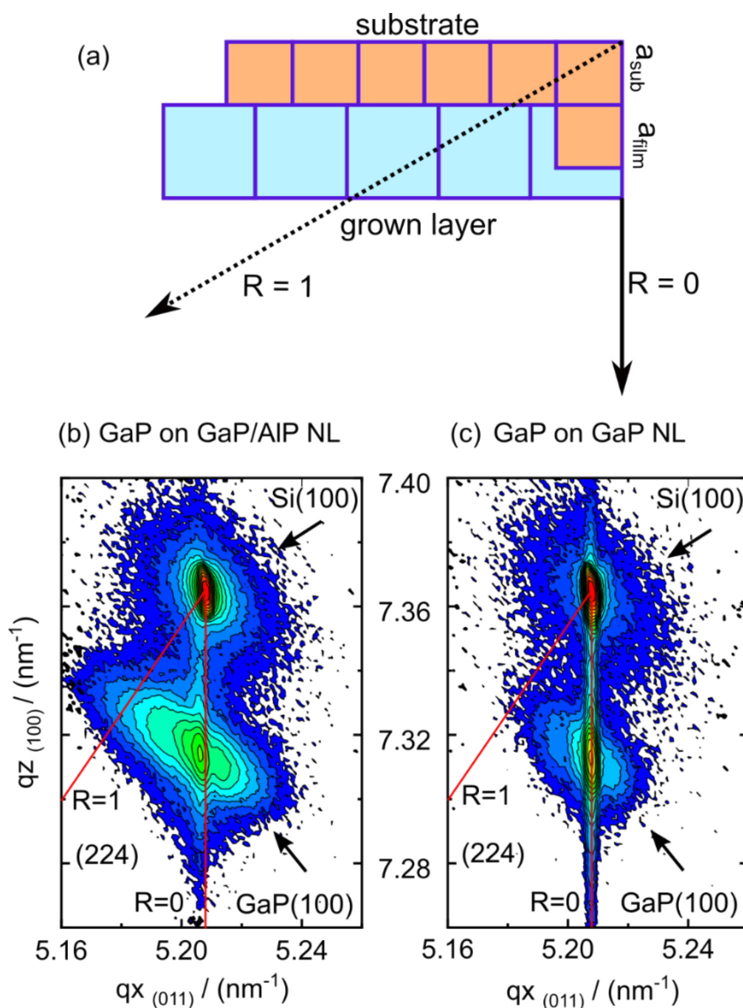

Figure 6.18: (a) A schematic of the substrate-layer relaxation Asymmetric (224) reflection of 100 nm thick GaP buffer layers grown on (b) GaP/AlP (c) GaP NLs on Si(100):As 2° by RSM measurement.

both, pure GaP and GaP/AlP NLs, respectively. In both XRD scans, Laue oscillations are clearly visible, which indicates a high crystallinity of both GaP buffer layers. The diffraction peak from the GaP film grown on a GaP/AlP NL (red line) is shifted by 0.02° towards the Si substrate compared to the diffraction peak of the GaP film grown on a pure GaP NL. The FWHM of the peak corresponding to the GaP buffer layer grown on the GaP/AlP NL is slightly narrower (0.06) than the FWHM from the GaP buffer layer grown on the pure GaP NL (0.07). The shift of the diffraction peak towards the Si substrate indicates that GaP grown on a GaP/AlP NL exhibits a small relaxation compared to GaP grown on pure GaP NLs. Therefore, qualitatively these measurements reveal that the longer MDs in the GaP films grown on GaP/AlP NLs cause a slightly enhanced relaxation in the buffer layer.

An additional RSM was carried out for both of these GaP layers in order to further confirm relaxation in the GaP buffer layer grown on the GAP/AlP NL. Here, the GaP buffer layers of 100 nm thick were separately grown on both GaP and GaP/AlP NLs, same as previously explained. By these RSM measurements the strain relaxation of each GaP buffer layers can further be determined. RSM for asymmetrical (224) reflection was carried out on both of the GaP buffer layers. A schematic of the substrate-layer relaxation is displayed in Fig. 6.18 (a). If the grown layer exhibits a higher lattice constant than that of the substrate, the grown film possesses a relaxation inside the film. Relaxation line R = 0 or R = 1 can be plotted such a way (see Fig. 6.18 (a)) in order to determine the degree of relaxation in the film. RSM of symmetrical (004) does not provide any significant difference in the signals of reciprocal lattice points and therefore, an accurate comparison was not possible between these samples. Fig. 6.18 (b) and (c) show the respective RSM scans taken at asymmetrical (224) reflection from the 100 nm thick GaP buffer layers grown on both (a) GaP/AlP and (b) GaP nucleation, respectively. The reciprocal lattice points of the GaP buffer layer grown on GaP/AlP NL form a stretched ellipsoid and partly shifted towards R=1 (shown in (b)), which indicates a partial relaxation in the [110] direction (the reciprocal space co-ordinate of the GaP layer is not directly below the Si substrate). A fully relaxed layer would follow the red line R=1. In contrast, the signal from the GaP buffer layer grown on GaP NL in Fig. 6.18 (c) is very narrow, and its ellipsoidal shape, stretched along the [110] direction (marked as the red line R=0), confirms a pseudo-morphic layer, where the in-plane lattice constants of the buffer layer and the substrate are equal. Therefore, qualitatively these measurements reveal that the longer MDs in the GaP buffer layer with GaP/AlP nucleation cause a small relaxation in the buffer layer whereas almost no strain relaxation occurred in the buffer layer with the GaP nucleation.

6.6 Influence of the Al on the GaP(100) surface morphology

In principle, three-dimensional GaP islands, which form at an early stage of growth, can lead to the formation of SFs or SFP upon coalescence [52,151]. Our calculations of the lateral dimensions of the SFPs indicate that most of the SFPs in the GaP films grown on GaP NLs originate at the GaP/Si(100) heterointerface. In order to observe the impact of Al on the GaP surface structure and morphology at the initial stage of growth, we prepared 2 nm GaP layers on either pure GaP or GaP/AlP NLs, as shown in Fig. 6.19 (a) and (b), respectively, on 1×1 μm^2 AFM images. These two samples were measured directly after growth in order to avoid exposure to air for an extended period of time, as the (buried) Al containing III-V NLs might be particularly sensitive to oxidation. Although the RMS surface roughness of both of these

samples is very smooth and similar (0.36 and 0.26 nm for GaP grown on pure GaP and GaP/AlP NL, respectively), their surface morphology is different.

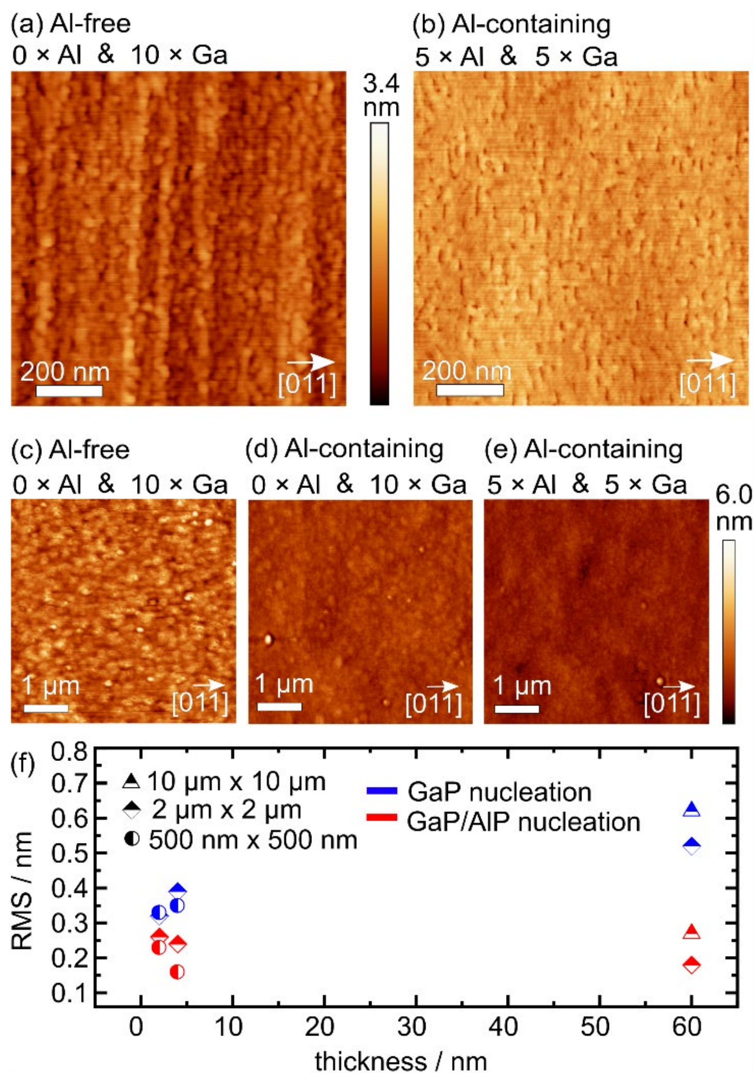

Figure 6.19: 1 µm × 1 µm AFM scans from 2 nm thick GaP buffer layers on GaP (a) and GaP/AlP (b) NLs. (c-e) show 5 µm × 5 µm AFM scans from 60 nm thick GaP buffer layers grown on (c) GaP NLs in Al-free, (d) Al-containing ambience, and (e) GaP/AlP NLs. (f) RMS shows GaP(100) surface roughness in dependence of the buffer thickness and the nucleation. The figure is redrawn after *Ref.* [123].

At the initial stage, GaP grown on the pure GaP nucleation exhibits a grain- and island-like structure, whereas GaP grown on the GaP/AlP NL exhibits trenches along the step-edges towards the [011] direction, with flat terraces. This difference in the surface structure between those two buffer layers might be due to the difference in surface diffusion mobilities

between Ga and Al [144]. Ga adatoms are expected to diffuse faster than Al adatoms, and Al adatoms might fill the position, where Ga adatoms drift away, providing a smoothening of the surface. Suppression of the island formation upon addition of Al was observed for both, GaP and GaAs NLs prepared on Si [144,145] (see also in introduction). This, again, indicates that replacing Ga pulses by Al can induce planar growth and strongly influence the surface structure and morphology of the subsequently grown GaP buffer layer.

Figs. 6.19 (c-e) show representative 5×5 μm^2 AFM scans from the 60 nm thick GaP buffer layer grown on GaP in (c) Al-free, (d) Al-containing reactors, and (e) GaP/AlP NLs (same samples as shown in Figs. 6.14). The surface roughness of GaP on a GaP/AlP NL (Fig. 6.19 (e)) remains remarkably low, 0.24 nm (5×5 μm^2), while the RMS of the 60 nm thick GaP buffer layer grown on pure GaP NLs (Fig. 6.19 (c)) increases slightly to 0.60 nm (5×5 μm^2). The GaP buffer layer grown on pure GaP NLs in an Al- containing reactor (see Fig. 6.19 (d)) exhibits almost comparable surface morphology and roughness of 0.27 nm as the GaP buffer layer grown on GaP/AlP NLs (Fig. 6.19 (e)). Since the density of SFs and SFPs in this buffer layer (8×10^8 cm^{-2}) is not significantly lower compared to the sample with pure GaP NLs prepared in an Al-free reactor (1.5×10^9 cm^{-2}), we conclude that the smoother surface morphology should be due to an influence of Al from the reactor ambience and not due to a lower density of defects [56]. The RMS surface roughness values are summarized in Fig. 6.19 (f) for 2, 4, and 60 nm thick GaP buffer layers grown on pure GaP (blue symbols) and GaP/AlP (red symbols) NLs. Thus, we conclude that the increased roughness of the buffer layer with pure GaP NLs in Al-free ambience does not depend on the thickness of the buffer, but it rather depends on the surface structure at the initial stage of growth. For reference, the RMS surface roughness of the Si(100):As substrate prior to the GaP growth is 0.07 nm (5×5 μm^2 scan), which excludes any roughening origin from the initial stage of the substrate. Evidently, we see that the particular surface of the NLs determines the surface morphology and roughness of the subsequently grown GaP buffer layers. Moreover, by ECCI we observe that smoother surfaces (GaP buffer layers grown on GaP/AlP NLs) exhibit a lower density of TDs, SFs, and SFPs, which indicates that the formation of these defects is mainly dependent on the initial layer deposition on the substrate.

6.7 Crystalline defects in GaPN

In a final design, GaPN/GaP/AlP/Si(100):As are a promising heterostructure for the elaboration of high efficient tandem solar cells on Si substrates. The growth of GaPN with diluted nitride alloy can be applicable as a top junction material due to its perfect lattice matching with the Si substrate and its ideal bandgap energy allowing a perfect current matching with the Si bottom cell. However, the efficiency of these heterostructure is very

sensitive to the structural defects such as MDs and TDs appearing during metamorphic III-V buffer layer growth, since they reduce the carrier lifetime and therefore reduction of the solar cell performance. As we discussed earlier, the first challenge during the growth of III–V/Si solar cells is to control and suppress the crystalline defects that arise mainly at the III–V/Si interface due to lattice mismatch. Our previous study on nucleation of GaP/AlP directly on Si(100) showed a significant improvement in defect density in the subsequently grown GaP buffer layers. Therefore, it was indeed challenging to grow a thick buffer layer on top of the nucleation layer in order to understand the impact of the GaP/AlP NL in defect density of the thick buffer layer.

Supplie et al., [100] showed a successful growth of P-rich GaPN layer on Si(100) substrate where the surface anisotropy of the GaPN by RAS and the surface morphology of the GaPN layer was studied in detail. However, the study on formation of crystal defects in the GaPN layer was not explored enough so far. Besides, in our study the Si(100) substrate was prepared with As terminated prior to the GaPN growth, in contrast to the *Ref.* [100], where the GaPN layer was directly grown on a Si(100):H surface. Here, for characterization of defects, a 30 nm thick GaP buffer layer was grown on GaP/AlP NL (5 PP Al and 5 PP Ga) and subsequently a 200 nm thick GaPN layer was grown on top of the GaP buffer layer. In order to grow a lattice matched GaPN layer on Si substrate, the nitride flow (UDMHy precursor) was optimized. XRD measurement confirmed a lattice matched GaPN layer on Si.

Fig. 6.20 (a) depicts selected ECCI scans from the 200 nm thick GaPN layer under the channeling condition $\vec{g}$ = (100). In Fig. (a), the GaP layer exhibits some dark features which appear as short lines. Under the same channeling condition, similar features were observed from different positions of the sample. In addition, an exemplary ECCI scan from the channeling condition $\vec{g}$ = $(00\overline{4})$ is shown in Fig. 6.20 (b). Similar to the channeling condition $\vec{g}$ = (100), the GaPN layer under the $\vec{g}$ = $(00\overline{4})$ exhibits dark lines distributed on the surface which we assume to be SFs or SFPs on the surface. In addition, there are some features of strong contrast in the layer indicated by green circles which seem to be SFs. Besides, there are features such as a pair of white/dark spots together, which are TDs (indicated by pink circle). This kind of appearance of TDs is commonly visible for a thick III-V layer [113].

The SFs observed here have very different appearance compared to the features of SFs observed in thin (60 nm) GaP layer explained earlier in this chapter. Here, these features could be either SFs or SFPs on the surface which only show a single edge of the defects and the rest of the edges are invisible. According to ECCI, under the channeling condition $\vec{g}$ = (100), it is most likely to resolve defects like SFs and SFPs rather than MDs unless the MDs

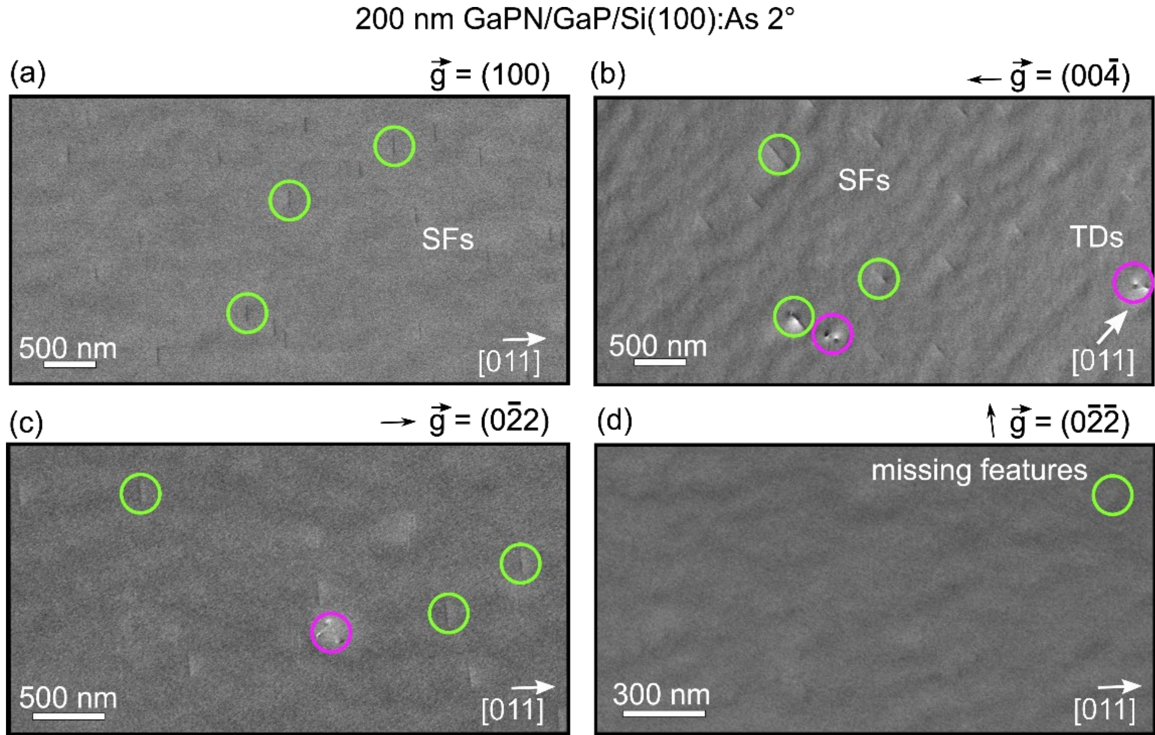

Figure 6.20: ECCI scans from 200 nm thick GaPN buffer layers under the channeling condition of (a) $\vec{g}$ = (100) and (b) $\vec{g}$ = (00$\bar{4}$). The appearance of SFs is confirmed by taking the scans from two channeling $\vec{g}$ = (0$\bar{2}$2) and $\vec{g}$ = (0$\bar{2}\bar{2}$). The contrast of SFs appears under the channeling $\vec{g}$ = (0$\bar{2}$2) whereas they turned to disappear under the channeling $\vec{g}$ = (0$\bar{2}\bar{2}$).

nucleate at the surface and propagate toward the interface. Therefore, with respect to the features observed under the $\vec{g}$ = (100), the probability is that they are either SFs or SFPs. A similar observation was observed in GaAs QD layer as shown in *Ref.* [20]. The defects which have the appearance of dark lines in (100) plan-view TEM are considered as 'V-shaped' defects [20]. The propagation of these 'V-shaped' defects are very similar to the propagation of SFs as they start from a dislocation at heterointerface and propagate after dissociation into two Shockley partial dislocations through two opposite {111} planes. In order to confirm that these features are SFs or SFPs and not due to the surface morphology, the ECCI scans were taken from two additional channeling conditions $\vec{g}$ = (0$\bar{2}$2) and $\vec{g}$ = (0$\bar{2}\bar{2}$), which are the two adjacent channeling conditions, to distinguish these features (see Fig. 6.20 (c) and (d)). If these features are defects, they will be visible only in one channeling condition, either under $\vec{g}$ = (0$\bar{2}$2) and or under the channeling $\vec{g}$ = (0$\bar{2}\bar{2}$) and the visible part observed in one channeling condition should be invisible under the other channeling condition. In Fig. 6.20 (c), under the channeling $\vec{g}$ = (0$\bar{2}$2), the features are clearly present in the layer whereas the features turn to invisible under the channeling $\vec{g}$ = (0$\bar{2}\bar{2}$) as shown in the Fig. 6.20 (d). This indicates that they are either SFs or SFPs. Quantitative assessment of defects from the GaPN

layer was also analyzed: The density of SFs/SFPs was calculated as 1.2×10^8 cm^{-2} and the density of TDs was found as 1×10^7 cm^{-2}. The surface morphology of the GaPN buffer also seem to be smooth as observed from the ECCI scan.

In summary, we conclude that a lattice matched GaPN layer after introducing GaP/AlP NL can be grown on the Si(100):As 2° substrate. For the GaPN layer, the calculated density of defects shows a bit higher, but still in a close range to the density of defects calculated from the thin GaP buffer layer grown on the GaP/AlP NL (explained earlier). However, further investigation is required to minimize the defect density in the GaPN layer.

6.8 Summary of this chapter

The formation of defects, in particular, SFs and SFPs depends on III-V NLs grown on the Si(100) substrates. Their formation and propagation into the bulk can be controlled by a modification of nucleation sequence as well as by the time of application of the precursor pulses. For the GaP nucleation on Si(100):H substrates, 10 alternating P-Ga sequence with 1 sec. break between these pulses reduces the density of SFs and SFPs significantly compared to the one when nucleated without break between these pulses. On the other hand, passivation of the Si(100) substrates whether by H or As strongly influences the formation of defects into the bulk layer. In our study, we observed that the Si(100) substrates with As passivation improves the overall defects density in the subsequently grown GaP(100) layers. Moreover, the substrate offcut plays crucial role in the density of defects in the bulk layers. Remarkable improvement of defects density is observed when the GaP nucleation is modified with Al at the heterointerface. A well-defined admixture of Al to a pulsed GaP nucleation sequence on Si(100) provides a promising pathway for further reduction of the defect density when integrating III-V compounds on Si. AFM scans show smoother surface morphologies for GaP buffer layers grown on the NLs with Al. At the initial growth stage of these buffer layers, the AFM scans show island-free, flat terraces in contrast to GaP buffer layers grown on NLs without Al. ECCI scans show that the adsorption of Al at the heterointerface leads to a significant reduction of the SFs and SFPs in the GaP buffer layers. The density of these defects in GaP buffer layers grown on GaP NLs prepared in an Al-containing MOCVD reactor is comparable to GaP buffer layers prepared in Al-free reactors. In Al-containing reactors, we observed in addition that the SFPs appear to start forming after the initial nucleation, i.e. during the GaP growth and not already at the GaP/Si heterointerface directly, as in the case of the GaP films grown on pure GaP NLs without Al. We also observed that in GaP buffer layers grown on pure GaP NLs only SFPs, which form at the GaP/Si heterointerface, block the propagation of MDs. Therefore, a lower density of SFs and SFPs reduces the probability that the glide of MDs will be blocked by these defects,

which is crucial for a crystal to relax residual lattice strain. More important, a smaller number of longer MDs reflects a significantly lower number of TDs, which is beneficial for reducing non-radiative recombination centers and for achieving an improved performance of optoelectronic devices such as solar cells. GaP buffer layers grown on GaP/AlP NLs or on GaP in Al-containing MOCVD reactors have higher line densities of MDs (longer MDs), which facilitate these layers to relax more easily compared to the layers grown on pure GaP NLs in Al-free reactors. The higher relaxation of these GaP layers suggests that the formation and glide of the MDs in the buffer layers prepared in Al-containing reactors occurs earlier. All studies of AFM, RAS, and ECCI discussed here reflect on significant different heterointerface formations between the samples prepared with or without Al. At the end, the heterostructure of GaPN/GaP/AlP/Si(100):As 2° also shows the defect density within the range of the density found in case of GaP/GaP/AlP/Si(100):As 2° thin layers. However, this still opens space for further improvement which will be studied by our group. Hence, a modified, well-defined pulsed nucleation sequence with the inclusion of Al at the (Al)GaP/Si heterointerface shows a route to drastically reduce the defect density in the subsequently grown III-V buffer layers.

7 III-V growth on Ge(100):As in coated GaAs MOCVD reactors

This subchapter summarizes Ge(100) surface preparation with double-layer steps followed by III-P(100) growth in a more realistic 'GaAs coated' MOCVD reactor. A pre-growth step on double layer stepped, As-modified vicinal Ge(100) surfaces by annealing under TBP precursor influences the chemical compositions as well as the surface reconstruction of the Ge(100) surfaces. The Ge(100) surfaces are monitored *in situ* by RAS and benchmarked with surface sensitive tools (LEED, XPS, STM). Finally, the defect formation in the III-P epilayers in dependence on the pre-growth procedure is investigated by ECCI. Parts of this subchapter is published in Ref. [152]. (M. Nandy et al., ACS Appl. Electron. Mater. xx (2023) xxxx).

7.1 Ge(100):As in phosphorus-rich MOCVD ambience

Preparation of well-defined and atomically abrupt III-V/Ge(100) heterointerfaces is crucial in order to prevent crystalline defects originating at the heterointerface, which can propagate through the III-V bulk epilayers [121,153]. In particular, it is important to avoid APDs in the III-V buffer layers, at which charge carriers can be trapped [154,155] by formation of single domain Ge(100) surfaces with double-atomic steps [13]. Preparation of these surfaces has been previously established in H_2-only [16], As-rich [17,156,157] and in more realistic, GaAs-rich CVD-ambience [18]. Subsequent growth of a high quality III-As layer on these As-rich prepared Ge(100) surfaces is straight forward, however, direct growth of a III-P layer directly on the As-rich Ge(100) surface with a sharp and atomically well-ordered heterointerface is challenging. Therefore, a controlled process condition, in particular, an exchange from As to P on the Ge(100) surface is carried out so that the Ge(100) surface preserves double layer stepped surface prior to the III-P layer on the Ge(100) surface. In this chapter, a pre-growth procedure on As-rich Ge(100) surfaces by annealing these surfaces under the TBP precursor and its influence on the defect formation in the subsequently grown III-P(100) buffer layer will be explained.

Prior to the pre-growth procedure, the As-terminated Ge(100) surface was prepared under the TBAs precursor in a 'GaAs coated' reactor. Fig. 7.1 (a) shows time-resolved RAS signals from the Ge(100):As surface (red line). The transient starts at 300°C while the Ge(100) surface is oxidized and the RAS signal related to the anisotropy is zero. The deoxidation

starts at around 90 s and annealing up to a certain temperature leads to a continuous increase of the amplitude of the negative RAS peak at 1.9 eV [18], which is related to the formation of a double atomic stepped, dimerized As-terminated Ge(100) surface with the prevalence of a (1×2) majority domain on the surface [16–18]. The formation of this surface was discussed in detail in *Ref.* [17].

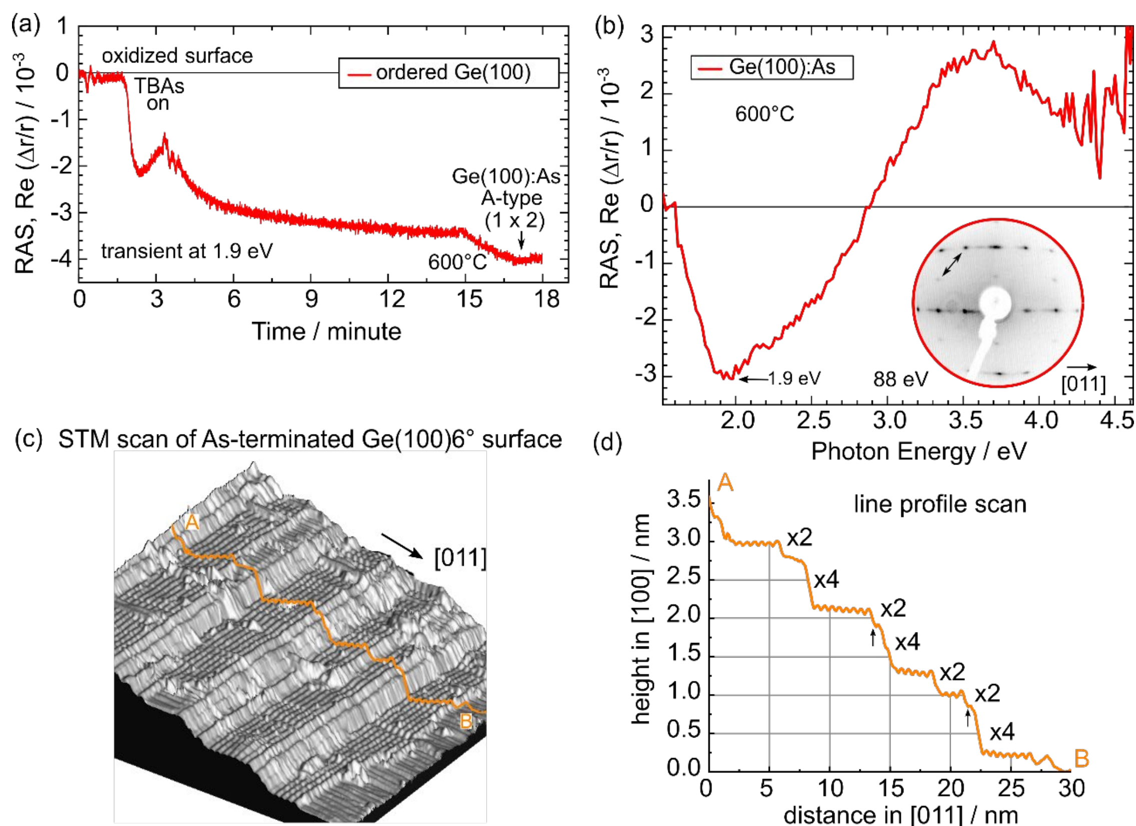

Figure 7.1: (a) *In situ* transient measurements at 1.9 eV photon energy of an ordered (red line) and disordered (light grey line) Ge(100):As surface along with (b) characteristic RA spectrum of As-terminated Ge(100) surfaces, taken at 600°C. The LEED pattern corresponding to the Ge(100):As surface is shown in the inset of (b) (taken from *Ref.* [18]). (c) and (d) represent selected STM scan of the Ge(100):As 6° surface with a corresponding line profile scan (orange line) from point A to B (z-scale factor = 1.4), respectively. The atomic terraces are separated by even number of atomic steps and some of the steps exhibit step bunching on the surface. Due to step bunching, not only double steps, but the steps have several atomic layer heights. The STM scan shown here is redrawn after *Ref.* [18].[5]

[5] The STM scan was done by Dr. Peter Kleinschmidt and B.Sc. Aaron Geiß.

For the As-terminated Ge(100) surface preparation, an optimized molar flow of TBAs precursor is required in order to maintain overpressure of As in the reactor ambient as well as to compensate desorption of Ga from the 'GaAs coating' of the reactor walls.

After around 15 min, once the Ge:(100):As surface is stable, the sample was cooled to 600°C. The observed change in the RAS intensity after 15 min (see the red transient in Fig. 7.1 (a)) is related to the change of the temperature and not due to the change of the surface structure [137,158]. The corresponding RA spectrum taken at 600°C is shown in Fig. 7.1 (b) which shows a characteristic line shape consisting of a well-defined minimum at 1.9 eV close to the E_1 transition of Ge and a maximum at 3.8 eV. The RA spectrum corresponds to a well-ordered, almost single-domain As-terminated Ge(100) surface [17], [18]. Such preparation of the Ge(100) surface results in atomically well-ordered surface with the prevalence of (1×2) surface reconstruction, as shown in inset of Fig. 7.1 (b) [18].

Fig. 7.1 (c) and (d) show selected STM scan with the corresponding line scan from a selected As-terminated Ge(100) surface, respectively. The sample was transferred from the MOCVD reactor to the STM chamber via UHV shuttle. Both, the STM scan and the line profile clearly show atomic terraces with dimer rows which are oriented parallel to the atomic step edges. The orientation of this dimer rows is equivalent to A-type As dimers which arrange as perpendicular to the step edges. In addition, we observe that the atomic steps are ordered along the offcut of the substrate [011] direction. The terraces are separated by even number of atomic steps. In most cases, the steps run together which reflects to step bunching on the surface. This means that not only double steps, but the steps exhibit several atomic layer heights, in particular, the preferred step has six atomic layers (see the line scan from A to B in Fig. 7.1 (d)). In this step structure, a small protrusion is formed with the width of a dimer row which separates the upper double step from the quadruple atomic steps below (see the arrows in the line scan). Besides A-type, small residuals of B-type terraces are also observed on the surface. Moreover, there are also some impurities found on the sample, which, however, can also come during the transfer to STM chamber. To conclude, the dimers rows are very straight and no zig-zag chains of dimers are observed, which indicates As-As dimers on the surface. Moreover, the As-terminated Ge(100) surface exhibits symmetrical dimers on the surface.

In order to observe influence of TBP molar flow on the line shape of RAS signals, the Ge(100):As surface was annealed under TBP molar flow at 580°C (when the TBAs was off) which was gradually decreased from 3.81×10^{-3} mol/min to 5.14×10^{-5} mol/min during 45 minutes. Here the maximum and minimum molar flow of the TBP precursor was limited by the mass flow controller. The TBP molar flow was gradually decreased and not increased because the MOCVD reactor was coated with 'GaAs', and very low TBP molar flow might not be sufficient to compensate the Ga desorption from the reactor walls and its adsorption

on the Ge(100):As surface. The respective changes on the Ge(100):As surface due to the exposure of the TBP precursor was continuously monitored *in situ* by RAS signals.

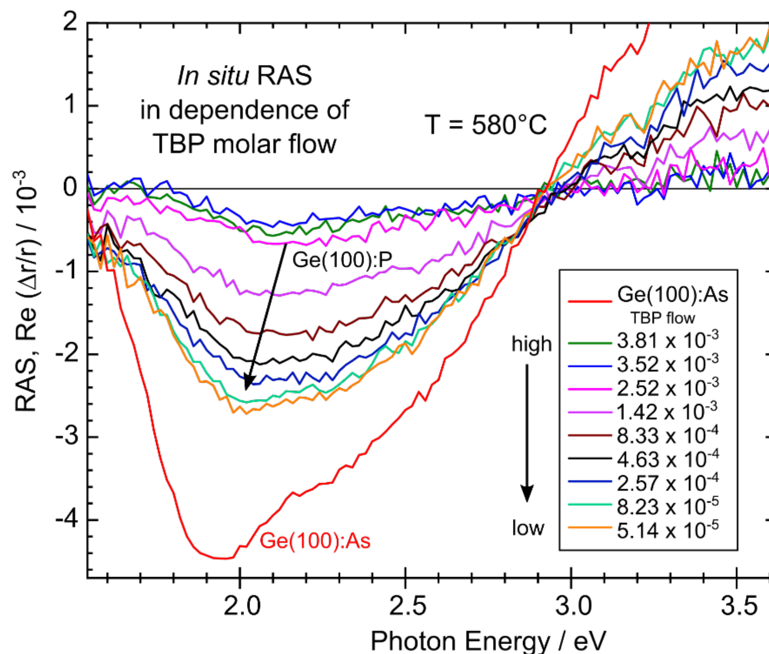

Figure 7.2: A continuous *in situ* monitoring of RA spectrum of the Ge(100) surface in dependence of the TBP molar flow. At the beginning, the molar flow of TBP was 3.81×10^{-3} mol/min and slowly decreased to 5.14×10^{-5} mol/min in a duration of 45 minutes. The green RA spectrum corresponds to the TBP molar flow of 3.81×10^{-3} mol/min, whereas, the orange RA spectrum is at TBP molar flow of 5.14×10^{-5} mol/min. A gradual decrease of the TBP molar flow influences the intensity of the RA spectrum which refers to a further evolution of the Ge(100) surface during annealing under the TBP precursor.

Fig. 7.2 depicts a continuous change in the RA spectrum of the Ge(100) surfaces in dependence of the TBP molar flow. Prior the TBP precursor was supplied, a reference RA spectrum of Ge(100):As surface was taken at 580°C and is shown in Fig. 7.2 (red spectrum). At the moment at which the TBP precursor was turned on (green RA spectrum), we observe an immediate change in the line shape and the intensity of the RA spectrum compared to the As-terminated Ge(100) surface. The low amplitude of the RA spectrum (green spectrum in Fig. 7.2) indicates a disordered surface or increased ratio of the minority to majority domain. An almost unchanged RA spectra were observed up to the TBP molar flow of 2.52×10^{-3} mol/min. Below this molar flow, a gradual increase of the intensity of the RA spectrum was observed. The increase of the amplitude of the RA spectrum suggests increased ratio of the majority to minority domain. Moreover, with gradual lowering of the TBP molar flow, a shift of minimum of the RA spectra towards the lower photon energy was observed (indicated by

a black arrow in Fig. 7.2). The final RA spectrum of the Ge(100):As surface annealed at the TBP molar flow of 5.14×10^{-5} mol/min (orange spectrum in Fig. 7.2) shows a similar line shape compared to the RA spectrum of the Ge(100):As surface (red spectrum taken prior to the exposure to TBP as shown in Fig 7.2). However, the amplitude of the RA spectrum is smaller, the minimum broader, and its position is shifted towards higher photon energy. The change of the amplitude and the line shape of the RA spectrum could be caused by a change in a ratio of the majority to the minority domain, a different chemical composition, and surface reconstruction most probably by additional phosphorus atoms on the surface. The line shape of this RA spectrum resembles to the RA spectrum of the TBP-modified Ge(100) surface studied by Barrigon et. al. [117]. Therefore, this supports our assumption that the observed change in the RA spectra are indeed due to the presence of phosphorus on the surface.

In order to investigate the surface structure of the Ge(100) surfaces after annealing under TBP molar flow, the Ge(100):As surfaces were annealed at 600°C at two different TBP molar flows based on previous experiment shown in Fig. 7.2, which we will refer a 'high TBP' flow and thereafter a 'low TBP' flow [152]. Here the molar flow of 'low TBP' was selected (compared to the experiment shown in Fig. 7.2) even less (by changing the pressure of the precursor bubbler) to see further influence of the TBP molar flow on the Ge(100) surface structure. Selected samples were transferred by a contamination-free MOCVD-to-UHV transfer system [159] to LEED and XPS to investigate the surface structure and the chemical composition. Prior to the transfer, directly after the pre-growth step, samples were cooled to 330°C under the TBP flow, and additional annealing without TBP at 380°C was performed to desorb excess of phosphorous atoms and the TBP precursor residuals from the surface. Each process was monitored *in situ* by RAS, in a time-resolved (transient) mode at a fixed photon energy at 1.9 eV, as at this photon energy the characteristic RAS minimum from both As- and P-terminated Ge(100) surfaces is related to the dimerized surface [17,18,117].

Fig. 7.3 (a) shows the same time resolved RAS (red RA spectrum) corresponding to the As-terminated Ge(100) surface as already shown in Fig. 7.1 (a) along with the transient signals of subsequently annealed Ge(100):As surfaces under the high and the low molar flow of the TBP precursor, the black and the orange transient, respectively [152]. The RAS transient signals taken during the preparation of the As-terminated Ge(100) surfaces were identical for both samples annealed with high and low TBP molar flow, and thus only one transient is shown. The *in situ* transients show that the anisotropy from the Ge(100):As surfaces changes immediately with the exposure to the TBP precursor (Fig. 7.3 (a)): a sudden decrease of the intensity of the RAS signal for the sample annealed under high TBP molar flow (black line), and a slower, gradual decrease towards lower RAS intensity for the sample annealed with low TBP molar flow (orange line). The RAS signal is stable after around 1 min and 5 min for

the samples annealed under high and low TBP molar flow, respectively, which indicates no further changes in the surface structure.

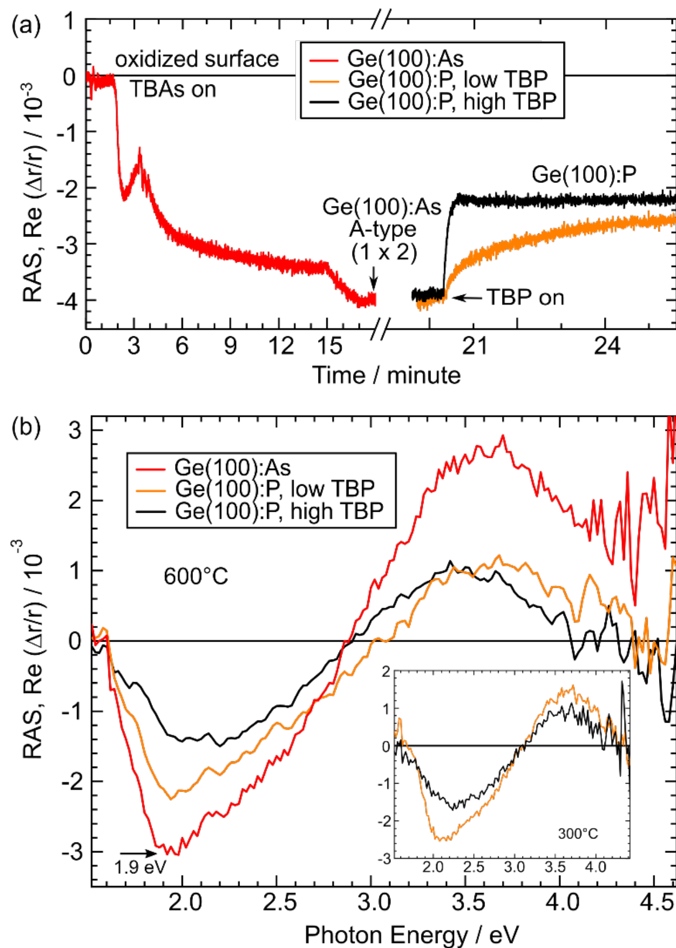

Figure 7.3: (a) *In situ* transient measurements at 1.9 eV photon energy of Ge(100):As surface (red line) along with the two Ge(100) surfaces after exposed to high (black line) and low (orange line) molar flow of TBP precursor; (b) corresponding RA spectra taken at 600°C and at 300°C in inset [152].

Fig. 7.3 (b) show RA spectrum at 600°C of the Ge(100):As surface already shown in Fig. 7.1 (b) and added here as for reference along with the RA spectra of the Ge(100):As surfaces exposed to the TBP precursor. The surfaces annealed with different TBP molar flow show two different characteristic RA spectra [152]. The negative sign of all RAS signals at around 2.0 eV confirms a prevalence of the A-type domain [17,18]. The RA spectrum of the P-modified Ge(100) sample prepared under low TBP flow has a higher intensity and exhibits a small additional feature at 1.9 eV, compared to the RA spectrum of the sample prepared under high TBP flow. The line shape of this RA spectrum is more similar to the Ge(100):As surface

(see the red spectrum in Fig. 7.1 (b) and Fig. 7.3 (b)). In contrast, the RA spectrum of the P-modified Ge(100) sample prepared under high TBP flow has a lower intensity and its negative peak is broader with a minimum at around 2.1 eV. The RAS line shape and the amplitude of the TBP-modified Ge(100) sample prepared under high TBP flow is almost identical to the one from Ge(100):P sample prepared in a Ga- and As-free CVD reactor in *Ref.* [117]. The difference in the line-shape and the position of the negative peak at around 2.0 eV between the 'high TBP' and 'low TBP' sample indicates different surface structure and/or surface chemical composition [152]. The Ge(100) surfaces exposed to high and low TBP molar flow were cooled under TBP and transfer to UHV for LEED and XPS measurements, see experimental part. At 300°C prior to the transfer in UHV, RA spectra were measured, as shown in the inset in Fig. (b). At this temperature there is no P or As thermal desorption from the Ge(100) surface. Compared to the RA spectra measured at 600°C, the line-shape of the RA spectra at 300°C is preserved, except for the shifts towards higher photon energy due to the lower temperature [137,158]. Therefore, the measured chemical composition and the surface reconstruction can be assigned to the Ge(100) surface prior to III-P epitaxial layer.

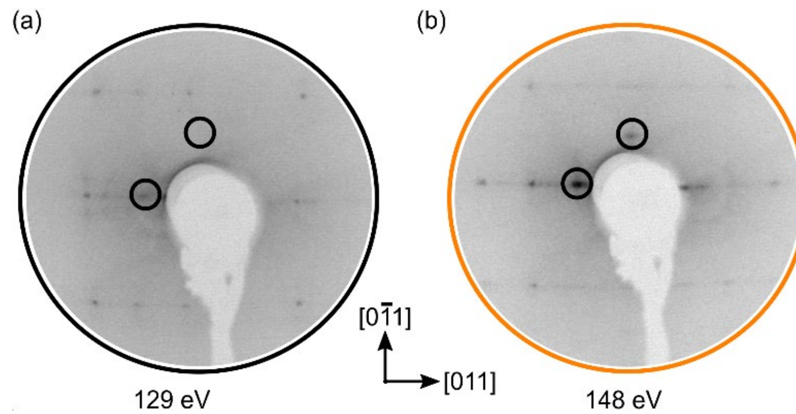

Figure 7.4: LEED patterns of the Ge(100) surface after annealing with (a) high and (b) low molar flow of TBP precursor. The surface prepared with the high TBP show a single domain, (1×2) reconstructed Ge(100) surface whereas the surface prepared with low TBP shows a two domain Ge(100) surface with the prevalence of (1×2) domain [152].

To examine the surface reconstruction of the Ge(100) surfaces exposed to high and low TBP molar flow, the samples were measured by LEED. Fig. 7.4 shows the corresponding LEED patterns. The contrast between the LEED spots and the background in both of the patterns is very weak and the LEED spots are blurry, which indicates that the surfaces are not very well-ordered. However, the Ge(100) surface after exposure to high molar flow of TBP (Fig. 7.4 (a)) exhibits a single domain, (1×2) like surface reconstruction along the [0$\bar{1}$1] direction and the Ge(100) surface exposed to low molar flow of TBP (Fig. 7.4 (b)) shows a rather mixed,

two domain (1×2)/(2×1) surface reconstruction, with a prevalence of the (1×2) domain. The P and As coverage in dependence on the pre-growth step was investigated by XPS [152].

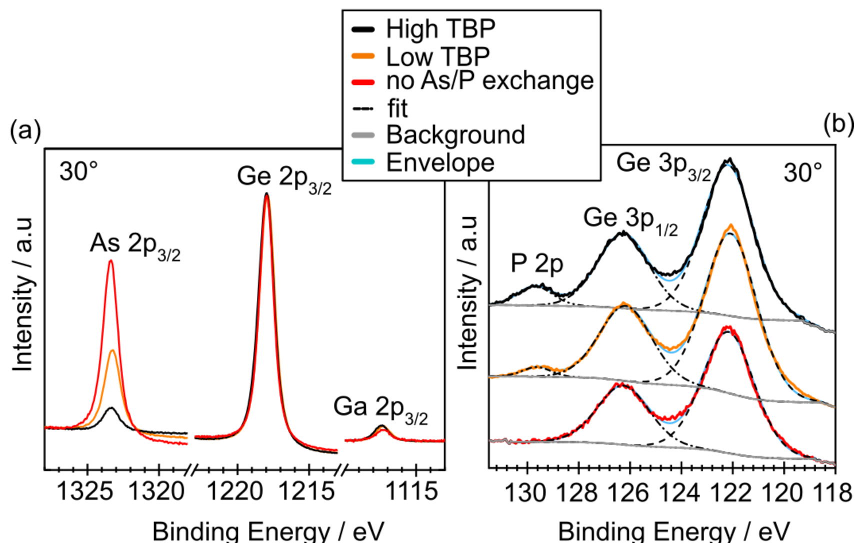

Figure 7.5: XPS measurements at 30° photoelectron takeoff angle of Ge $2p_{3/2}$, As $2p_{3/2}$ and Ga $2p_{3/2}$ (a) and Ge 3p and P 2p (b) PE lines from Ge(100):As (red line) and two Ge(100) surfaces after exposure to high (black line) and low (orange line) TBP molar flow [152].

Fig. 7.5 (a) and (b) show the photoemission (PE) lines of As $2p_{3/2}$, Ge $2p_{3/2}$ and Ga $2p_{3/2}$ and deconvolution of Ge 3p from all three Ge(100) samples, respectively. To facilitate a direct comparison of the data, the intensities of the As and Ga $2p_{3/2}$ core levels were normalized by matching the intensities of the Ge $2p_{3/2}$ line. Neither oxygen nor carbon were detected on all the samples (not shown here) by XPS. Arsenic is present on all three Ge(100) samples shown in Fig. 7.5 (a) and P is present on the 'low TBP' and 'high TBP' Ge(100) samples as shown in Fig. 7.5 (b). The intensity of the As $2p_{3/2}$ PE line is significantly lower for the sample 'high TBP' compared to the sample 'low TBP' and the P coverage is higher for the sample 'high TBP'. On all samples we observe small amount of Ga residuals due to uncontrollable desorption from the reactor walls.

Table III: Area ratio of P 2p / Ge 3p, As $2p_{3/2}$ / Ge $2p_{3/2}$ PE lines for all prepared Ge(100) surfaces.

PE line	High TBP	Low TBP	TBP free
P 2p / Ge 3p	0.17	0.07	-
As $2p_{3/2}$ / Ge $2p_{3/2}$	0.02	0.09	0.22

To quantify the difference in the P and As coverage on the Ge(100) surfaces the peak areas shown in Fig. 7.5 were corrected by photoelectron ionization cross sections taken from Yeh and Lindau [129] and transmission functions exported form the spectrometer, and are summarized in the Table III shown above. The P coverage is more than double for the 'high TBP' sample compared with the 'low TBP' sample and the As coverage is 4.5 times lower. Since the inelastic mean free path is larger than at least few monolayers [160] adding one ML of P would not lead to such a decrease of the As/Ge ratio. Therefore, we conclude that P at least partially substitutes the As atoms. Both, RAS and XPS indicate two different chemical compositions of the Ge(100) surfaces after the annealing under the TBP precursor supply.

7.2 Defects in the III-P(100) buffer layers in dependence on the pre-growth procedure applied on the Ge(100) surfaces

In the following we will investigate the impact of the pre-growth procedures of the Ge(100):As surfaces on the epitaxy of thin III-P buffer layers. Fig. 7.6 shows the RA transient signals at 1.9 eV of the Ge(100) surfaces during the pre-growth step (same as shown in Fig. 7.3 (a)) and transient signals during the subsequent III-P epitaxial growth, annealed under high (black line), low (orange line) TBP molar flow and without (blue line) the exposure to the TBP precursor right before the growth [152]. For ease of comparison, the transients were shifted on the time axis to the moment of the start of growth (i.e. the moment when group-III precursors are injected at around 29.5 min).

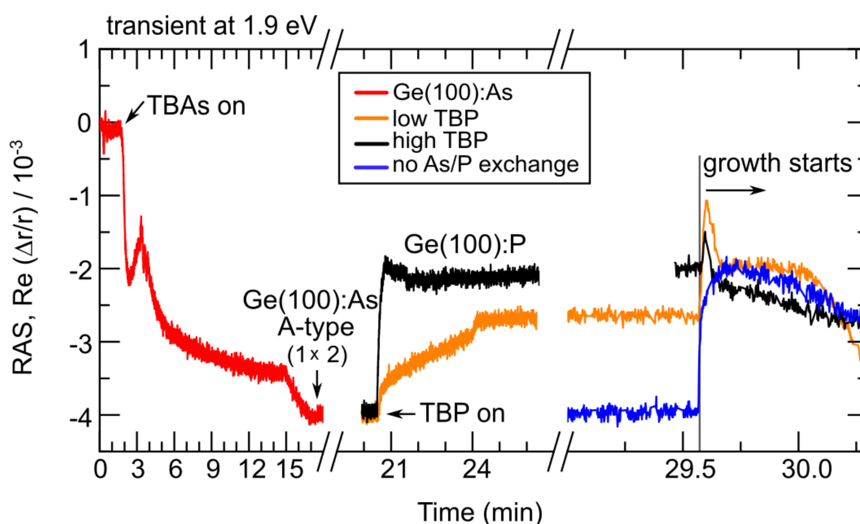

Figure 7.6: *In situ* transient from the Ge(100):As and subsequent As-P exchange on the surfaces and III-P samples grown on 'high TBP' (black line), 'low TBP' (orange line) and on Ge(100) surface of 'no As/P exchange' (blue line) samples, respectively [152].

The RA transients show different evolution of the RAS signal intensity already at the beginning of the initial III-P growth indicating different interaction of the precursors with the Ge(100) surface. Right after the group-III precursors were injected, the Ge(100) surfaces annealed under high (black line) and low (orange line) TBP molar flow, show a steep decrease of the negative RAS intensity for a duration of around 2 seconds followed by a fast recovering of the intensity which suggest temporarily reduced anisotropy on the surface due to an isotropic nanoscopic event. Most likely, we captured here the initial build up and the final coalescence of homogenous distributed III-V nucleation islands on top of the TBP-modified Ge(100):As surface. In contrast, the transient RA signal from the III-P layer grown on the Ge(100) surfaces without prior exposure to a TBP flow (blue line) do not exhibit a steep decrease and recovering during the injection of the group III precursors. This indicates a III-V nucleation event with insufficient isotropic homogeneity creating as a result a dynamic superposition of the RA signals of TBP-prepared Ge(100):As and III-P(100) surface domains until coalescence of the III-P buffer layer is reached. The transient signal of the sample without pre-exposure to TBP shows an abrupt decrease in the intensity with the injection of the group-III and -V precursors. During the first 20 seconds of the III-P growth, the intensity and the trajectory of the RA transient is very similar for all samples. At this stage, during III-V growth, all transient signals start to oscillate due to Fabry-Pérot interferences.

The influence of the III-V/Ge(100) heterointerface on the surface morphology of the III-P layer was investigated by AFM. Fig. 7.7 shows selected AFM scans (5 µm × 5 µm) from the initial grown III-P layers prepared on the samples with high (a), low (b) and no exposure (c) to TBP prior to the growth. A line scan from each image is plotted in Fig. 7.7 (d). All samples show a similar surface morphology with small islands stretched and oriented along the step edges of the Ge(100) substrate, but they differ in the surface roughness. The RMS roughness values on sample (a), (b), and (c) are 0.90, 2.80 and 1.53 nm, respectively. In particular, the III-P surface shown in Fig. 7.7 (b) exhibits some dark morphological features, which are approximately 60 nm – 80 nm wide on the surface. The difference in line profile scans and corresponding surface roughness from all the III-P samples confirms that a modification of the heterointerface by As-P exchange on the Ge(100) surface has a high impact on the surface morphology of the epitaxial grown buffers [152].

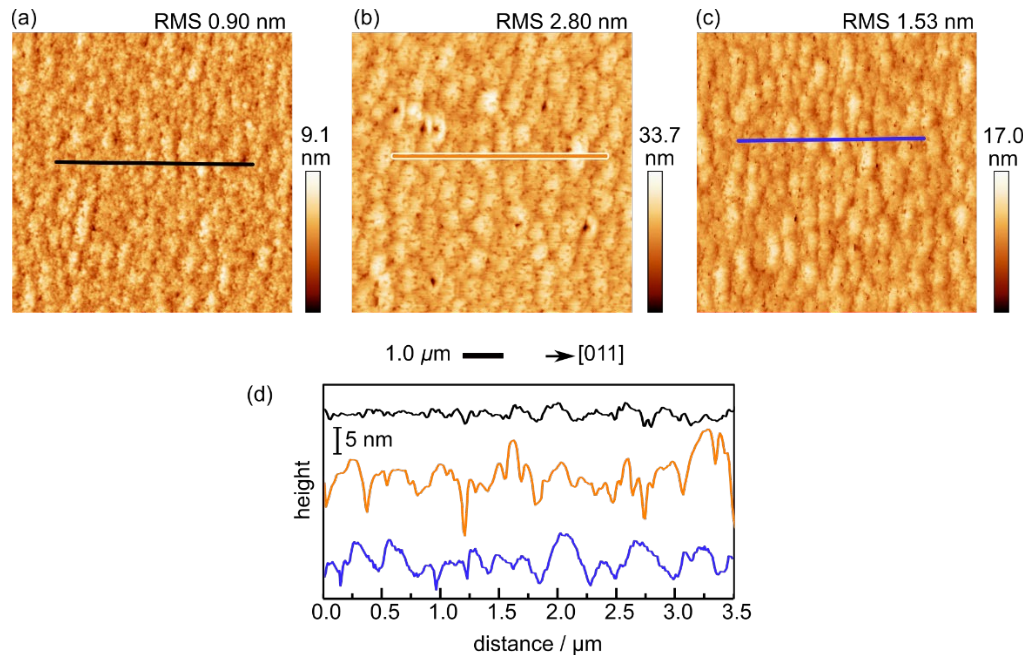

Figure 7.7: AFM scans from III-P samples grown on the Ge(100):As surface annealed with (a) high TBP, (b) (low TBP) and (c) on the surface without annealing under TBP, respectively. (d) represents the corresponding line profiles from these samples [152].

The defect density in the III-P(100) buffers was studied by ECCI [152]. In principle, ECCI scans reflect a superposition of two signals, a signal from presence of defects in the buffer layer and the signal from the surface morphology of the investigated sample. In conventional SEM mode, with commonly applied voltage below ≤ 20 kV, the surface morphology can be imaged. If the acceleration voltage is set higher, to 30 kV, the electron channeling effect is possible and defects can be visible in the SEM scans. However, during the conventional SEM measurements, the penetration depth of the electron beam is much lower than in the ECCI mode and therefore only defects close to the surface can be resolved. Thus, in order to clearly distinguish defects in the bulk, close to the surface and between the surface morphology, from each position on all samples both, ECCI and SEM scans were performed.

Fig. 7.8 shows selected ECCI scans from three different III-P(100) buffer layers discussed above. These samples were measured under the channeling conditions which carry both of the surface and bulk sensitive signals. Surface sensitive ECCI scans were taken under the channeling $\vec{g}$ = (100) for all of the III-P samples grown on the Ge(100) surfaces prepared with (a) 'high TBP', (b) 'low TBP', (c) 'no As/P exchange', respectively. In addition, corresponding SEM scans from the same positions measured in ECCI are shown as for comparison. The substrate offcut direction as well as the channeling conditions were mentioned above each of the images. The acceleration voltage used during the scans were notified at the bottom of each of the images. The III-P sample shown in (a) exhibits no defects

features and therefore no contrast of defect is visible in the corresponding SEM scans. In contrast, all the III-P samples shown in (b), (c) exhibit defects and they are visible in the corresponding SEM scans. These defects appear as dark spots and are observed on all the sample surfaces. However, the sample shown in (b) exhibit high density of these features compared to the other III-P samples shown in (c). In order to understand whether these defects originate at the heterointerface or are formed during the growth, in the bulk, ECCI scans corresponding to the bulk sensitive signals under specific channeling conditions were carried out for all of the III-P samples. Fig. 7.8 (a'), (b') are the selected ECCI scans from the III-P samples nucleated on 'high TBP' and 'low TBP' procedure, respectively. For comparison, for sample 'high TBP' (a'') and 'low TBP' (b'') corresponding to the SEM scans from the same position are shown. The ECCI micrograph of III-P(100) buffer layer (taken under the channeling $\vec{g}$ = (040) condition) shown in Fig. 7.8 (a') exhibits no features or defects as same as observed under the channeling condition of $\vec{g}$ = (100) (shown in (a)). The corresponding SEM image from the same position (Fig. 7.8 (a''), applied voltage 30 kV) shows the surface without defects and with smooth morphology. In contrast, the ECCI scan from the III-P(100) buffer layer grown on the 'low TBP' Ge(100) surface shown in Fig. 7.8 (b') (channeling of $\vec{g}$ = $(02\overline{2})$) exhibits oblong and circular black spots, with a diameter (or radius) of approximately 120 nm - 140 nm. ECCI scans measured under channeling $\vec{g}$ = (040) and surface sensitive $\vec{g}$ = (100) show very similar features (as shown in (b)). The contrast of the images indicates that these features are holes and since the channeling condition, $\vec{g}$ = $(02\overline{2})$ allows for the electrons to channel close to the heterointerface we conclude that the defects originate at the III-P/P-modified Ge(100):As heterointerface. The corresponding SEM image from the same position taken with the acceleration voltage of 30 kV (Fig. 7.8 (b'')) shows defects at the same position (see red circles) and confirms that the defects propagate through the III-P(100) buffer layer up to the close to the surface region. These features are not visible in the SEM scan, which was taken from the same position at the acceleration voltage of 20 kV (red dot circles) in which only surface morphology is visible. This confirms that the features visible in the scans are indeed due to defects in the bulk and not due to the surface morphology. Fig. 7.8 (c') show ECCI scans from III-P(100) samples grown on the Ge(100):As surface without exposure to TBP. This ECCI scans was taken under the channeling $\vec{g}$ = (004). Compared to Fig. 7.8 (a') and (b'), selected scan under the channeling $\vec{g}$ = (004) is shown here since better contrast of defects was observed.

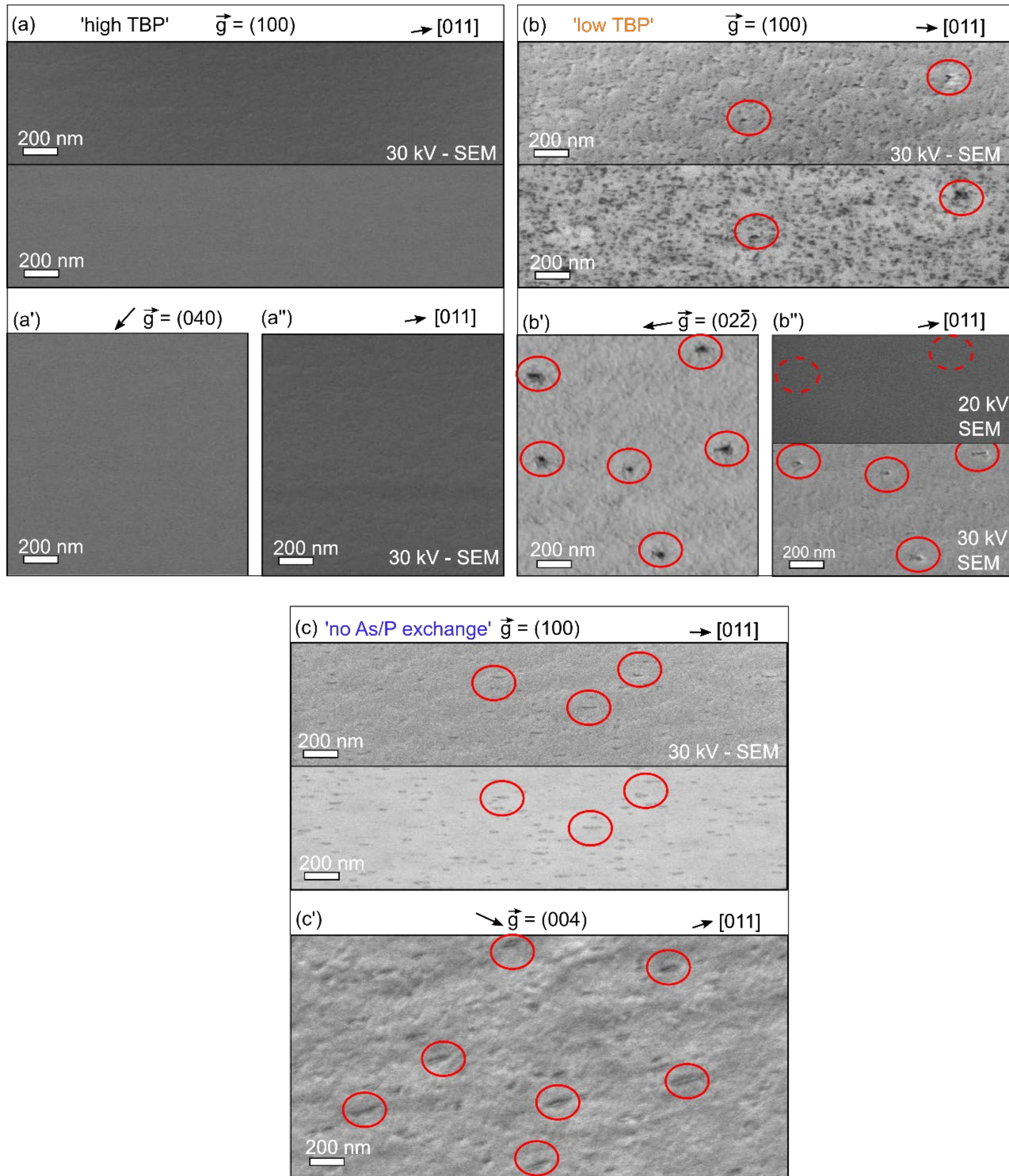

Figure 7.8: ECCI and SEM scans from III-P samples (a), (a'), (a'') grown on the TBP modified surface (high TBP) under the $\vec{g} = (100)$, $\vec{g} = (040)$, (b), (b'), (b'') grown on the TBP modified surface (low TBP) under the $\vec{g} = (100)$, $\vec{g} = (02\bar{2})$ and (c), (c') grown on the As-terminated Ge(100) surface without exposure to TBP under the $\vec{g} = (100)$, $\vec{g} = (004)$, respectively. The channeling condition $\vec{g} = (100)$ allows to resolve defects close to the surface and all other channeling conditions taken here allow the electron beam channels through the layers and therefore carry bulk sensitive signals [152].

In comparison to Fig. 7.8 (b’) we observe mostly longer oblong features with the length of approximately 140 nm (marked by red circles). Same as for the sample (b’), SEM scans (20 kV) of the sample shown in (c’) do not show these features (not shown here) and thus, we correlate them to defects which originate close to the heterointerface. Since the ECCI scans taken at more surface sensitive $\vec{g}$ = (100) condition, these features are also observed (same as from the SEM scans taken at 30 kV, see (c), which confirms that the defects propagate through the III-P bulk. The defects shown in samples ((b’), (c’)) are oriented along offcut of the substrate, i.e. perpendicular to the step edges. An estimation on the defect density (the observed oblong features and the holes) was calculated from the selected ECCI scans. The defect densities of 1.7×10^{9} cm^{-2} and 9.78×10^{8} cm^{-2} were estimated from the III-P samples grown on the Ge(100) surfaces annealed with ‘low TBP’ (Fig. 7.8 (b’)) and the Ge(100) surface with ‘no As/P exchange’ (Fig. 7.8 (c’)), respectively. The defect densities mentioned here is a total of densities calculated from both of the ECCI scans corresponding to the surface and bulk sensitive channeling conditions. We did not observe other defects, such as misfit dislocations or threading dislocations. We assume that the thickness of the thin epilayers does not reach critical limit in which the misfit dislocation could form. The exact origin of the defects requires a further study; however, we can clearly conclude that the different process routes of the As-P exchange on the Ge(100) surface strongly influence the defect formation at the III-P/Ge(100) heterointerface.

7.3 Summary of this chapter

We have studied a pre-growth step on Ge(100):As surfaces prior to III-P(100) buffer growth in which the molar flow of TBP precursor was varied. Different molar flows of TBP precursor during the pre-growth step impacts the chemical compositions as well as the surface reconstructions of Ge(100):As surfaces. This reflects on the characteristic *in situ* RAS signals, in particular, the line shape, peak position and intensity of the RA spectra, which indicate a competition of two different Ge(100):As/P surface structures. XPS measurements confirm a partial replacement of As with P on the Ge(100) surface annealed with high molar flow of TBP. While the AFM scans shows very similar surface morphologies of subsequent III-P(100) buffer layers grown after different pre-growth steps, the ECCI measurements exhibit a strong dependence of formation defects on substrate surface preparation.

8 Conclusion

Epitaxial growth of III-V materials on Si(100) or Ge(100) substrates open opportunities for a wide range of cost effective high performance photovoltaic, photoelectrochemical and optoelectronic devices. Lattice matched GaP/Si(100) can serve as a high quality virtual substrates for subsequent heteroepitaxial growth. Prior to the growth of III-P epilayers, formation of a double atomic stepped, single domain, Si(100) and Ge(100) surfaces is prerequisite in order to avoid APDs in the III-P layers. Research shown in this work focused on: (i) preparation of Si(100) double-layers stepped surface, in both As-rich and GaP-rich reactor conditions and understanding the surface structure in atomic scale, (ii) a modifying GaP nucleation by introducing Al at the GaP/Si(100) heterointerface in order to reduce density of crystalline defects in the GaP bulk and (iii) investigation of a pre-growth step applied on Ge(100):As surface to achieve low defect density in III-P epilayers.

The surface preparation as well as the entire growth process studied in this work was carried out in a MOCVD reactor. Growth process in the MOCVD environment is complex since the process gas and the precursors strongly interact with the semiconductor surface. In addition, a precise control of the process parameters (substrate temperature, reactor pressure, molar flows of the precursors and total gas flow in the reactor) is required to achieve an optimum growth condition. In order to monitor the changes in the surface during a process, *in situ* RAS was employed. The *in situ* RA spectrum corresponding to a processed sample was further benchmarked by surface sensitive tools (XPS, LEED, STM) after transferring the sample through contamination free UHV transfer shuttle. This allows to understand the origin of changes in the RA spectra during a process and to further establish an optimized process conditions for a required sample preparation. *Ex situ* methods AFM and ECCI allow to investigate the surface morphology and the crystalline defects in the processed samples. The ECCI has been established in Ilmenau during this work and proved as a fast, non-destructive mothed for defect quantification on a large scale.

Presence of crystalline defects in the III-V epilayers, such as anti-phase domains, misfit dislocations, threading dislocations (TDs), stacking faults (SFs) and stacking fault pyramids (SFPs) significantly limits the carrier lifetime in the final device structure and therefore the theoretical photovoltaic solar conversion efficiency. Thus, the Si(100) and Ge(100) surface and the III-V/substrate heterointerface must be precisely controlled. In this study, it was demonstrated that a precise control of dimer formation on the Si(100) surface can be possible by varying the reactor pressure and temperature. In addition, depending on the different source of arsenic (TBAs or background As_4) applied during the process, the orientation of dimers can be controlled: The Si(100):As 4° surface exhibit a prevalence of (1×2) and (2×1) surface reconstruction when processed under the TBAs and the background As_4, respectively

and in contrast, the Si(100):As 0.1° exhibits a prevalence of (1×2) surface reconstruction while preparing under the background As_4. The surface preparation with the TBAs is found to be a kinetically driven process whereas the one with the background As_4 is energetically favorable process. XPS measurements confirm presence of arsenic and high amount of arsenic content is present on the Si(100):As 0.1° surface while preparing the surface with the background As_4 compared to the arsenic content on the Si(100):As 4° surface prepared with the TBAs. The surface preparation becomes more challenging when the III-V residuals from previous MOCVD processes are present in the reactor. We have showed that the maximum process temperature of the Si surface preparation can be lowered by employing a wet chemical HF pre-treatment while preparing in this III-V-rich reactor conditions. This allows to remove the oxide layer chemically and provides a faster surface preparation route. The STM measurements at atomic scale showed that the dimerized Si(100) surfaces exhibit dimer rows along steps on the surface. The Si(100) surfaces prepared with either TBAs or with background As_4, show both symmetric As-As dimers and asymmetric, e.g As-Si-H dimers.

The novelty of this research is the application of Al during GaP nucleation, which shows a remarkable reduction of defects in the subsequent GaP layers. For GaP/AlP nucleation, the nucleation sequence starts with five alternating pulses of TMAl and TBP followed by five pulses of TEGa and TBP in contrast to ten alternating pulses of TEGa and TBP established for pure GaP nucleation. Quantitative analysis shows that the densities of SFs and SFPs are reduced by about 2 orders of magnitude in the epilayers grown on the GaP/AlP/Si:As(100) nucleation layers compared to pure GaP ones (2×10^7 cm^{-2} compared to 1.5×10^9 cm^{-2}). Concomitantly, the TD density in these GaP epilayers is reduced by nearly 1 order of magnitude from 3×10^7 cm^{-2} to 6.5×10^6 cm^{-2}. The examination of the nucleation layer deposition utilizing XPS, LEED and optical RAS, has showed clear signatures of Al on top of the As-terminated Si(100) surface in the interfacial formation. AFM scans from GaP epilayers grown on the pure GaP nucleation exhibits small grains and a rougher surface morphology compared to the GaP epilayers grown on the GaP/AlP/Si:As nucleation, which exhibits flat terraces, and small trenches along the Si(100) step edges. The results studied here indicate that the different surface structure and morphologies of the nucleation layers have a strong impact on the subsequent GaP growth and layer properties: formation of SFs, SFPs in the epilayer, and density of TDs. In addition to the GaP/Si(100) heteroepitaxy, it is also demonstrated here that the quality of the III-V/substrate heterointerface determines the defect density of the III-P epilayers while grown on the Ge(100):As surface. Prior to the growth of III-P layers, a pre-growth step, which involves thermal annealing of the Ge(100):As surface under TBP precursor, is found to be a decisive step in which the As atoms are partially replaced with P atoms. It has been found that the molar flow of the TBP precursor strongly influence the chemical composition and the surface structure of the

Ge(100) surface. These changes were monitored by *in situ* RAS and a characteristic RA spectrum with different line shapes were benchmarked with their surface chemical composition and reconstruction. The LEED pattern of the Ge(100) surface prepared with a high molar flow of TBP shows a single domain, (1×2) surface reconstruction whereas the surface prepared with a low molar flow of TBP exhibits a two-domain surface structure. The investigation of crystalline defects by ECCI in the subsequently grown III-P epilayers has showed that a defect-free III-P epilayers can be grown on the Ge(100) surface with a pre-growth step which involves annealing under high molar flow of TBP for not longer than 5 min. In contrast, the III-P epilayer grown on the other pre-growth route with not optimized TBP molar flow exhibits high density of defects. A combined SEM measurement along with the ECCI confirm that the defects observed in the III-P layers originate from close to the heterointerface and propagate through the buffer layer towards the surface. The III-P surface morphologies show similar surface structure but different roughness. A precisely controlled pre-growth step is crucial in order to achieve a defect-free III-P epilayers on the Ge(100) surface.

The work presented in this thesis opens the opportunity to establish MOCVD processing of planar growth of GaP/Si(100) and III-P/Ge(100) with low defect density in the III-V buffer for III-V-on-IV highly efficient devices. This involves a quick and low thermal budget Si(100) surface preparation with well-defined surface with double-layer atomic steps. Future work will focus on further reduction of the defect density in the GaP/Si(100) epilayer by optimizing the nucleation and growth conditions. Future work will also involve understanding the origin and the atomic structure of the defects in the GaP(100) and III-P(100) buffer layers.

References

[1] G. Carr, Sunny Uplands: Alternative energy will no longer be alternative, Econ. (2012).

[2] A. Grimm, W.A. de Jong, G.J. Kramer, Renewable hydrogen production: A techno-economic comparison of photoelectrochemical cells and photovoltaic-electrolysis, Int. J. Hydrogen Energy. 45 (2020) 22545–22555.

[3] W.H. Cheng, M.H. Richter, M.M. May, J. Ohlmann, D. Lackner, F. Dimroth, T. Hannappel, H.A. Atwater, H.J. Lewerenz, Monolithic Photoelectrochemical Device for Direct Water Splitting with 19% Efficiency, ACS Energy Lett. 3 (2018) 1795–1800.

[4] J.F. Geisz, R.M. France, K.L. Schulte, M.A. Steiner, A.G. Norman, H.L. Guthrey, M.R. Young, T. Song, T. Moriarty, Six-junction III–V solar cells with 47.1% conversion efficiency under 143 Suns concentration, Nat. Energy. 5 (2020) 326–335.

[5] F. Dimroth, M. Grave, P. Beutel, U. Fiedeler, C. Karcher, T.N.D. Tibbits, E. Oliva, G. Siefer, M. Schachtner, A. Wekkeli, A.W. Bett, R. Krause, M. Piccin, N. Blanc, C. Drazek, E. Guiot, B. Ghyselen, T. Salvetat, A. Tauzin, T. Signamarcheix, A. Dobrich, T. Hannappel, K. Schwarzburg, Wafer bonded four-junction GaInP/GaAs//GaInAsP/GaInAs concentrator solar cells with 44.7% efficiency, Prog. Photovolt Res. Appl. 20 (2012) 1114–1129.

[6] S. Fan, Z.J. Yu, R.D. Hool, P. Dhingra, W. Weigand, M. Kim, E.D. Ratta, B.D. Li, Y. Sun, Z.C. Holman, M.L. Lee, Current-Matched III–V/Si Epitaxial Tandem Solar Cells with 25.0% Efficiency, Cell Reports Phys. Sci. 1 (2020) 100208.

[7] M. Feifel, D. Lackner, J. Schön, J. Ohlmann, J. Benick, G. Siefer, F. Predan, M. Hermle, F. Dimroth, Epitaxial GaInP/GaAs/Si Triple-Junction Solar Cell with 25.9% AM1.5g Efficiency Enabled by Transparent Metamorphic AlxGa1−xAsyP1−y Step-Graded Buffer Structures, Sol. RRL. 2000763 (2021) 1–7.

[8] O. Supplie, M.M. May, S. Brückner, N. Brezhneva, T. Hannappel, E. V. Skorb, In Situ Characterization of Interfaces Relevant for Efficient Photoinduced Reactions, Adv. Mater. Interfaces. 4 (2017) 1601118.

[9] M.M. May, D. Lackner, J. Ohlmann, F. Dimroth, R. Van De Krol, T. Hannappel, K. Schwarzburg, On the benchmarking of multi-junction photoelectrochemical fuel generating devices, Sustain. Energy Fuels. 1 (2017) 492–503.

[10] I. Vurgaftman, J.R. Meyer, L.R. Ram-Mohan, Band parameters for III-V compound semiconductors and their alloys, J. Appl. Phys. 89 (2001) 5815–5875.

[11] J.F. Geisz, J.M. Olson, M.J. Romero, C.S. Jiang, A.G. Norman, Lattice-mismatched GaAsP solar cells grown on silicon by OMVPE, Conf. Rec. 2006 IEEE 4th World Conf. Photovolt. Energy Conversion, WCPEC-4. 1 (2006) 772–775.

[12] K.N. Yaung, M. Vaisman, J. Lang, M.L. Lee, GaAsP solar cells on GaP/Si with low threading dislocation density Cite, Appl. Phys. Lett. 109 (2016) 032107.

[13] H. Kroemer, Polar-on-nonpolar epitaxy, J. Cryst. Growth. 81 (1987) 193–204.

[14] S. Brückner, H. Döscher, P. Kleinschmidt, O. Supplie, A. Dobrich, T. Hannappel, Anomalous double-layer step formation on Si(100) in hydrogen process ambient, Phys. Rev. B - Condens. Matter Mater. Phys. 86 (2012) 195310.

[15] O. Supplie, M.M. May, P. Kleinschmidt, A. Nägelein, A. Paszuk, S. Brückner, T. Hannappel, In situ controlled heteroepitaxy of single-domain GaP on As-modified Si(100), APL Mater. 3 (2015) 126110.

[16] S. Brückner, E. Barrigón, O. Supplie, P. Kleinschmidt, A. Dobrich, C. Löbbel, I. Rey-stolle, H. Döscher, T. Hannappel, A. Dobrich, E. Barrigón, O. Supplie, C. Löbbel, I. Rey-stolle, P. Kleinschmidt, T. Hannappel, Ge(100) surfaces prepared in vapor phase epitaxy process ambient, Phys. Status Solidi - Rapid Res. Lett. 6 (2012) 178–180.

[17] S. Brückner, O. Supplie, E. Barrigón, J. Luczak, P. Kleinschmidt, I. Rey-Stolle, H. Döscher, T. Hannappel, In situ control of As dimer orientation on Ge(100) surfaces, Appl. Phys. Lett. 101 (2012) 121602.

[18] A. Paszuk, O. Supplie, S. Brückner, E. Barrigón, M.M. May, M. Nandy, A. Gieß, A. Dobrich, P. Kleinschmidt, I. Rey-Stolle, T. Hannappel, Atomic surface control of Ge(100) in MOCVD reactors coated with (Ga)As residuals, Appl. Surf. Sci. 565 (2021) 150513.

[19] J. Faucher, T. Masuda, M.L. Lee, Initiation strategies for simultaneous control of antiphase domains and stacking faults in GaAs solar cells on Ge, J. Vac. Sci. Technol. B, Nanotechnol. Microelectron. Mater. Process. Meas. Phenom. 34 (2016) 041203.

[20] K. Sears, J. Wong-Leung, H.H. Tan, C. Jagadish, A transmission electron microscopy study of defects formed through the capping layer of self-assembled InAs/GaAs quantum dot samples, J. Appl. Phys. 99 (2006) 113503.

[21] W. Shockley, H.J. Queisser, Detailed balance limit of efficiency of p-n junction solar cells, J. Appl. Phys. 32 (1961) 510–519.

[22] D.J. Friedman, J.F. Geisz, S.R. Kurtz, J.M. Olson, 1-eV GaInNAs solar cells for ultrahigh-efficiency multijunction devices, 2nd World Conf. Exhib. Photovolt. Sol. Energy Convers. (1998) 3–7.

[23] C.H. Henry, Limiting efficiencies of ideal single and multiple energy gap terrestrial solar cells, J. Appl. Phys. 51 (1980) 4494–4500.

[24] A. De Vos, Detailed balance limit of the efficiency of tandem solar cells, J. Phys. D. Appl. Phys. 13 (1980) 839–846.

[25] S. Bremner, P, Y.M. Levy, B.C. Honsberg, Analysis of Tandem Solar Cell Efficiencies Under AM1.5G Spectrum Using a Rapid Flux Calculation Method, Prog. Photovoltaics Res. Appl. 16 (2008) 225–233.

[26] J.F. Geisz, M.A. Steiner, I. García, S.R. Kurtz, D.J. Friedman, Enhanced external radiative efficiency for 20.8% efficient single-junction GaInP solar cells, Appl. Phys. Lett. 103 (2013) 041118.

[27] P.P. Nayak, J.P. Dutta, G.P. Mishra, Efficient InGaP/GaAs DJ solar cell with double back surface field layer, Eng. Sci. Technol. an Int. J. 18 (2015) 325–335.

[28] T. Takamoto, E. Ikeda, H. Kurita, M. Ohmori, T. Takamoto, E. Ikeda, H. Kurita, Over 30 % efficient InGaP / GaAs tandem solar cells Over 30 % efficient InGaP / GaAs tandem solar cells, 381 (2014) 30–33.

[29] R.R. King, D.C. Law, K.M. Edmondson, C.M. Fetzer, G.S. Kinsey, H. Yoon, R.A. Sherif, N.H. Karam, 40% efficient metamorphic GaInPGaInAsGe multijunction solar cells, Appl. Phys. Lett. 90 (2007) 90–93.

[30] D.L. Lepkowski, J.T. Boyer, C. Yi, A.H. Soeriyadi, Z.H. Blumer, M.K. Juhl, D. Derkacs, C. Kerestes, A. Stavrides, H. Mehrvarz, A.W.Y. Ho-Baillie, S. Bremner, S.A. Ringel, T.J. Grassman, Loss Analysis and Design Strategies Enabling >23% GaAsP/Si Tandem Solar Cells, Conf. Rec. IEEE Photovolt. Spec. Conf. 2020-June (2020) 1884–1886.

[31] M. Feifel, D. Lackner, J. Ohlmann, J. Benick, M. Hermle, F. Dimroth, Direct Growth of a GaInP/GaAs/Si Triple-Junction Solar Cell with 22.3% AM1.5g Efficiency, Sol. RRL. 3 (2019) 1–7.

[32] M. Feifel, J. Ohlmann, J. Benick, M. Hermle, J. Belz, A. Beyer, K. Volz, T. Hannappel, A.W. Bett, D. Lackner, F. Dimroth, Direct growth of III-V/Silicon triple-junction solar cells with 19.7% efficiency, IEEE J. Photovoltaics. 8 (2018) 1590–1595.

[33] C. Kost, J.N. Mayer, J. Thomsen, N. Hartmann, C. Senkpiel, S. Philipps, S. Nold, S. Lude, N. Saad, T. Schlegl, Levelized Cost of Electricity Renewable Energy Technologies, (2013).

[34] M. Feifel, T. Rachow, J. Benick, J. Ohlmann, S. Janz, M. Hermle, F. Dimroth, D. Lackner, Gallium phosphide window layer for silicon solar cells, IEEE J. Photovoltaics. 6 (2016) 384–390.

[35] H. Wagner, T. Ohrdes, A. Dastgheib-Shirazi, B. Puthen-Veettil, D. König, P.P. Altermatt, A numerical simulation study of gallium-phosphide/silicon heterojunction passivated emitter and rear solar cells, J. Appl. Phys. 115 (2014) 044508.

[36] S.A. Ringel, J.A. Carlin, T.J. Grassman, B. Galiana, A.M. Carlin, C. Ratcliff, D. Chmielewski, L. Yang, M.J. Mills, A. Mansouri, S.P. Bremner, A. Ho-Baillie, X. Hao, H. Mehrvarz, G. Conibeer, M.A. Green, Ideal GaP/Si heterostructures grown by MOCVD: III-V/active-Si subcells, multijuntions, and MBE-to-MOCVD III-V/Si interface science, Conf. Rec. IEEE Photovolt. Spec. Conf. (2013) 3383–3388.

[37] A. Paszuk, O. Supplie, B. Kim, S. Brückner, M. Nandy, A. Heinisch, P. Kleinschmidt, Y. Nakano, M. Sugiyama, T. Hannappel, GaAsP/Si tandem solar cells: In situ study on GaP/Si:As virtual substrate preparation, Sol. Energy Mater. Sol. Cells. 180 (2018) 343–349.

[38] T.J. Grassman, J.A. Carlin, C. Ratcliff, D.J. Chmielewski, S.A. Ringel, Epitaxially-Grown Metamorphic GaAsP / Si Dual-Junction Solar Cells, 2013 IEEE 39th Photovolt. Spec. Conf. (PVSC), Tampa, FL, USA. (2013) 0149–0153.

[39] K.N. Yaung, M. Vaisman, J. Lang, M.L. Lee, GaAsP solar cell on GaP with low threading disloaction density, Appl. Phys. Lett. 109 (2016) 032107.

[40] J.H. van der Merwe, Misfit Dislocation Generation in Epitaxial Layers, Crit. Rev. Solid State Mater. Sci. 17 (1991) 187–209.

[41] M. Tachikawa, H. Mori, Dislocation generation of GaAs on Si in the cooling stage, Appl. Phys. Lett. 56 (1990) 2225–2227.

[42] R.M. Sieg, S.A. Ringel, S.M. Ting, E.A. Fitzgerald, R.N. Sacks, Anti-phase domain-free growth of GaAs on offcut (001) Ge wafers by molecular beam epitaxy with suppressed Ge outdiffusion, J. Electron. Mater. 27 (1998) 900–907.

[43] B. Galiana, I. Rey-Stolle, C. Algora, K. Volz, W. Stolz, A GaAs metalorganic vapor phase epitaxy growth process to reduce Ge outdiffusion from the Ge substrate, Appl. Phys. Lett. 92 (2008) 152102.

[44] I. Vurgaftman, J.R. Meyer, L.R. Ram-Mohan, Band parameters for III–V compound semiconductors and their alloys, J. Appl. Phys. 89 (2001) 5815.

[45] H. Döscher, T. Hannappel, In situ reflection anisotropy spectroscopy analysis of heteroepitaxial GaP films grown on Si(100), J. Appl. Phys. 107 (2010) 123523.

[46] S.-D. Kim, S.M. Lord, J.S. Harris, Strain relaxation in compositionally graded epitaxial layers, J. Vac. Sci. Technol. B Microelectron. Nanom. Struct. 14 (1996) 642–646.

[47] R.M. France, M. Feifel, J. Belz, A. Beyer, K. Volz, J. Ohlmann, D. Lackner, F. Dimroth, Single- and dual-variant atomic ordering in GaAsP compositionally graded buffers on GaP and Si substrates, J. Cryst. Growth. 506 (2019) 61–70.

[48] B. Kunert, K. Volz, J. Koch, W. Stolz, Direct-band-gap Ga(NAsP)-material system pseudomorphically grown on GaP substrate, Appl. Phys. Lett. 88 (2006) 1–4.

[49] S. Miyoshi, H. Yaguchi, K. Onabe, R. Ito, Y. Shiraki, Metalorganic vapor phase epitaxy of $GaP_{1-x}N_x$ alloys on GaP, Appl. Phys. Lett. 63 (1993) 3506–3508.

[50] F. Dimroth, High-efficiency solar cells from III-V compound semiconductors, Phys. Status Solidi C Conf. 3 (2006) 373–379.

[51] B. Kunert, Y. Mols, M. Baryshniskova, N. Waldron, A. Schulze, R. Langer, How to control defect formation in monolithic III/V hetero-epitaxy on (100) Si? A critical review on current approaches, Semicond. Sci. Technol. 33 (2018) 093002.

[52] K. Volz, A. Beyer, W. Witte, J. Ohlmann, I. Nmeth, B. Kunert, W. Stolz, GaP-nucleation on exact Si (0 0 1) substrates for III/V device integration, J. Cryst. Growth. 315 (2011) 37–47.

[53] Y. Takagi, H. Yonezu, K. Samonji, T. Tsuji, N. Ohshima, Generation and suppression process of crystalline defects in GaP layers grown on misoriented Si(100) substrates, J. Cryst. Growth. 187 (1998) 42–50.

[54] T.J. Grassman, M.R. Brenner, S. Rajagopalan, R. Unocic, R. Dehoff, M. Mills, H. Fraser, S.A. Ringel, Control and elimination of nucleation-related defects in GaP/Si(001) heteroepitaxy, Appl. Phys. Lett. 94 (2009) 232106.

[55] K. Sears, J. Wong-Leung, H.H. Tan, C. Jagadish, A transmission electron microscopy study

of defects formed through the capping layer of self-assembled InAs/GaAs quantum dot samples, J. Appl. Phys. 99 (2006).

[56] M. Feifel, J. Ohlmann, M.F. Ryan, D. Lackner, F. Dimroth, Electron channeling contrast imaging investigation of stacking fault pyramids in GaP on Si nucleation layers, J. Cryst. Growth. 532 (2020) 125422.

[57] J. A. Appelbaum, G. A. Baraff, D. R. Hamann, The Si (100) surface. III. Surface reconstruction, Angew. Chemie Int. Ed. 6(11), 951–952. 14 (1967) 5–24.

[58] H. Over, J. Wasserfall, W. Ranke, C. Ambiatello, R. Sawitzki, D. Wolf, W. Moritz, Surface atomic geometry of Si(001)-(2×1): A low-energy electron-diffraction structure analysis, Phys. Rev. B - Condens. Matter Mater. Phys. 55 (1997) 4731–4736.

[59] H.J.W. Zandvliet, The Ge(0 0 1) surface, Phys. Rep. 388 (2003) 1–40.

[60] Mönch. W, Semiconductor Surfaces and Interfaces, 3rd ed., Springer US, 2001.

[61] D.J. Chadi, Stabilities of single-layer and bilayer steps on Si(001) surfaces, Phys. Rev. Lett. 59 (1987) 1691–1694.

[62] S. Brückner, O. Supplie, A. Dobrich, P. Kleinschmidt, T. Hannappel, Control Over Dimer Orientations on Vicinal Si(100) Surfaces in Hydrogen Ambient: Kinetics Versus Energetics, Phys. Status Solidi. 255 (2018) 1870117.

[63] J.J. Boland, Structure of the H-saturated Si(100) surface, Phys. Rev. Lett. 65 (1990) 3325–3328.

[64] P. Gupta, V. L. Colvin, S. M. George, Hydrogen desorption kinetics from monohydride and dihydride species on silicon surfaces, Phys. Rev. B. 37 (1988) 8234–8243.

[65] A. Laracuente, L.J. Whitman, Step structures and energies on monohydride-terminated vicinal Si(0 0 1) surfaces, Surf. Sci. 476 (2001) L247–L253.

[66] J. E. Griffith, G. P. Kochanski, J. A. Kubby, P. E. Wierenga, Steps on Si (001), J. Vac. Sci. Technol. A. 7 (1989) 1914–1918.

[67] A. Paszuk, O. Supplie, M. Nandy, S. Brückner, A. Dobrich, P. Kleinschmidt, B. Kim, Y. Nakano, M. Sugiyama, T. Hannappel, Double-layer stepped Si(1 0 0) surfaces prepared in As-rich CVD ambience, Appl. Surf. Sci. 462 (2018) 1002–1007.

[68] A. Paszuk, O. Supplie, B. Kim, S. Brückner, M. Nandy, A. Heinisch, P. Kleinschmidt, Y. Nakano, M. Sugiyama, T. Hannappel, GaAsP/Si tandem solar cells: In situ study on GaP/Si:As virtual substrate preparation, Sol. Energy Mater. Sol. Cells. 180 (2018) 343–349.

[69] H. Dscher, S. Brckner, A. Dobrich, C. Hhn, P. Kleinschmidt, T. Hannappel, Surface preparation of Si(1 0 0) by thermal oxide removal in a chemical vapor environment, J. Cryst. Growth. 315 (2011) 10–15.

[70] A. Dobrich, P. Kleinschmidt, H. Döscher, T. Hannappel, Quantitative investigation of hydrogen bonds on Si(100) surfaces prepared by vapor phase epitaxy, J. Vac. Sci. Technol. B, Nanotechnol. Microelectron. Mater. Process. Meas. Phenom. 29 (2011) 04D114.

[71] H.M. Manasevit, Single-crystal gallium arsenide on insulating substrates, Appl. Phys. Lett. 12 (1968) 156–159.

[72] H.M. Manasevit, Simpson, W. I, The use of metalorganics in the preparation of semiconductor materials: Growth on insulating substrates, J. Electrochem. Soc. 116 (1969) 1725–1732.

[73] M.S. Dresselhaus, SOLID STATE PHYSICS, Part II: Optical Properties of Solids, Phys. Status Solidi. 34 (1969) 815–824.

[74] D.E. Aspnes, A.A. Studna, Anisotropies in the above-band-gap optical spectra of cubic semiconductors, Phys. Rev. Lett. 54 (1985) 1956–1959.

[75] D.E. Aspnes, J.P. Harbison, A.A. Studna, L.T. Florez, Application of reflectance difference spectroscopy to molecular-beam epitaxy growth of GaAs and AlAs, J. Vac. Sci. Technol. A Vacuum, Surfaces, Film. 6 (1988) 1327–1332.

[76] Haberland. K, Optical in-situ studies during metal-organic vapor phase epitaxy with respect to III-V device production, Ph.D. Thesis. (2002).

[77] H. Hertz, Ueber einen Einfluss des ultravioletten Lichtes auf die electrische Entladung; von H. Hertz., Ann. Phys. 267 (1887) 983–1000.

[78] A. Einstein, Über einen die Erzeugung und Verwandlunglung des Lichtes betreffenden heuristischen Gesichtspunkt; von A. Eilzstein., Ann. Phys. 326 (1905) 132–148.

[79] J.G. Jenkin, R.C.G. Leckey, J. Liesegang, The development of x-ray photoelectron spectroscopy: 1900-1960, J. Electron Spectros. Relat. Phenomena. 12 (1977) 1–35.

[80] M.P.Seah, W.A.Dench, Quantitative Electron Spectroscopy of Surface, Surf. Interface Anal. 1 (1979) 2–11.

[81] D.G. Coates, Kikuchi like reflection patterns obtained with the scanning electron microscope.pdf, Philos. Mag. 16:144 (1967) 1179–1184.

[82] G.R. Booker, A.M.B. Shaw, M.J. Whelan, P.B. Hirsch, Some comments on the interpretation of the ‘kikuchi-like reflection patterns’ observed by scanning electron microscopy, Philos. Mag. 16 (1967) 1185–1191.

[83] Y.N. Picard, R.J. Kamaladasa, Basic Principles and Application of Electron Channeling in a Scanning Electron Microscope for Dislocation Analysis, Microsc. Sci. Technol. Appl. Educ. (2010) 1583–1590.

[84] A.J. Wilkinson, P.B. Hirsch, Electron diffraction based techniques in scanning electron microscopy of bulk materials, Micron. 28 (1997) 279–308.

[85] R.H. Fowler, F.R.S., L. Nordheim, Electron Emission in Intense Electric Fields, Semicond. Devices Pioneer. Pap. 14 (1991) 683–691.

[86] P.K. Hansma, J. Tersoff, Scanning tunneling microscopy, Nanosci. Nanotechnologies Nanophysics. 61 (1987) R1–R23.

[87] I. Horcas, R. Fernández, J.M. Gómez-Rodríguez, J. Colchero, J. Gómez-Herrero, A.M. Baro, WSXM: A software for scanning probe microscopy and a tool for nanotechnology, Rev. Sci. Instrum. 78 (2007) 013705.

[88] R.L. Jackson, Roughness parameters, Handb. Lubr. Tribol. Vol. II Theory Des. Second Ed. 123 (2012) 14-1-14–14.

[89] S. Brückner, O. Supplie, A. Dobrich, P. Kleinschmidt, T. Hannappel, Control Over Dimer Orientations on Vicinal Si(100) Surfaces in Hydrogen Ambient: Kinetics Versus Energetics, Phys. Status Solidi. 255 (2018) 1870117.

[90] S. Brückner, H. Döscher, P. Kleinschmidt, T. Hannappel, In situ investigation of hydrogen interacting with Si(100), Appl. Phys. Lett. 98 (2011) 211909.

[91] S. Brückner, Atomic scale in situ control of Si (100) and Ge (100) surfaces in CVD ambient PhD thesis, (2014).

[92] O. Romanyuk, O. Supplie, T. Susi, M.M. May, T. Hannappel, Ab initio density functional theory study on the atomic and electronic structure of GaP/Si(001) heterointerfaces, Phys. Rev. B. 94 (2016) 1–9.

[93] S. Brückner, P. Kleinschmidt, O. Supplie, H. Döscher, T. Hannappel, Domain-sensitive *in situ* observation of layer-by-layer removal at Si(100) in H_2 ambient, New J. Phys. 15 (2013) 113049.

[94] S.G. Jaloviar, J.L. Lin, F. Liu, V. Zielasek, L. Mc Caughan, M.G. Lagally, Step-induced optical anisotropy of vicinal si(001), Phys. Rev. Lett. 82 (1999) 791–794.

[95] H. Döscher, S. Brückner, T. Hannappel, Investigation of oxide removal from Si(1 0 0) substrates in dependence of the MOVPE process gas ambient, J. Cryst. Growth. 318 (2011) 563–569.

[96] M. Palummo, N. Witkowski, O. Pluchery, R. Del Sole, Y. Borensztein, Reflectance-anisotropy spectroscopy and surface differential reflectance spectra at the Si(100) surface: Combined experimental and theoretical study, Phys. Rev. B - Condens. Matter Mater. Phys. 79 (2009) 1–8.

[97] E.L. Warren, A.E. Kibbler, R.M. France, A.G. Norman, P. Stradins, W.E. McMahon, Growth of antiphase-domain-free GaP on Si substrates by metalorganic chemical vapor deposition using an in situ AsH3 surface preparation, Appl. Phys. Lett. 107 (2015) 082109.

[98] T.J. Grassman, D.L. Lepkowski, J.T. Boyer, D.J. Chmielewski, C. Yi, N. Western, H. Mehrvarz, A. Ho-Baillie, C. Kerestes, D. Derkacs, S.G. Whipple, A.P. Stavrides, S.P. Bremner, S.A. Ringel, Toward >25% Efficient Monolithic Epitaxial GaAsP/Si Tandem Solar Cells, Conf. Rec. IEEE Photovolt. Spec. Conf. (2019) 734–737.

[99] J.F. Geisz, J.M. Olson, D.J. Friedman, K.M. Jones, R.C. Reedy, M.J. Romero, Lattice-matched GaNPAs-on-silicon tandem solar cells, Conf. Rec. IEEE Photovolt. Spec. Conf. (2005) 695–698.

[100] O. Supplie, M.M. May, H. Stange, C. Höhn, H.J. Lewerenz, T. Hannappel, Materials for light-

induced water splitting: In situ controlled surface preparation of GaPN epilayers grown lattice-matched on Si(100), J. Appl. Phys. 115 (2014) 113509.

[101] T. Hannappel, W.E. McMahon, J.M. Olson, An RDS, LEED, and STM Study of MOCVD-prepared Si(1 0 0) surfaces, J. Cryst. Growth. 272 (2004) 24–29.

[102] A. Beyer, J. Ohlmann, S. Liebich, H. Heim, G. Witte, W. Stolz, K. Volz, A. Beyer, J. Ohlmann, S. Liebich, H. Heim, G. Witte, W. Stolz, K. Volz, GaP heteroepitaxy on Si (001): Correlation of Si-surface structure, GaP growth conditions, and Si-III / V interface structure, J. Appl. Phys. 111 (2012) 083534.

[103] K. Volz, A. Beyer, W. Witte, J. Ohlmann, I. Németh, B. Kunert, W. Stolz, GaP-nucleation on exact Si (001) substrates for III/V device integration, J. Cryst. Growth. 315 (2011) 37–47.

[104] O. Supplie, M.M. May, G. Steinbach, O. Romanyuk, F. Grosse, A. Nägelein, P. Kleinschmidt, S. Brückner, T. Hannappel, Time-resolved in situ spectroscopy during formation of the GaP/Si(100) heterointerface, J. Phys. Chem. Lett. 6 (2015) 464–469.

[105] L. Töben, T. Hannappel, K. Möller, H.J. Crawack, C. Pettenkofer, F. Willig, RDS, LEED and STM of the P-rich and Ga-rich surfaces of GaP(100), Surf. Sci. 494 (2001) L755–L760.

[106] H. Döscher, K. Möller, T. Hannappel, GaP(1 0 0) and InP(1 0 0) surface structures during preparation in a nitrogen ambient, J. Cryst. Growth. 318 (2011) 372–378.

[107] H. Hahn, G. Schmidt, F. Bechstedt, O. Pulci, R. Del Sole, P-rich GaP(001)(2×1)/(2×2) surface: A hydrogen-adsorbate structure determined from first-principles calculations, Phys. Rev. B - Condens. Matter Mater. Phys. 68 (2003) 2–5.

[108] P. Vogt, T. Hannappel, S. Visbeck, K. Knorr, N. Esser, W. Richter, Atomic surface structure of the phosphorous-terminated InP(001) grown by MOVPE, Phys. Rev. B - Condens. Matter Mater. Phys. 60 (1999) R5117–R5120.

[109] O. Supplie, S. Brückner, O. Romanyuk, H. Döscher, C. Höhn, M.M. May, P. Kleinschmidt, F. Grosse, T. Hannappel, Atomic scale analysis of the GaP/Si(100) heterointerface by in situ reflection anisotropy spectroscopy and ab initio density functional theory, Phys. Rev. B - Condens. Matter Mater. Phys. 90 (2014) 235301.

[110] H. Döscher, B. Kunert, A. Beyer, O. Supplie, K. Volz, W. Stolz, T. Hannappel, In situ antiphase domain quantification applied on heteroepitaxial GaP growth on Si(100), J. Vac. Sci. Technol. B. 28 (2010) C5H1-C5H6.

[111] K.J. Bachmann, Heteroepitaxy of GaP on Si(100), J. Vac. Sci. Technol. B Microelectron. Nanom. Struct. 14 (1996) 3019.

[112] U. Rossow, Optical investigations of surface processes in GaP heteroepitaxy on silicon under pulsed chemical beam epitaxy conditions, J. Vac. Sci. Technol. B Microelectron. Nanom. Struct. 14 (1996) 3040.

[113] S.D. Carnevale, J.I. Deitz, J.A. Carlin, Y.N. Picard, M.D. Graef, S.A. Ringel, T.J. Grassman, Rapid misfit dislocation characterization in heteroepitaxial III-V/Si thin films by electron channeling contrast imaging, Appl. Phys. Lett. 104 (2014) 232111.

[114] S.D. Carnevale, J.I. Deitz, J.A. Carlin, Y.N. Picard, D.W. McComb, M. De Graef, S.A. Ringel, T.J. Grassman, Applications of electron channeling contrast imaging for the rapid characterization of extended defects in III-V/Si heterostructures, IEEE J. Photovoltaics. 5 (2015) 676–682.

[115] E. Barrigón, S. Brückner, O. Supplie, P. Kleinschmidt, I. Rey-Stolle, T. Hannappel, Optical in situ monitoring of hydrogen desorption from Ge(100) surfaces, Appl. Phys. Lett. 102 (2013) 111608.

[116] S. Brückner, O. Supplie, E. Barrigón, J. Luczak, P. Kleinschmidt, I. Rey-Stolle, H. Döscher, T. Hannappel, In situ control of As dimer orientation on Ge(100) surfaces, Appl. Phys. Lett. 101 (2012) 121602.

[117] E. Barrigoń, S. Bruc̆kner, O. Supplie, H. Dos̆cher, I. Rey-Stolle, T. Hannappel, In situ study of Ge(100) surfaces with tertiarybutylphosphine supply in vapor phase epitaxy ambient, J. Cryst. Growth. 370 (2013) 173–176.

[118] M.K. Hudait, S.B. Krupanidhi, Transmission electron microscopic study of GaAs/Ge heterostructures grown by low-pressure metal organic vapor phase epitaxy, Mater. Res. Bull. 35 (2000) 125–133.

[119] M. Zorn, P. Kurpas, A.I. Shkrebtii, B. Junno, A. Bhattacharya, K. Knorr, M. Weyers, L. Samuelson, J.T. Zettler, W. Richter, Correlation of InGaP(001) surface structure during growth and bulk ordering, Phys. Rev. B - Condens. Matter Mater. Phys. 60 (1999) 8185–8190.

[120] E. Barrigon, B. Galiana, I. Rey-Stolle, Reflectance anisotropy spectroscopy assessment of the MOVPE nucleation of GaInP on germanium (1 0 0), J. Cryst. Growth. 315 (2011) 22–27.

[121] B. Galiana, E. Barrigón, I. Rey-Stolle, V. Corregidor, P. Espinet, C. Algora, E. Alves, Compositional analysis and evolution of defects formed on GaInP epilayers grown on Germanium, Superlattices Microstruct. 45 (2009) 277–284.

[122] A. Paszuk, O. Supplie, M. Nandy, S. Brückner, A. Dobrich, P. Kleinschmidt, B. Kim, Y. Nakano, M. Sugiyama, T. Hannappel, Double-layer stepped Si(1 0 0) surfaces prepared in As-rich CVD ambience, Appl. Surf. Sci. 462 (2018) 1002–1007.

[123] M. Nandy, A. Paszuk, M. Feifel, C. Koppka, P. Kleinschmidt, F. Dimroth, T. Hannappel, A Route to Obtaining Low-Defect III-V Epilayers on Si(100) Utilizing MOCVD, Cryst. Growth Des. 21 (2021) 5603–5613.

[124] L. Kipp, D.K. Biegelsen, J.E. Northrup, L.E. Swartz, R.D. Bringans, Reflectance difference spectroscopy: Experiment and theory for the model system si(001):As and application to Si(001), Phys. Rev. Lett. 76 (1996) 2810–2813.

[125] S. Logothetidis, P. Lautenschlager, M. Cardona, Temperature dependence of the dielectric function and the interband critical points in orthorhombic GeS, Phys. Rev. B. 33 (1986) 1110–1117.

[126] O.L. Alerhand, J. Wang, J.D. Joannopoulos, Kaxiras, Adsorption of As on stepped Si(100): Resolution of the sublattice-orientation dilemma, Phys. Rev. B. 44 (1991) 6534–6537.

[127] T. Hannappel, S. Visbeck, L. Töben, F. Willig, Apparatus for investigating metalorganic chemical vapor deposition-grown semiconductors with ultrahigh-vacuum based techniques, Rev. Sci. Instrum. 75 (2004) 1297–1304.

[128] F. Rochet, C. Poncey, G. Dufour, H. Roulet, W.N. Rodrigues, M. Sauvage, J.C. Boulliard, F. Sirotti, G. Panaccione, The As-terminated Si(001) surface and its oxidation in molecular oxygen: an Si 2p and As 3d core-level study with synchrotron radiation, Surf. Sci. 326 (1995) 229–242.

[129] J.J. Yeh, I. Lindau, Copyright 0 1985 by Academic Press, Inc., At. Data Nucl. Data Tables. 32 (1985) 1–155.

[130] T.J.Z. Stock, O. Warschkow, P.C. Constantinou, J. Li, S. Fearn, E. Crane, E.V.S. Hofmann, A. Kölker, D.R. Mckenzie, S.R. Schofield, N.J. Curson, Atomic-Scale Patterning of Arsenic in Silicon by Scanning Tunneling Microscopy, ACS Nano. 14 (2020) 3316–3327.

[131] M. Nandy, A. Paszuk, M. Feifel, C. Koppka, P. Kleinschmidt, F. Dimroth, T. Hannappel, A Route to Obtaining Low-Defect III–V Epilayers on Si(100) Utilizing MOCVD, Cryst. Growth Des. 21 (2021) 5603–5613.

[132] C. Frigeri, G. Attolini, C. Pelosi, Stacking fault pyramids, island growth and misfit dislocations in InxGa1−xAs-InP heterostructures grown by vapour phase epitaxy, Mater. Sci. Eng. B. 9 (1991) 115–119.

[133] V. Emberger, F. Hatami, W. Ted Masselink, S. Peters, AlP/GaP distributed Bragg reflectors, Appl. Phys. Lett. 103 (2013) 031101.

[134] M. Kumagai, T. Takagahara, E. Hanamura, Optical properties and indirect-to-direct transition of GaP/AlP (001) superlattices, Phys. Rev. B. 37 (1988) 898–915.

[135] M.P. Semtsiv, U. Müller, W.T. Masselink, N. Georgiev, T. Dekorsy, M. Helm, Intersubband transitions in GaP-AlP heterostructures, Appl. Phys. Lett. 89 (2006) 1–4.

[136] S.Y. Hwang, T.J. Kim, Y.W. Jung, N.S. Barange, H.G. Park, J.Y. Kim, Y.R. Kang, Y.D. Kim, S.H. Shin, J.D. Song, C.T. Liang, Y.C. Chang, Dielectric function and critical points of AlP determined by spectroscopic ellipsometry, J. Alloys Compd. 587 (2014) 361–364.

[137] S. Visbeck, T. Hannappel, M. Zorn, J.T. Zettler, F. Willig, Temperature dependence and origin of InP(100) reflectance anisotropy down to 20 K, Phys. Rev. B - Condens. Matter Mater. Phys. 63 (2001) 2453031–2453036.

[138] K. Werner, A. Beyer, J.O. Oelerich, S.D. Baranovskii, W. Stolz, K. Volz, Structural characteristics of gallium metal deposited on Si (0 0 1) by MOCVD, J. Cryst. Growth. 405 (2014) 102–109.

[139] K. Yamane, T. Kobayashi, Y. Furukawa, H. Okada, H. Yonezu, A. Wakahara, Growth of pit-free GaP on Si by suppression of a surface reaction at an initial growth stage, J. Cryst. Growth. 311 (2009) 794–797.

[140] G. Brocks, P.J. Kelly, R. Car, Adsorption of Al on Si(100): A surface polymerization reaction, Phys. Rev. Lett. 70 (1993) 2786–2789.

[141] B. Bourguignon, S.R. Leone, L. Carleton, Surface structures and growth, Surf. Sci. 204 (1988) 455–472.

[142] H. Maruyama, K. Pak, K. Sakakibara, H. Yonezu, Realization of nearly two-dimensional growth mode for AlP on Si(100) substrate by a low temperature migration enhanced epitaxy, Appl. Phys. Lett. 63 (1993) 2375–2377.

[143] C.J. Santana, C.R. Abernathy, S.J. Pearton, K.S. Jones, Initial growth stages of AlxGa1-xP on epitaxial silicon, J. Cryst. Growth. 164 (1996) 248–255.

[144] A. C . Lin, J. S Harris, Two-dimensional III-V nucleation on Si for nonlinear optics, J. Vac. Sci. Technol. B, Nanotechnol. Microelectron. Mater. Process. Meas. Phenom. 29 (2011) 03C120.

[145] T. George, R.E. Weber, S. Nozaki, W.T.A. and N.Noto, M. Umeno, Nucleation and defect generation in lattice matched and mismatched heteroepitaxial layers in the GaAs/$Al_x Ga_{1-x}$ P/Si system, J. Appl. Phys. 67 (1990) 2441–2446.

[146] P. Sippel, O. Supplie, M.M. May, R. Eichberger, T. Hannappel, Electronic structures of GaP(100) surface reconstructions probed with two-photon photoemission spectroscopy, Phys. Rev. B - Condens. Matter Mater. Phys. 89 (2014) 165312.

[147] O. Supplie, M.M. May, C. Höhn, H. Stange, A. Müller, P. Kleinschmidt, S. Brückner, T. Hannappel, Formation of GaP/Si(100) heterointerfaces in the presence of inherent reactor residuals, ACS Appl. Mater. Interfaces. 7 (2015) 9323–9327.

[148] A. Paszuk, A. Dobrich, C. Koppka, S. Brückner, M. Duda, P. Kleinschmidt, O. Supplie, T. Hannappel, In situ preparation of Si p-n junctions and subsequent surface preparation for III-V heteroepitaxy in MOCVD ambient, J. Cryst. Growth. 464 (2017) 14–19.

[149] C.A. Schneider, W.S. Rasband, K.W. Eliceiri, NIH Image to ImageJ: 25 years of image analysis, Nat. Methods. 9 (2012) 671–675.

[150] M.D. Abràmoff, P.J. Magalhães, S.J. Ram, Image processing with ImageJ Part II, Biophotonics Int. 11 (2005) 36–43.

[151] F. Ernst, P. Pirouz, Formation of planar defects in the epitaxial growth of GaP on Si substrate by metal organic chemical-vapor deposition, J. Appl. Phys. 64 (1988) 4526–4530.

[152] M. Nandy, A. Paszuk, K.D. Hanke, P. Kleinschmidt, T. Hannappel, Optical In Situ Studies of Ge(100) Interfacial Exchange Reactions in GaAs-Rich MOVPE Reactors for Low-Defect III-P Growth, ACS Appl. Electron. Mater. xx (2023) xxxx.

[153] B. Galiana, K. Volz, I. Rey-Stolle, W. Stolz, C. Algora, Influence of nucleation layers on MOVPE grown GaAs on Ge wafers for concentrator solar cells, Conf. Rec. 2006 IEEE 4th World Conf. Photovolt. Energy Conversion, WCPEC-4. 1 (2006) 807–810.

[154] S.N.G. Chu, S. Nakahara, S.J. Pearton, T. Boone, S.M. Vernon, Antiphase domains in GaAs grown by metalorganic chemical vapor deposition on silicon-on-insulator, J. Appl. Phys. 64 (1988) 2981–2989.

[155] G. Brammertz, Y. Mols, S. Degroote, V. Motsnyi, M. Leys, G. Borghs, M. Caymax, Low-temperature photoluminescence study of thin epitaxial GaAs films on Ge substrates, J. Appl. Phys. 99 (2006) 093514.

[156] W.E. McMahon, I.G. Batyrev, T. Hannappel, J.M. Olson, S.B. Zhang, 5-7-5 line defects on As/Si (100) : A general stress-relief mechanism for V/IV surfaces, Phys. Rev. B. 74 (2006) 033304.

[157] W.E. McMahon, J.M. Olson, Atomic-resolution STM study of a structural phase transition of steps on vicinal As/Ge(100), Phys. Rev. B. 60 (1999) 15999–16005.

[158] N.S. Fernando, T.N. Nunley, A. Ghosh, C.M. Nelson, J.A. Cooke, A.A. Medina, S. Zollner, C. Xu, J. Menendez, J. Kouvetakis, Temperature dependence of the interband critical points of bulk Ge and strained Ge on Si, Appl. Surf. Sci. 421 (2017) 905–912.

[159] T. Hannappel, S. Visbeck, L. Töben, F. Willig, Apparatus for investigating metalorganic chemical vapor deposition-grown semiconductors with ultrahigh-vacuum based techniques, Rev. Sci. Instrum. 75 (2004) 1297–1304.

[160] C.J. Powell, A. Jablonski, NIST Electron Inelastic-Mean-Free-Path Database-Version 1.2, Gaithersburg, 2010.

Acknowledgement

Throughout this Ph.D work I have received a great deal of support and assistance from many people. This work would not have been possible without their advice, guidance and encouragement. I owe special gratitude to:

- Prof. Dr. Thomas Hannappel for the continuous support of my Ph.D study and research, for his patience, enthusiasm, and immense knowledge. His dynamism, vision, sincerity and motivation have deeply inspired me. It was a great privilege and honor to work and study under his guidance.

- Prof. Dr. Stefan Krischok for taking interest to be a reviewer of this thesis.

- Dr. Frank Dimroth for his willingness to be an external reviewer.

- Dr. Sebastian Bruckner, Dr. Oliver Supplie, Dr. Anja Dobrich for their help and continuous support during the first phase of my Ph.D work. I express my special thanks to Dr. Agnieszka Paszuk who continuously helped me in experimental as well as in scientific discussions and to Dr. Peter Kleinschmidt for correcting my English and exchanging constructive discussion.

- Christian Koppka and Henry Romanus, who helped me a lot to understand the method and guided me to develop ECCI in Ilmenau.

- Antonio Müller to keep his patience to teach me in the cleanroom at the beginning and for taking care of our experimental equipment, and helping in preparing ‘transfer shuttle’ to make the work less laborious.

- Simone Gutsche for all the organizational and bureaucratic help and of course for understanding my English.

- the financial supports from German Federal Ministry of Education and Research through the project ‘MehrSi’ (BMBF, project no 03SF0525B), “H2DEMO” (ref. no. 03SF0619I), German Science Foundation (DFG, projects with ref. no. HA 3096/14-1 (PAK 981) and HA3096/10-1) and ‘Thuringian State Graduate Support’ fellowship.

- all the junior researchers in the group; Kai, Juliane, David, Amin and Sahar for your beautiful friendship and doing all the crazy things and telling hilarious stories which always bring smile on my face.

- my parents and my elder sister for their love, prayers, caring and sacrifices for educating and preparing me for my future. They have been supporting me throughout my Ph.D journey. Staying far away from home, sometimes it was difficult for them as well as for me to understand situations, but they always hold their patience and keep motivating me to be a happy and positive person.

- all the people who have supported me to complete the research work directly or indirectly.

Declaration

I certify that I have prepared this thesis without the unauthorized assistance of third parties and without the use of other than the stated aids. Data and concepts taken directly or indirectly from other sources are marked with the source. Further persons were not involved in the content wise-material production of the present work. In particular, I have not made use of the paid assistance of intermediary or consulting services (doctoral advisors or other persons) for this purpose. No one has received from me, directly or indirectly, any pecuniary benefits for work related to the content of the thesis presented. The thesis has not been submitted to any examination authority in the same or similar form, either in Germany or abroad. I have been informed that the incorrectness of the above declaration will be regarded as an attempt to deceive and will result in the unsuccessful termination of the doctoral procedure.

Place, Date Signature

List of samples

Figure	Sample(s) number
Fig. 5.1, Fig. 5.3	U1176, U1177, U0814, U0749
Fig. 5.2	U0742
Fig. 5.3	U1176, U1177
Fig. 5.4, Fig. 5.5	U1028
Fig. 5.6	U0814
Fig. 5.7	F0101
Fig. 5.8, Fig. 5.9	U0701
Fig. 5.10	U1140, U1141 - RAS and XPS
Fig. 6.1	U0949
Fig. 6.2	U0902
Fig. 6.3	U0949, U0902
Fig. 6.4	U0885, U1142
Fig. 6.5	U0576
Fig. 6.6	U0628
Fig. 6.7	U0586
Fig. 6.9, Fig. 6.10	U0865, U0867, U0868, U0869
Fig. 6.11	U1070, U1071, U1011,
Fig. 6.12	U1011, U1012
Fig. 6.13, Fig. 6.14, Fig. 6.15, Fig. 6.19	U0884, U0956, U0958
Fig. 6.16	U0959, U1029
Fig. 6.17	U0884, U0958

Fig. 6.18	U1030, U1032
Fig. 6.20	U1040
Fig. 7.1	W4223, W4188, W4209 - STM
Fig. 7.2	W4228
Fig. 7.3	W4359, W4360, W4363, W4364
Fig. 7.4	W4363, W4364
Fig. 7.5	W4144-Ref, W4363, W4364
Fig. 7.6, Fig. 7.7, Fig. 7.8	W4359, W4360, W4361, W4362